

AD-A084 120

GENERAL MOTORS CORP INDIANAPOLIS IN DETROIT DIESEL A--ETC F/6 21/5

HIGH-TEMPERATURE RADIAL TURBINE DEMONSTRATION.(U)

APR 80 B A EWING, D S MONSON

DAAJ02-77-C-0031

UNCLASSIFIED

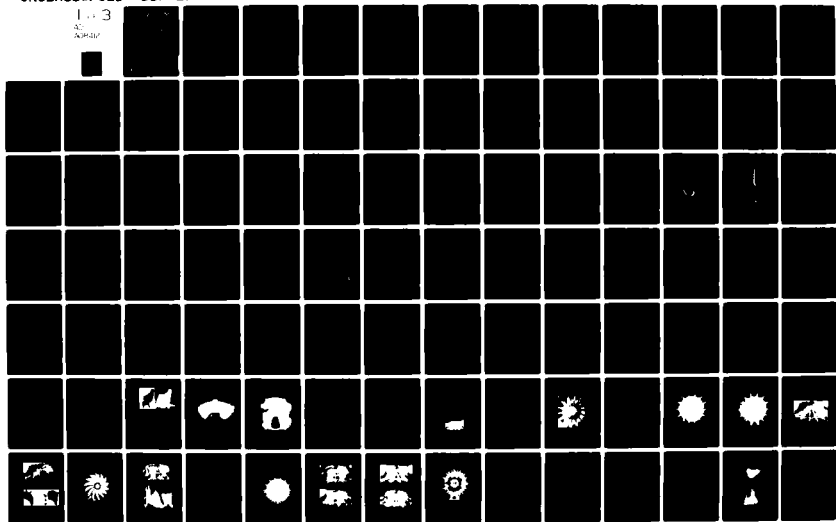
DDA-EDR-9990

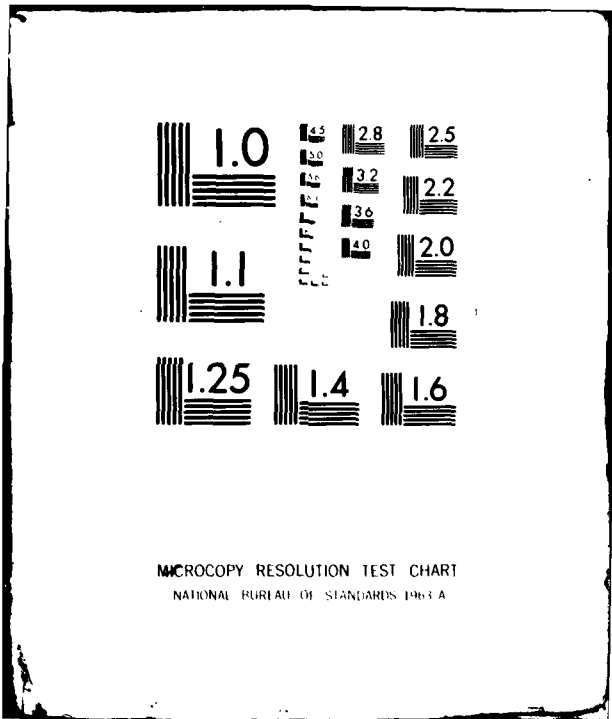
USAAVRADCOM-TR-80-D-6

NL

1-3

AD
A084120





MICROCOPY RESOLUTION TEST CHART
NATIONAL BUREAU OF STANDARDS 1963-A

USAAVRADCOM-TR-80-D-6

LEVEL III



HIGH-TEMPERATURE RADIAL TURBINE DEMONSTRATION

Donald S. Monson, B. A. Ewing
DETROIT DIESEL ALLISON DIVISION
General Motors Corporation
Box 894
Indianapolis, Ind. 46206



April 1980

ADA084120

Final Report for Period 15 June 1977 - 15 November 1979

Approved for public release;
distribution unlimited.

Prepared for
APPLIED TECHNOLOGY LABORATORY
U. S. ARMY RESEARCH AND TECHNOLOGY LABORATORIES (AVRADCOM)
Fort Eustis, Va. 23604

DDG FILE COPY

80 5 12 058

APPLIED TECHNOLOGY LABORATORY POSITION STATEMENT

This report provides the documentation for a program which has developed the manufacturing capability for high-temperature cooled radial turbines for small gas turbine engines. The resulting technology is considered feasible and significantly expands the usable cycle conditions under which a radial turbine can be utilized. The tests and substantiation of this turbine and materials technology are considered meaningful and sufficient and provide complete validation of this technology short of full-scale engine testing. Results of this contract will be utilized extensively in the future for new high performance small gas turbine engines.

Mr. Jan M. Lane of the Aeronautical Technology Division, Propulsion Technical Area, served as Project Engineer for this effort.

DISCLAIMERS

The findings in this report are not to be construed as an official Department of the Army position unless so designated by other authorized documents.

When Government drawings, specifications, or other data are used for any purpose other than in connection with a definitely related Government procurement operation, the United States Government thereby incurs no responsibility nor any obligation whatsoever; and the fact that the Government may have formulated, furnished, or in any way supplied the said drawings, specifications, or other data is not to be regarded by implication or otherwise as in any manner licensing the holder or any other person or corporation, or conveying any rights or permission, to manufacture, use, or sell any patented invention that may in any way be related thereto.

Trade names cited in this report do not constitute an official endorsement or approval of the use of such commercial hardware or software.

DISPOSITION INSTRUCTIONS

Destroy this report when no longer needed. Do not return it to the originator.

Unclassified

SECURITY CLASSIFICATION OF THIS PAGE (When Data Entered)

19 REPORT DOCUMENTATION PAGE		READ INSTRUCTIONS BEFORE COMPLETING FORM	
18 1. REPORT NUMBER USAAVRADCOM TR-80-D-6	2. GOVT ACCESSION NO. AD-A084120	3. RECIPIENT'S CATALOG NUMBER repts	
6 4. TITLE (and Subtitle) HIGH-TEMPERATURE RADIAL TURBINE DEMONSTRATION	7. AUTHOR(s) B. A. Ewing & S. Monson	8. PERFORMING ORG. REPORT NUMBER DDA-EDR-9990	5. TYPE OF REPORT & PERIOD COVERED Final 15 Jun 1977 - 15 Nov 1979
		9. PERFORMING ORGANIZATION NAME AND ADDRESS Detroit Diesel Allison Division General Motors Corp Box 894, Indianapolis, Indiana 46206	10. PROGRAM ELEMENT, PROJECT, TASK AREA & WORK UNIT NUMBERS 62209A 1L262209AH76 00194 EK
		11. CONTROLLING OFFICE NAME AND ADDRESS Applied Technology Laboratory, US Army Research and Technology Laboratories (AVRADCOM) Fort Eustis, Virginia 23604	12. REPORT DATE Apr 80
		14. MONITORING AGENCY NAME & ADDRESS (if different from Controlling Office) 2047	13. NUMBER OF PAGES 203
			15. SECURITY CLASS. (of this report) Unclassified
			15a. DECLASSIFICATION/DOWNGRADING SCHEDULE
16. DISTRIBUTION STATEMENT (of this Report) Approved for public release; distribution unlimited.			
17. DISTRIBUTION STATEMENT (of the abstract entered in Block 20, if different from Report)			
18. SUPPLEMENTARY NOTES			
19. KEY WORDS (Continue on reverse side if necessary and identify by block number) Hot Isostatic Pressing, Investment Casting, Gas Turbine Components, Radial Turbine Design, Nondestructive Testing, Powder Metallurgy, Superalloys, High Temperature Materials			
20. ABSTRACT (Continue on reverse side if necessary and identify by block number) The objective of this program was to provide and demonstrate the technology required to economically manufacture a cooled, high-temperature, radial turbine with sufficient integrity and aerodynamic performance to meet future Army requirements for a reliable, low-cost, high performance, small gas turbine engine. The work to accomplish this objective was subdivided into three phases.			

019200

Unclassified

SECURITY CLASSIFICATION OF THIS PAGE(When Data Entered)

The first phase was the detailed design of an air cooled radial turbine rotor and the development of the process required for its manufacture. A dual material property design was selected which used a cast Mar-M247 airfoil shell diffusion bonded to a PA101 powder metal disk. This approach provided the required material strength for the temperature/stress environment for both components. Seven stylized castings were produced using modified existing tooling to establish casting parameters. Four shell and disk assemblies were cut up to examine the bond line and to obtain material property specimens. Excellent bond line quality was obtained and material properties met design goals. Nondestructive inspection (NDI) techniques, using ultrasonic scanning, were developed.

The second phase was that of the fabrication of the detail design developed in Phase I. Six castings were poured. Following the adjustment of casting parameters, four castings were poured which exhibited excellent wall thickness control and surface finish. Four final design rotor assemblies were produced for mechanical integrity and aerodynamic evaluation. In addition, two stylized rotor assemblies were made and subjected to NDI and cup-up evaluation. Specimens were obtained from these rotors for further material property evaluation.

The third phase was that of mechanical integrity verification consisting of nondestructive bond line inspection, additional material property determination, and rotor spin test. One final design rotor was cut up to verify an NDI indication of a no-bond area. This condition was verified and was found to result from poor braze seal. The material properties obtained during this phase showed good agreement with the design goals and Phase I results. Spin test of the strain gaged instrumented rotor showed excellent agreement between predicted and actual bore stress. A spin to burst test was terminated at 131 percent of design speed by a test equipment failure. The demonstrated over-speed capability was in excess of that normally associated with gas generator turbine design. A 6000 cycle low cycle fatigue spin test with the rotor bore temperature maintained at 1100^oF was successfully accomplished.

Aerodynamic testing is to be conducted with the rotor assembly. The results of this work will be published in a subsequent report.

Unclassified

SECURITY CLASSIFICATION OF THIS PAGE(When Data Entered)

PREFACE

The authors are grateful for the significant contributions made to the program by other Detroit Diesel Allison (DDA) personnel. Messrs. D. L. Tipton, R. E. Jeffries, and A. F. Ahles provided technical guidance for the aero, mechanical, and heat transfer design, respectively. G. L. Vonnegut, S. J. Miller, E. W. Sodeberg, J. L. Pierson, and K. A. Green are acknowledged for their contributions to the manufacturing process development effort. The DDA Electronics and Parts Test Department provided the special skills and equipment required for conducting the difficult testing associated with this program.

The authors are also grateful for the program guidance, suggestions, and technical support provided by Mr. Jan Lane of the Applied Technology Laboratory, U. S. Army Research & Technology Laboratories (AVRADCOM).

Accession For	
NTIS GWS&I	<input checked="" type="checkbox"/>
DDC TAB	
Unannounced	
Justification	
By _____	
Distribution/	
Availability Codes	
Dist	Available/or special
A	

TABLE OF CONTENTS

	<u>Page</u>
PREFACE.	3
LIST OF ILLUSTRATIONS.	7
LIST OF TABLES	11
INTRODUCTION	12
PHASE I--DETAILED DESIGN AND MANUFACTURING PROCESS DEVELOPMENT	14
Detailed Design	14
Design Point and Overall Engine Configuration.	14
Design Constraints	19
Aerodynamic Design	25
Mechanical Design	34
Structural Design	44
Heat Transfer.	54
Manufacturing Process Development	66
Airfoil Shell Fabrication Development.	68
Shell/Disk Bond Development.	91
Weld Seal Development.	121
Nondestructive Inspection Development.	128
Production Cost Analysis.	137
PHASE II--FABRICATION.	140
Tool Construction	140
Material Property Specimens	140
Stylized Rotor Specimens	140
Ultrasonic C-Scan Inspection	144
Laboratory Specimens	146
Final Design Rotor Fabrication.	147
Castings	147
Disks.	160

	<u>Page</u>
PHASE III--MECHANICAL INTEGRITY VERIFICATION.	172
Material Property Verification	172
PA101/Mar-M247 Butt Joint Test Results.	172
Parent Metal PA101 Test Results	174
Cast-to-Size Mar-M247 Test Results.	177
Final Design Rotor Spin Testing.	177
Stress Correlation Test	181
Low Cycle Fatigue Test.	182
Rotor Burst Test.	189
CONCLUSIONS	196
RECOMMENDATIONS	197
REFERENCES	198
APPENDIXES	
A - Certificate of Test.	199
B - Chemistries and Casting Parameters of Mar-M247 Test Bars	200
C - Chemistry, Tip Response, and Mechanical Properties for Test Rings	201
D - Wall Metal Temperatures.	202

LIST OF ILLUSTRATIONS

<u>Figure</u>		<u>Page</u>
1	High-temperature radial turbine (HTRT) cycle parameters, intermediate rated power	15
2	HTRT cycle parameters, 75% IRP.	16
3	Engine configuration comprising air-cooled radial turbine . . .	17
4	Influence of exducer hub-tip radius ratio on turbine efficiency.	21
5	Influence of tip diameter on 100% speed line performance. . . .	21
6	Influence of tip diameter on efficiency at design expansion ratio	22
7	Influence of vane angle on efficiency at design expansion ratio	23
8	Experimental effect of blade number on turbine efficiency . . .	24
9	HTRT flow path and mean velocity diagrams	26
10	Meridional distribution of blade angle along hub streamline . . .	27
11	Radial distribution of relative blade exit angle.	28
12	Radial distribution of turbine work and exit swirl angle. . . .	29
13	HTRT design point diagrams.	30
14	Blade-to-blade velocity distribution--hub streamlines	31
15	Blade-to-blade velocity distribution--mean streamlines.	31
16	Blade-to-blade velocity distribution--shroud streamlines. . . .	32
17	Calculated streamline positions of HTRT rotor	33
18	HTRT efficiency	35
19	HTRT equivalent flow.	36
20	Radial distribution of rotor trailing edge radius	37
21	Isometric view of HTRT rotor.	37
22	y-z view of HTRT rotor.	38
23	Location of y and z planar slices	39
24	Planar y-cuts of HTRT rotor	40
25	Planar z-cuts of HTRT rotor	41
26	HTRT rotor final configuration.	43
27	Finite element model used for stress analysis	45
28	Line of constant tangential blade wall thickness.	46
29	Lines of constant true blade wall thickness	47
30	Equivalent stress (elastic)	48
31	Tangential stress (elastic)	49
32	Radial stress (elastic)	50
33	Axial stress (elastic).	51
34	Isotherm plot for 100% intermediate rated power	52
35	Stress rupture life in hours.	53
36	Low cycle fatigue properties.	55
37	Blade external heat transfer coefficient.	58
38	Blade external adiabatic wall temperature	59
39	Platform film adiabatic wall temperature.	60
40	Forward face boundary conditions.	61
41	IRP internal flow pressures	64
42	Isotherm plot for 75% IRP	65
43	Manufacturing process development program	68
44	Stylized airfoil shell detail	69

<u>Figure</u>		<u>Page</u>
45	Typical core before and after wax injection	70
46	Airfoil waxes in the assembly fixture	71
47	Wheel assembly with wax welded airfoils in position	72
48	Core printout variations investigated during Phase I.	74
49	No. 1 airfoil casting	75
50	No. 2 airfoil casting	77
51	Macroetched No. 1 airfoil casting	79
52	Macroetched No. 2 airfoil casting	80
53	Side view of macroetched No. 1 airfoil casting.	81
54	Side view of macroetched No. 2 airfoil casting.	82
55	Typical airfoil cross sections from airfoil casting No. 2	82
56	Macroetched No. 3 airfoil casting	83
57	Side view of macroetched No. 3 airfoil casting.	84
58	Core shift which occurred during wax injection.	84
59	Macroetched No. 4 airfoil casting	86
60	Side view of No. 4 airfoil casting.	87
61	Side view of No. 5 airfoil casting.	87
62	Side view of No. 6 airfoil casting.	88
63	Side view of No. 7 airfoil casting.	88
64	Airfoil casting No. 7 conical ID printout	89
65	Bonding development program	92
66	Subscale PA101 plug for bonding development	93
67	Powdered metal plug	94
68	Stylized rotor assembly	97
69	Machined plug and shell details for rotor assembly No. 1.	97
70	Braze sealed stylized rotor assembly.	98
71	Stylized rotor assembly with blade tips removed	100
72	Macro cross section of the No. 1 HIP-bonded assembly.	101
73	Macro cross section of the No. 2 HIP-bonded assembly.	101
74	Photomicrographs of bond lines.	102
75	Joint specimen location	103
76	Cut-up diagram for PA101 plug material.	104
77	Microshrinkage in radius section of bond joint that failed on loading.	108
78	Fine microshrinkage associated with low ductility--1400°F Mar-M247 stress rupture bar	110
79	Plug braze of three printout holes in rotor No. 3	111
80	Rotor No. 3 after grinding excess braze and polishing	112
81	Mar-M247 core printout plugs.	113
82	Rotor No. 4 rough machined showing three plugs prior to insertion into printouts.	113
83	Rotor No. 4 following plug braze cycle.	114
84	Rotor No. 4 following grind operation	115
85	Rotors No. 3 and 4 following HIP bonding	117
86	Brazed plugs in rotors No. 3 and 4.	118
87	Bond line in rotors No. 3 and 4	119
88	Interface of PM hub, cast shell, and printout plug in rotor No. 4	120
89	Weld seal test coupon prior to assembly	122
90	Weld seal test coupon with Hastelloy S filler wire laser tacked over joint areas	122

<u>Figure</u>		<u>Page</u>
91	HIP-bond sample following vacuum sealing by electron beam welding	122
92	Cracking observed in conventional electron beam welds	123
93	Cracking observed in circle generator electron beam welds	124
94	Completed weld coupons.	126
95	Weld coupon bond joint OG-3	126
96	Cast alloy failure location in PA101/Mar-M247 weld sealed joint specimen.	128
97	Schematic showing joint design for a HIP-bond processed air-cooled radial turbine wheel	129
98	Test setup for the ultrasonic inspection of the cylindrical portion of a bond line.	130
99	Test setup for the ultrasonic inspection of the conical portion of the bond line.	131
100	Test pieces and associated transducers employed to develop ultrasonic inspection techniques.	132
101	Resolution test piece sketch.	132
102	Stylized and full-scale resolution test pieces.	133
103	Resolution piece multiple C-scans with increasing gain for stylized cylindrical section.	135
104	Resolution piece multiple C-scan record for stylized conical section	135
105	Resolution piece multiple C-scan record for full-scale cylindrical section	136
106	Resolution piece multiple C-scan record for full-scale conical section	136
107	Wax injection die for full-scale HTRT airfoil shells.	141
108	Core die and resultant core for an air-cooled HTRT airfoil shell	142
109	Fixture used to assemble full-scale HTRT airfoil patterns	143
110	Diffusion bond joint in rotor No. 5	145
111	Diffusion bond between core printout plug and hub in rotor No. 5	145
112	Contaminant layer in portion of joint in rotor No. 5.	146
113	Full-scale HTRT casting No. 1	149
114	Wall thicknesses in comparable sections of eight airfoils	152
115	Gating arrangement for full-scale HTRT casting No. 2.	153
116	Bottom fill and "spoke-type" gating to improve fill in exducer airfoil tips.	154
117	Microstructure of full-scale HTRT casting No. 2	155
118	Full-scale HTRT casting No. 2	156
119	Wax pattern and gating assembly for full-scale HTRT casting No. 3	156
120	Oblique view of wax pattern and gating assembly for HTRT casting No. 3	157
121	Ingates, tapered downpole, exducer gates, and ID grain size in HTRT casting No. 3	158
122	Macrostructure of HTRT casting No. 3.	158
123	Casting No. 4 with area of shrinkage.	159
124	Schematic of full-scale PA101 plug detail for HTRT rotors	160
125	Full-scale PA101 plug detail as received from Special Metals.	162

<u>Figure</u>		<u>Page</u>
126	Typical braze-plugged shell for full-scale HTRT assembly. . . .	162
127	Machined details prior to assembly.	163
128	Ultrasonic C-scan trace showing predicted no-bond area on full-scale rotor assembly No. 1.	163
129	Macrostructure of section taken through HTRT assembly No. 1 . . .	165
130	Microstructures showing good bond quality in sections of HTRT assembly No. 1.	166
131	Appearance of braze seals in rear conical joint locations . . .	167
132	Core plug that has lost seal integrity.	168
133	Machined shell and hub details for rotor assembly No. 3	170
134	Forward face of finish-machined HTRT rotor assembly showing retention scheme.	170
135	Aft face of HTRT rotor assembly	171
136	Side view of finish-machined HTRT rotor assembly.	171
137	Specimen location for PA101 hubs.	172
138	Specimen location for stylized rotors	173
139	Microshrinkage in cast alloy surface of PA101/Mar-M247 butt joint specimen.	175
140	SEM photomicrograph of aluminum-hafnium-rich inclusion.	177
141	Analysis of inclusion in Figure 140	178
142	Pore-type origin in fracture surface of smooth-bar LCF specimen.	179
143	Comparison of hybrid processed and non-HIP-bond-processed Mar-M247 bars	180
144	HTRT rotor mounted on spin pit cover/drive assembly	181
145	Strain gage locations	182
146	Microstrain and stress versus speed	183
147	Microstrain and stress versus speed	184
148	Heat enclosure configuration.	185
149	Equivalent bore stress versus speed	186
150	Elevated temperature low cycle fatigue test time-speed-temperature sample record.	187
151	Attempted HTRT rotor burst.	189
152	Rotor assembly following burst test	190
153	Spin adapter.	191
154	Rotor assembly front face	192
155	Macroetched polished section of rotor assembly.	194
156	Photomicrographs of bond line	195
D-1	HTRT wall metal temperatures.	203

LIST OF TABLES

<u>Table</u>		<u>Page</u>
1	HTRT design point conditions	18
2	Compressor design goals vs experience.	18
3	Comparison of Mar-M200, Mar-M246, and Mar-M247 compositions. . .	67
4	PA101 alloy composition (IN-792 + Hf).	67
5	Casting conditions for stylized air-cooled Mar-M247 rotor shells	75
6	Wall thickness data for air-cooled stylized airfoil castings . .	76
7	PA101 TIP response	96
8	Mechanical properties for material representative of PA101 plug details	96
9	Test results for rotor assemblies 1 through 4.	105
10	Electron beam weld parameters.	125
11	Test results for PA101/Mar-M247 joint specimens machined from HIP-bonded weld seal coupons	127
12	Smallest detectable flat-bottom hole	134
13	Processing history for parent metal PA101 and Mar-M247	146
14	Wax pattern wall thickness measurements.	148
15	Metal wall thicknesses of full-scale HTRT castings	149
16	Phase III material property tests.	173
17	Test results for PA101/Mar-M247 butt joints.	174
18	Test results for hybrid processed parent metal PA101	176
19	Test results for hybrid processed metal Mar-M247 cast-to-size test bars.	179
20	Bore stresses at maximum stress locations.	182
21	Rotor dimensional comparison	188
22	Rotor dimensional comparison	193

INTRODUCTION

The radial turbine has proved to be a very attractive component for small Army gas turbine engines. The concept of radial entry and axial discharge, both on paper and in actual engine operation, has clearly demonstrated a capability to utilize hot gas energy beyond the levels small axial turbines can accommodate and in a more efficient manner. For engines approximately 5 lbm/sec or less, the radial turbine permits somewhat higher cycle pressure ratios with higher turbine and cycle efficiencies at essentially equivalent turbine inlet temperatures. This permits reduced fuel consumption while also reducing the number of parts, engine length, and cost. While the use of radial turbines has been limited basically because of geometric/flow constraints on engine size, the primary limitation has been fabricability and the constraint to operate at lower turbine inlet temperatures consistent with uncooled designs machined from forgings vs integral castings.

The need for increased cycle performance and further reduced fuel consumption therefore dictates the requirement for higher turbine inlet temperatures. For Army gas turbines with power turbine requirements, 2300 to 2500°F appears to be an attractive goal. In the absence of advanced materials such as ceramics, the extension of cooling technology from axial turbines has been attempted; however, the design approaches integrated with fabrication technology have been fraught with difficulty. It has been shown, nonetheless, that a single radial turbine operating at elevated temperatures can generate sufficient work to produce attractive cycle pressure ratios and significant reductions in fuel consumption.

Additionally, it has been concluded that for high temperature operation including cooled blading, the single most critical parameter limiting radial turbine performance is the stress distribution. Rotor stresses limit the achievable tip speeds to nonoptimum levels because of excessive bore stresses particularly in the presence of front drive power turbine shafting causing sizable bore holes in the rotor. Rotor stresses also force the designer to utilize radial blade sections to prevent additional bending loads superimposed on already high centrifugal blade stresses, and this creates nonoptimum incidence at the rotor inlet.

The first major attempt at an internally cooled radial turbine rotor was initiated under US Army Aviation Material Laboratories funding in 1968.^{1,2} This program, with Pratt & Whitney Aircraft, produced a rather bold design for 2300°F turbine inlet temperature including a 2300 ft/sec tip speed and an expansion ratio of 5:1 which yielded a corrected stage work of better than 40 Btu/lbm. This resulting design was matched with an 18:1 compressor at 5-lbm/sec engine airflow, and the 220 Btu/lbm was a respectable work output

1. G. S. Calvert, and U. Okapuu, Design and Evaluation of a High-Temperature Radial Turbine--Phase I, USAAVLABS, Technical Report 68-69, U.S. Army Aviation Materiel Laboratories, Fort Eustis, Virginia, January 1969, AD688164.
2. G. S. Calvert, S. C. Beck, and U. Okapuu, Design and Experimental Evaluation of a High Temperature Radial Turbine, USAAVLABS Technical Report 71-20, Eustis Directorate, U.S. Army Air Mobility R&D Laboratory, Fort Eustis, Virginia, May 1971, AD726466.

at the predicted efficiency of 87.5%. This design required 3% of engine airflow for rotor blade cooling, and design life constraints dictated allowable stresses in the blades and hub which were consistent with the material capabilities of cast IN-100 material. The bore hole for this design was considerably smaller than current front drive requirements would dictate; this factor relieved the tip speed limitation somewhat.

Although this design clearly displayed the significant advantages of radial turbines, in Army gas turbine engines the fabrication of test hardware was met with problems. First attempts to cast the rotors as integral pieces with ceramic cores forming cooling passages resulted in gross nonfill, core breakage, and distortion. Bicasting was investigated where the blades were separately cast and the hub was cast around the blade roots. This technique was also unsuccessful; however, with the incorporation of weld repair, the structurally limited rotor was tested anyway. The subsequent testing was halted after achieving 2045°F at well below design speeds; however, measured performance at lower, corrected conditions verified rotor design point performance. The desire for cooled, radial turbines fabricated in a structurally sound manner was growing still stronger.

Since the bicasting approach offered a less complex problem incorporating state-of-the-art casting of turbine blades, this effort was continued by the Army Materials and Mechanics Research Center.³ Although positive recommendations surfaced from this effort, a complete solution to the structural integrity problem was not achieved.

Early in 1976 several other potential solutions to the cooled radial turbine fabrication problem surfaced. Both in-house and Government-funded effort at several locations indicated that new fabrication technologies may exist that could be scaled up to production processes for fabricating these rotors. While casting technology had also advanced, it was clear that in order to provide realistic bore diameters under properly imposed fatigue life and burst requirements, wrought properties in the bore are necessary to achieve maximum tip speeds.

Detroit Diesel Allison was awarded Contract DAAJ02-77-C-0031 in June 1979 with an objective of providing and demonstrating the technology required to manufacture economically a cooled, high temperature radial turbine with sufficient integrity and aerodynamic performance to meet future Army requirements for small gas turbine engines. The design approach selected for the turbine utilized a cast Mar-M247 air-cooled airfoil shell Hot Isostatic Pressure (HIP) bonded to a PA101 powder metal hub. This approach provided the material properties required for both the airfoil shell and the hub. A program that consisted of detailed design and manufacturing process development, fabrication of rotor assemblies, and mechanical integrity verification was conducted. The results of this program are reported in the subsequent text.

3. P. R. Smoot, Turbine Blade Joining by Casting, AMMRC TN78-9, Army Materials and Mechanics Research Center, Watertown, Maine, November 1978.

PHASE I--DETAILED DESIGN AND MANUFACTURING PROCESS DEVELOPMENT

DETAILED DESIGN

A detailed design of a high-temperature, air-cooled, radial turbine suitable for a small, front-drive turboshaft engine has been completed. To ensure that the design is representative of that required for a viable production engine, the following studies were made:

- Design point and overall engine configuration
- Design constraints
- Aerodynamic design
- Structural design
- Heat transfer

Design Point and Overall Engine Configuration

The high-temperature radial turbine (HTRT) rotor design is based on a hypothetical engine configuration which incorporates the following requirements:

- o Required Turbine Design Point Parameters
 - o Rotor inlet temperature 2300°F
 - o $\Delta H/\theta_{std}$, $\theta_{std} = RIT/T_{std}$ 32 Btu/lb
 - o Total-to-total efficiency 86%
- o Required Engine Characteristics
 - o Free-turbine turboshaft engine application
 - o Front drive concentric with engine center line
 - o Small engine, approximately 5 lb/sec
 - o Air cooled

The cycle selected to satisfy these desired characteristics is presented in Figure 1. The radial inflow gas generator turbine with an equivalent work ($\Delta H/\theta_{std}$) of 32 Btu/lb would be capable of driving a 12:1-pressure-ratio compressor. The engine sized for a compressor airflow of 5.35 lb/sec would provide a 100% intermediate rated power (IRP) shaft horsepower of 1000 under sea level standard (SLS) conditions. The part-power specific fuel consumption (SFC) of such a configuration is .50 lb/HP hr as indicated in Figure 2. Design point conditions for the radial-inflow gas generator (HTRT) turbine are presented in Table 1.

The general engine arrangement, illustrated in Figure 3, comprises an axial-centrifugal compressor, a reverse-flow annular combustor, a radial-inflow gas generator turbine, and a two-stage axial power turbine. The engine compressor configuration is an adaptation of Allison XC-9 and Model 250-C30 technology. The design goals and the demonstrated experience are compared in Table 2. The centrifugal stage is based on the -C30 impeller with a 0.150-inch reduction in impeller exit radius to account for the decrease in design pressure ratio from 8.5 to 8.0. The -C30 ID and OD have been modified to account for the reduction in corrected inlet flow from 5.6 to 3.826 lbm/sec. The -C30 diffuser OD remains unchanged; its ID is reduced by 0.300 inch.

MIP BOND RADIAL TURBINE
TAMB = 518.670 PAMB = 14.696 VEL KT = 0.0 VEL MN = 0.0 APR = 0.990 ALT = 77/347 11:08:12 13DEC-77
COMP TIME = 0.01 SEC

TEMP	14.569	WRT/D	4.96	PRES RATIO	0.7890	ETA	1.000	DELTA	0.999	F/A	0.0	ENHALPY	123.92	AREA	0.0
518.670	13.494	4.95	10.550	3.285	0.9900	2.191	10.288	0.02299	0.0	0.0	273.12	1.931	0.0	0.0	
1330.10	11.191	4.75	3.485	3.842	0.8650	3.842	3.023	0.02299	0.0	0.0	218.19	0.744	0.0	0.0	
1992.84	4.244	4.75	3.390	3.899	0.0	3.899	3.023	0.02299	0.0	0.0	203.92	0.0	0.0	0.0	
1992.84	4.244	4.90	1.000	3.038	0.8870	3.038	1.000	1.000	0.02187	0.0	398.20	14.385	0.0	0.0	
1992.84	4.244	4.98	0.0	3.046	0.0	3.046	1.000	1.000	0.02147	0.0	398.20	14.385	0.0	0.0	
1579.81	16.149	4.98	0.0	0.0	0.0	0.0	0.0	0.0	0.0	0.0	389.13	39.283	0.0	0.0	
1579.81	16.149	0.0	0.0	0.0	0.0	0.0	0.0	0.0	0.0	0.0	389.13	39.283	0.0	0.0	
1543.19	14.696	4.98	1.099	0.0	0.0	0.0	0.0	0.0	0.0	0.0	389.13	39.283	0.0	0.0	
1543.19	14.696	4.98	1.099	0.0	0.0	0.0	0.0	0.0	0.0	0.0	389.13	39.283	0.0	0.0	

BLEED PERCENTAGES, DT RISE, FLOWS, TEMPERATURES, PRESSURES, AND RETURN STA.

COMP NO.	0.0300	0.0150	0.0080	0.0	0.0	0.0	0.0	0.0	0.0	0.0	0.0	0.0	0.0	0.0	0.0
1	1.0000	0.0000	0.0000	0.0	0.0	0.0	0.0	0.0	0.0	0.0	0.0	0.0	0.0	0.0	0.0
1	0.4475	0.0116	0.0073	0.0	0.0	0.0	0.0	0.0	0.0	0.0	0.0	0.0	0.0	0.0	0.0
1	1133.49	157.49	1133.49	0.0	0.0	0.0	0.0	0.0	0.0	0.0	0.0	0.0	0.0	0.0	0.0

SMP 0.747990E+03 0.503304E+00 0.109790E+03 0.791906E+03 0.475393E+00 0.375467E+03
MGT VEL 0.769987E+03 0.184000E+05 0.120000E+02 0.990000E+00

RC = 10.550 EFF = 0.7890 WRTZD = 4.96 HP = 1061.9
R = 0.9850 EFF = 0.9900 ROT = 2530.0
RE = 3.342 EFF = 0.8650 AIT = 2530.0 WRTZD = 1.068 MP = 1061.9
R = 0.9850
WC = 0.030 MTC = 11
RE = 2.760 EFF = 0.8870 AIT = 1969.0 WRTZD = 3.221 MP = 748.0
WC = 0.015 MTC = 21
R = 1.0000
RJ = 1.099 AREA = 39.28 WC = 4.975

MA = 4.910 ALT = 0. TAMB = 518.67 VEL = 0.0 MACH = 0.0

FUEL FLOW 0.375467E+03
INLET EFF 0.990000E+00

1
MPC
2
PBURN
3
MPT
4 DELP
5 TCOOL
6
7 TCOOL
8 DELP
9
NOZZLE
11

Figure 2. High-temperature radial turbine cycle parameters, 75% IRP.

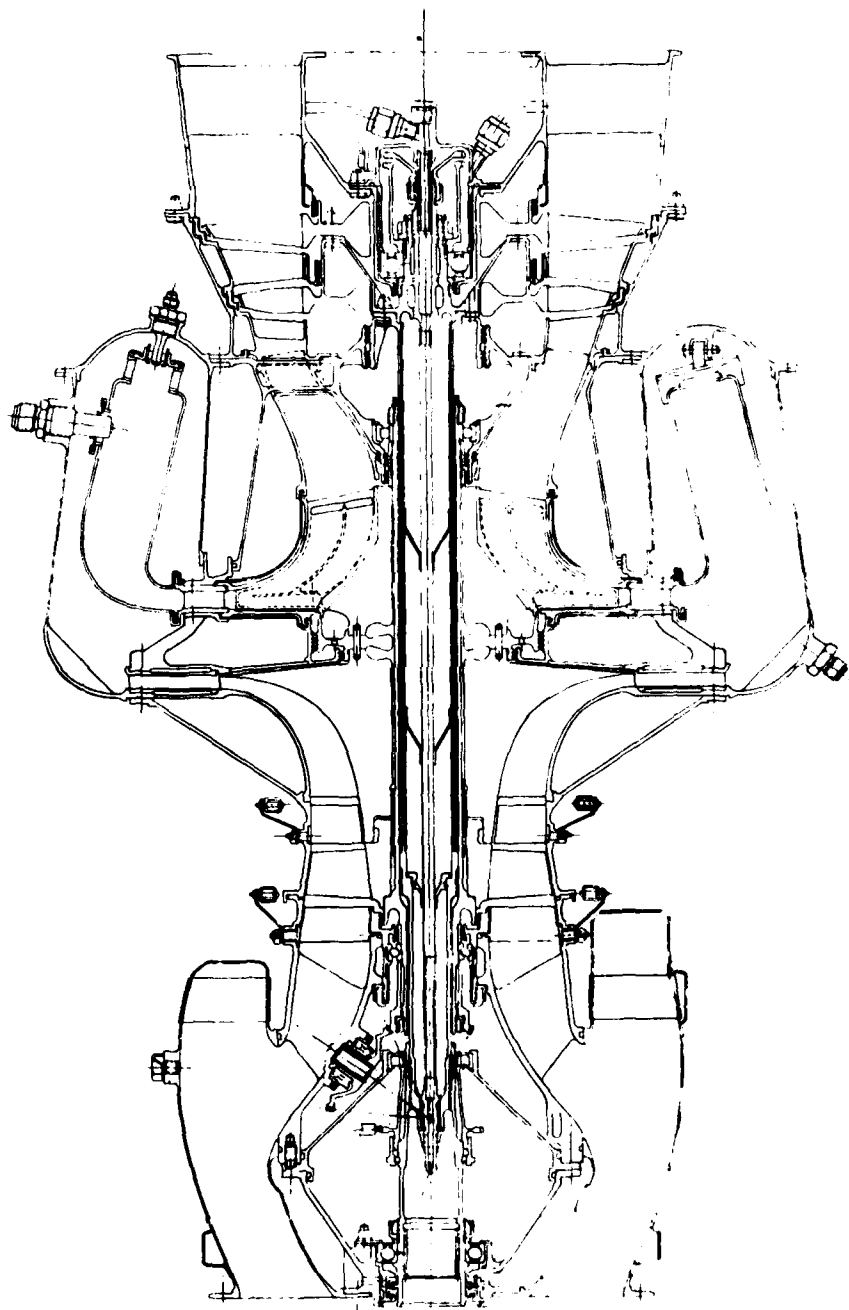


Figure 3. Engine configuration comprising air-cooled radial turbine.

TABLE 1. HTRT DESIGN POINT CONDITIONS

Blade Inlet Total Temperature (T_T)	2760°R (2300°F)
Theta Critical (θ_{CR})	5.1541
Epsilon (ϵ)	1.0448
Gamma (γ)	1.3158
Vane Inlet Total Pressure (P_T), psia	172.0
Blade Inlet Gas Flow (W_G), lb/sec	5.20
Blade Inlet Corrected Gas Flow ($W_G \sqrt{\theta_{CR} \epsilon / \delta}$), lb/sec	1.05
Blade Inlet Fuel/Air Ratio (F/A)	0.02593
Rotational Speed (N), rpm	54862
Corrected Rotational Speed ($N \sqrt{\theta_{CR}}$), rpm	24099
Direction of Rotation as Viewed from the Rear of the Turbine	Counterclockwise
Horsepower	1258
Work (Δh), Btu/lb	171.0
Corrected Work ($\Delta h / \theta_{CR}$), Btu/lb	33.2
Expansion Ratio (R_e)	3.30 (total-total)
Efficiency Goal (η), %	86.5% (total-total)

TABLE 2. COMPRESSOR DESIGN GOALS VS EXPERIENCE

	Design Goals		DDA Experience	
	Axial	Centrifugal	KC-9 (80% $N \sqrt{\theta}$)	-C30
R_c	1.50	8.0	1.56	8.5
Number of stages	1	1	1	1
$U_T / \sqrt{\theta}$, ft/sec	1357	1234	1320	1237
(H/T) _{inlet}	0.45	0.606	0.528	0.367
η_c , %	82 (est)	79-80 (est)	88 (test)	78 (test)
$W \sqrt{\theta \delta}$, lbm/sec	---	3.83	---	5.6
$N \sqrt{\theta}$, rpm	---	50,880	---	51,000

The reverse-flow annular combustor is very similar to the one used in the GMA500 demonstrator engine. Lamilloy* construction is used to provide adequate skin cooling and long life. The power turbine is also a GMA500 design reset to accommodate the increased corrected flow.

The gas generator turbine rotor bore diameter has been sized to allow passage of the power turbine extension drive shaft capable of transmitting in excess of 1000 shp.

Included in the study was a dynamic analysis of both rotor systems. The gas generator rotor system exhibits no resonances within the operating speed range. The power turbine rotor system, incorporating a beryllium sleeve insert and a mass isolator (100,000 lb/in.) at the rear bearing, shows no resonances within the operating speed range.

The associated mode shapes and frequencies for the gas generator and power turbine rotor systems are described as follows:

<u>Gas Generator System</u> (Operating Range: 32,920 to 55,410 rpm)		
Model 1	27,458 rpm	Rigid body mode with slight bending
Model 2	95,777 rpm	Rigid body mode with slight bending
<u>Power Turbine System</u> (Operating Range: 26,860 to 33,500 rpm)		
Model 1	17,974 rpm	Rigid body mode with slight bending
Model 2	40,942 rpm	First bending mode
Model 3	129,772 rpm	Second bending mode

Design Constraints

The design of the cooled radial turbine rotor involves a systematic integration of fabrication, aerodynamic, heat transfer, stress, and vibration disciplines. Constraints imposed by the structural disciplines must be considered in the selection of aerodynamic design parameters.

Mechanical Speed

Maximum engine performance necessitates an optimum speed match between the compressor and the turbine. Multistage compression tends to require lower RPM than the optimum value for single-stage radial turbines. The selected engine gas generator speed of 54,862 rpm results in a turbine specific speed of 65 and provides a good component performance match. As indicated by stress analyses, this reduced speed selection provides the required structural integrity.

*Lamilloy is a registered trademark of the General Motors Corporation.

Rotor Exit Annulus Area

A large exit area provides a low exit Mach number to ensure a slight acceleration in the transition duct between the gas generator and the power turbine; therefore, the rotor exit area was selected as large as possible consistent with the required blade stress levels. The arithmetic mean exit Mach number for the HTRT rotor is 0.272 for the selected exit annulus area of 20.0 in.². This results in an exducer AN⁻ value of 6×10^{-10} in.² rpm².

Rotor Exit Hub Diameter

The exit hub diameter selected was 2.4 inches to allow sufficient bore diameter to accommodate shafting such as that used in a front-drive engine. The selection of the hub diameter and the exit annulus area gives rise to an exducer hub-tip radius ratio of 0.434. The predicted effect of exducer hub-tip radius ratio on total-total and total-static efficiencies is shown in Figure 4. These predicted efficiency reduction characteristics compare favorably with experimental data of Watanabe.⁴ The front drive requirement, by dictating the hub diameter, results in an efficiency penalty of approximately one percent.

Rotor Tip Diameter

Since stress levels are approximately proportional to the square of tip speed, structural design requirements suggest minimum tip speed. Tip speed, however, has a strong influence on turbine efficiency. In general, the optimum tip speed occurs at 70% of the isentropic spouting velocity ($\sqrt{2gJA_{h1s}}$). A value of 67% has been applied to the HTRT design.

This selection results in an efficiency penalty of less than 1/2% but offers approximately an 8% reduction in disk stress. For a given gas generator RPM, tip speed is directly proportional to tip diameter. Figure 5 illustrates the influence of rotor tip diameter on 100% speed line performance characteristics. Reduced tip diameters, as would be expected, cause the efficiency to optimize at reduced expansion ratios. Peak efficiencies tend to be higher for reduced-diameter rotors because of lower velocity levels and reduced surface area. At the design expansion ratio, however, the small-diameter rotors suffer a substantial efficiency penalty. Figure 6 presents the effect of tip diameter on turbine efficiency at the design expansion ratio of 3.25. The selected HTRT tip diameter of 8.71 inches appears to be an optimum value.

4. I. Watanabe, I. Ariga, and T. Mashimo, Effect of Dimensional Parameters of Impellers on Performance Characteristics of a Radial Inflow Turbine, American Society of Mechanical Engineers Paper No. 70-GT-90, May 1970.

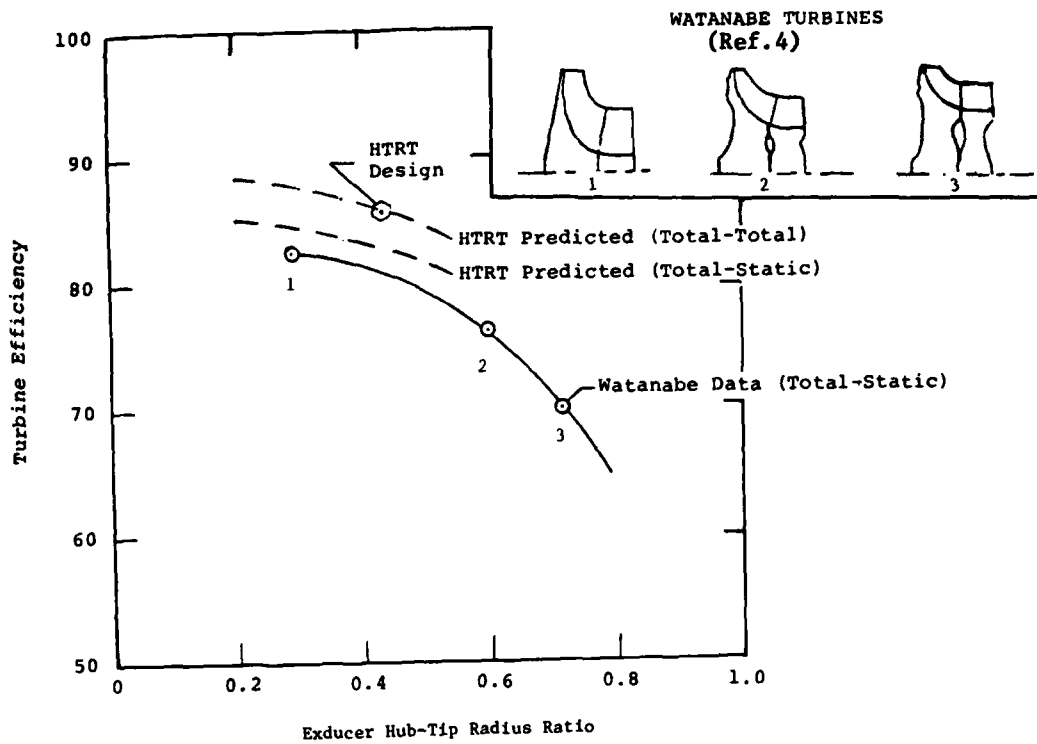


Figure 4. Influence of exducer hub-tip radius ratio on turbine efficiency.

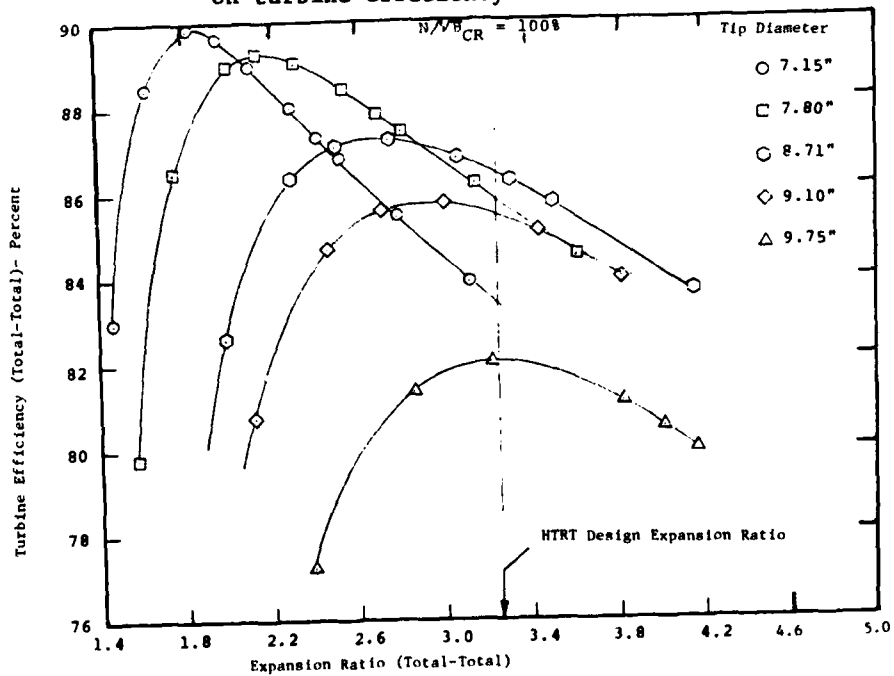


Figure 5. Influence of tip diameter on 100% speed line performance.

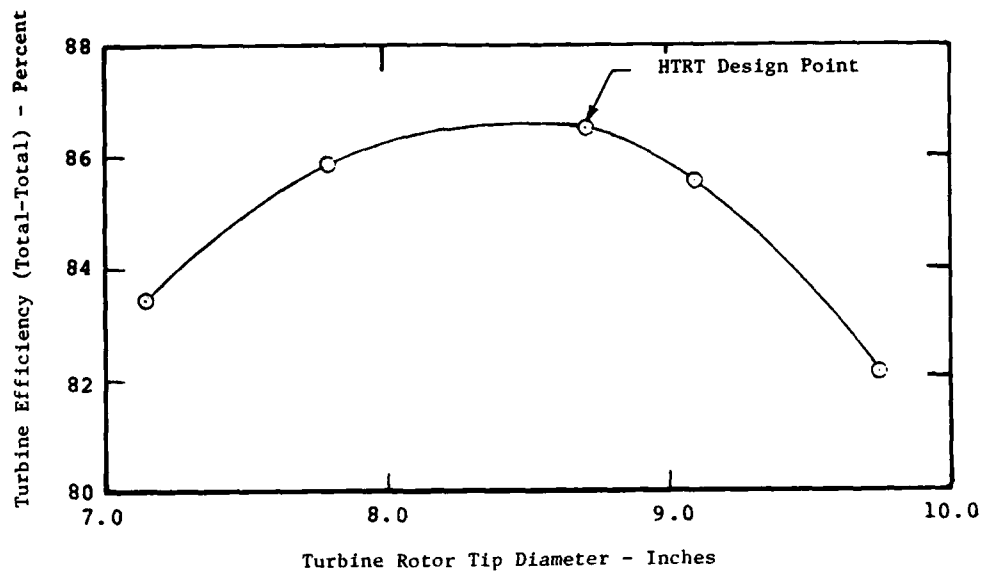


Figure 6. Influence of tip diameter on efficiency at design expansion ratio.

Vane Exit Angle

Reduction in the rotor inlet blade width reduces blade and disk stresses as a result of lower blade weight. For a specified flow rate, a reduction in inlet width necessitates a reduced exit flow angle (measured from radial). This tends toward reduced efficiency because of reduced reaction and increased end-wall loss levels. Figure 7 illustrates the predicted effect of vane exit angle on turbine efficiency. The HTRT vane angle selection of 75° provides optimum performance.

Rotor Blade Number

Reducing the blade number has the obvious effect of reducing the disk stress and cooling airflow. However, too few blades produce excessive blade diffusion and, thus, reduce efficiency. On the other hand, too many blades also reduce efficiency by excessive blade surface friction

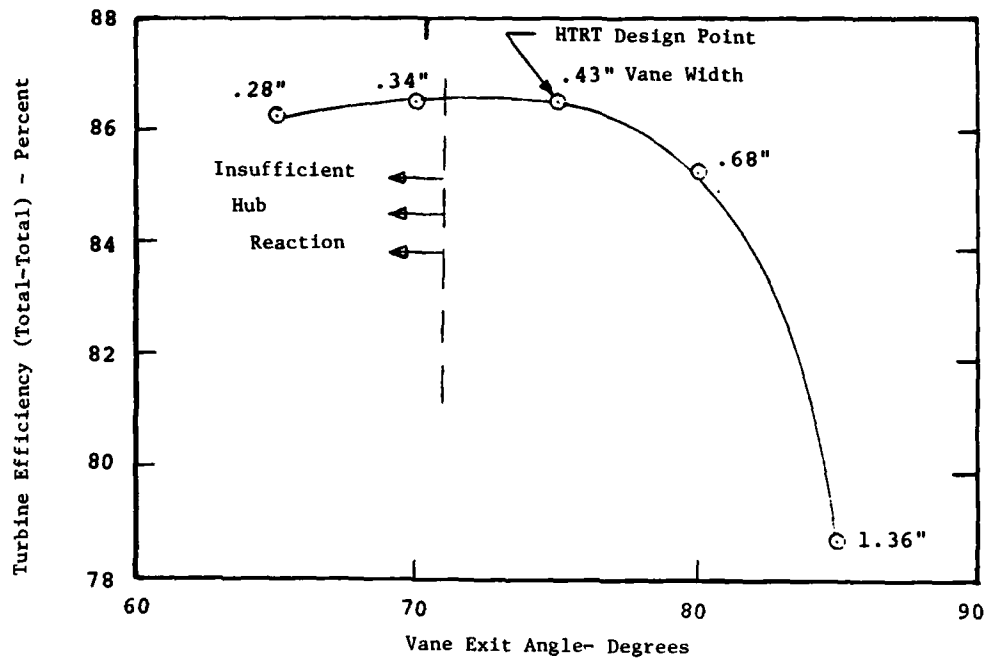


Figure 7. Influence of vane angle on efficiency at design expansion ratio.

loss. Figure 8 illustrates the experimental effect of blade number on turbine efficiency. Mizumachi data⁵ show that a larger number of blades is required for optimum performance than do the United Aircraft data.¹ DDA experience and preliminary HTRT velocity distribution studies coincide more closely with the United Aircraft results. A blade number of 12 has been selected for the HTRT rotor design.

5. Mizumachi, Endo, and Kitano, A Study of Aerodynamic Characteristics of Rotating Blades in a Radial Inflow Turbine, JSME-7, October 1971.

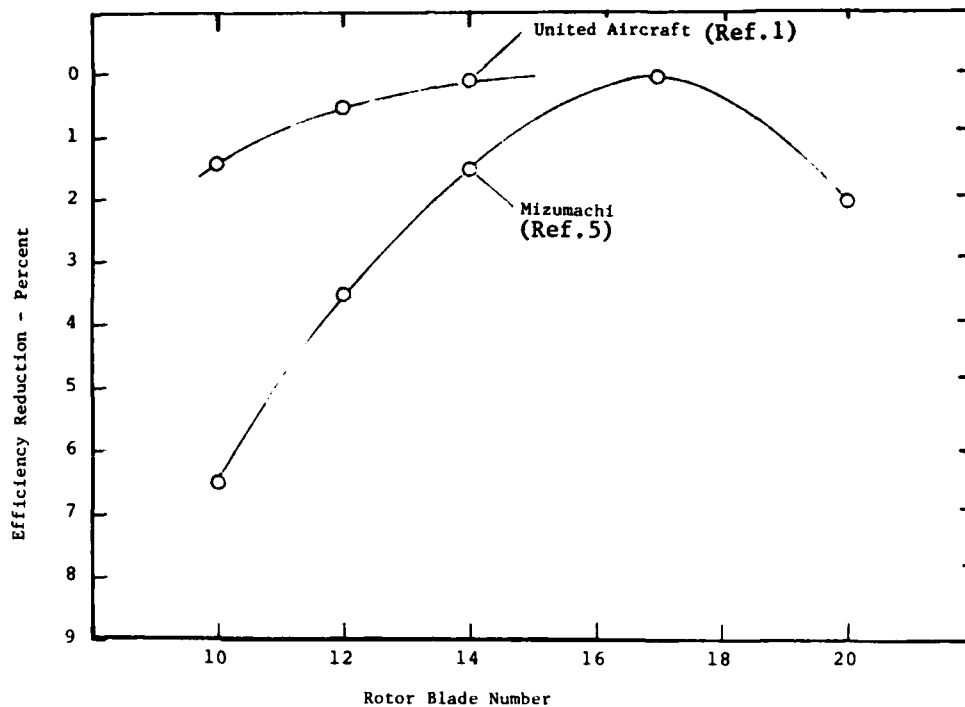


Figure 8. Experimental effect of blade number on turbine efficiency.

Radial Blading

Radial blading virtually eliminates blade bending stress and therefore becomes a desirable structural design criterion. More simplified fabrication techniques also make this type of blading less expensive to produce. However, radial blades do restrict aerodynamic design in achieving optimum radial distribution of blade loading. Nevertheless, the structural benefits and cost effectiveness led to the selection of radial blading for the HTRT rotor.

Hub Contour

An optimum contour exists along the hub to achieve a proper balance between blade and disk stress levels. A small-diameter hub exhibits a low hub rim velocity and tends to reduce disk stress; however, the resulting longer blade results in excessive blade stresses. These stress problems revert from the blade to the disk for larger-diameter hubs. Aerodynamically, the hub contour selection becomes a trade-off between

excessive passage velocity levels with a large hub and excessive hub diffusion with the small hub. The HTRT hub contour has been selected to provide a nearly optimum trade-off between blade and disk stress levels while providing satisfactory blade velocity distributions. The HTRT is a fully scalloped (no backplate) design. Elimination of the backplate reduces dead load on the disk, thus reducing disk stresses. The efficiency penalty associated with a fully scalloped rotor is not severe because the loss attributable to clearance is virtually offset by a reduction of loss from backplate disk friction.

Blade Taper

A logarithmic radial blade taper has been selected for the HTRT rotor. This distribution provides the lowest taper ratio that can be used to achieve the desired stress levels, thus minimizing dead load on the disk. To further reduce blade weight, the metal thickness has been held constant from the tip inward to a radius at which limiting stress is reached. The logarithmic blade taper eases aerodynamic design by minimizing the blade thickness and thus providing lower trailing edge blockage and passage velocity levels.

Aerodynamic Design

The turbine rotor flow path and initial meanline velocity diagrams resulting from the specification of design point conditions and the selection of aerodynamic design parameters are shown in Figure 9. Salient features of the flow path include the following:

Rotor tip diameter	8.710 in.
Rotor inlet width	0.438 in.
Rotor exit hub diameter	2.433 in.
Rotor exit tip diameter	5.611 in.
Rotor axial length	2.750 in.
Exducer hub-tip radius ratio	0.434
Inlet width/tip diameter ratio	0.050
Tip diameter/exducer tip diameter ratio	1.552

Uniform inlet flow conditions have been applied for the rotor design. The input meridional distribution of blade angle along the hub streamline is presented in Figure 10. Blade angles for all other streamlines are calculated via specification of radial blade elements. The radial distribution of exit blade angle is presented in Figure 11. Calculated distributions of design point work and exit swirl are presented in Figure 12. Final velocity diagrams, based on meridional flow analysis, are presented in Figure 13. The approximate blade-to-blade velocity distributions are illustrated in Figures 14 through 16 for the hub, mean, and shroud streamlines. Calculated streamline positions are shown in Figure 17.

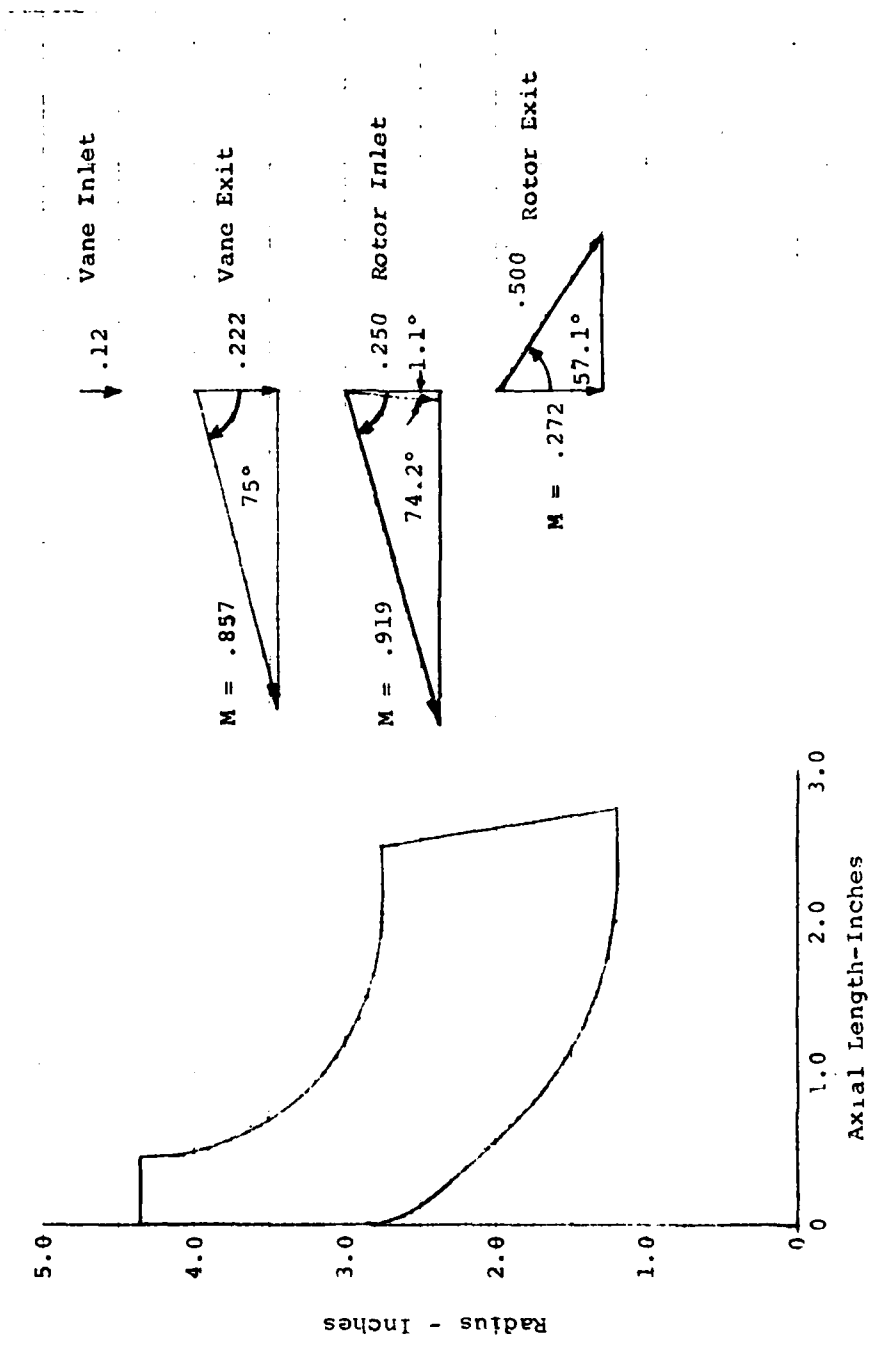


Figure 9. HTRT flow path and mean velocity diagrams.

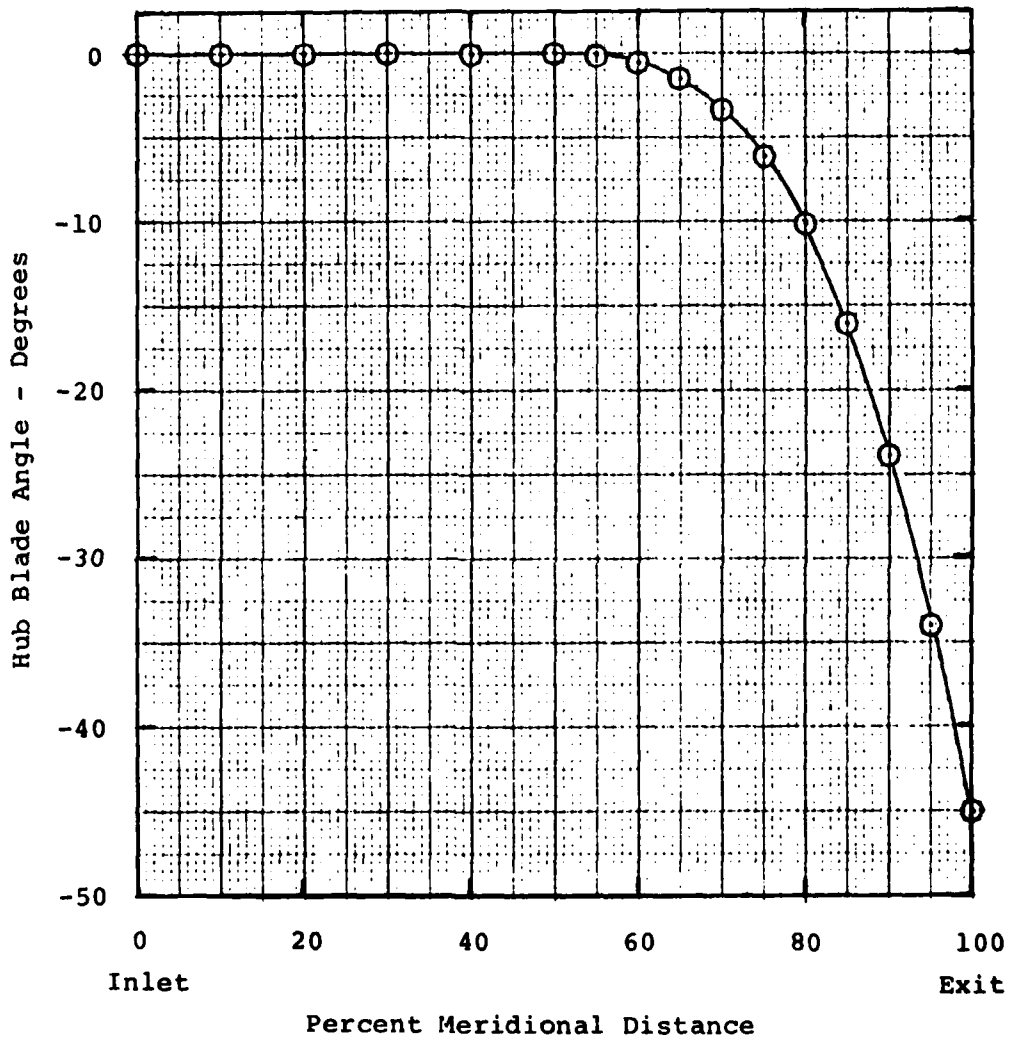


Figure 10. Meridional distribution of blade angle along hub streamline.

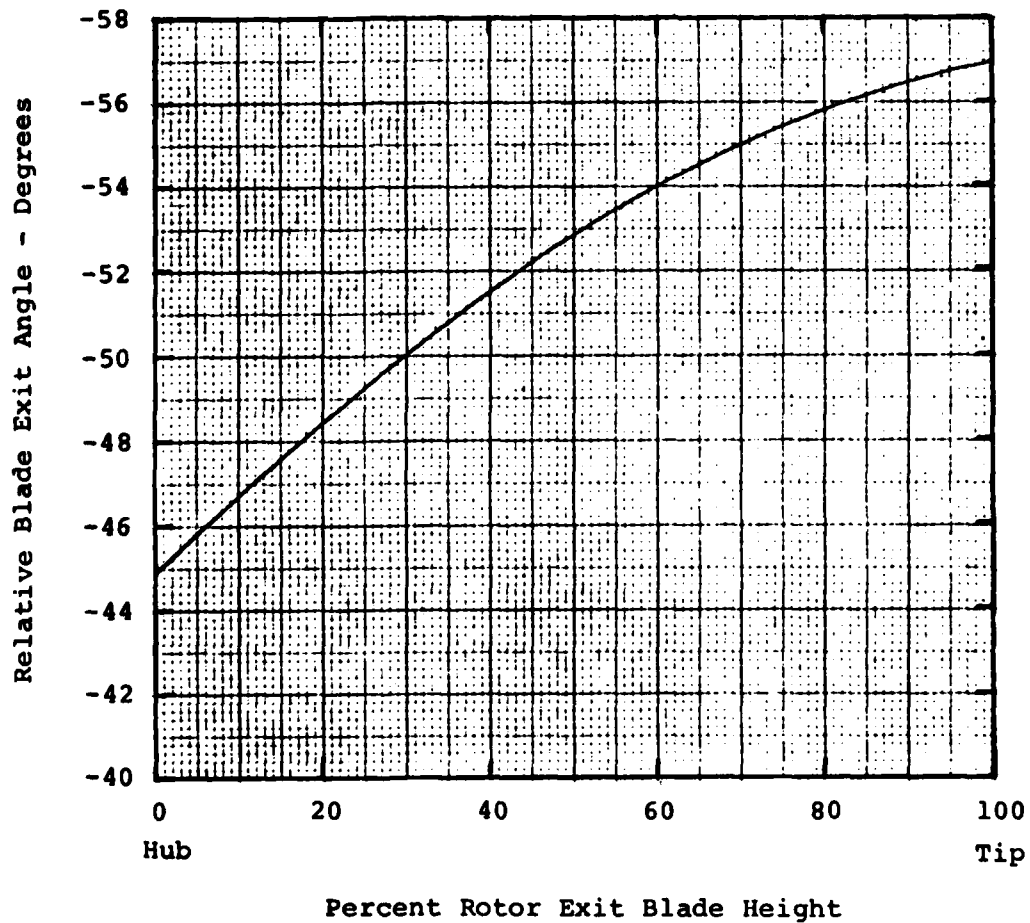


Figure 11. Radial distribution of relative blade exit angle.

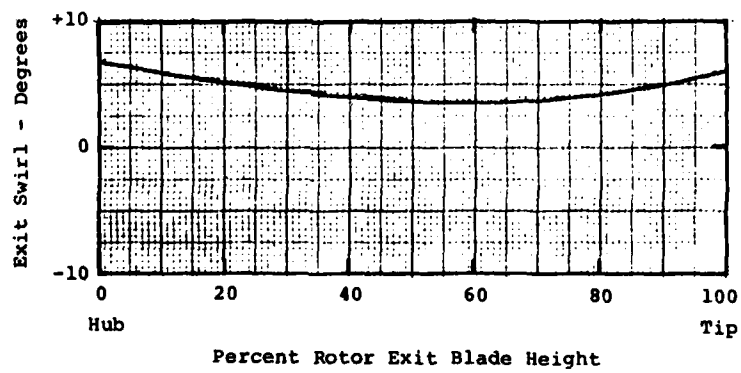
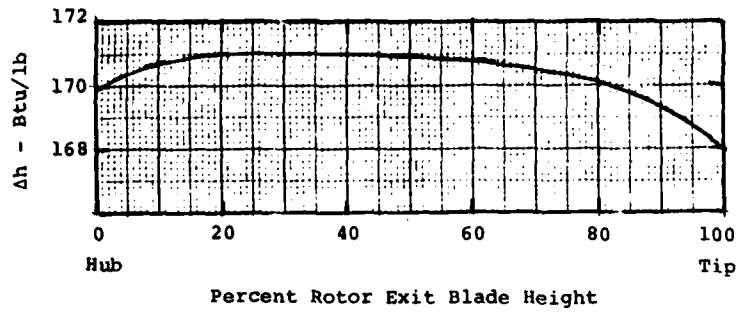


Figure 12. Radial distribution of turbine work and exit swirl angle.

TIP

$R = \frac{2.214}{\text{HUB}}$

HUB

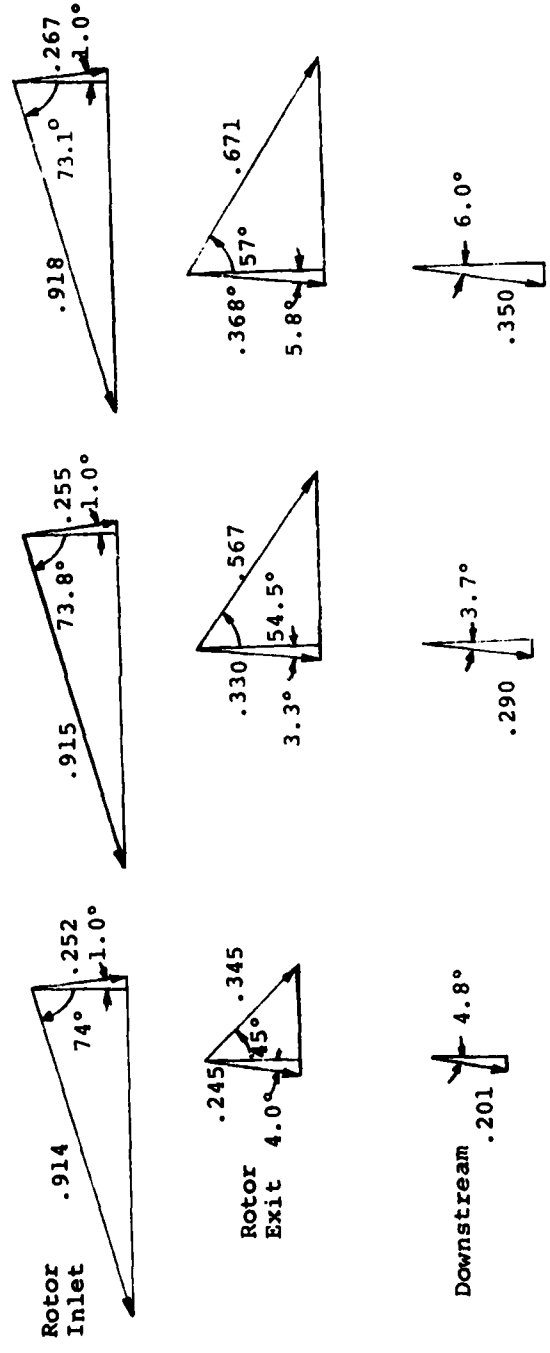


Figure 13. HRT design point diagrams.

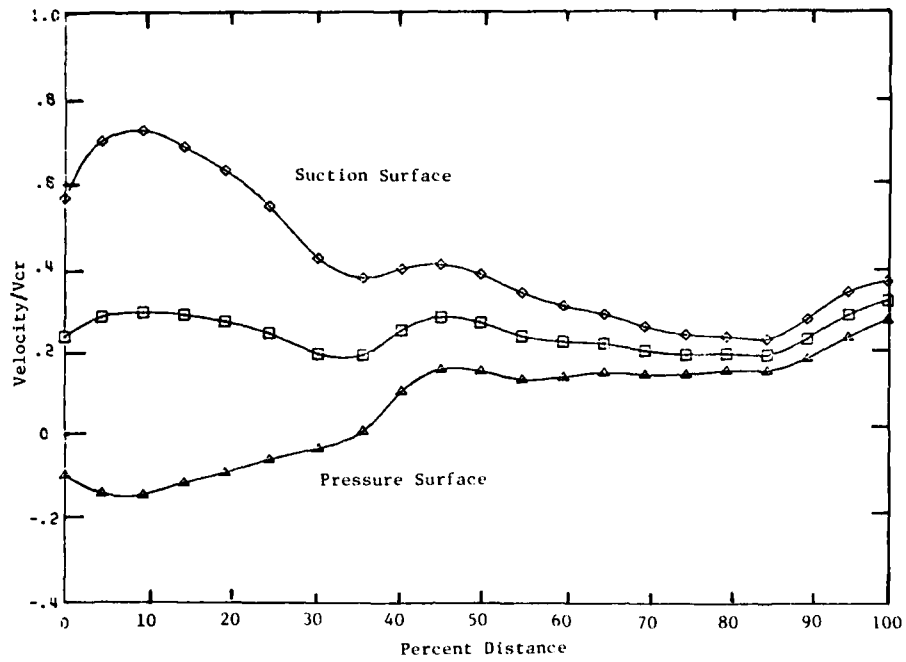


Figure 14. Blade-to-blade velocity distribution--hub streamlines.

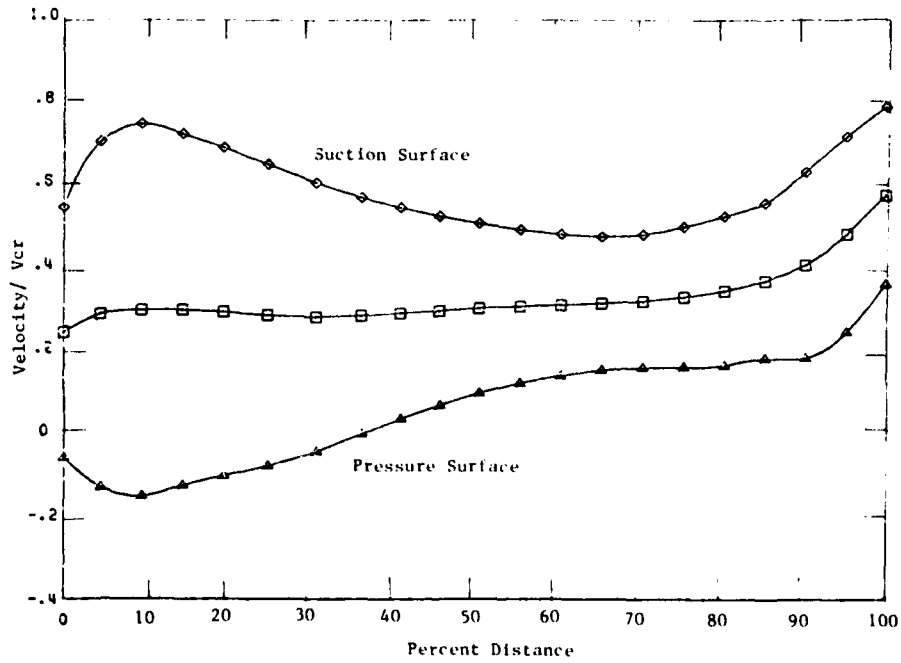


Figure 15. Blade-to-blade velocity distribution--mean streamlines.

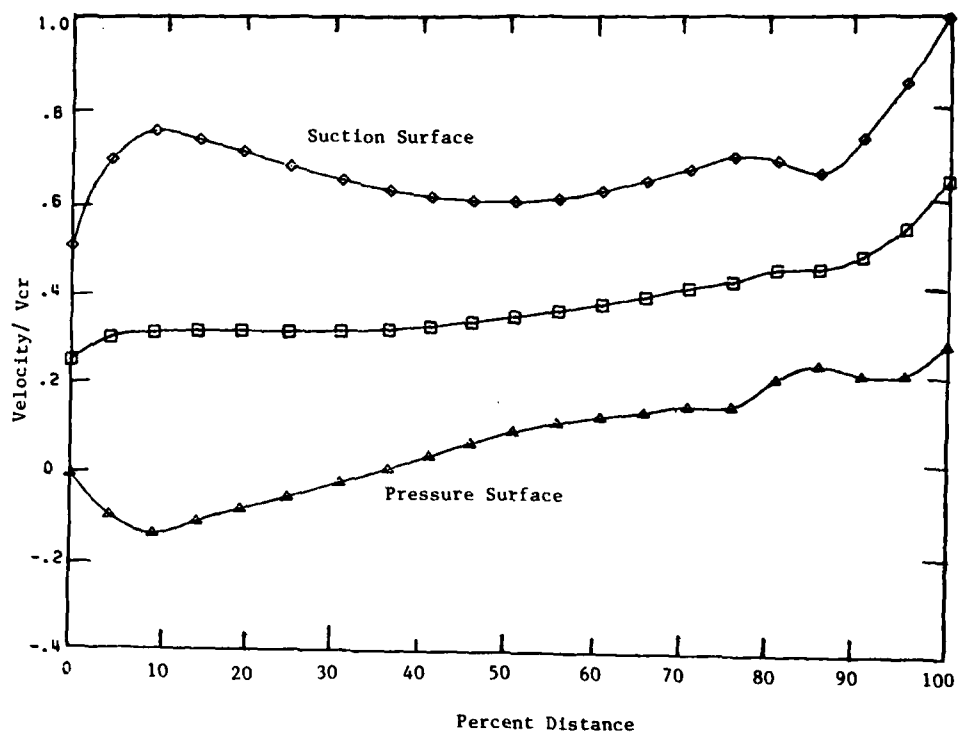


Figure 16. Blade-to-blade velocity distribution--shroud streamlines.

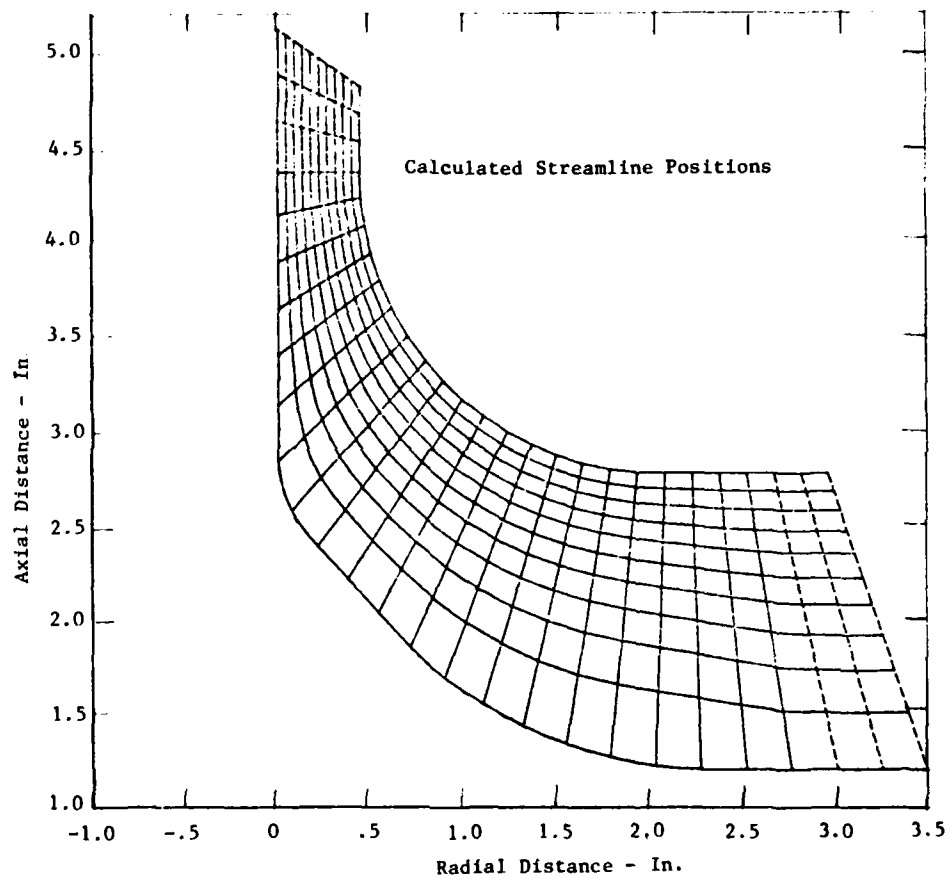


Figure 17. Calculated streamline positions of HTRT rotor.

Preliminary off-design efficiency and equivalent flow characteristics for the HTRT turbine are illustrated in Figures 18 and 19.

The HTRT rotor incorporates an internal core for coolant airflow. Total blade thickness is therefore larger than normally encountered in an integrally cast, uncooled rotor. The leading edge thickness of 0.090 inch allows for a core thickness of 0.040 inch. Discharge of the coolant is along the blade pressure surface. The trailing edge radii are illustrated in Figure 20. An isometric view of the rotor is presented in Figure 21. A y-z view is shown in Figure 22. Planar slices for y and z cuts have been defined (Figure 23) and are illustrated in Figures 24 and 25.

Mechanical Design

The hybrid rotor configuration dual property design concept is aimed at usage of variable material properties such that a hybrid rotor will yield greater life than a monolithic rotor. The cast M247 outer ring exhibits superior stress rupture properties and a low-cost method of airfoil fabrication. The inner ring of PA101 PM material has higher strength, greater ductility, and superior fatigue properties over an integrally cast wheel. The hot isostatic press (HIP) bonding process allows the two materials to be used in a bladed rotor without the inefficiencies of a mechanical fastener.

The required design life for the turbine is 5000 hours, based on the following engine loading schedule:

<u>% IRP</u>	<u>% Time</u>
100	20
75	50
55	20
35	5
Idle	5

The required low cycle fatigue life (LCF) is 6000 cycles based on the following duty cycle:

- (1) Start engine and accelerate to Idle
- (2) Run at Idle for 5 min
- (3) Accelerate to Intermediate Rated Power (IRP)*
- (4) Run at IRP for 5 min
- (5) Decelerate to Idle*
- (6) Run at Idle for 5 min
- (7) Shut engine down*
- (8) Allow engine to cool for 60 min

*It is assumed that all accelerations and decelerations will be accomplished within 3 seconds.

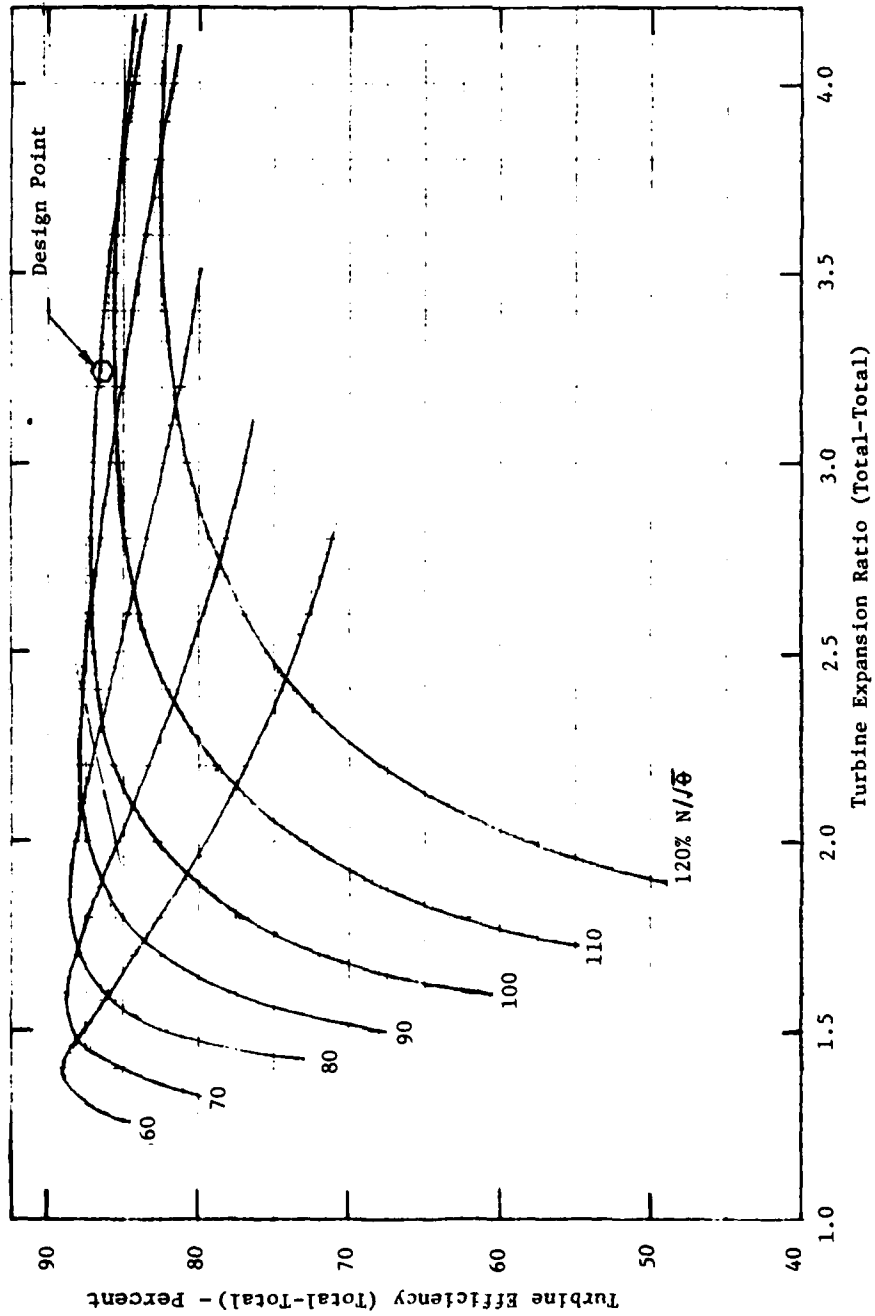


Figure 18. HTRT efficiency.

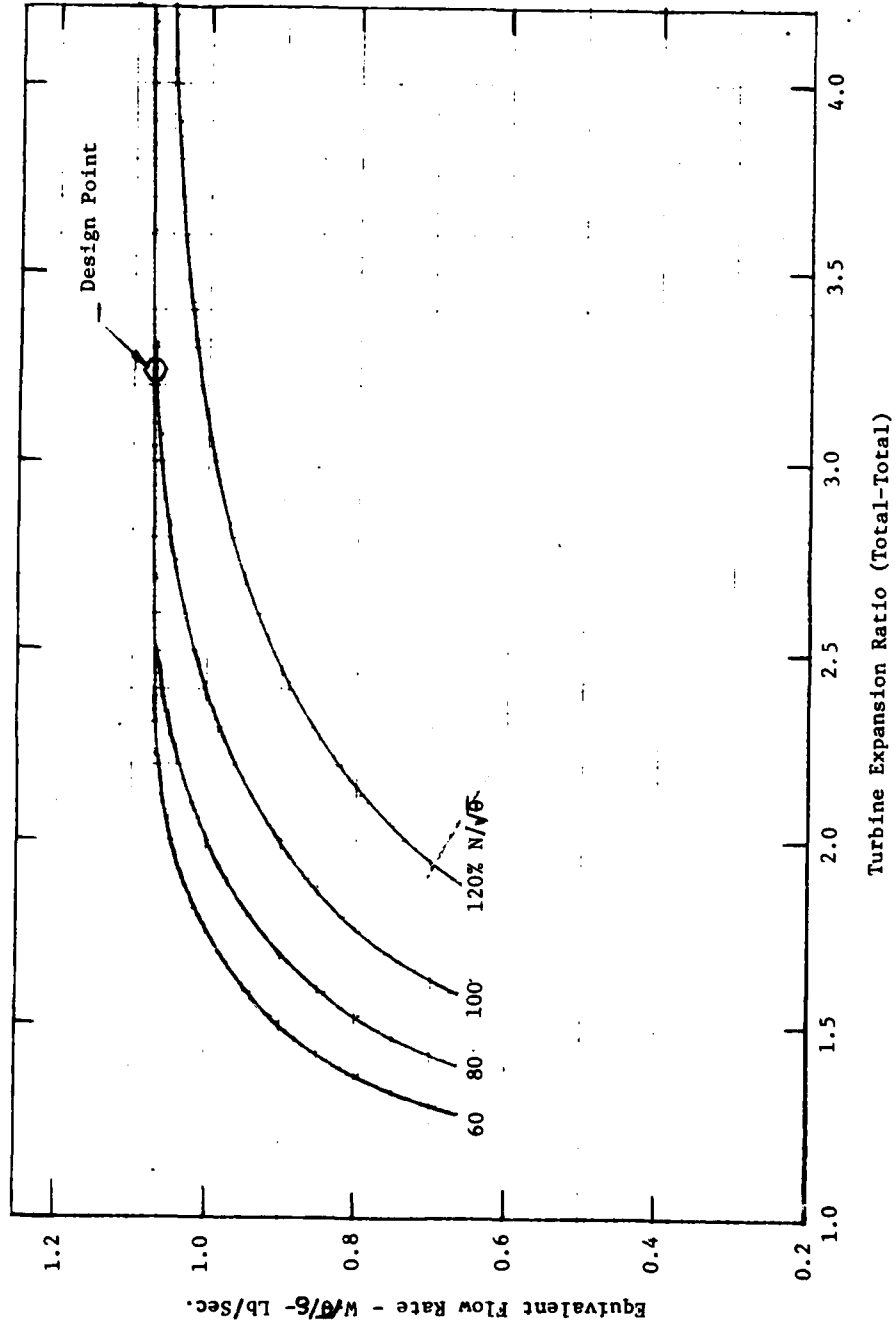


Figure 19. HTRT equivalent flow.

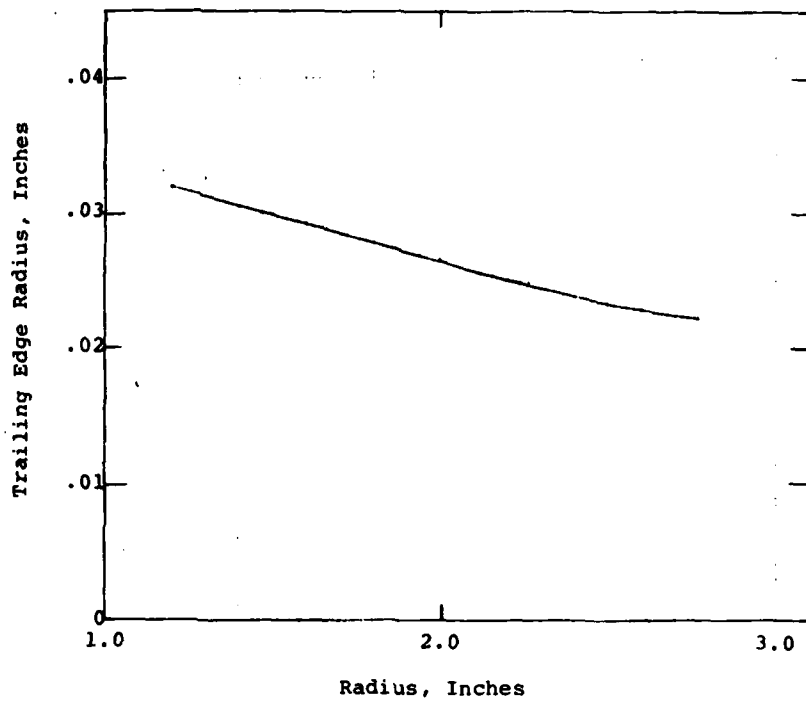


Figure 20. Radial distribution of rotor trailing edge radius.

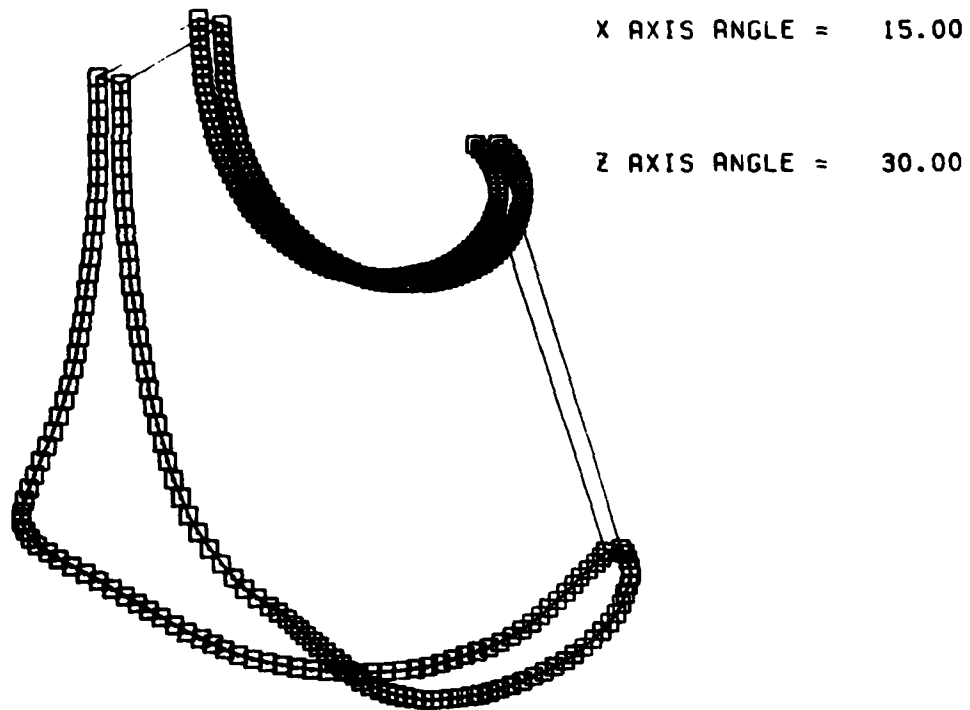


Figure 21. Isometric view of HTRT rotor.

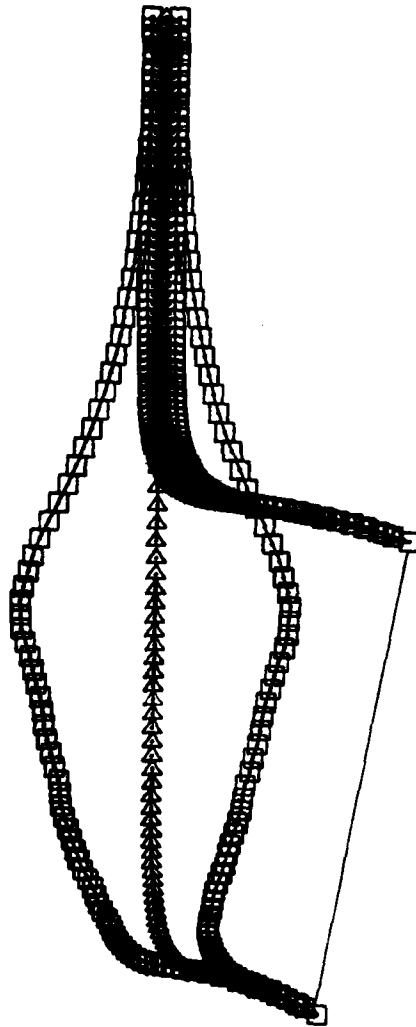


Figure 22. y-z view of HTRT rotor.

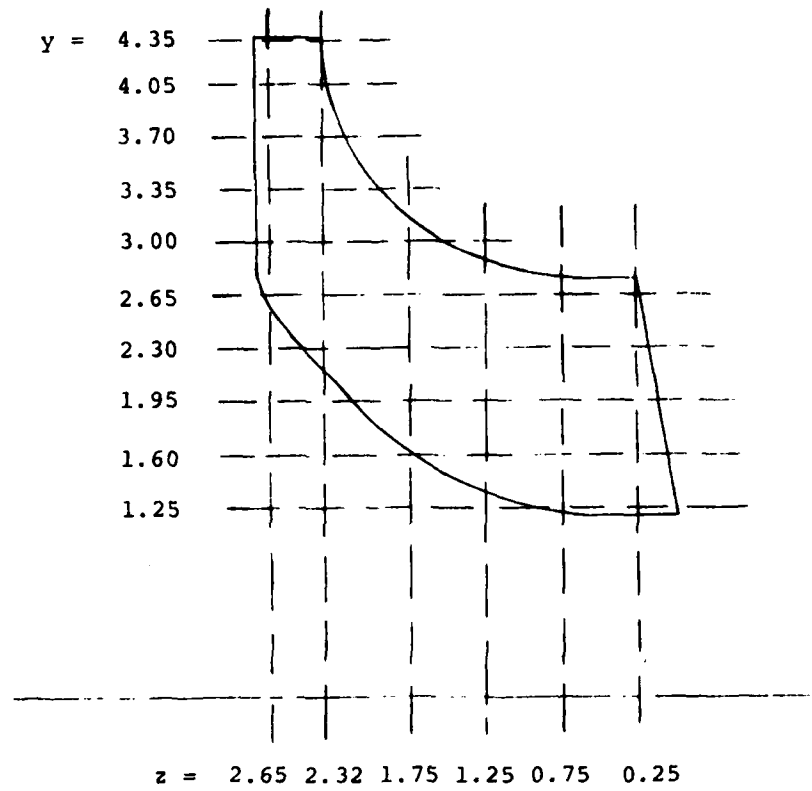


Figure 23. Location of y and z planar slices.

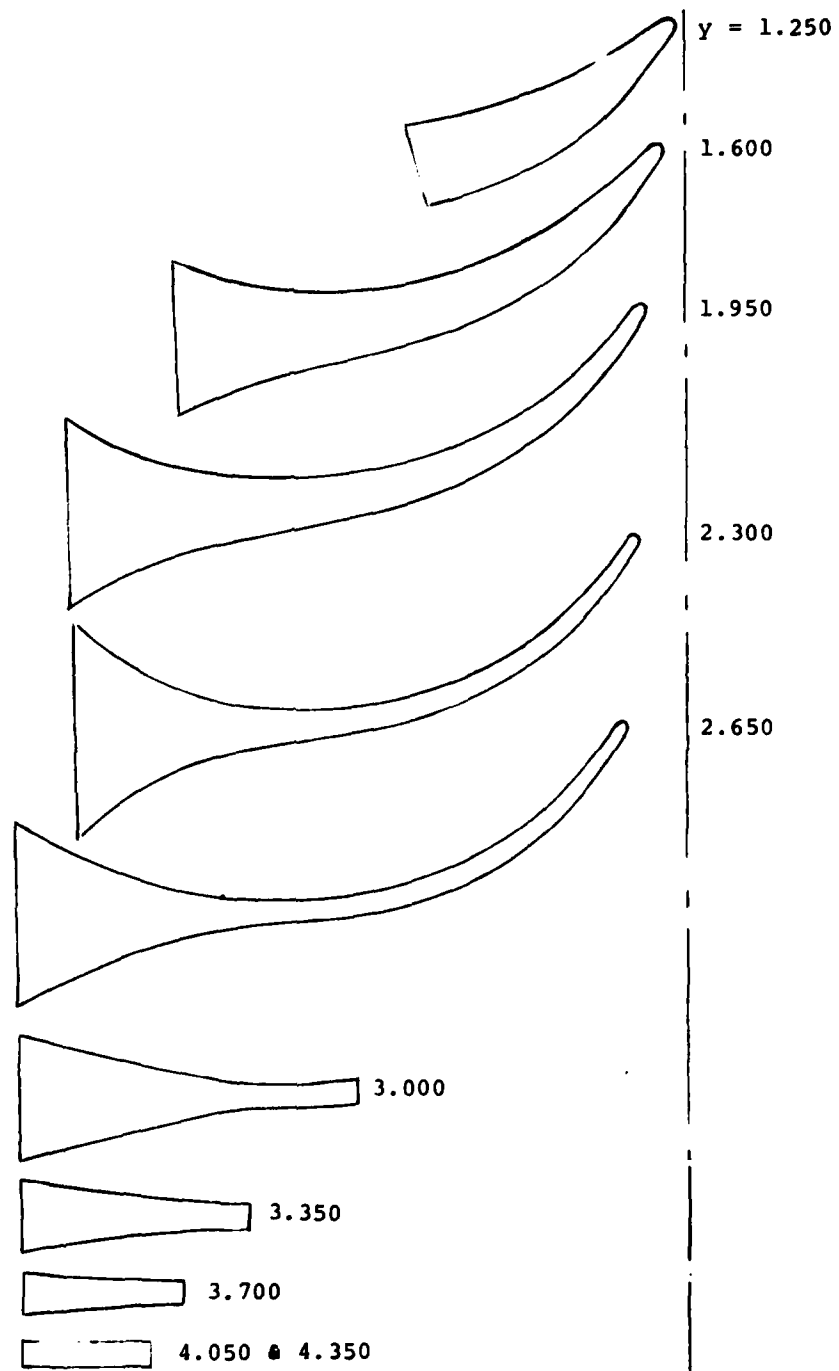


Figure 24. Planar y-cuts of HTRT rotor.

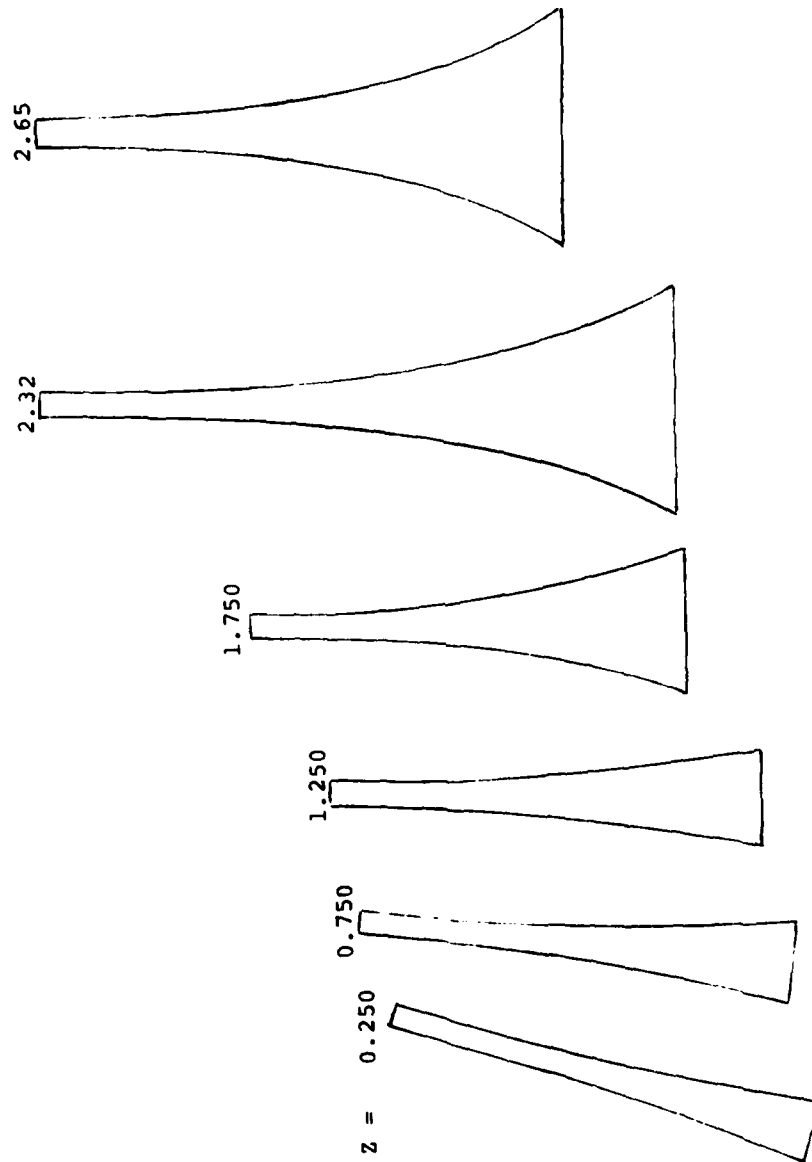


Figure 25. Planar z-cuts of HIRT rotor.

For this analysis, the 5000-hour mission design life has been truncated to 1000 hours at 100% IRP. This is based on the assumption that all other engine loading conditions consume negligible life.

The engine duty cycle includes five-minute dwell times at idle for start-up as well as shutdown. Experience with small engines has demonstrated that this relatively long dwell time at idle tends to eliminate life-limiting transient stress conditions. The startup to the 100% IRP operating point then becomes the life-limiting LCF cycle. For this reason, the LCF design goal was established as 6000 cycles from zero to 100% IRP operating point stresses.

All other design limits have been established to -3 sigma design limits.

The preliminary design of the high-temperature radial turbine was completed in the proposal stage. The rotor configuration derived from this study was based on cost, ease of manufacture, and reliability. This configuration consists of an integrally cast ring of airfoils HIP bonded to a powder metal "plug."

A material selection study was also conducted during the proposal stage. The materials selected, M247 and PA101, have exhibited compatibility in the diffusion bonding cycle as well as combined properties which offer strength and life advantages in a hybrid wheel.

The turbine rotor resulting from detailed design (Figure 26) has a bore diameter sized to accommodate a power turbine shaft of the 1000-shp class engine. In an extension of the aft rotor hub, opposed radial slots provide a means of driving the test rotor. The extension also facilitates piloting of the drive shaft and provides stock for rotor balance. An extension at the forward face of the rotor hub would serve as a drive mechanism in an engine application. A pilot is machined at the outer diameter of this "dummy" drive extension, and a provision for removal of balance stock has been made at the inner diameter.

Figure 3 shows the turbine rotor in a typical design application as a radial gas generator turbine in a small, front-drive turboshaft engine.

The rotor incorporates as-cast finishes on all blade surfaces and the outer diameter of the wheel. The wall thickness at the blade tip (0.025 in.) was determined by minimum casting thickness. Blade taper was then established to yield the required design life but minimize wheel load.

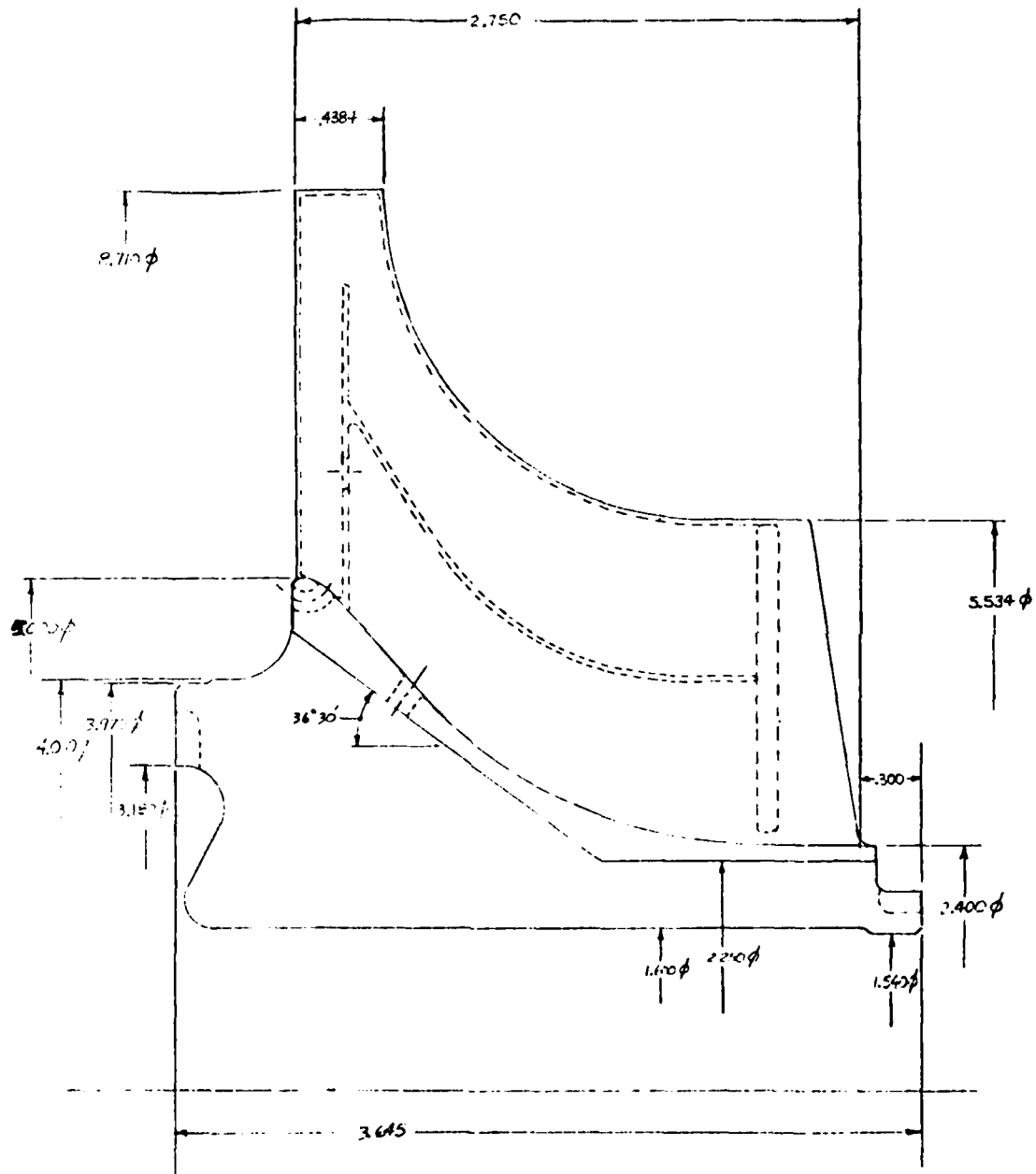


Figure 26. HTRT rotor final configuration.

The airfoil internal geometry is smooth wall, double channel, and convection cooled. The two-channel geometry is accomplished by inserting a ceramic core in the cast blade shell. This ceramic core is positioned and supported with four printouts (i.e., protrusions extending through the casting). When the ceramic core is removed, two of the printouts allow passage for the entry and exit of blade cooling air. These are located at the forward wheel face, just below the rim, and in the blade near the trailing edge. The remaining two printouts must be plugged and brazed closed. One of these is located at the blade tip (turbine inlet) and the other is on the conical section of the bond line.

Structural Design

Stress was analyzed with a finite element computerized model. The blades were added to this model as plates with equivalent tangential thicknesses. The analysis is elastic and "in plane" (i.e., creep and out-of-plane blade loading are not included). Figure 27 shows the finite element stress model. Figure 28 shows blade tangential thickness, and Figure 29 shows the true blade thickness for the final design.

Isostress plots for equivalent tangential, radial, and axial stresses for the 100% IRP design point are shown in Figures 30 through 33. Peak stresses and location are also indicated on these plots. Calculated metal temperatures for this condition are shown in Figure 34.

Stress rupture has been analyzed on a local stress, local temperature basis. Because of the large variation in blade thickness, two Larson-Miller stress rupture curves were used to assess life. Data derived from 0.030-in.-thick stylized Alpak coated specimens were used for the portions of the blade up to 0.030 in. thick. Bar data from 0.25-in. Alpak coated specimens were used for the 0.25-in. or thicker portions of the blade. Thicknesses within this range (0.030 in. to 0.25 in.) were linearly interpolated between these two data sets. Figure 35 shows isolife lines for the airfoil for the 100% IRP design point. One point at the blade trailing edge has a calculated life of 610 hr. This limiting life point indicates that a decrease of 17°F in calculated metal temperature is needed to reach the design goal of 1000 hr life at 100% IRP. Because a 35°F margin has been added to calculated temperatures, and creep redistribution is not included in the analysis, this calculated discrepancy at one location is not significant.

The wheel design limiting stresses are creep and bore tangential. Although creep data for the PA101 alloy are not available, data for forged AF95 material were used in the analysis.

Design life 0.2% creep for an average wheel temperature of 1120°F at 74,725 psi average tangential stress is:

	<u>IRP life (hr)</u>	
Typical	28,000	(at Intermediate Rated Power)
-3 sigma	6,000	(at Intermediate Rated Power)

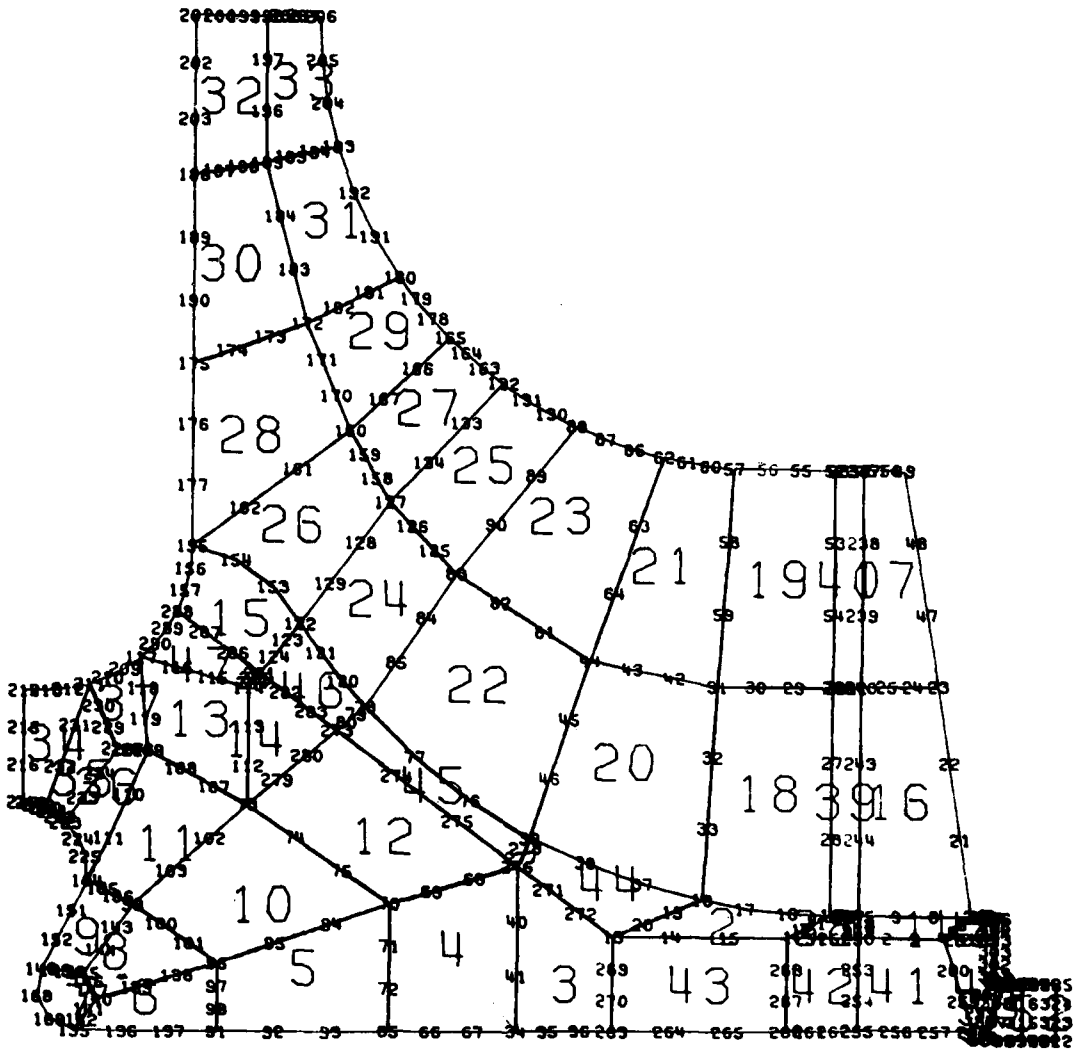


Figure 27. Finite element model used for stress analysis.

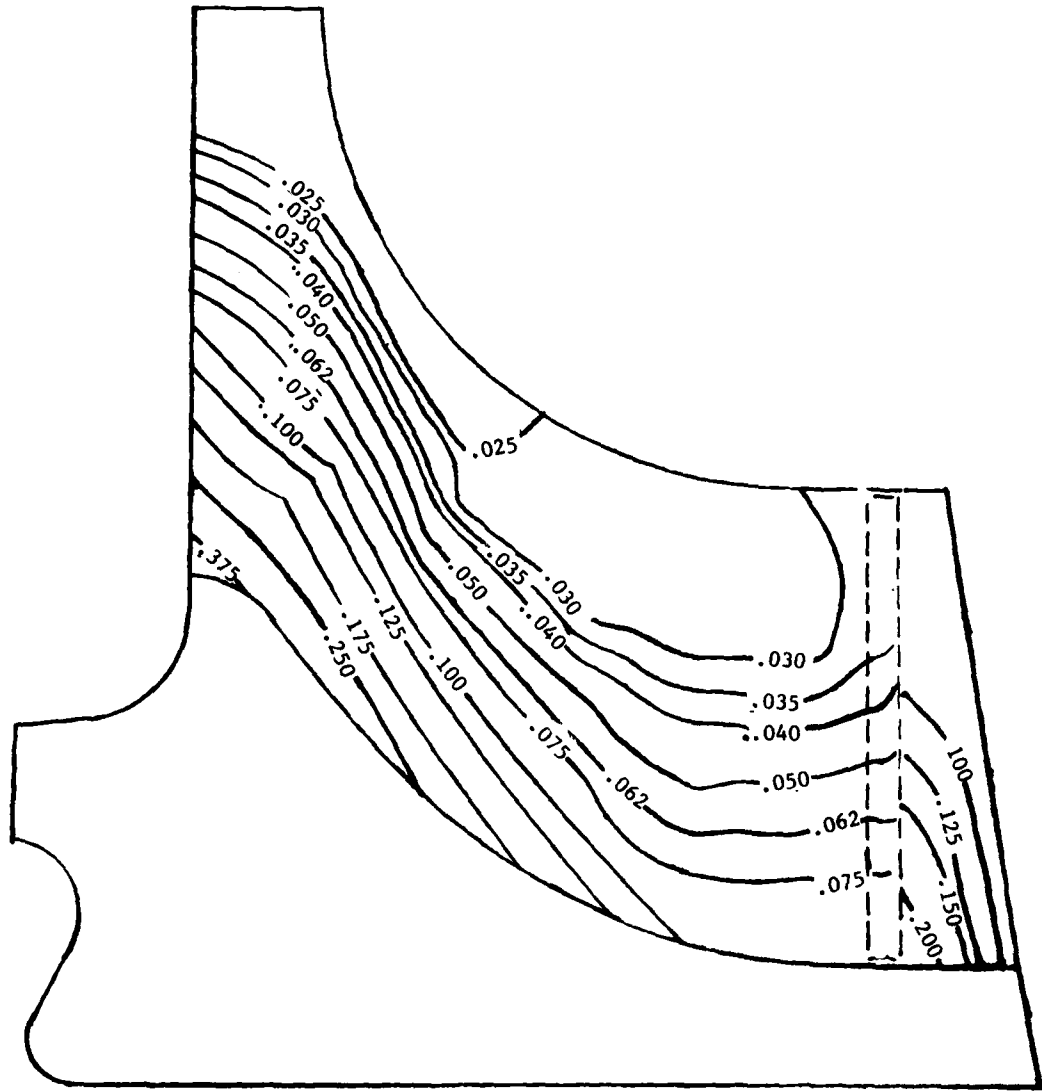


Figure 28. Lines of constant tangential blade wall thickness.

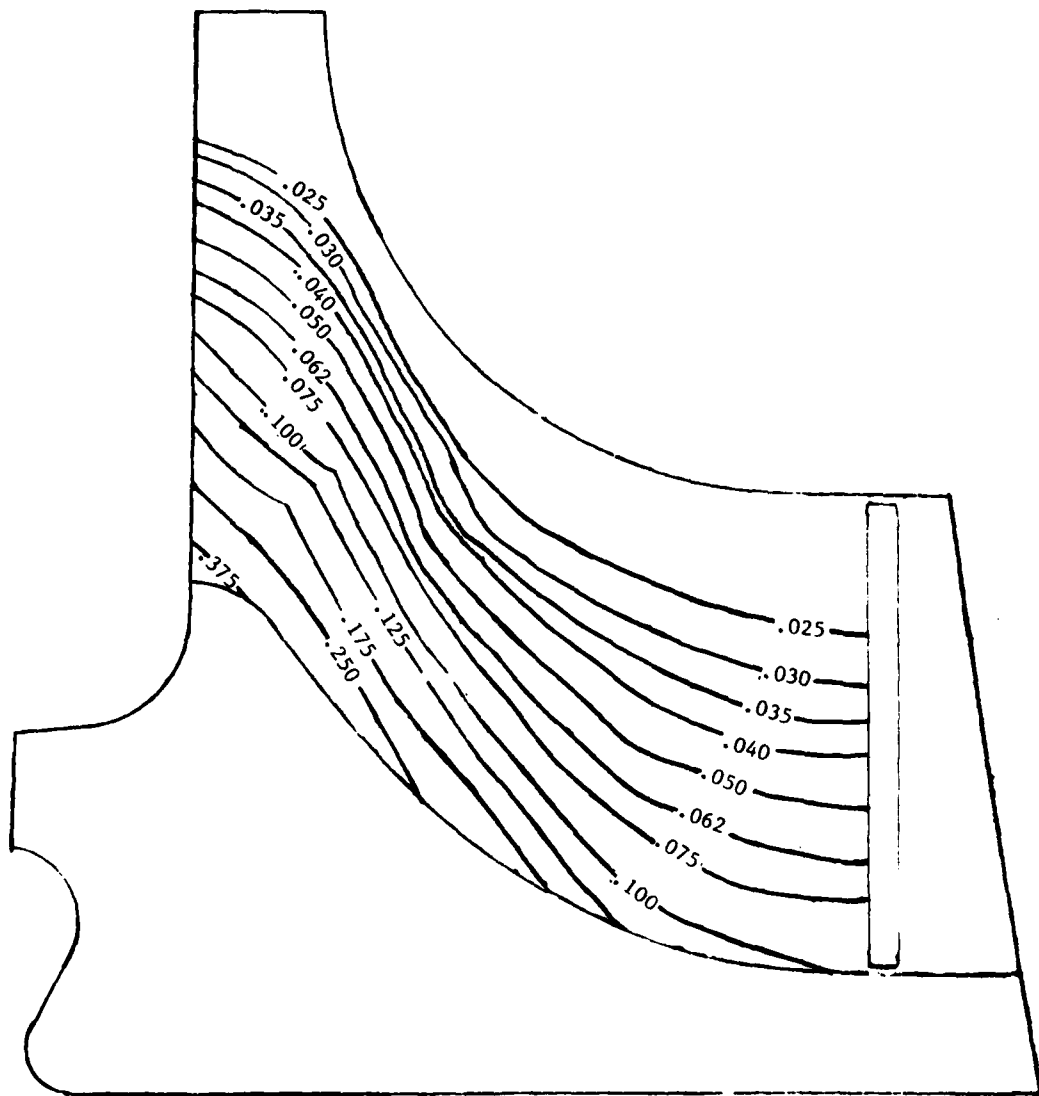


Figure 29. Lines of constant true blade wall thickness.

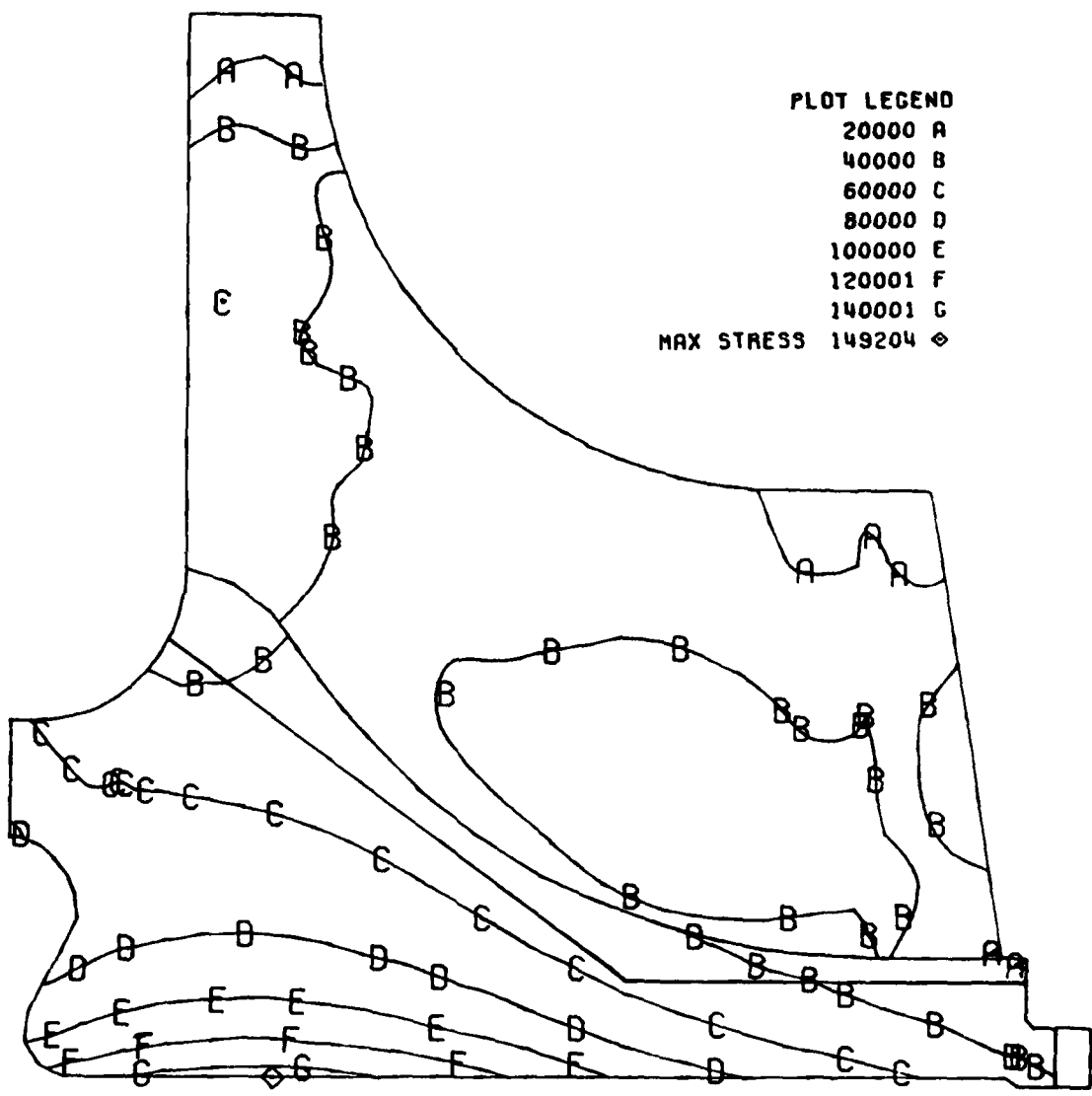


Figure 30. Equivalent stress (elastic).

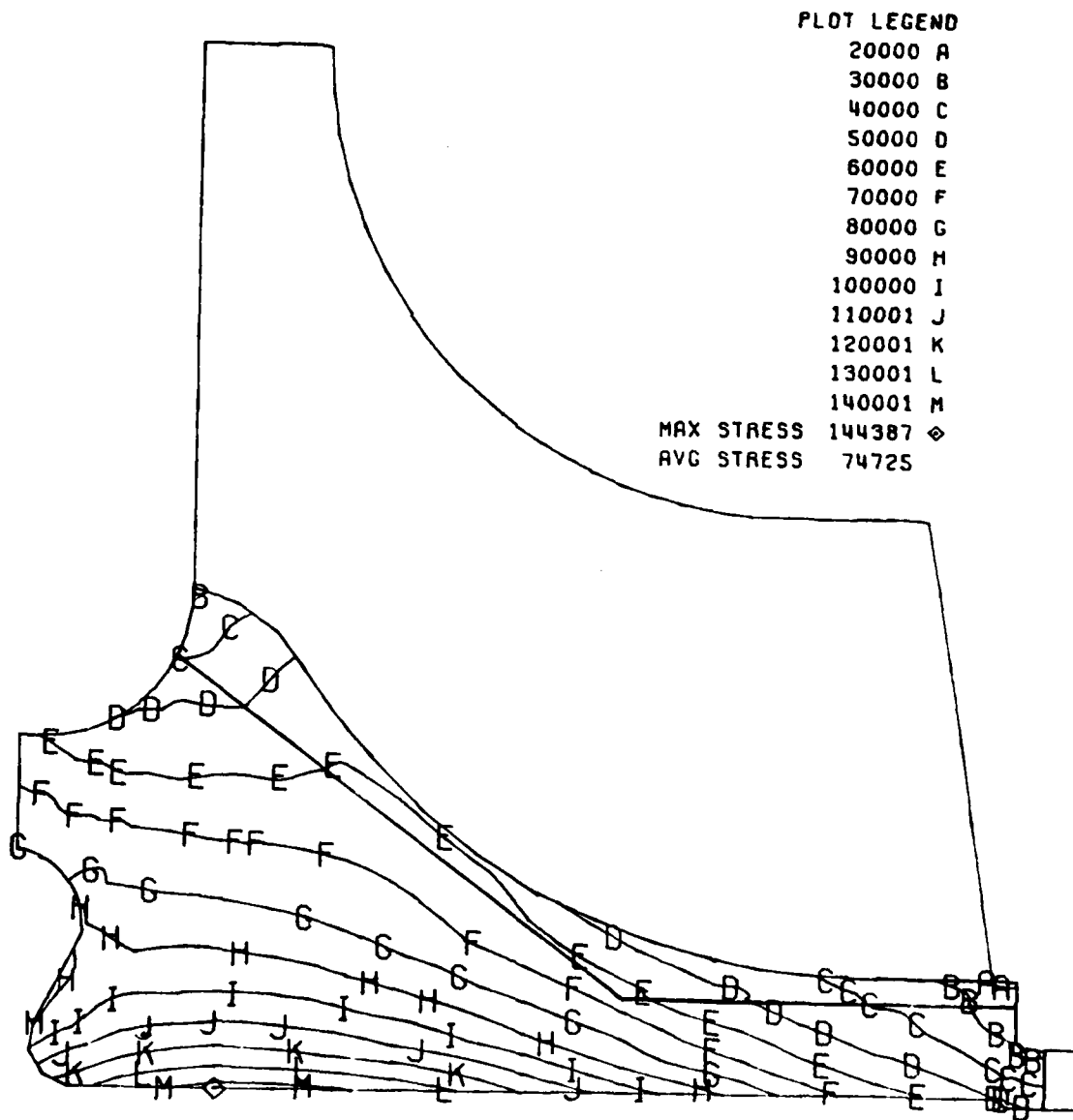


Figure 31. Tangential stress (elastic).

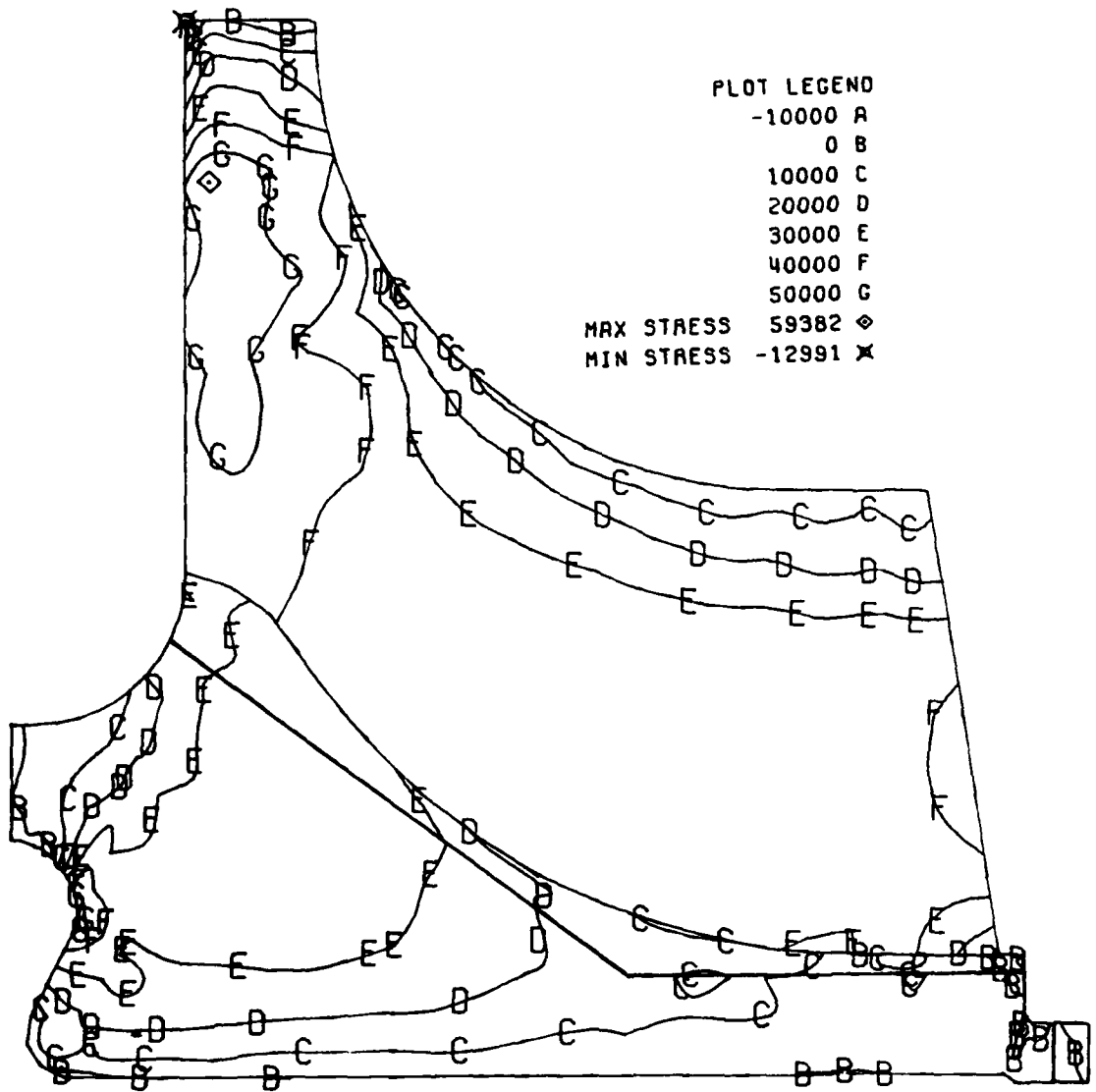


Figure 32. Radial stress (elastic), 100% IRP.

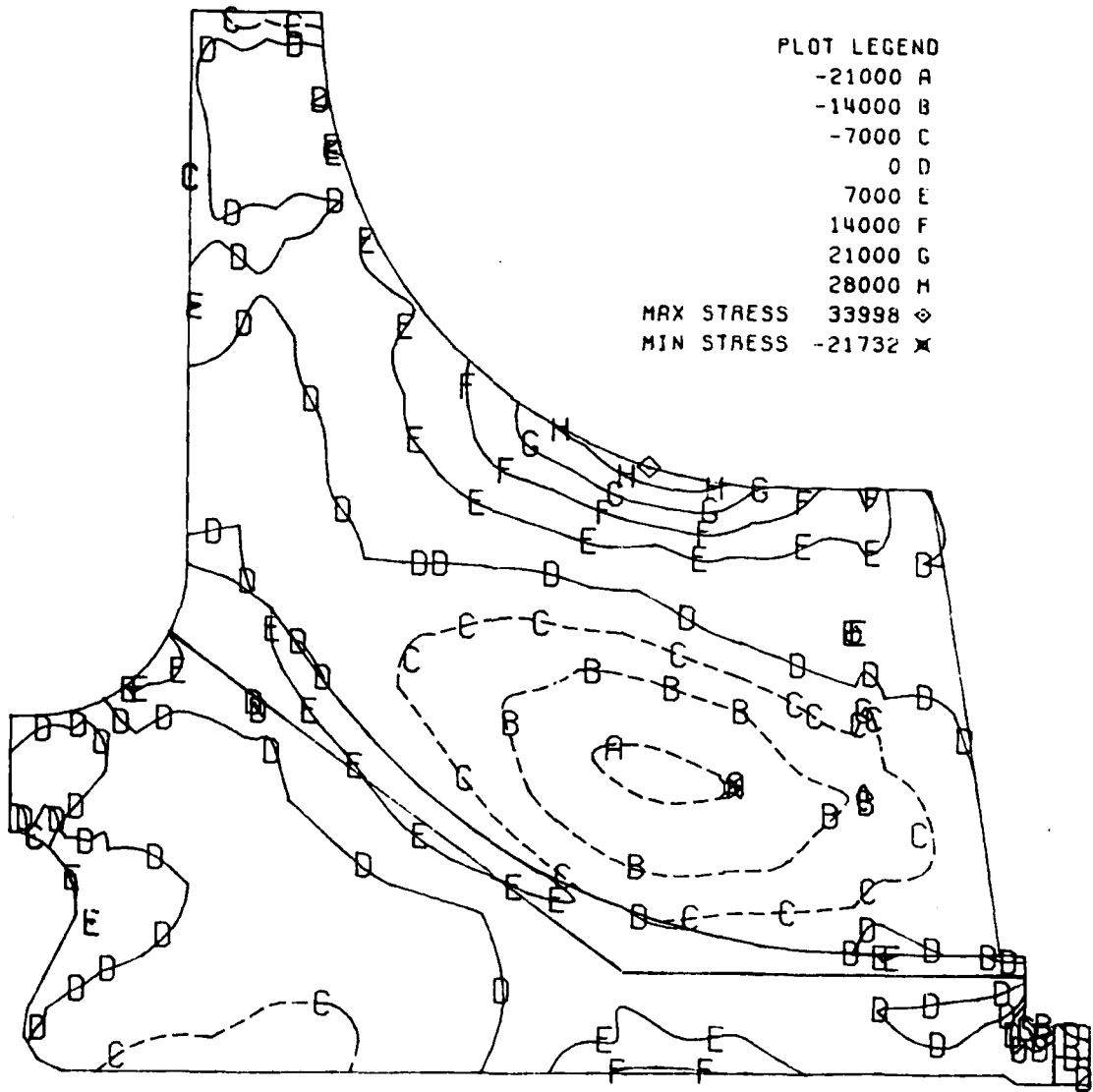


Figure 33. Axial stress (elastic).

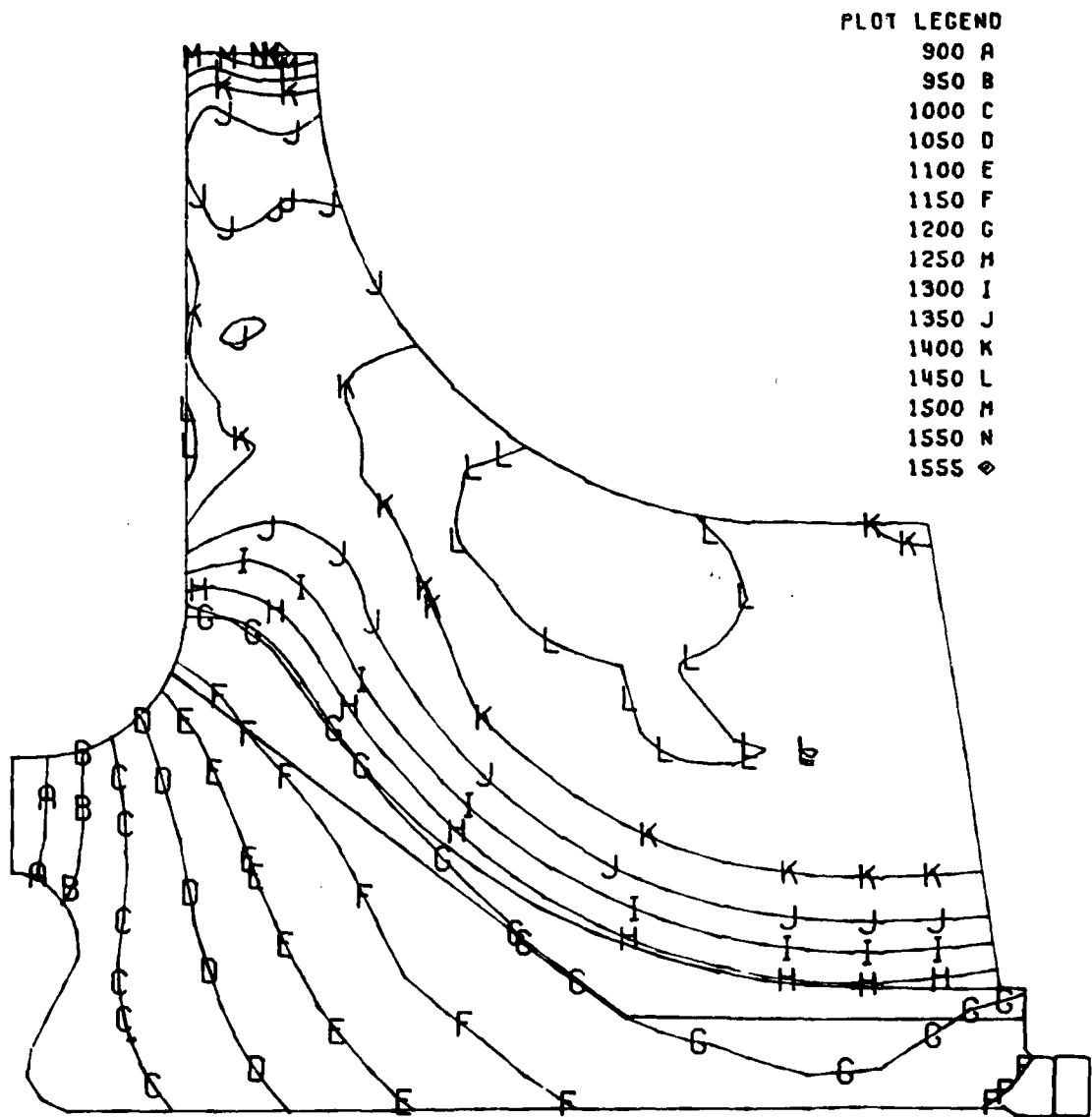


Figure 34. Isotherm plot for 100% intermediate rated power.

STRESS RUPTURE ISOLIFE LINES 100% IRP
 BLADE COOLING FLOW 3% SPLIT 2.3% - .7%
 FILM COOLING BETWEEN BLADES 1%
 BORE COOLING .5%
 INLET PROFILE 1.05
 Q INPUT AT TIP AND FWD BLADE SURFACE
 M246 COATED THIN WALL DATA
 COMBINED WITH
 M247 1/2 IN BAR DATA DEGRADED FOR COATING
 LINEAR INTERPOLATION CURVES FOR THICK-
 NESSES BETWEEN .03 IN AND .25 IN.
 -3 SIGMA LIFE WITH CALC TEMP +35° F

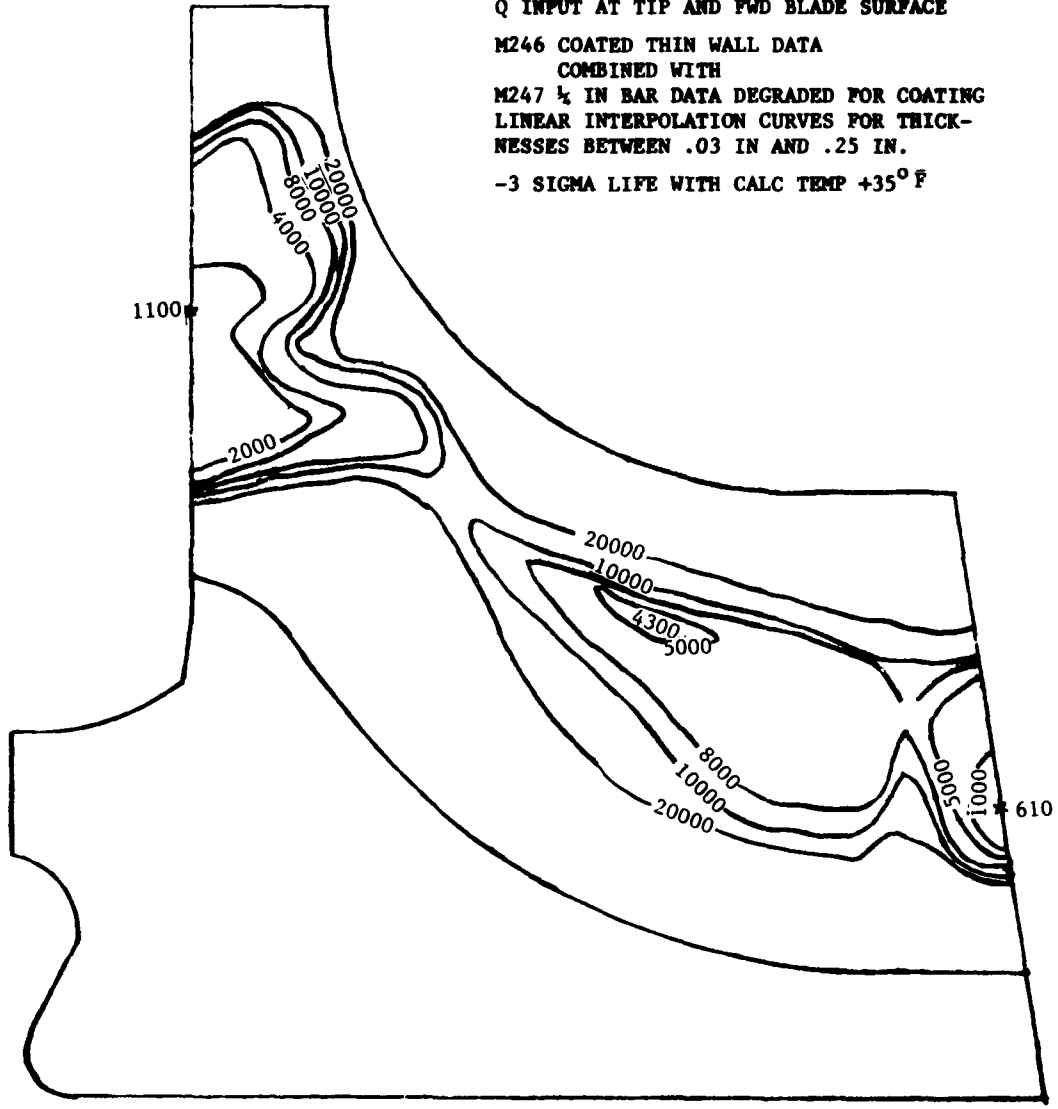


Figure 35. Stress rupture life in hours.

The outer portion of the wheel, which is cast M247 material, has an average tangential stress of 50,300 psi and an average temperature of 1203°F. The inner portion of the wheel, PA101 material, has an average tangential stress of 79,300 psi and an average temperature of 1104°F.

Following is the calculated wheel burst speed assuming a material utilization factor of 0.9:

Material utilization factor =	$\frac{\text{average tangential stress at rupture}}{\text{ultimate tensile strength}}$
Design speed, 100% IRP	54,862 rpm
Typical burst speed	85,148 rpm (1.55 x design speed)
-3 sigma burst speed	78,502 rpm (1.43 x design speed)

The maximum calculated equivalent bore stress, 149,204 psi, was compared with 900°F test data.⁶ These data were degraded 15% for -3 sigma scatter and 9% to allow for a decrease in material properties as the result of a temperature increase from 900°F to 1050°F. These data are shown in Figure 36. When compared with this design curve, the -3 sigma design life is 3800 cycles. Several factors indicate that the LCF life would be greater than this conservatively calculated value. First, the data are load cycled and the wheel bore will see a strain cycle. Also, creep and minimum fatigue properties would most likely occur with minimum yield properties; yielding would tend to be greater when fatigue properties are on the low side of the scatter band. The 15% degrading for -3 sigma scatter reflects DDA experience with forgings. HIP processing of the PM wheel is expected to reduce this LCF property scatter.

Heat Transfer

The rotor heat transfer study was based on the following assumptions:

- o Forward end "dummy" drive shaft end is specified as a constant temperature boundary of 850°F.
- o 100% Intermediate Rated Power coolant temperature is 800°F at the rotor.
- o Inlet gas profile peak temperature is 1.05 x average inlet temperature and is skewed to peak at 70% of span.
- o Heat input at the blade surface adjacent to the outer flow path boundary was negligible.
- o Temperatures calculated are average for the pressure and suction surfaces.

6. Rizzo and Fiedler, Manufacturing Methods for Superalloy Powder Production and Consolidation, Lycoming IR 271-3 (IV) for interim period 1 May to 31 August 1974.

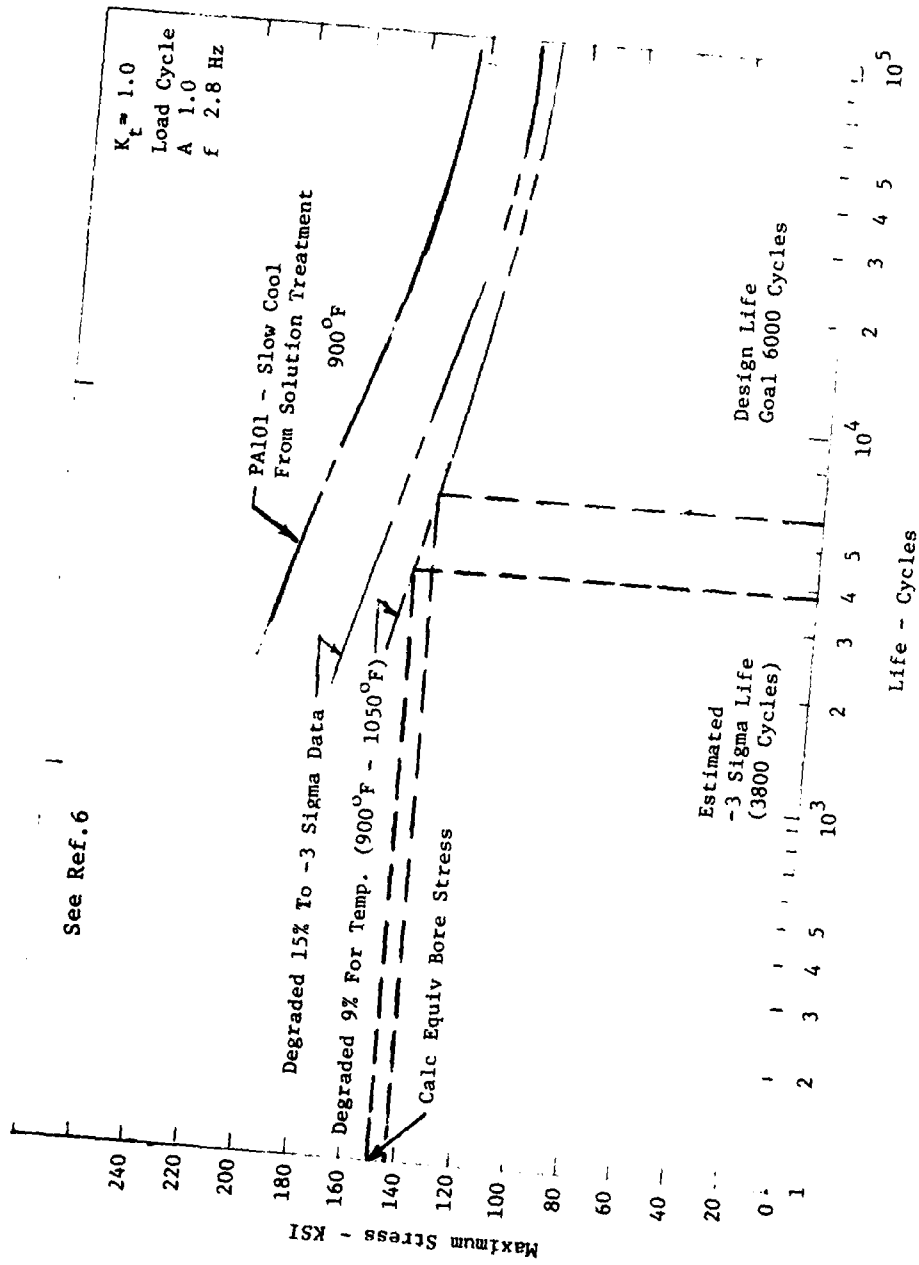


Figure 36. Low cycle fatigue properties.

In the design of the rotor, the following variables were studied and the effect of each was evaluated:

- o Pin fins
- o Forward versus aft cooling flow entry
- o Inlet temperature profile
- o Heat input at tip
- o Heat input at forward face
- o Bore cooling (0.2%, 0.5%, and 0.75%)
- o Blade cooling (2%, 2.2% and 3.0%)
- o Insulated bore
- o Wheel rim cooling (none, 1%)

The finite element model used for the heat transfer analysis of this rotor is similar to the stress model shown in Figure 27. The model is basically a two dimensional axial and radial representation of the rotor justified by the assumption that axisymmetric conditions will result from rotor motion to average out the circumferential variation in the inlet flow conditions. The computer model coordinates were selected to form quadrilateral elements from the sketches and drawings provided by the aerodynamic flow path and rotor layout. The hub elements are 360° ring elements; the blade elements are segmented into 12 parts defined by the actual blade thickness.

After the geometric model is developed for the turbine, the analysis proceeds by applying the thermal loading to this model and calculating the metal temperatures by established analytical procedures.

The computer program, a two-dimensional (2-D) or three-dimensional (3-D) axisymmetric finite element method, is used for the heat transfer analysis. This procedure is 2-D in the sense that only radial and axial hub and blade temperatures are calculated (i.e., no circumferential temperature variations), but it is 3-D in the manner in which blade convection is accounted for. Metal heat conduction is based on a complete (360°) hub and the thickness of 12 turbine blades with the temperature-dependent thermal properties of Mar-M247. The surface heat transfer (convection) is based on the normal blade surfaces, surface between blades, and completes 360° rotor side and bore surfaces with the empirically determined heat transfer coefficients of each surface.

Heat transfer calculations of a cooled turbine require complex analyses aided by empirical input of internal and external heat transfer coefficients. The boundary conditions associated with the thermal loading and cooling of the turbine are as follows:

- o Convection on the blade external normal surfaces developed from the aerodynamic data
- o Convection on the rotor platform (surface between blades) from aerodynamic data modified by film cooling
- o Convection on backside and leading edge external blade edge surfaces from aerodynamic data
- o Convection on the blade internal surfaces developed from blade cooling air and internal passage geometry

- o Convection on the rotor disk and bore surfaces developed from bore cooling air
- o Specified shaft end metal temperature

The external blade surface heat transfer coefficients are calculated for length, using flat-plate theory on the basis of 5.35-lb/sec total flow and relative local conditions. Thermal conductivity, viscosity, etc, of the gas stream are based on the thermal properties of air as a function of temperature. The external boundary layer over the blade surfaces was assumed to be fully turbulent.

The blade surface gas temperatures are the adiabatic wall temperatures calculated from the aerodynamic relative temperatures and velocities.*

The external blade heat transfer coefficients and adiabatic wall temperatures used for this turbine study are shown in Figures 37 and 38.

The rotor platform surface between blades requires a convection boundary condition. For the non-film-cooled platform, the heat transfer coefficients and adiabatic wall temperatures were calculated from the aerodynamic output at the gas path hub streamline, using the same flat-plate theory. Film cooling of the platform introduces a secondary airstream which alters the adiabatic wall temperature along the rotor hub platform surface. The local adiabatic film cooling effectiveness at a distance (x) from the injection point is defined by

$$\eta = (T_{\text{gas}} - T_{\text{aw}}) / (T_{\text{gas}} - T_{\text{coolant in}})$$

The resulting adiabatic wall temperature which is applied to the surface between blades is shown in Figure 39.

The blade forward face thermal loading results from hot gas between the rotating blade and the stationary plate. The heat transfer to this portion of the blade is dependent on the blade thickness. Because of the high rotational speeds, the heat transfer coefficient approaches the free rotating disk values and is calculated at any radius r by the expression

$$h = (0.0196 k/r) (\rho \omega r^2 / \mu)^{0.8} \text{ Btu/hr/ft}^2/\text{°F}$$

- where k = air thermal conductivity at T_{aw} (Btu/hr/ft/°F)
 μ = air dynamic viscosity at T_{aw} (lb/hr/ft)
 ρ = air density at T_{aw} & P_{rel} (lb/ft³)
 ω = rotational speed (rad/hr)
r = radius (ft)

The heat transfer coefficients and adiabatic wall temperatures (from aero hub streamline data) as a function of blade forward face edge radius are shown in Figure 40.

* The basic thermal analysis used an axisymmetric model to calculate an average circumferential blade temperature. This effort was supplemented with an approximation of the blade circumferential temperature gradients as presented in Appendix D.

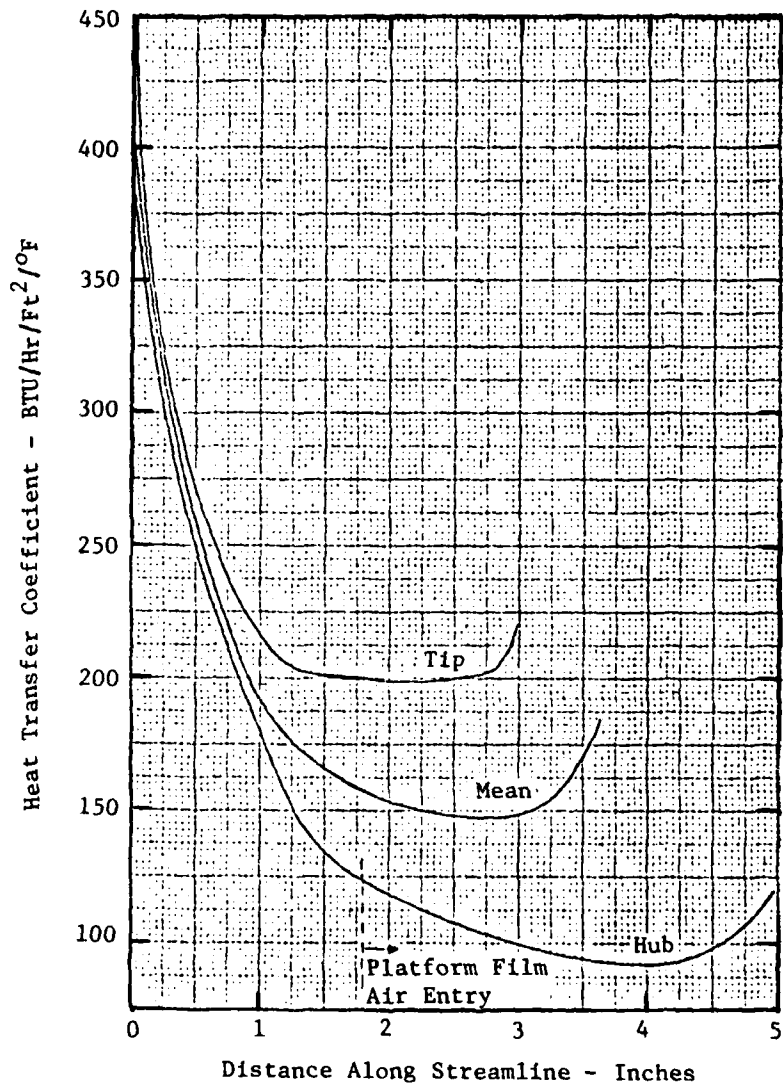


Figure 37. Blade external heat transfer coefficient.

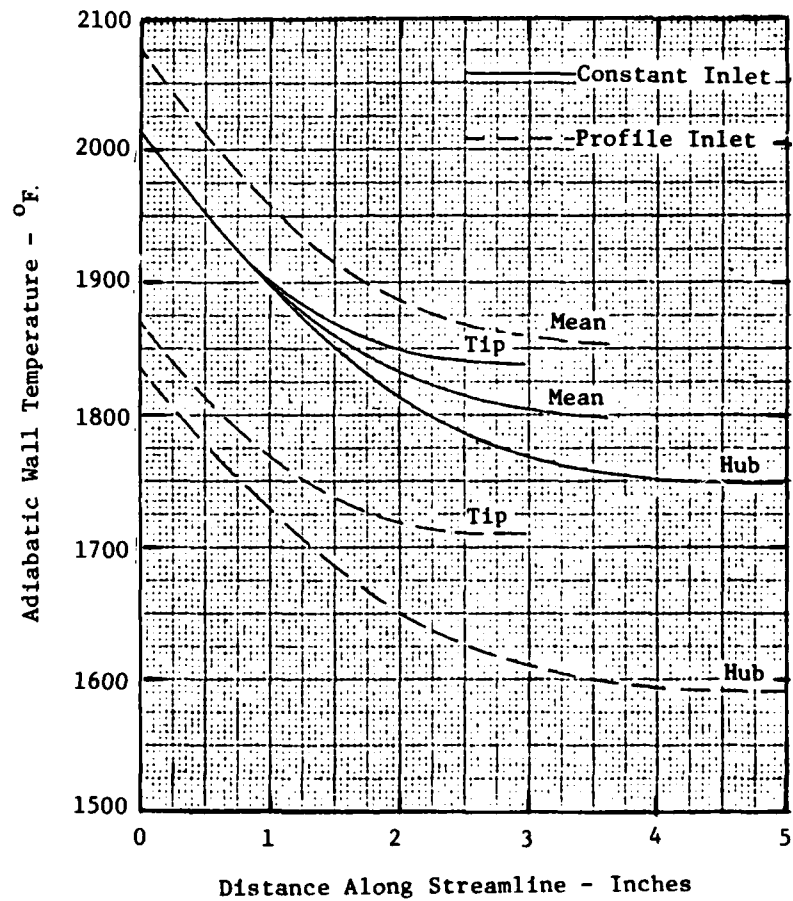


Figure 38. Blade external adiabatic wall temperature.

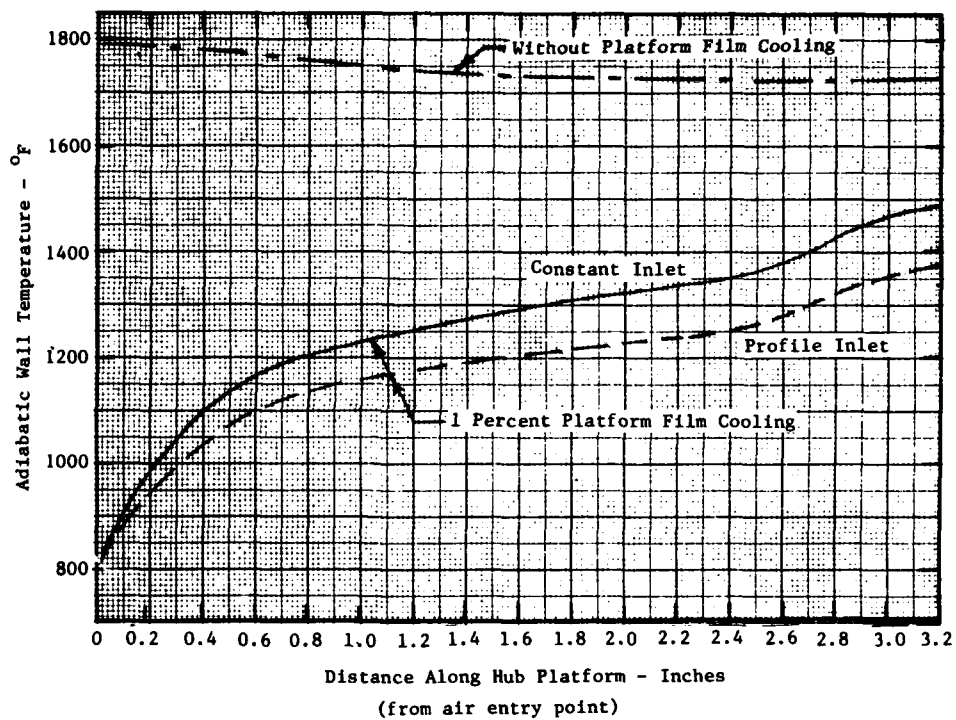


Figure 39. Platform film adiabatic wall temperature.

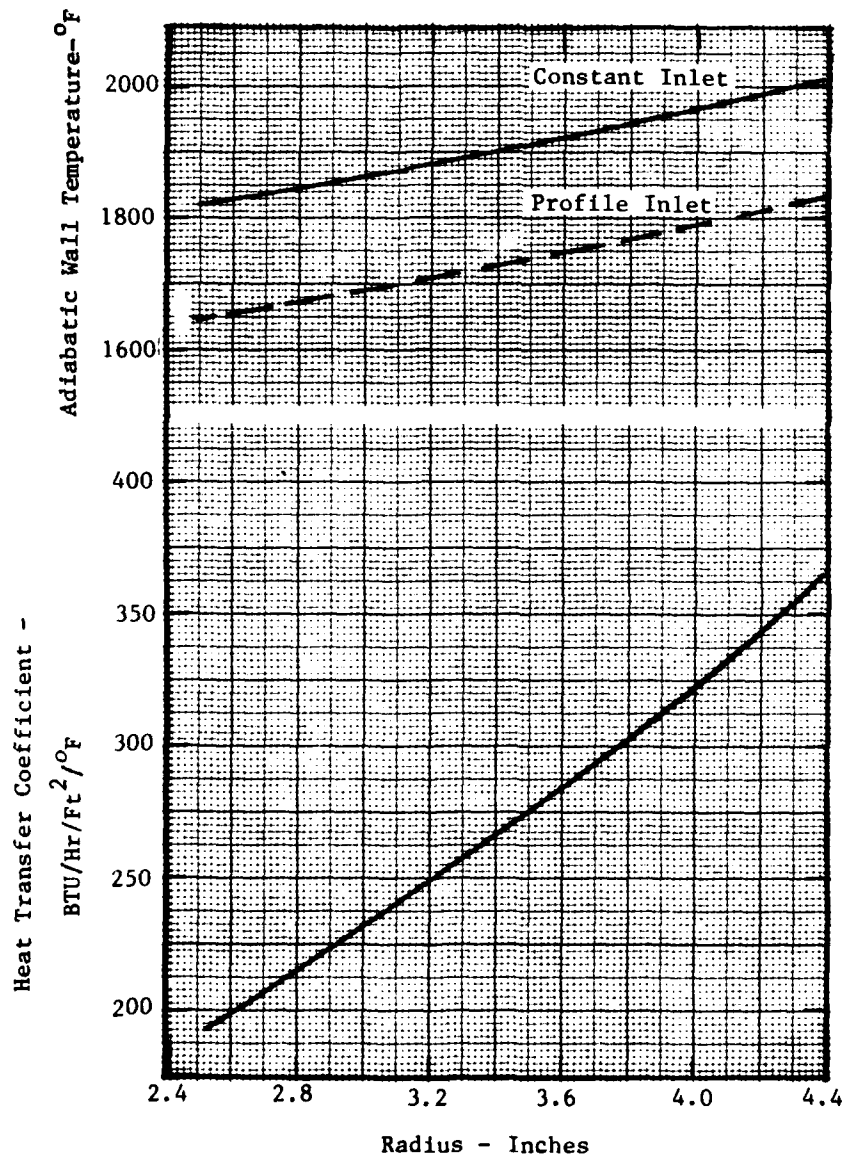


Figure 40. Forward face boundary conditions.

The average convection heat transfer coefficient at the blade inlet is determined using an empirical relation for cylinders in cross flow:

$$h = (1.14 k/D) (\rho V D/\mu)^{0.5} N_{PR}^{0.4} \text{ Btu/hr/ft}^2/\text{°F}$$

where $k = 0.048 \text{ Btu/hr/ft/°F at } 2021\text{°F}$
 $\mu = 0.121 \text{ lb/hr/ft at } 2021\text{°F}$
 $N_{PR} = 0.728 \text{ at } 2021\text{°F}$
 $\rho = 0.1154 \text{ lb/ft}^3 \text{ at } 2021\text{°F and } 106 \text{ psia}$
 $V = 565 \text{ ft/sec} = 2,034,000 \text{ ft/hr}$
 $D = 0.09 \text{ in.} = 0.0075 \text{ ft}$
 Therefore $h = 775 \text{ Btu/hr/ft}^2/\text{°F}$

The internal blade smooth passage heat transfer coefficients are calculated, using the empirical expression for turbulent internal flow from duct theory, using local flow areas and hydraulic diameters:

$$N_{NU} = 0.023 N_{RE}^{0.8} N_{PR}^{1/3}$$

or

$$h = (0.023 k/D_H)(W D_H/A\mu)^{0.8} N_{PR}^{1/3} \text{ Btu/hr/ft}^2/\text{°F}$$

where $N_{NU} = \text{Nusselt No.} = h D_H/k$
 $N_{RE} = \text{Reynolds No.} = W D_H/A\mu$
 $N_{PR} = \text{Prandtl No.} = \mu C_p/k$
 $h = \text{Heat transfer coefficient (Btu/hr/ft}^2/\text{°F)}$
 $k = \text{Thermal conductivity of air (Btu/hr/ft-°F)}$
 $D_H = \text{Hydraulic diameter of passage (ft)}$
 $W = \text{Flow rate of air in passage (lb/hr)}$
 $A = \text{Flow area of passage (ft}^2)$
 $\mu = \text{Dynamic viscosity of air (lb/hr/ft)}$
 $C_p = \text{Specific heat of air (Btu/lb/°F)}$

The heat transfer coefficients were calculated as an average value for each element of the model, using an average fluid temperature of 900°F.

Pin fin heat transfer coefficients were calculated from data in McAdams⁷ while the heat transfer coefficients for the exposed wall area were calculated from the correlation for turbulent flow in a channel. The effective heat transfer coefficient was then taken as an area-weighted average of h_{pins} and h_{wall} .

⁷W. H. McAdams, Heat Transmission, McGraw Hill, 1954.

The internal coolant temperature was calculated by an iterative heat balance procedure within the computer program, starting from the given inlet coolant temperature.

The bore heat transfer coefficients were calculated from the correlations for flow in annulus. The values for 800°F air are:

37 Btu/hr/ft²/°F at 0.2% h
76 Btu/hr/ft²/°F at 0.5% h
105 Btu/hr/ft²/°F at 0.75% h

The boundary temperature at the shaft end was specified at 850°F.

The final cooling concept for the rotor was a smooth-wall (i.e., without pin fins) blade with two internal channels. Cooling air (3%) is taken on board the rotor through a channel in the cast outer portion of the forward wheel face. Within the blade, the flow is divided 2.3% to the outer channel and 0.7% to the inner channel. Air is exited from the blade on the pressure surface near the trailing edge. The wheel outer rim (i.e., between blades) is cooled by 1% film leakage from the forward face. In the engine configuration this flow would be provided by design leakage over the labyrinth seal between the compressor and the turbine. The wheel bore will be cooled by 0.5% film flowing between the wheel bore and tie-bolt and returning to the flow path through scallops at the aft rotor pilot.

The cooling air feed orifice into the blade has been sized for 3% flow with a pressure differential across the inlet orifice of 46 psi and a pressure drop in the outer channel of 10 psi. The orifice into the inner channel has been sized for 0.7% flow with a ΔP across the orifice of 8 psi and a pressure drop in the channel of 2 psi. Figure 41 shows internal pressures and cooling flows.

Pin fins in the blade offer improved cooling at the cost of increased loading. The square pattern pin spacing of 0.09 in. center to center results in an increase of dead load of approximately 7% in the constant-thickness blade tip region. Because of this added dead load, the blade taper must start at a larger radius and increase at a greater rate. Decreasing the rotor speed to compensate for the increase in load would result in a loss in turbine efficiency.

Thermal analysis indicates that adequate blade cooling has been accomplished with 3% flow to the blade without the use of pin fins. This level of coolant flow has no adverse effect on turbine efficiency but does cause a penalty in specific fuel consumption of 0.7% per 1% of blade cooling flow.

Although the design of the rotor has been completed without the use of pin-fin cooling, local usage to reduce the temperature of problem areas or control the redistribution of load from thermal gradients would not be discounted in an engine development program.

Compressor Discharge Pressure
174.6 PSI At 100% IRP

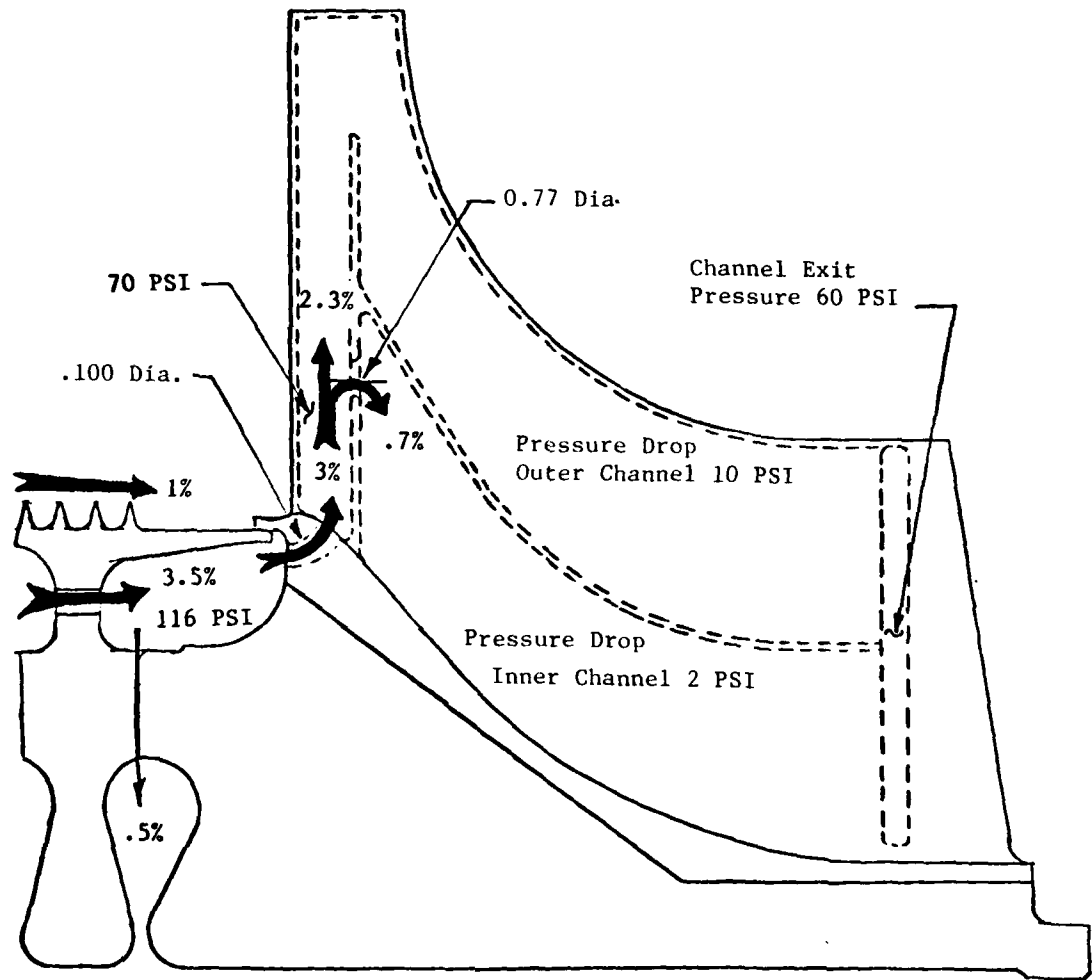


Figure 41. IRP internal flow pressures.

An isotherm plot for the 100% IRP design point is shown in Figure 34. An analysis was also completed for the 75% IRP point. An isotherm plot for this condition is shown in Figure 42.

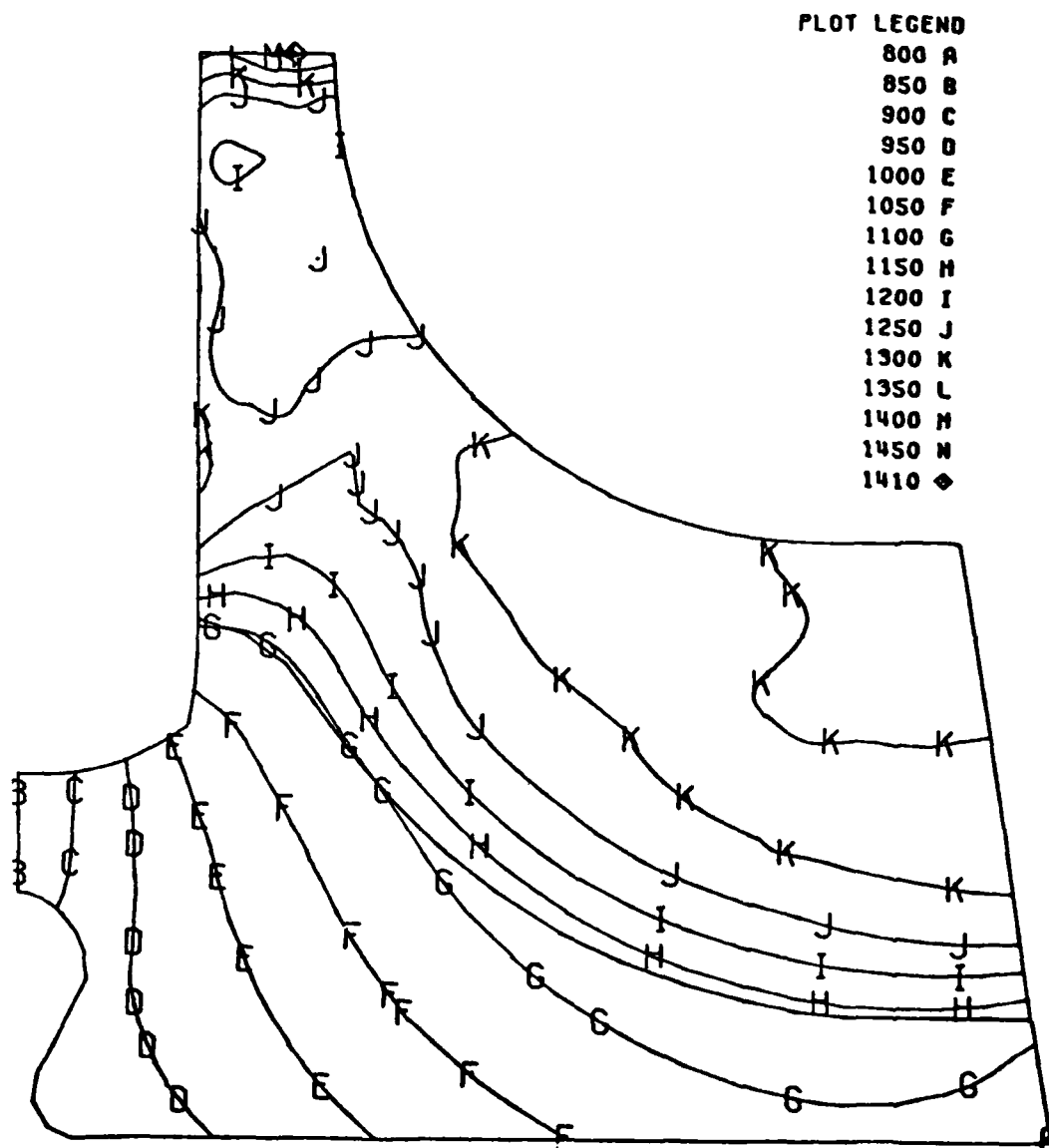


Figure 42. Isotherm plot for 75% IRP.

MANUFACTURING PROCESS DEVELOPMENT

The HIP-bond process is a technique for the fabrication of high performance turbine components with direct applicability to air-cooled radial turbine wheel designs. The concept has evolved from extensive in-house development activities at DDA and has the potential for low cost and inspectability. Because of the high efficiencies developed in diffusion bond joints, attachment problems between cast alloy details and high-strength powder metal (PM) hubs are minimized. This process has the potential for a high degree of design flexibility leading to advantages in weight, cost, integrity, and performance over alternate fabrication approaches that involve laminated photoetched sheets, bicasting, and brazing.

In this process, hot isostatic pressing (HIP) is used to exert temperature and pressure simultaneously to effect diffusion bonding of dissimilar blade and disk materials in a butt-type joint arrangement. However, for effective utilization of HIP bonding, the airfoils must be brought into intimate contact with the disk rim or hub and the joint area must be sealed from the pressure-transmitting inert gases used during the HIP cycle. The intimate contact in a radial turbine wheel design is effected by machining a cast airfoil shell to form a conical cavity which will form a tight fit with an OD-ground disk hub. The machined ID and OD contours are designed to facilitate ultrasonic inspection through the bore of the hub.

After fit-up of the airfoil shell and disk hub details, the ends of the joint on the front and rear faces are sealed by vacuum brazing with a boron-silicon modified Mar-M247 alloy which, after diffusion, is capable of withstanding the high temperatures and pressures of HIP bonding. Final machining removes the braze seal on the front and rear faces.

An overall materials fabrication objective of this program was to apply the principles already developed in the diffusion bonding of a wide variety of stylized and full-scale HIP-bond turbine components to an advanced-technology air-cooled radial turbine wheel design. Specific goals were to develop butt-type metallurgical bonds exhibiting 100% joint efficiencies between cast air-cooled alloy airfoil shells and near-net-shape powdered metal disks. A further goal was to demonstrate bond inspectability by ultrasonic techniques. The casting of the air-cooled airfoil shells, the consolidation of the PM hub, the machining of details, and the inspection of the bonded high-performance assembly have been designed so as to be cost and performance effective.

The keys to the development of high casting yields with uniform airfoil wall thicknesses and minimized core breakage and movement are:

- o Airfoil wall thicknesses well within the state of the art of 0.025 inch nominal minimum
- o Core dimension of 0.040 inch minimum thickness tapered to 0.120 inch to provide high strength and resistance to buckling
- o Core printout capability in the shell OD and ID and blade leading and trailing edge locations to provide core support as required.

The air-cooled radial airfoils are an integrally cast shell detail in Mar-M247 alloy. The nickel-based Mar-M247 alloy was selected for this application because of its outstanding strength capabilities, good castability, and demonstrated tolerance for the high temperatures employed in the bonding process. The Mar-M247 alloy, as shown in Table 3, is a newer, improved hafnium modification of the Mar-M200 and Mar-M246 class of alloy with superior stability. It is comparable in strength to these alloys.

TABLE 3. COMPARISON OF MAR-M200, MAR-M246, AND MAR-M247 COMPOSITIONS

Alloy	C	Cr	Mo	Al	Ti	Co	W	Hf	Zr	B	Ta	Ni	Other
Mar-M200	0.15	9.0	-	5.0	2.0	10.0	12.5	-	0.05	0.015	-	Bal	1.0Cb
Mar-M246	0.15	9.0	2.5	5.5	1.5	10.0	10.0	-	0.05	0.015	1.5	Bal	-
Mar-M247	0.15	9.0	0.5	5.5	1.5	10.0	10.0	1.35	0.05	0.015	3.1	Bal	-

The hub portion of the HIP-bond radial wheel is a near-net-shape powder metallurgy product in PA101 alloy. This alloy is a powder metallurgy form of hafnium-modified IN-792, which was developed for near-net-shape turbine disks under Air Force sponsorship (Contract F33615-73-C-5040). The composition of PA101 alloy is defined in Table 4. The selection of this alloy for the wheel material is based on DDA experience with the alloy, its thermal expansion compatibility with the Mar-M247 blade casting material, its superior homogeneity and fine grain structure, and its ability to be HIP consolidated to near-net-shape configurations. The superior homogeneity and fine grain structure improve inspectability and allow for the development of high fatigue strength. The alloy can be heat treated to strength/ductility levels comparable to those of Astroloy, one of the highest-performance, time-proved disk materials available. The ability to HIP consolidate PA101 powder metal alloy to near-net-shape forms reduces material requirements and machining times and contributes significantly to a more cost effective design.

TABLE 4. PA101 ALLOY COMPOSITION (IN-792 + Hf)

C	Cr	Co	Mo	W	Ta	Ti	Al	B	Zr	Hf	Ni
0.11	12.6	9.0	2.0	4.0	4.0	4.0	3.5	0.015	0.06	1.0	Bal

To demonstrate the applicability of the HIP-bond process to the fabrication of cost effective air-cooled radial turbine wheel designs, a limited process development program (shown schematically in Figure 43) was

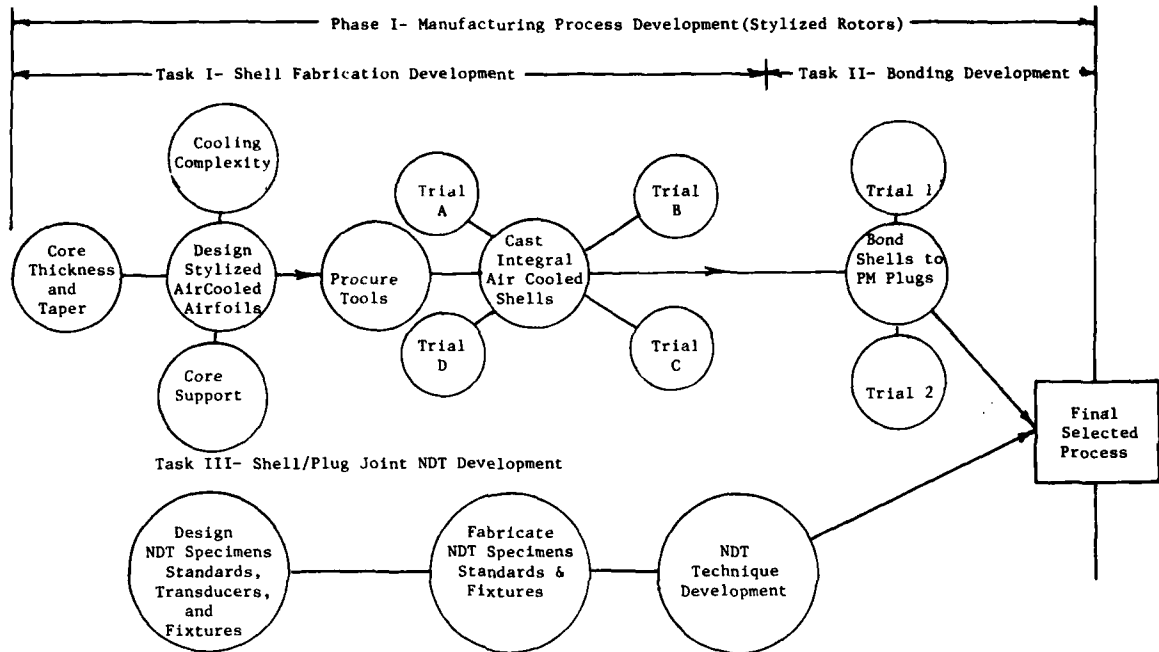


Figure 43. Manufacturing process development program.

conducted. The program consisted of three main tasks:

- o Airfoil Shell Fabrication Development - Core support and casting technique development to maximize casting quality and yield rates of integral air-cooled blade shells
- o Shell/Disk Bond Development - Development of processing parameters required for the attainment of high-integrity diffusion bond joints between Mar-M247 cast shells and PA101 disk details
- o Nondestructive Inspection Development - Development of NDI techniques required to ensure shell/disk bond joint integrity

Airfoil Shell Fabrication Development

This task consisted of the design of a stylized, hollow, cast airfoil; the design and procurement of blade casting tooling; and the subsequent trial casting of stylized, integrally cast blade shells. The external

surface contours of the stylized airfoil were the same as those of the Detroit Diesel automotive gas turbine (AGT-2) airfoil to simplify construction and reduce initial tooling costs. The AGT-2 radial inflow turbine rotor is representative in size and shape of the HTRT.

Tooling Construction and Pattern Assembly

The wax pattern die for the existing uncooled AGT-2 rotor was used as the primary "work aid" for the construction of stylized airfoil wax pattern and ceramic core dies. The airfoil shell detail is presented schematically in Figure 44. Figure 45 is a photograph of the core before and

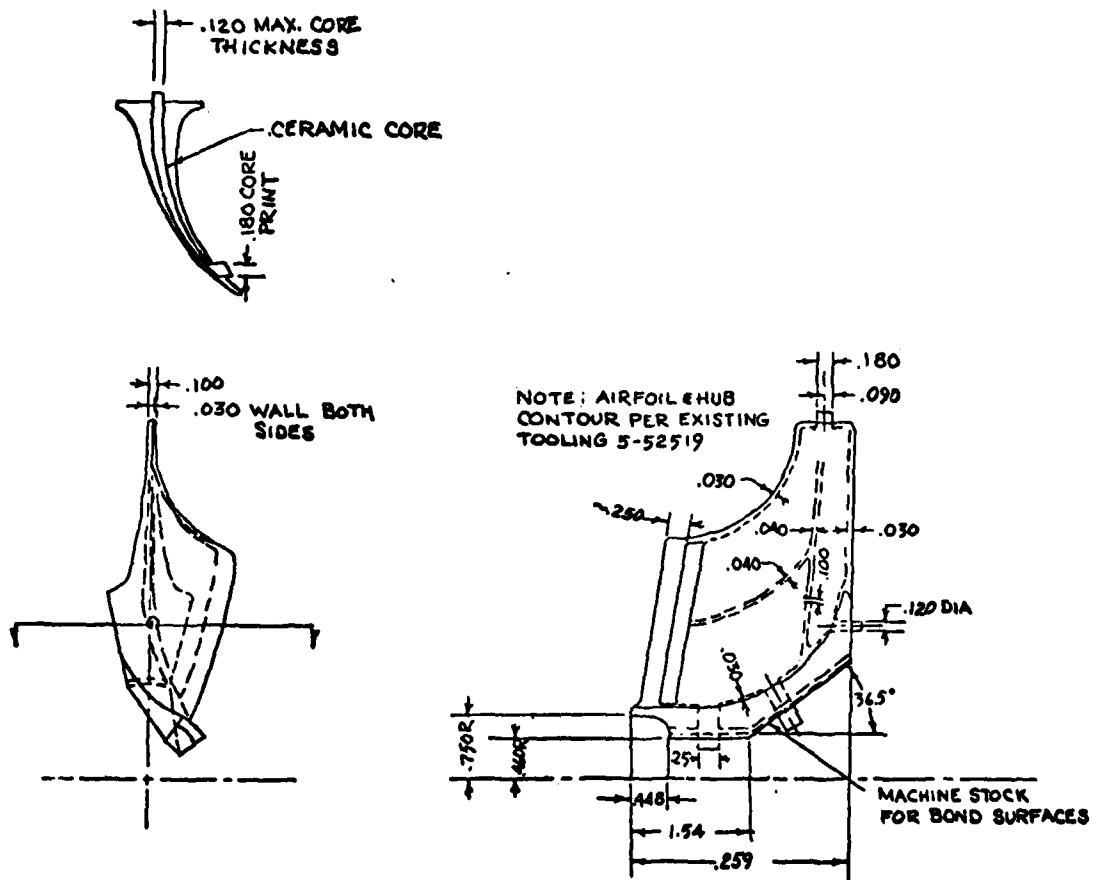


Figure 44. Stylized airfoil shell detail.



Figure 45. Typical core before and after wax injection.

after wax injection. To assemble the individual airfoil patterns with contained cores, they were placed in a fixture and joined by wax welding to form a complete 360° airfoil ring. Typical airfoils in the assembly fixture are shown in Figure 46. An assembled HTRT rotor is shown in Figure 47.

Casting Trials

A series of four casting trials was conducted to optimize the total foundry process and provide producibility information which could influence the final rotor design. The first trial involved the manufacture of castings with maximum core printout in ID locations and embodied best engineering judgment with regard to:

- o Mold fabrication procedure
- o Mold insulation
- o Mold preheat temperature
- o Metal pouring temperature
- o Mechanics of pouring

Subsequent casting trials incorporated changes in printout locations and one or more of the aforementioned factors based on the results of preceding trials.

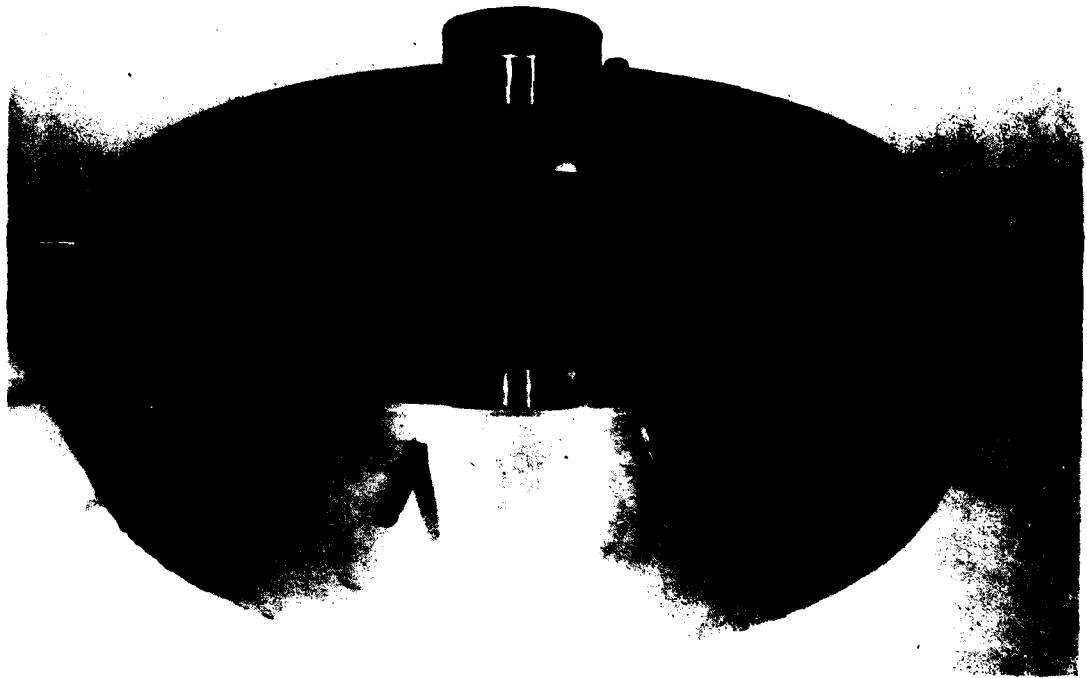


Figure 46. Airfoil waxes in the assembly fixture.

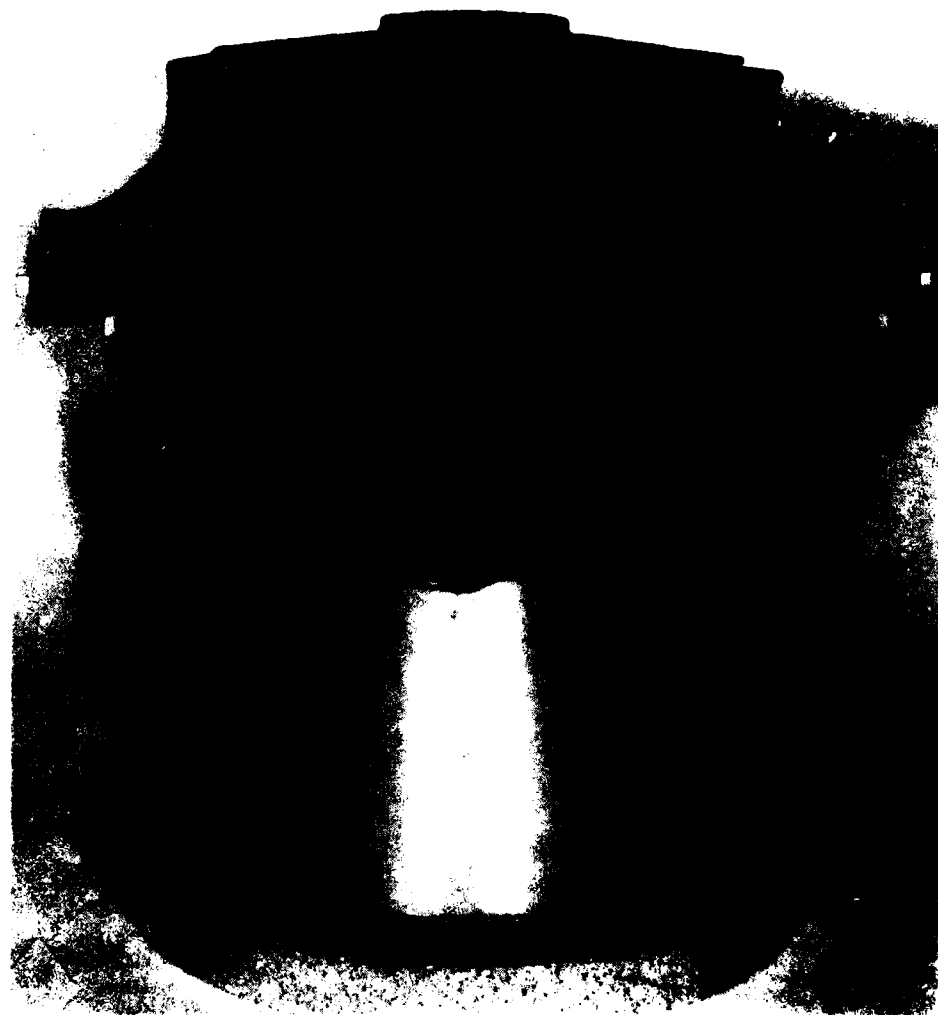


Figure 47. Wheel assembly with wax welded airfoils in position.

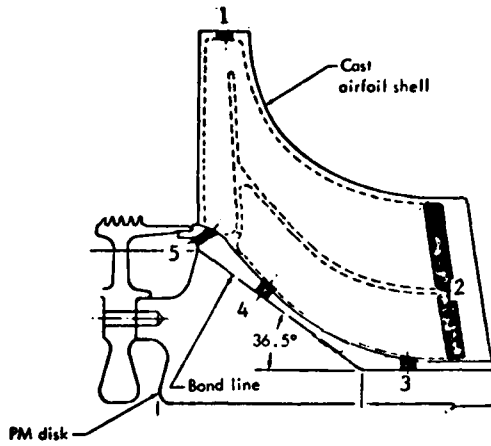
Castings from each trial were subjected to visual, radiographic, fluorescent penetrant, and ultrasonic wall thickness checks. Emphasis was placed on evaluations to assess core stability and its resulting influence on wall thickness. The ability to produce a complex thin-walled shell component free of core shift and related "kissout" was considered as one of the key technology items essential to the success of the program. Figure 48 and Table 5, respectively, summarize the core printout and casting parameter variations employed for the four Phase I casting trials in which a total of seven HTRT castings were produced.

As is indicated by Figure 48, the maximum support that was built into the stylized HTRT casting tooling was employed to produce the pattern assembly for the first shell casting of the program. The fabrication of this first rotor assembly, however, was complicated when, during the injection of cored details, a small amount of core shift developed in a localized area near the exducer portion of the airfoil which necessitated the application of a slight amount of wax to build the wall thickness up to a desired minimum of 0.020 in. The absence of core pins in this simplified tooling to locate the core die consistently within the die cavity during the wax injection process resulted in extra efforts during follow-on casting trials to stabilize the core during injection. For the full-scale rotor, production quality tooling with core locating pins was used, thereby precluding the problem.

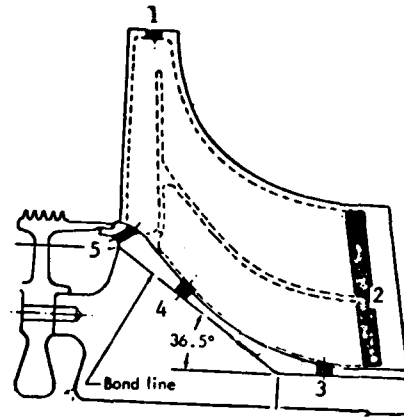
After the first wax assembly was fabricated, it was dipped in ceramic slurry, burned out, fully backed in an MgO grog, and poured in the Mar-M247 alloy. As is indicated by Table 5, a pour temperature of 2900°F and a mold preheat temperature of 2000°F were employed. As can be seen in Figure 49, the resulting casting exhibited excellent fill and no visual evidence of core "kissout." X-ray and fluorescent penetrant inspection (FPI) of the casting disclosed no anomalies.

Ultrasonic wall thickness determinations at exducer tip locations verified the stability of the cores within the shell. As is shown in Table 6, wall thickness measurements were relatively consistent and indicated no significant core shifting.

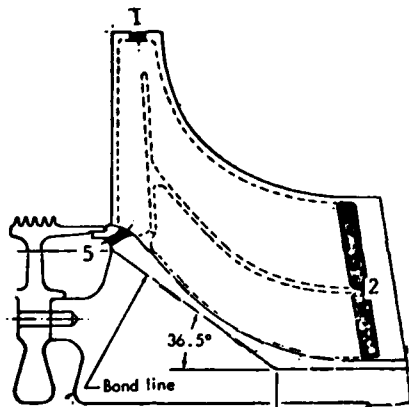
Pattern assembly 2 was fabricated to gain further insight into the degree of core support that would be required to satisfactorily produce integral air-cooled airfoil shell details. As shown in Figure 48, this assembly employed four airfoils with maximum core support (printouts at exducer, inducer, rear face, ID shaft, and ID conical locations) to provide a baseline condition. These core printouts were identical to those employed in the construction of shell number 1. In addition to these four airfoils, five others with the printout removed from the ID shaft location (core printout in the ID conical location was maintained) were used. Five additional airfoils with the printout removed from both ID cylindrical and ID conical locations rounded out the airfoils used in the assembly. A photograph showing the ID areas in which core printout locations were varied is shown in Figure 50.



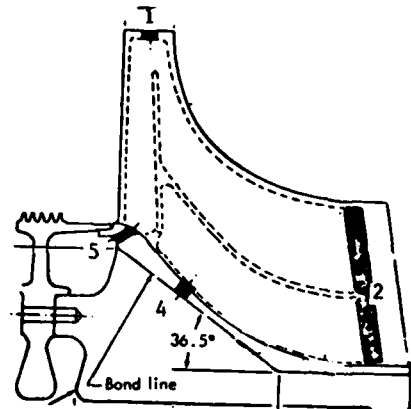
Trial 1- Maximum core support-locations 1-5 each of 14 blades



Trial 2- Rainbow core support-locations 1 through 5
4 blades locations 1 through 5
5 blades locations 1,2,4&5
5 blades locations 1,2&5



Trial 3- No ID core support-locations 1,2&5 each of 14 blades



Trial 4- Partial ID support-locations 1,2,4&5 each of 14 blades

Figure 48. Core printout variations investigated during Phase I.

TABLE 5. CASTING CONDITIONS FOR STYLIZED AIR-COOLED
MAR-M247 ROTOR SHELLS*

Trial No.	Casting No.	Mold Temp (°F)	Pour Temp (°F)	Pour Rate (seconds)	Airfoil Insulation	ID Core Support	Results
1	1	2000	2900	2-3	No	Full	Good, no kissout
2	2	1950	2850	2-3	No	Rainbow	Good, no kissout but 5 misruns
3	3	1925	2900	3+	No	None	Gross misruns, questionable kissout
	4	2000	2900	1-2	Yes	None	1 kissout
	5	2000	2900	2-3	Yes	None	1 kissout
	6	2000	2950	3-4	Yes	None	1 kissout
4	7	2000	2950	3-4	Yes	Conical only	Good, no kissout

*Heat Code V 2741

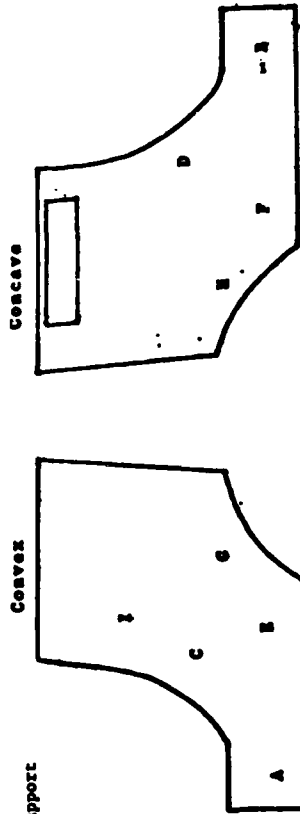


Figure 49. No. 1 airfoil casting.

TABLE 6. WALL THICKNESS DATA FOR AIR-COOLED STYLIZED AIRFOIL CASTINGS

CASTING TRIAL NO.	A		B		C		D		E		F		G		H		G+H		I							
	AVG.	RANGE	AVG.	RANGE	AVG.	RANGE	AVG.	RANGE	AVG.	RANGE	AVG.	RANGE	AVG.	RANGE	AVG.	RANGE	AVG.	RANGE	AVG.	RANGE						
1	.031-	.027-.029	.032-.034	.027-.030	.027-.032	.025-.028	.066-.068	.054-.056	.038-.040	.047-.049	.090-.092	.097-.099	.020-.022	.027-.029	2	.033-	.029-.032	.033-.035	.026-.029	.034-.036	.053-.055	.044-.046	.053-.055	.091-.093	.025-.027	
	.034	.030	.034	.030	.032	.028	.066	.060	.047	.050	.095	.095	.031	.031												
2	.031-	.027-.030	.031-.034	.025-.028	.027-.032	.025-.028	.062-.064	.054-.056	.032-.034	.041-.043	.087-.089	.097-.099	.024-.026	.033	3	.033-	.029-.032	.033-.035	.027-.030	.032-.035	.062-.064	.054-.056	.032-.034	.045-.047	.092-.094	.025-.027
	.035	.031	.034	.028	.032	.028	.062	.054	.034	.045	.092	.092	.024	.033												
3	.033-	.029-.032	.033-.035	.027-.030	.030-.033	.028-.031	.069-.071	.058-.060	.041-.043	.045-.047	.097-.099	.097	.025-.027	.033	4	.033-	.029-.032	.033-.035	.027-.030	.032-.035	.069-.071	.058-.060	.041-.043	.045-.047	.097	.025-.027
	.035	.031	.034	.028	.032	.028	.069	.058	.041	.045	.097	.097	.025	.033												
4	.030-	.026-.029	.030-.033	.024-.027	.027-.030	.025-.028	.066-.068	.054-.056	.036-.038	.045-.047	.092-.094	.092	.022-.024	.030	5	.035-	.031-.034	.035-.037	.029-.032	.032-.035	.071-.073	.067-.069	.043-.045	.056-.058	.101-.103	.022-.024
	.035	.031	.034	.029	.032	.028	.066	.065	.043	.045	.092	.092	.022	.030												
5	.032-	.028-.031	.032-.035	.026-.029	.029-.032	.027-.030	.065-.067	.055-.057	.046-.048	.051-.053	.097-.099	.093	.023-.025	.035	6	.038-	.034-.037	.038-.041	.032-.035	.035-.038	.064-.066	.055-.057	.042-.044	.055-.057	.101-.103	.023-.025
	.038	.034	.037	.030	.033	.030	.064	.064	.042	.042	.097	.097	.023	.035												
6	.032-	.028-.031	.032-.035	.026-.029	.029-.032	.027-.030	.062-.064	.053-.055	.047-.049	.092-.094	.092	.092	.024-.026	.030	7	.032-	.028-.031	.032-.035	.026-.029	.029-.032	.063-.065	.057-.059	.043-.045	.058-.060	.101-.103	.024-.026
	.035	.031	.034	.029	.032	.028	.063	.063	.043	.043	.092	.092	.024	.030												
7	.037-	.033-.036	.037-.040	.031-.034	.034-.037	.032-.035	.074-.076	.060-.062	.038-.040	.054-.056	.089-.091	.089	.024-.026	.034	8	.040-	.036-.039	.040-.043	.034-.037	.037-.040	.076-.078	.063-.065	.043-.045	.054-.056	.101-.103	.027-.029
	.040	.036	.039	.034	.037	.035	.076	.063	.043	.043	.089	.089	.027	.034												

* internal diameter core support



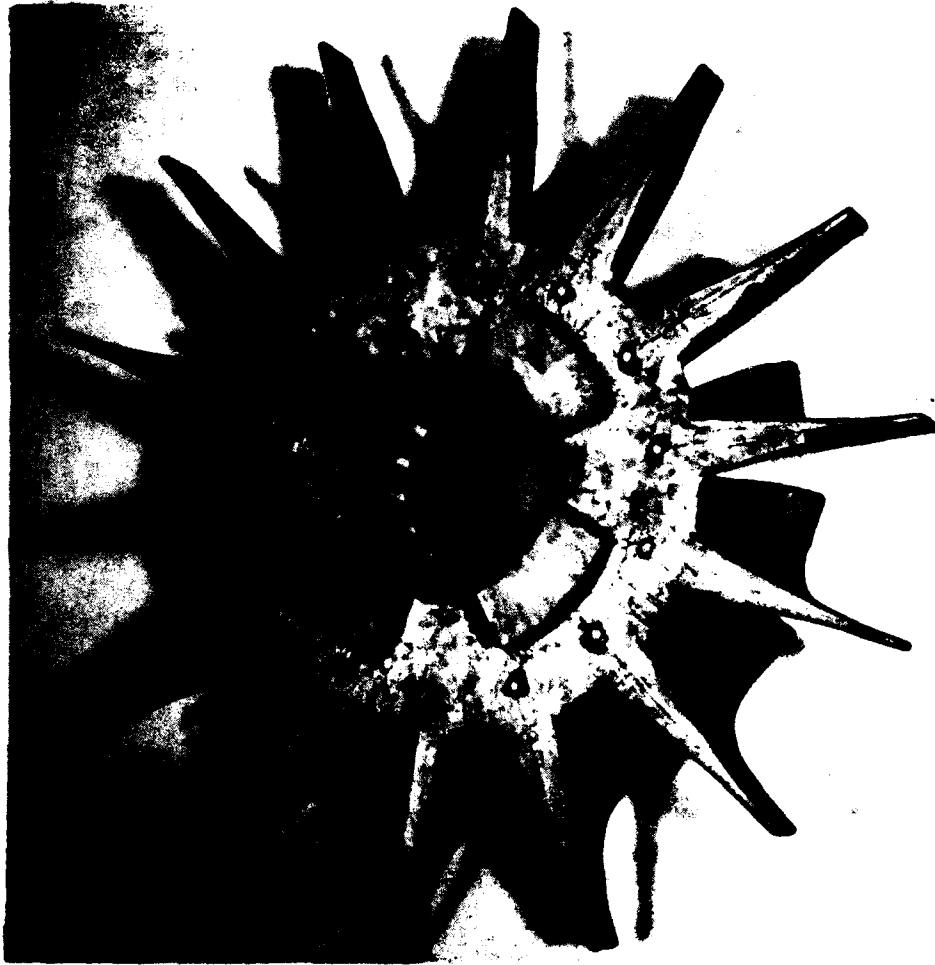


Figure 50. Oblique rear face view of No. 2 airfoil casting showing the ID and where core printout variations were investigated.

The pouring conditions for this assembly were modified slightly from those used for the first wheel assembly in an attempt to achieve a finer and more uniform grain by lowering the mold and pour temperatures from 2000°F to 1950°F and from 2900°F to 2850°F, respectively. As shown in Figures 51 through 54, a grain size refinement was achieved; however, reduced fluidity caused misruns in five airfoils.

Visual inspection of the No. 2 casting revealed excellent core stability for all airfoils irrespective of core printout design. This was subsequently verified by X-ray and ultrasonic wall thickness inspection as well as cut-up evaluations. The wall thickness data generated for the two extremes of core support evaluated (no inner support and full core support) are compared in Table 6 and illustrate the excellent core stability achieved despite the misrun encountered.

Figure 55 is a typical cross section of one of the airfoils from this casting and shows the complexity and uniform wall thickness of the airfoil.

Because of the promise shown for the core printout design involving no inner support and the process simplification afforded by this concept, it was decided to fabricate assemblies 3 and 4 with no inner ID core support. (The surfaces to be joined must be pressure tight; consequently, any core printout holes in the ID area of the shell will require a separate plugging/brazing step to ensure pressure tightness.)

As is indicated by Table 5 and Figures 56 and 57, gross misrun occurred in casting 3 because too low a mold temperature was used inadvertently. (A mold temperature of 2000°F was to have been used; however, thermocouple records indicated that the mold temperature was 1925°F.) As with the first two castings, wall thicknesses were ultrasonically determined for nine locations on each blade. As indicated in Table 6, the wall thickness varied significantly between locations G and H where the thicknesses would have been expected to be nearly the same.

In an attempt to determine whether the disparity in wall thickness occurred as a result of core shift during the wax injection process or whether it occurred during the casting process, a wax airfoil pattern produced in the same run with those used for the No. 3 and 4 rotor assemblies was cut up. Clearly shown (Figure 58) was a shifting of the core in the hub region of the airfoils which indicated a high probability that the core shift was a preexisting condition. A cut-up of injected cored airfoils during tool tryout failed to detect a major problem in this area. However, the results indicated the need for core locating pins in the full-scale rotor tooling.

The wax pattern for casting 4 was assembled slightly behind that of casting 3; as a result, there was no special effort to maintain registry of the core within the wax die as there was for subsequent assemblies 5 and 6.

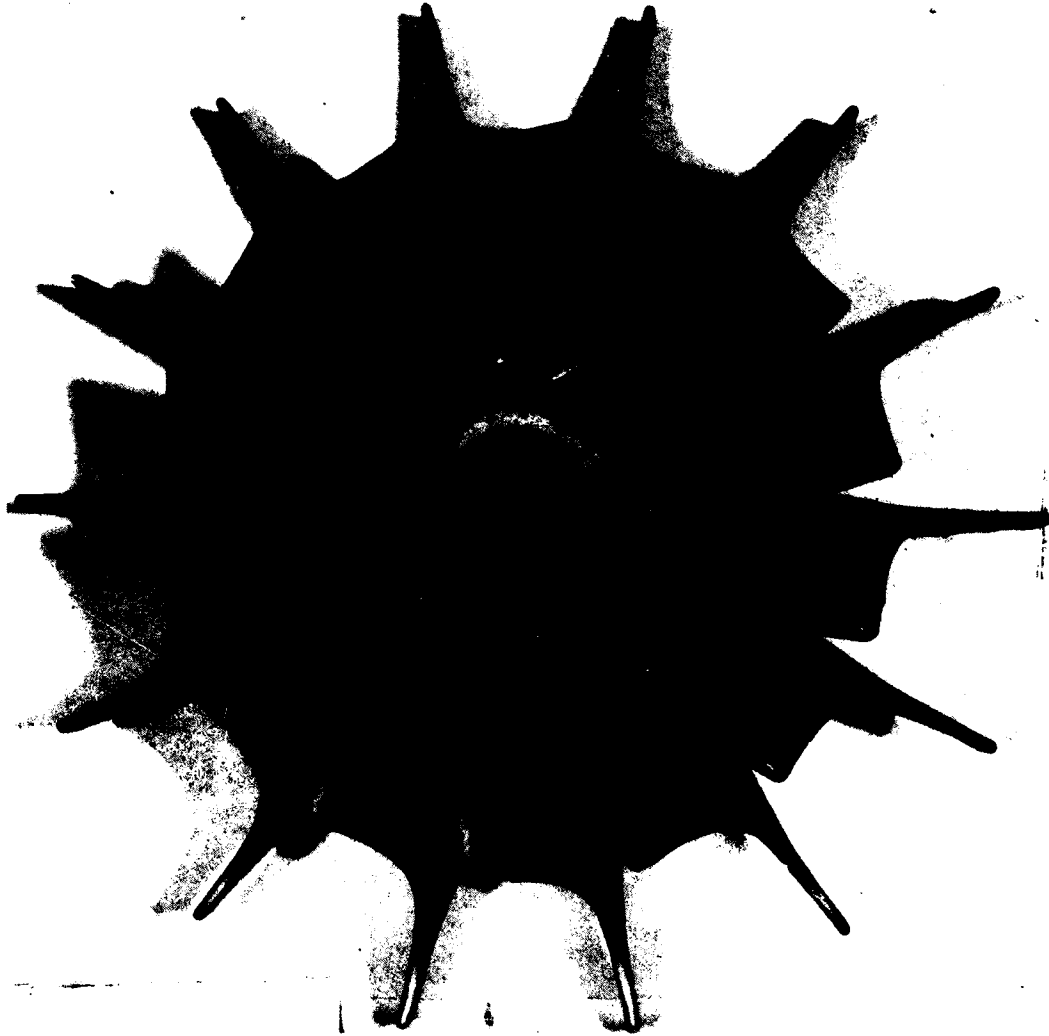


Figure 51. Macroetched appearance of No. 1 airfoil casting.
(Excellent fill and core stability were realized
for this casting.)

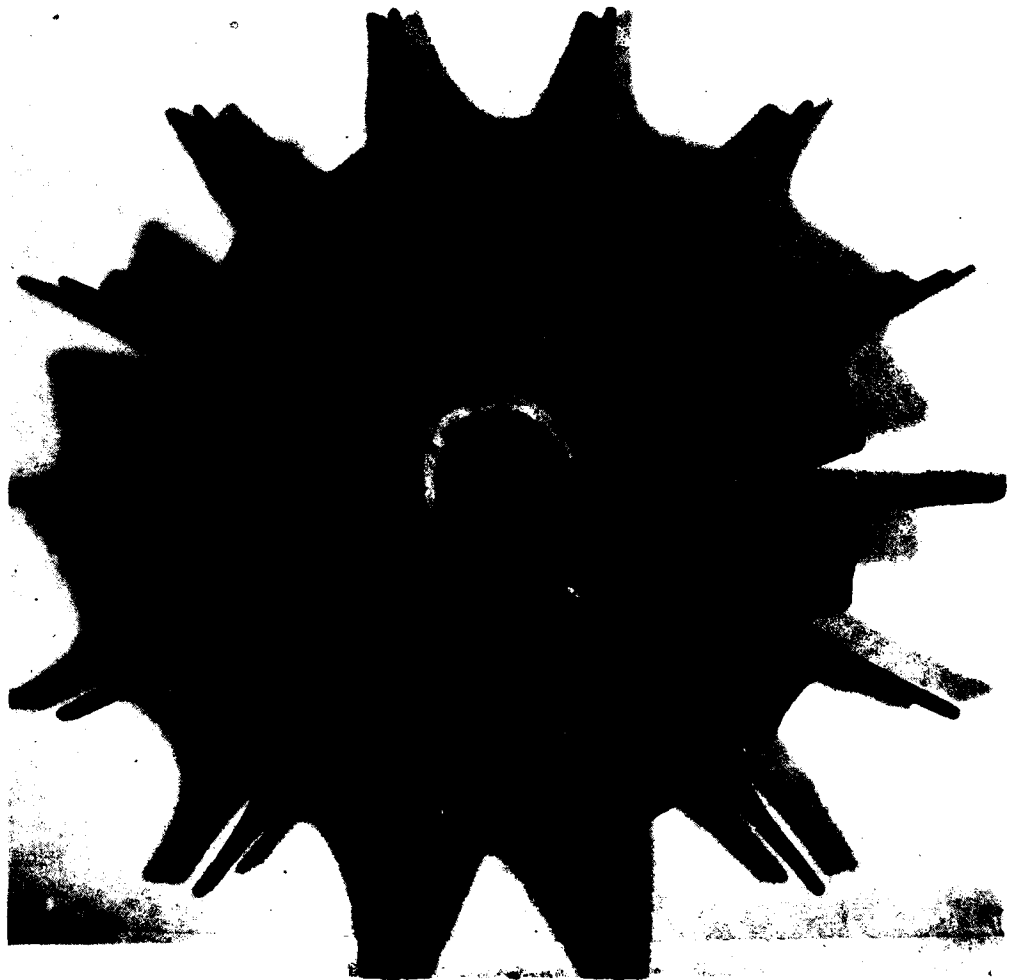


Figure 52. Macroetched appearance of No. 2 airfoil casting. (Casting was produced by employing a 50°F lower mold preheat and pour temperature than for No. 1 rotor; grain size was refined and core stability excellent; however, slight misrun was developed in five airfoils.)

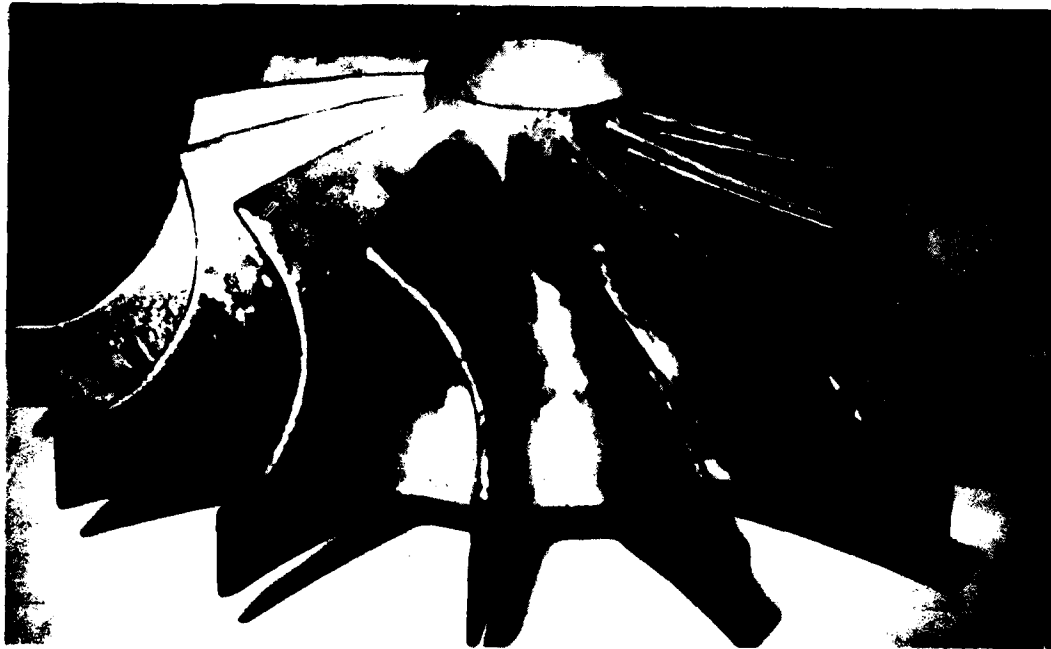


Figure 53. Side view of macroetched No. 1 airfoil casting.
(Excellent fill was achieved in this casting.)



Figure 54. Side view of macroetched No. 2 airfoil casting showing misrun in inducer vane location.



Figure 55. Typical airfoil cross sections from airfoil casting No. 2 (shows cooling channels).

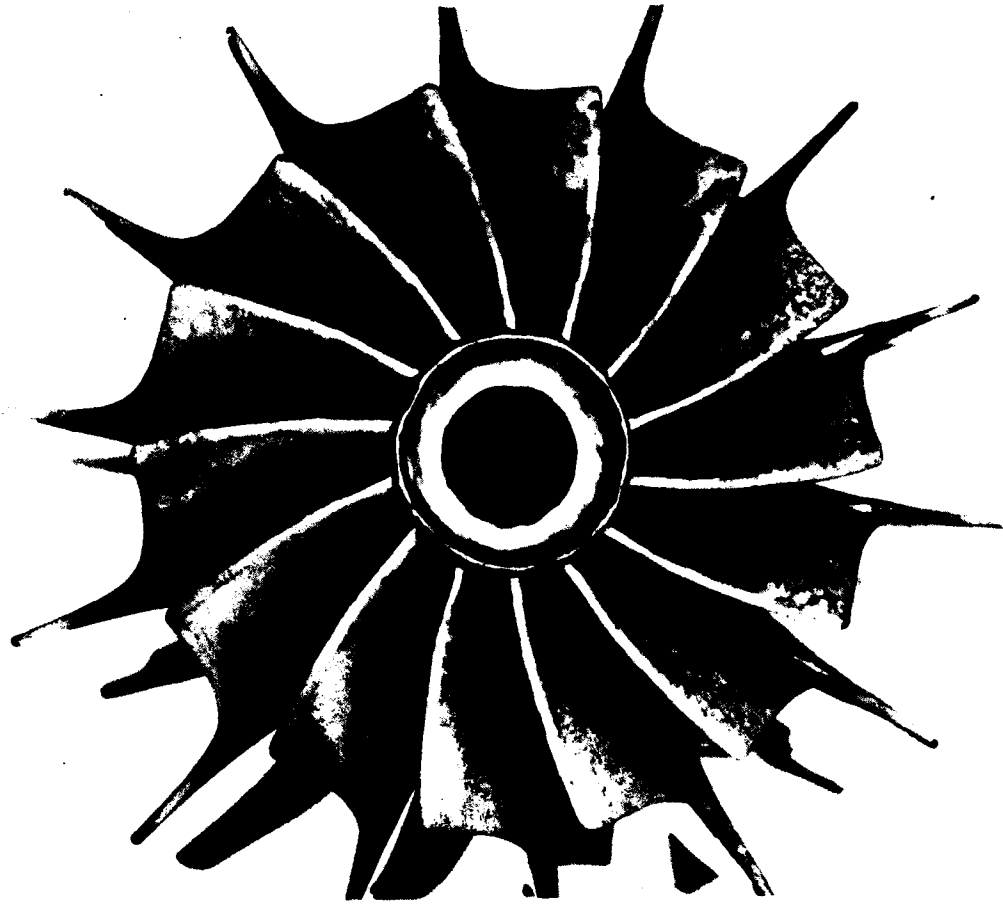


Figure 56. Macroetched appearance of No. 3 airfoil casting. (Mold preheat temperature was inadvertently 75^oF lower than desired and gross misrun resulted.)



Figure 57. Side view of macroetched No. 3 airfoil casting.

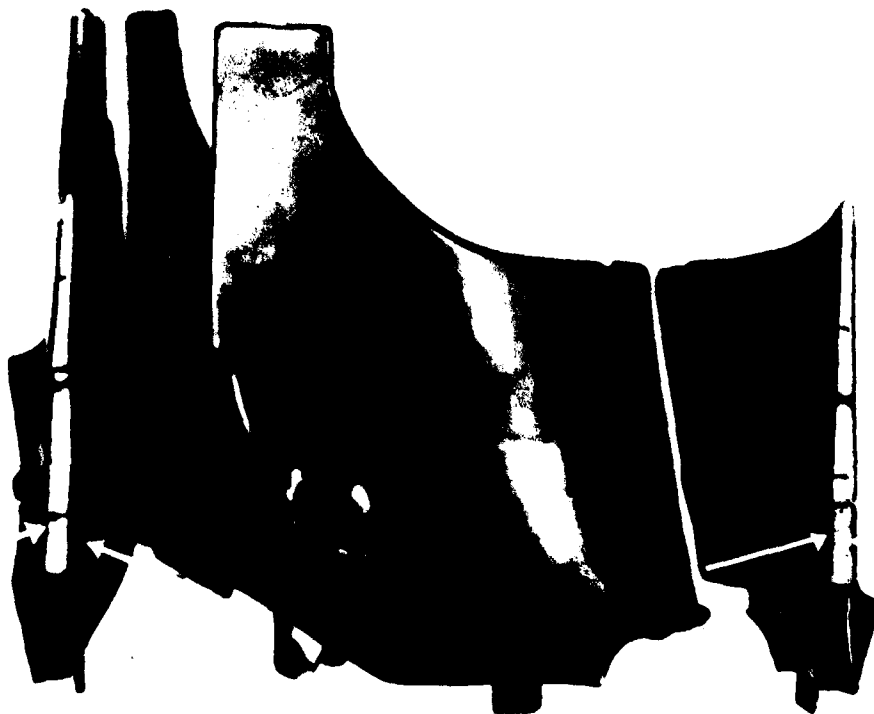


Figure 58. Core shift (see arrows) which occurred during wax injection of airfoils for assemblies 3 and 4.

Special emphasis was placed upon achieving total fill for cast shell No. 4. In addition to the 2900°F pour and 2000°F mold preheat successfully used on the No. 1 casting, a faster pour rate was used in addition to the application of a Fiberfax wrap around airfoil tips in the inducer location.

As is seen in Figures 59 and 60, total fill was achieved in this casting, and a more refined macrostructure was obtained. Unfortunately, core "kissout" developed on the convex surface of one blade. Relative to wall thickness results, the data for this rotor in the critical G location, on an average basis, seemed slightly better than those for casting 3. There was, however, significant variation in the thickness data (a range of 0.028 to 0.045) as there was for rotor 3.

To reduce the possibility of core shifting during the wax injection process, assemblies 5 and 6 were made up of wax airfoils which were produced by waxing steel shot of appropriate thickness onto the cores. During the injection process, the shot served as pins to keep the cores from shifting; subsequently, the shot was removed and waxed over to provide an airfoil with a more controlled fit-up of core within the airfoil. Only those airfoils which displayed proper wax wall thicknesses in the areas of suspected kissout (location G) were used.

The pour rate for casting 5 was slowed from that of casting 4. The intended effect of the slower pouring rate was to provide a "gentler" metal stream so as to lessen the possible disturbance to the airfoil cores. The other pouring parameters remained the same as for casting 4, which exhibited good fill characteristics. As shown in Figure 61, the result for casting 5 was a single defect in the convex surface of one airfoil similar to the apparent kissout observed in casting 4. Wall thickness data in the problem area (G) were generally improved over those for castings 3 and 4; however, the improvement apparently was not sufficient to keep the core from flexing during pouring.

The pouring parameters for casting 6 were altered to introduce a still "gentler" metal stream. The pour rate was slowed to 3-4 seconds and the amount of superheat applied to the melt was increased 50°F to 2950°F to ensure fill. All other pouring parameters remained the same as for casting 5, as shown in Table 5.

The result for casting 6 was again a kissout in one of the blades. Figure 62 shows the casting with a core kissout on the convex side of one blade. As with casting 5, the wall thickness data were generally improved over those of castings 3 and 4; however, core instability appeared to have occurred during pouring.

The results for castings 5 and 6 conclusively indicated that conical ID core support was required for the stylized HTRT rotor assemblies. Consequently, a seventh pattern assembly incorporating this type of core support was produced. The selection of this core printout technique was

based on the successful results obtained with similar ID printouts during the casting of assemblies 1 and 2.

Pouring parameters for casting 7 were identical to those of casting 6. They resulted in an excellent casting, free of kissout and possessing good surface quality, as shown in Figure 63. Wall thickness checks (Table 6) were very satisfactory and showed good consistency. Especially notable is the consistency of wall thicknesses in location G where previous kissouts had surfaced. The reduced scatter of wall thicknesses in location G (0.006 in.) indicates a greatly improved core stability and is attributable to the added ID core printout. The ID printout in the conical surface is shown in Figure 64.



Figure 59. Macroetched appearance of No. 4 airfoil casting. (Excellent fill and good grain size control were developed in this casting; however, core "kissout" developed in one airfoil.)

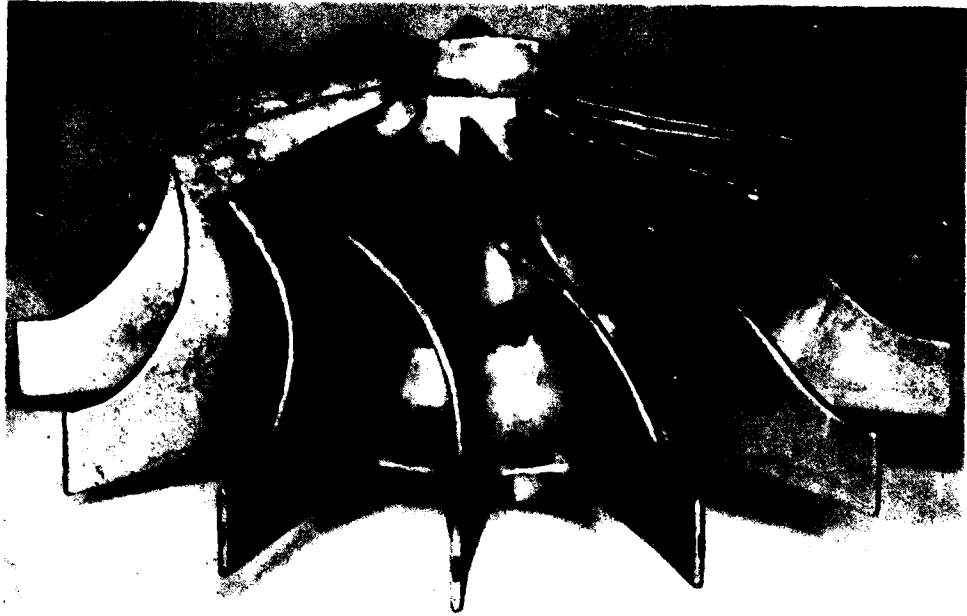


Figure 60. Side view of No. 4 airfoil casting.



Figure 61. Side view of No. 5 airfoil casting.



Figure 62. Side view of No. 6 airfoil casting.



Figure 63. Side view of No. 7 airfoil casting showing good fill and core stability.

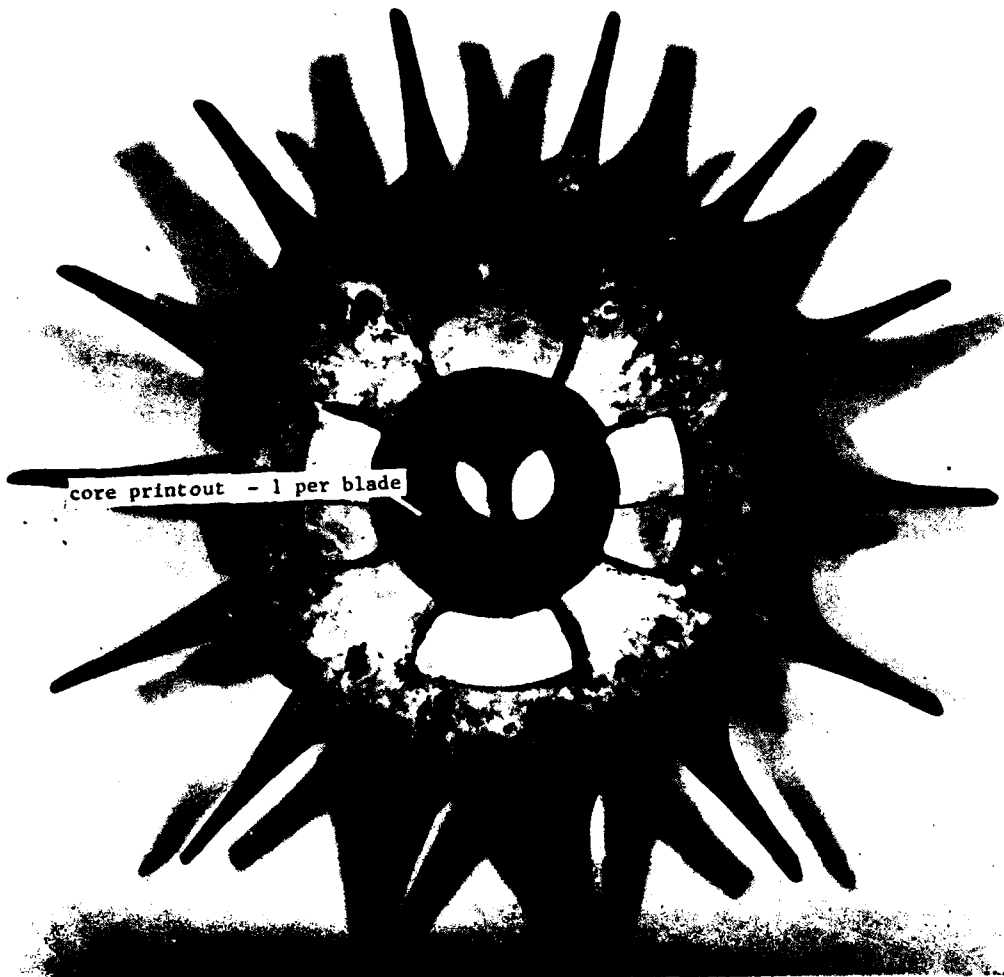


Figure 64. Airfoil casting No. 7 conical ID printout.

Conclusions and Recommendations

The airfoil shell fabrication development task produced the following conclusions:

- o The feasibility of producing a sophisticated integral air-cooled radial turbine wheel shell was demonstrated.
- o ID core support is required for the stylized design to keep the cores from flexing at the hub locations. This will necessitate a braze plugging operation at the ID surface location prior to HIP bonding of the shell and plug details.
- o The limited experience with seven castings precludes an accurate assessment of casting yields. However, a review of this work with representatives of a leading supplier of integral turbine components indicated that the DDA approach to the casting of this component is commercially viable. Based on related experience with air-cooled radial turbine wheels and air-cooled integral nozzles, production yields in excess of 65% seem entirely feasible.
- o The cast airfoil ring approach employed for the full-scale HTRT rotor should incorporate a core printout in the conical ID location and follow the basic core printout scheme utilized for stylized casting No. 7.

Shell/Disk Bond Development

The bonding development effort was aimed at establishing the parameters essential for the attainment of high-integrity diffusion bond joints between the air-cooled Mar-M247 radial airfoil shell and PA101 disk details. To evaluate HIP bonding effects on overall quality, four cast shells were machined to form a close-tolerance fit-up with finish machined near-net-shape PA101 hub details.

Complementing the stylized rotor fabrication was development work directed at alternate methods of sealing the bond joint interface prior to HIP bonding. The baseline method, braze sealing, is well within the state of the art; however, it requires an additional vacuum furnace thermal cycle, which is an additional cost factor.

The development of an alternative method using electron beam welding could reduce thermal distortion risks associated with braze sealing. This alternative method also has the potential for the application of automated processing, which could substantially improve the consistency of bond quality and reduce manufacturing costs. As shown in Figure 65, a series of development trials aimed at optimizing joint integrity was conducted.

Baseline Definition Studies

Initial efforts were aimed at defining the baseline microstructural bond quality and mechanical property response obtainable with a Mar-M247/PA101 HIP-bond radial turbine wheel system when processed to selected bonding parameters derived from earlier DDA studies.

For this purpose 11 metal can HIP-consolidated PA101 preforms were obtained from the Udimet Powder Metals Division of Special Metals Corporation. The configuration obtained is shown schematically in Figure 66; the composition and sieve analysis of the material are listed in Appendix A. Photographs of the canned and fully machined appearance of the PA101 plug are shown in Figure 67. Upon receipt at DDA, the material was fluorescent penetrant and sonic inspected and judged to be acceptable. Following the NDT work, thermally induced porosity (TIP) tests and microstructural checks were run on samples cut from each of the PA101 plugs. A flat pancake, approximately five inches in diameter and one inch thick, representative of the same master heat and consolidation practices employed for the plug, was also TIP tested. It was also heat treated to a cycle consisting of 2 hours at 2050°F, gas fan cooled to room temperature, 24 hours at 1600°F, and air cooled to room temperature. Specimens from the pancake were then evaluated for tensile and stress rupture capability.

The TIP cycle was to have consisted of an exposure at 2200°F for four hours, following which the before- and after-exposure densities were to be checked for changes. However, the test coupons were inadvertently started at 2000°F and exposed for three hours before the error was dis-

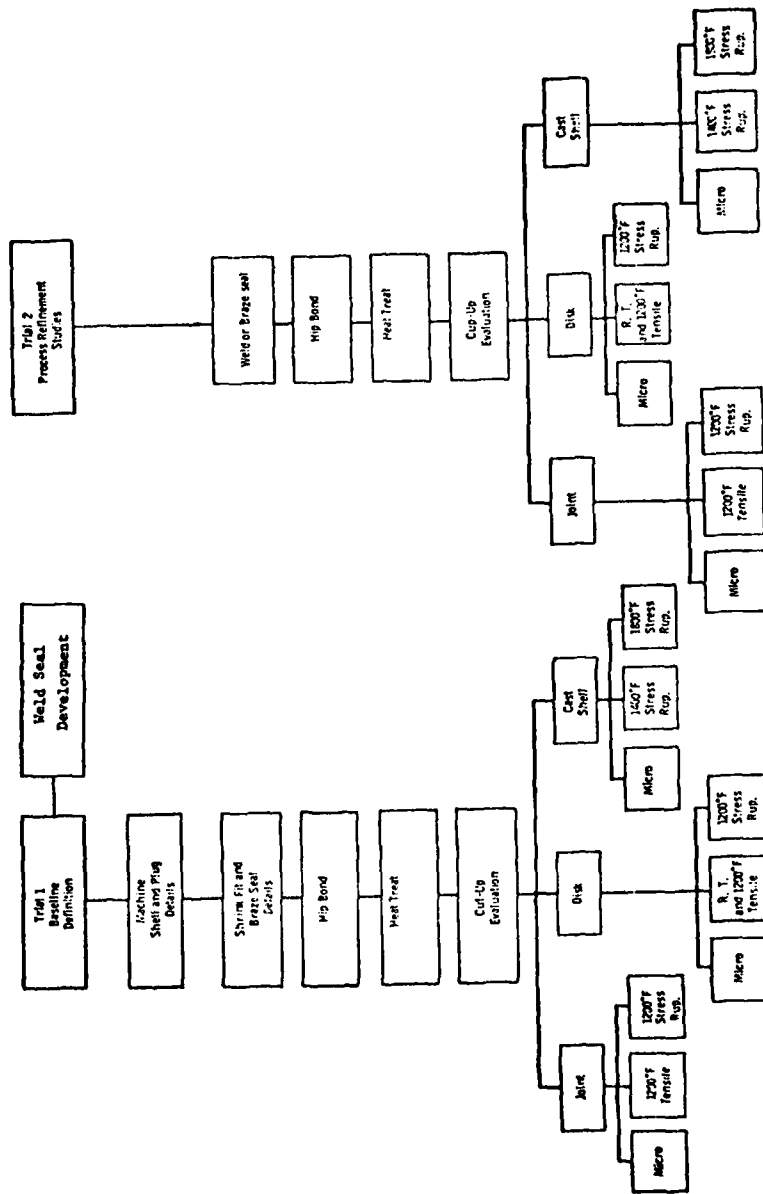


Figure 65. Bonding development program.

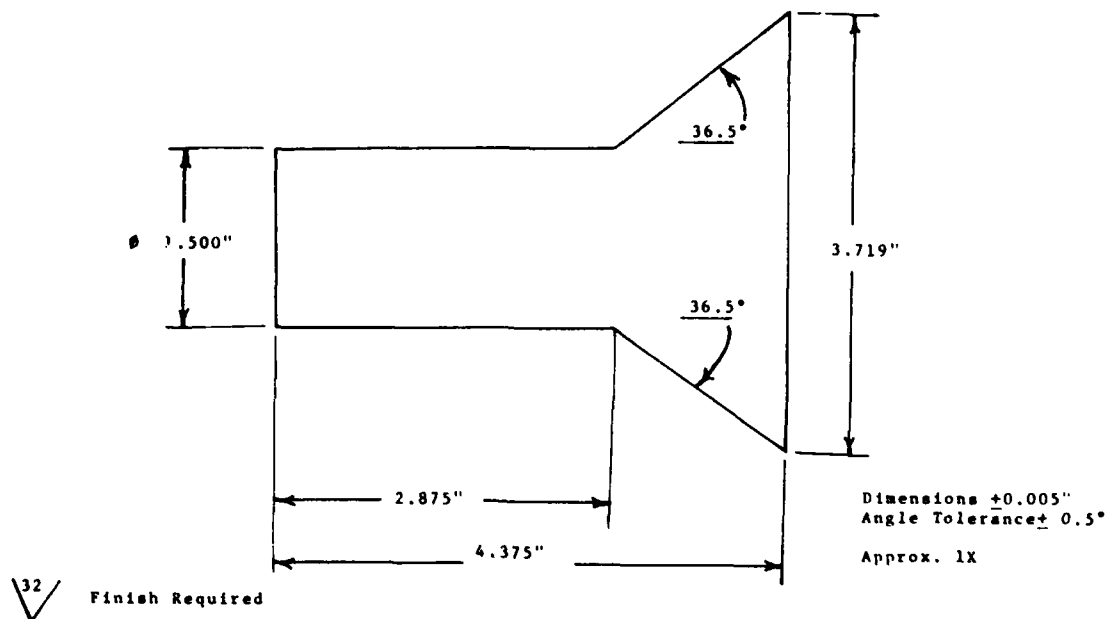


Figure 66. Subscale PA101 plug for bonding development.

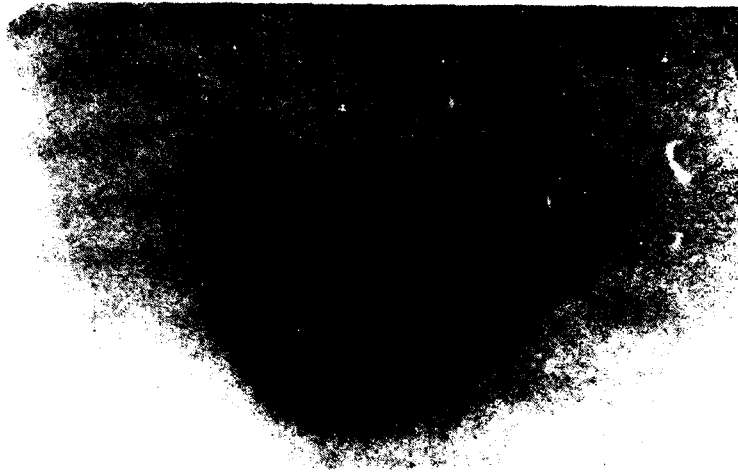


Figure 67. Powdered metal plug.

covered. The effect on TIP response was felt to be insignificant, and the TIP temperature was increased to 2200°F and run for the scheduled four hours.

The results of these exposures are summarized in Table 7. Plug 5 showed a significantly higher degree of density change than did the balance of the material, indicating that a seal malfunctioned during HIP consolidation. These results were consistent with independent metallographic TIP tests performed by Special Metals on fill tubes removed from the consolidated material.

The room temperature and 1200°F stress rupture results for the pancake representative of the plugs are shown in Table 8. The results generally meet the minimum program goals; however, tensile ductilities tend to be on the minimal side of acceptable.

Following inspection of the PA101 plug material and upon availability of castings, two shell castings (3 and 4, with no ID core support) and two plugs (1 and 4) were machined to the configurations defined by Figure 68. The appearance of typical details in their as-machined condition is shown in Figure 69.

Bonding Trial 1

The assembly details selected for the first HIP bonding trial received identical processing. Preparation of the rotor shell and plug details began with an outgas cycle (2100°F/1 hr/vacuum) to clean the mating surfaces. The shell was then heated to 450°F and the plug was cooled in liquid nitrogen (-320°F) to create a loose slip fit when the plug was inserted in the shell. An interference fit resulted when the detail temperatures were equalized. The exposed shell-to-plug interfaces were braze sealed with a boron-silicon modified Mar-M247 braze alloy as indicated in Figure 70. The following braze cycle was used in successive steps.

2225°F (30 min)
2000°F (10 min)
2100°F (1 hr)

Following brazing, the seams were leak checked by pressurizing the brazed assemblies in helium gas and then scanning the braze area with a probe attached to a mass spectrometer. Helium outgassing from the braze joint would have been detected by the mass spectrometer.

HIP bonding was performed at the Udimet Powder Division of Special Metals Corporation, Ann Arbor, Michigan. Rotor assemblies 1 and 2, weld coupons from the complementary electron beam weld seal effort, cast-to-size (CTS) Mar-M247 test bars, and a PA101 plug were processed together in the initial HIP run. The parts were suspended in the HIP can with

AD-A084 120

GENERAL MOTORS CORP INDIANAPOLIS IN DETROIT DIESEL A--ETC F/6 21/5
HIGH-TEMPERATURE RADIAL TURBINE DEMONSTRATION. (U)

APR 80 B A EWING, D S MONSON

DAAJ02-77-C-0031

UNCLASSIFIED

DDA-EDR-9990

USAAVRADCOM-TR-80-D-6

NL

2 - 3

of
frames

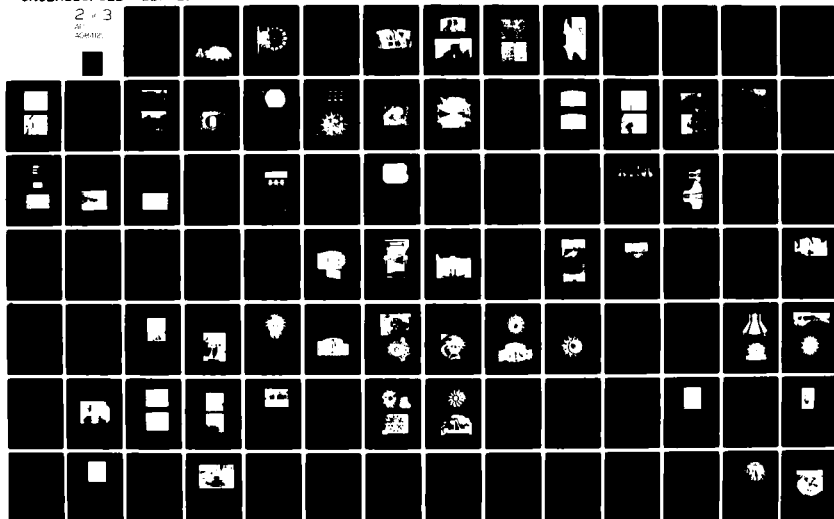




TABLE 7. PA101 TIP RESPONSE*	
<u>Plug No.</u>	<u>% Density Change</u>
1	0.18
3	0.37
4	0.22
5	1.00
6	0.40
7	0.41
8	0.47
9	0.18
10	0.21
11	0.22
12	0.16
101-2 Pancake	0.16
*2000°F (3 hr) + 2200°F (4 hr) exposure	

TABLE 8. MECHANICAL PROPERTIES* FOR MATERIAL REPRESENTATIVE OF PA101** PLUG DETAILS				
Tensile				
<u>Test Temperature, °F</u>	<u>0.2% yield strength (ksi)</u>	<u>UTS (ksi)</u>	<u>% Elong</u>	<u>% RA</u>
Room temperature min program goals	120.0	190.0	8.0	10.0
Pancake results	140.5	197.0	8.2	9.4
1200 min program goals	115.0	160.0	8.0	10.0
Pancake results	128.8	187.2	9.6	12.5
1200°F/125 ksi stress rupture				
	<u>Hours to failure</u>	<u>% Elong</u>		
Min program goals	50.0	3.0		
Pancake results	213.4	10.0		
*2050°F (2 hr) vacuum, gas fan cool + 1600°F (24 hr) air cool heat treatment				
**Pancake 101-2				

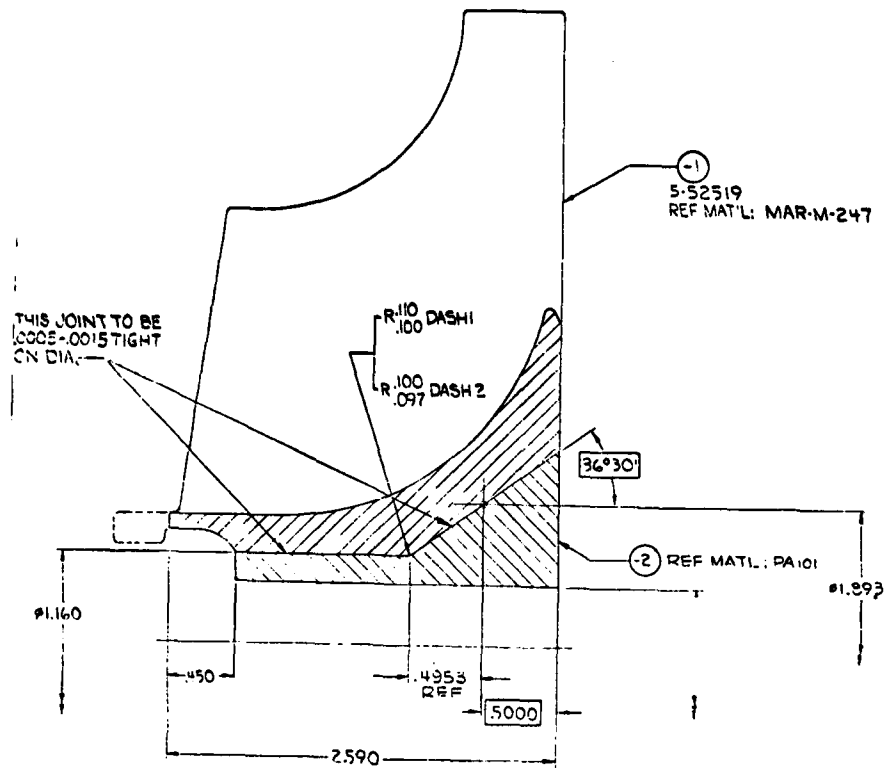


Figure 68. Stylized rotor assembly.

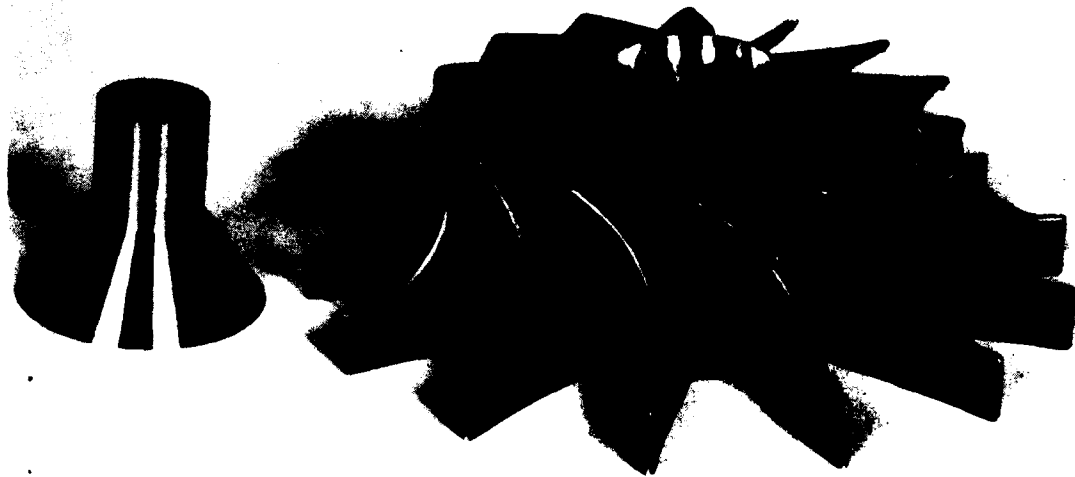


Figure 69. Machined plug and shell details for rotor assembly No. 1.

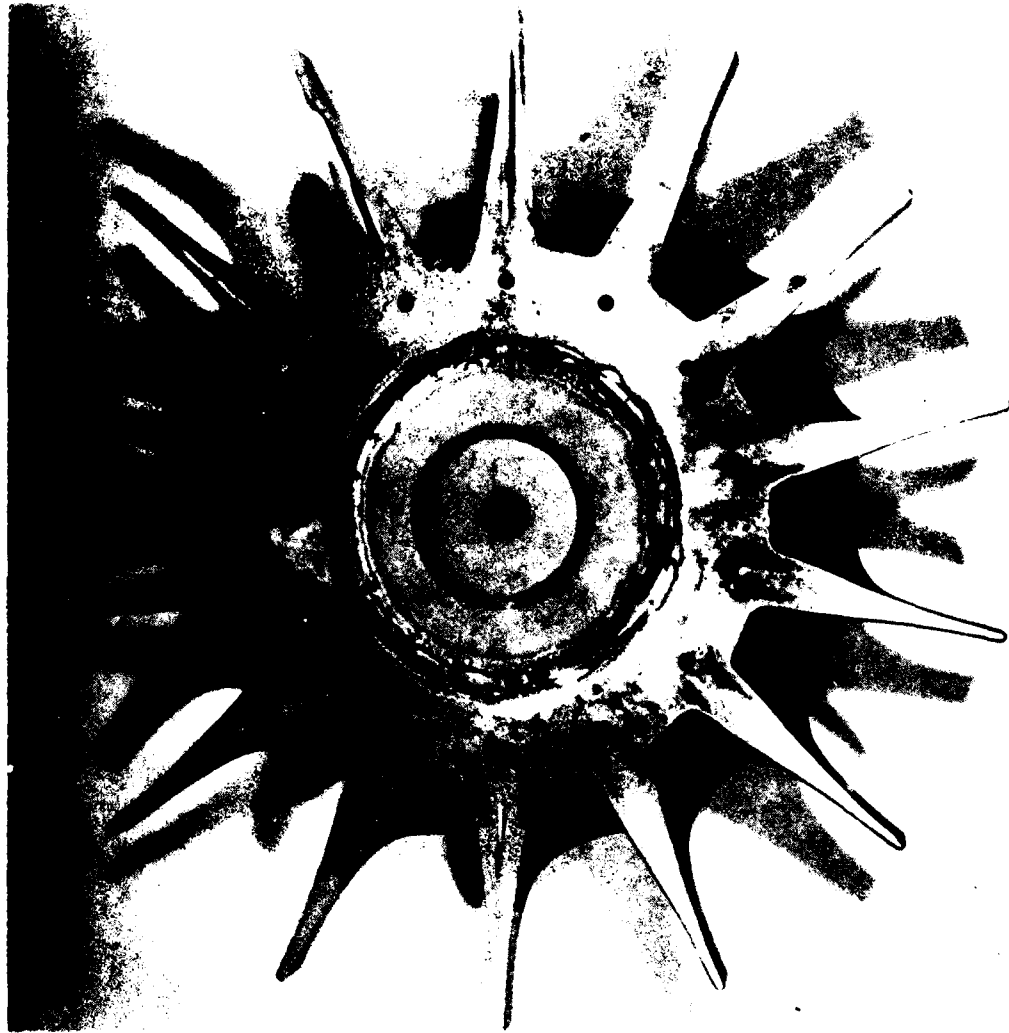


Figure 70. Braze sealed rotor assembly prior to HIP bonding.

spherical aluminum oxide packing material which provided support for the rotors as shown in Figure 71. The HIP parameters were 2215°F/15 ksi/3 hr. The HIP unit was instrumented with four thermocouples in various locations of the work zone and indicated that the load temperatures were within 25°F.

The rotors were cut in half, polished, and etched as shown in Figures 72 and 73. The bond joint was examined at high magnification and appeared to be sound and continuous in both rotors. There had been some concern regarding the fit-up of the shell and plug radii; however, the HIP process blended the radii in a complete bond, eliminating any mismatch that may have existed. Figure 74 shows photomicrographs of a typical bond joint at 100X and 500X magnification. The photomicrographs show an excellent metallurgical bond.

Following HIP processing, Rotors 1 and 2, Mar-M247 test bars, and a PA101 plug were heat treated to the following schedule:

2050°F/2 hr/vacuum, gas fan cooled +
1550°F/4 hr/argon, air cooled +
1400°F/16 hr/argon, air cooled

After heat treatment, the PA101 plug as well as the two rotors were sectioned into blanks for testing as shown in Figures 75 and 76. In the case of the rotors, the bond joint was centered normal to the major axis of the blank and at the approximate mid-length so that half of the bar was Mar-M247 material and the other half was PA101. Following blanking (1 inch long by 1/4 inch square for the joint specimens and 1-1/2 inch long by 3/8 inch square for the parent metal PA101), the material was sent to Metcut Research Associates of Cincinnati, Ohio, for final machining and specimen testing. Accompanying this material for testing were the cast-to-size Mar-M247 test bars (heat 2741) which had been ground approximately 0.003 inch per surface in the gage area to remove a thin film (0.001 inch) of oxidation that developed during the HIP bonding cycle. (Chemistries and casting parameters for Mar-M247 heat 2741 as well as for the other Mar-M247 heat used in the program are summarized in Appendix B.)

Table 9 is a summary of the tests of joint specimens from assemblies 1 and 2 as well as the parent metal PA101 and Mar-M247 material which had been processed along with the rotors. An excellent level of joint integrity was realized in this testing; all tensile and stress rupture failures occurred away from the joint in the parent metal Mar-M247. However, one stress rupture specimen failed prematurely away from the joint in the radius portion of the Mar-M247. Examination of this specimen (Figure 77) revealed microshrinkage which apparently had not been densified by the 3-hour, 15-ksi exposure at 2215°F. (This specimen was from casting No. 3, which was poured cold and experienced gross misrun and, as a result, represented a casting with questionable internal soundness prior to HIP bonding.)

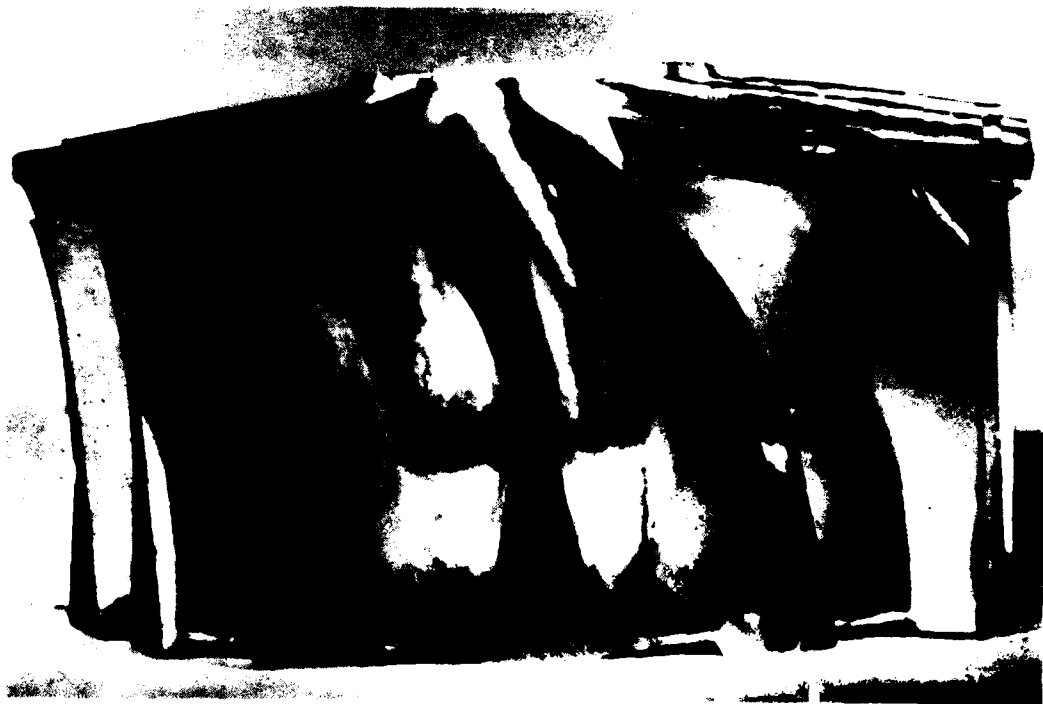


Figure 71. Stylized rotor assembly with blade tips removed to facilitate loading in the 6-inch-diameter Special Metals HIP unit.



Figure 72. Macro cross section of the No. 1 HIP-bonded assembly.

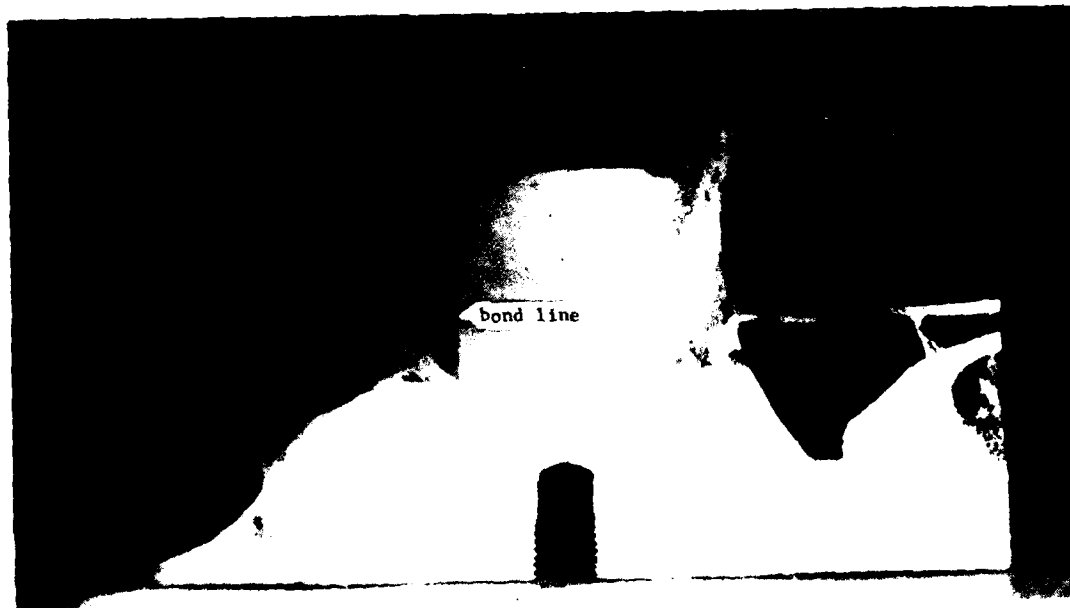


Figure 73. Macro cross section of the No. 2 HIP-bonded assembly.

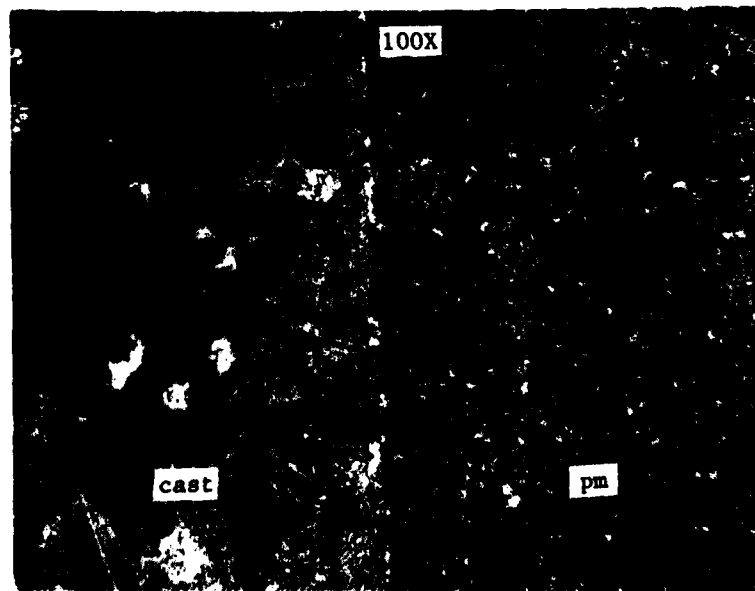
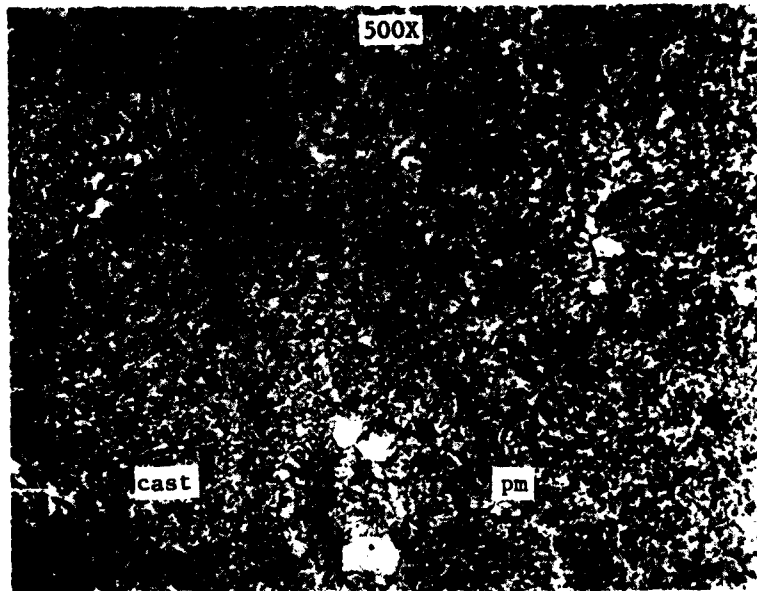


Figure 74. Photomicrographs of bond lines.

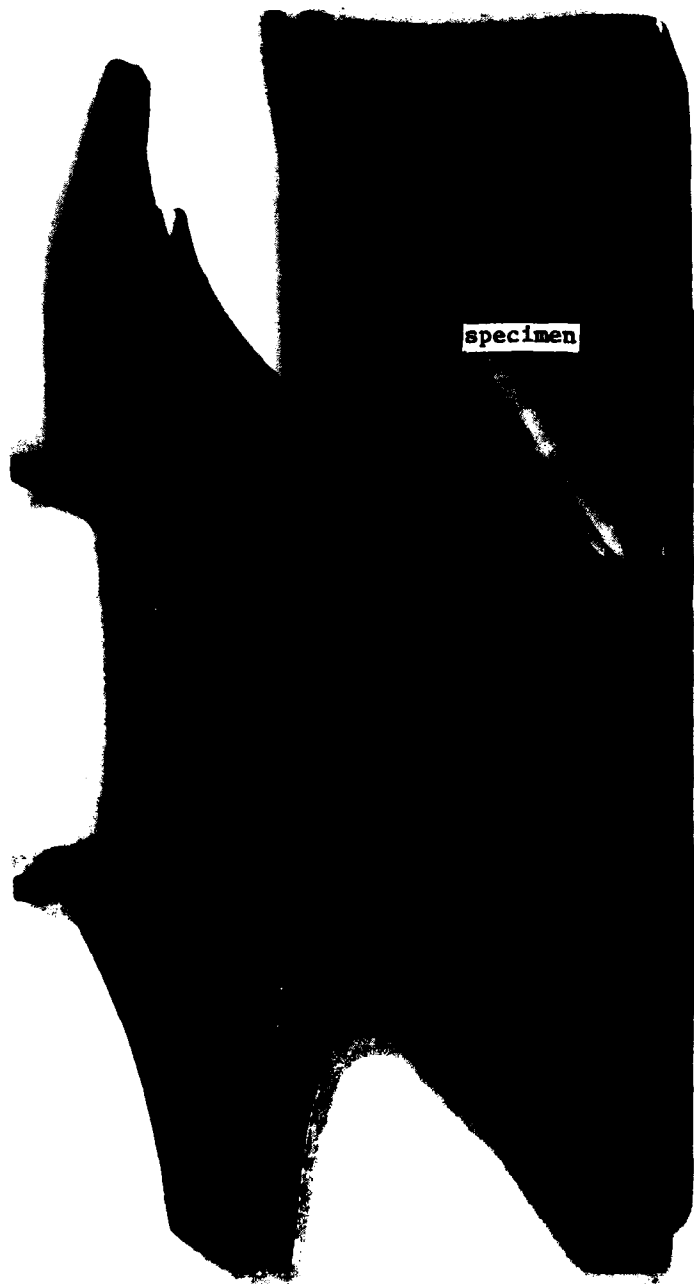
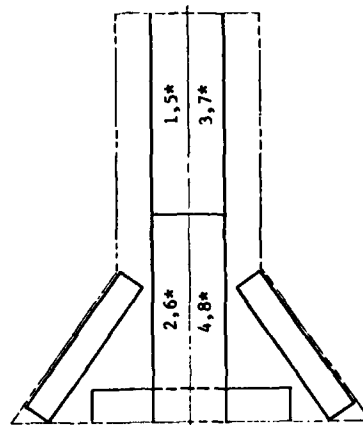
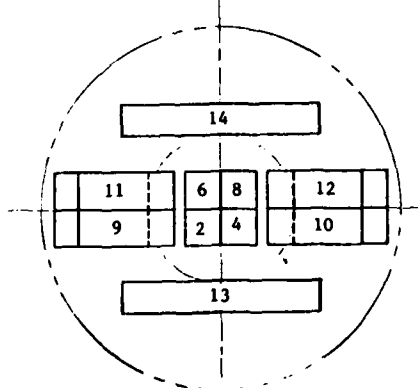


Figure 75. Joint specimen location.



side view



bottom view

*specimen in rear plane

Figure 76. Cut-up diagram for PA101 plug material.

TABLE 9. TEST RESULTS FOR ROTOR ASSEMBLIES 1 THROUGH 4.

Heat treated to 2050°F, 2 hr, GFC, + 1550°F, 4 hr, AC,
+ 1400°F, 16 hr, AC following HIP bonding

PA101/Mar-M247 Butt Joint Specimens

1200°F Tensile

<u>Trial No.</u>	<u>Rotor No.</u>	<u>Spec Code</u>	<u>0.2% Y.S. (ksi)</u>	<u>UTS (ksi)</u>	<u>% Elong</u>	<u>% RA</u>	<u>Remarks</u>
1	1	1A1	123.8	140.4	2.8	3.9	Cast alloy failure
1	1	1B5	123.5	138.9	5.2	5.9	Cast alloy failure
1	2	2A1	131.1	146.5	5.7	5.5	Cast alloy failure
1	2	2B5	133.6	151.3	3.3	7.8	Cast alloy failure
2	3	3B5	117.5	126.1	6.1	11.6	Cast alloy failure
2	3	3A3	135.9	161.9	3.8	8.8	Cast alloy failure
2	4	4A2	114.2	130.4	5.3	10.6	Cast alloy failure
2	4	4A4	128.0	155.1	4.1	9.7	Cast alloy failure

1200°F/125 ksi Stress Rupture

<u>Trial No.</u>	<u>Rotor No.</u>	<u>Spec Code</u>	<u>% Hours to Failure</u>	<u>% Elong</u>	<u>% RA</u>	<u>Remarks</u>
1	1	1B6	53.7	2.8	3.9	Cast alloy failure
1	1	1A3	167.7	4.2	3.2	Cast alloy failure
1	1	1A2	Failed on loading in cast radius			Microshrinkage
1	2	2B6	75.8	1.4	8.0	Cast alloy failure
1	2	2A2	413.0	---	---	Specimen discontinued
2	3	3B7	41.1	1.9	6.7	Cast alloy failure
2	3	3A4	Failed on loading in cast gage			*
2	3	3A1	55.8	4.2	10.8	Cast alloy failure
2	4	4A3	76.8	3.7	7.4	Cast alloy failure
2	4	4B7	Failed on loading in cast gage			*
2	4	4A1	71.6	1.9	9.4	Cast alloy failure

*No material defects; apparent tensile overload

TABLE 9. (cont)

PA101 Parent Metal Disk Specimens					
<u>Trial No.</u>	<u>Spec Code</u>	<u>0.2% Y.S. (ksi)</u>	<u>UTS (ksi)</u>	<u>% Elong</u>	<u>% RA</u>
Room Temperature Tensile					
Typical Astroloy	---	150.0	204.0	16.0	18.0
1	10-1	139.0	201.5	10.6	11.0
1	10-2	138.9	216.9	15.5	12.8
1	10-13	141.9	220.5	15.4	13.4
2	6-1	136.0	206.5	12.6	9.2
2	6-2	133.5	198.9	10.7	9.8
2	6-13	137.5	209.3	12.2	11.6
1200°F Tensile					
Typical Astroloy		133.0	170.0	18.0	20.0
1	10-3	131.8	200.7	19.2	18.6
1	10-4	131.6	198.9	20.1	18.6
1	10-14	131.6	197.9	21.3	20.9
2	6-4	126.9	194.9	20.5	21.9
2	6-4	128.4	192.4	21.0	21.4
2	6-7	129.4	196.4	16.7	16.8
1200°F Stress Rupture					
<u>Trial No.</u>	<u>Spec Code</u>	<u>Stress (ksi)</u>	<u>Hours to failure</u>	<u>% Elong</u>	<u>Remarks</u>
Typical Astroloy		125	400	----	
1	10-5	125	579.3	5.8*	Test discontinued
1	10-6	125	579.7	5.0*	"
1	10-8	125	604.4	6.9*	"
2	6-6	150	2.8	7.5	
2	6-5	140	31.8	8.7	
2	6-8	140	9.3	5.0	

*Elongation measured after retirement

TABLE 9. (cont)

Mar-M247 Cast-To-Size Test Bars						
<u>Trial No.</u>	<u>Spec No.</u>	<u>Heat Code</u>	<u>Hours to Failure</u>	<u>% Elong</u>	<u>% RA</u>	
1400°F/105 ksi Stress Rupture						
1	1	V2741	58.1	2.3	3.9	
2	2	"	5.6*	0.7	2.6	
1	3	"	23.9*	0.8	2.7	
2	12	"	39.7	1.7 (1.5)	2.6	
2	13	"	16.8	1.2 (0.95)	2.8	
2	19	V5134	27.6	1.7 (1.5)	3.5	
2	20	"	23.8	1.3 (1.1)	2.0	
*Microshrinkage observed in failure area () Prior creep						
1800°F/32 ksi Stress Rupture						
1	4	V2741	29.6	15.2	11.2	
1	5	"	30.0	7.4	11.7	
1	6	"	44.2	8.0	11.5	
2	15	"	26.9	7.8	15.4	
2	16	"	36.1	9.3	14.6	
2	21	V5134	26.2	12.9	14.5	
2	22	"	29.7	9.5	13.5	
Room Temperature Tensile						
<u>Trial No.</u>	<u>Spec No.</u>	<u>Heat Code</u>	<u>0.2% Y.S. (ksi)</u>	<u>UTS (ksi)</u>	<u>% Elong</u>	<u>% RA</u>
2	11	V2741	132.3	165.6	8.8	6.8
2	14	"	127.3	156.1	6.4	6.2
2	17	V5134	125.9	156.8	6.7	7.6
2	18	"	123.5	152.5	6.4	6.8



50X



300X

Figure 77. Microshrinkage in radius of a bond joint that failed prematurely on loading.

The parent metal PA101 exhibited excellent room temperature and 1200°F tensile and 1200°F stress rupture properties with strength and ductility comparable to those of parent metal Astroloy.

In the case of the Mar-M247 cast-to-size test bars, good properties were generally realized. However, in the case of testing at 1400°F, low life (one specimen) and ductility (two specimens) were observed; based on metallographic analysis (Figure 78), microshrinkage was found in the failure area, indicating a probable cause for the anomalies in performance. Overall, however, the results of testing performed on the HIP-bond processed Mar-M247 test bars revealed attractive levels of strength/temperature capability.

Bonding Trial 2

This portion of the effort was aimed at incorporating any process modifications identified as being required by Trial 1 and related casting activities into the manufacturing sequence. As in Trial 1, cast-to-size Mar-M247 test bars and PA101 plug material were processed through all appropriate fabrication steps to evaluate disk and airfoil capability. Included with Mar-M247 bars representative of those used in the first trial were bars representative of a second heat of material to improve on the Mar-M247 data base.

Integrated into this portion of the program was an evaluation of core printout plugging procedures that became apparent as being required as a result of casting trials. Forming a basis for this work were two shell castings (6 and 7) which were match machined, respectively, to plugs 9 and 12 to form the details for rotor assemblies 3 and 4. Detail configuration and dimensions were identical to those of the Trial 1 assemblies.

Shell casting 6 was produced minus ID core printouts. However, after the casting was machined on the ID surface to accept the PM hub, it was detected that the final grind broke into cored areas immediately behind the mating ID surface. This situation was caused by incomplete removal of the conical ID core printout prior to the wax injection process. As a result, three core printout holes in the mating conical ID surface required plugging to seal the mating surfaces effectively prior to HIP bonding. The core printout holes were ground out to nearly their original rectangular shape with the use of hand-held carbide burrs. For plugs, rectangular blocks of Mar-M247 alloy were machined to the approximate size of the individual printout and then hand ground to fit the printout hole with approximately 0.003 inch clearance for braze fill. To maintain equal clearance on each side of the plug, a series of small laser "pips" of sufficient height to wedge the plug securely in the printout hole and space it properly were produced. A small wire was tack welded on the end of each plug to bridge the printout and prevent the plug from sliding in the printout during the braze cycle. The plugs were then pressed into the printout holes. The fit-up of the plugs was less than ideal because of the irregularity of the ground-out interface, especially in the corners.

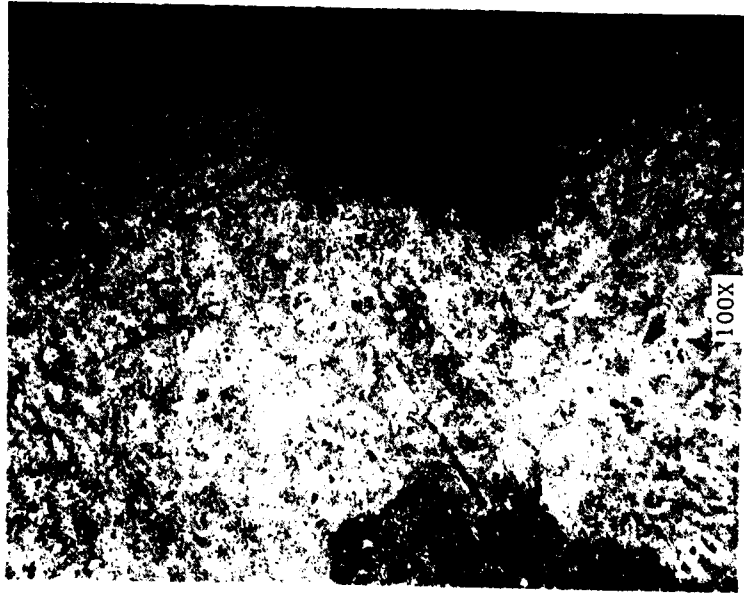


Figure 78. Fine microshrinkage associated with low ductility-
1400° F Mar-M247 stress rupture bar.

The boron-silicon-modified Mar-M247 braze alloy previously employed was used for brazing the plugs in the printout holes to the same heat cycle as used in the previous braze: 2225°F (30 min) + 2000°F (10 min) + 2100°F (60 min) in vacuum. Figure 79 shows the ID conical surface of rotor 3 following plug brazing of the three printouts. Following the first plug braze cycle, the excess braze was ground away to relieve the plugs slightly from the surface. After grinding the excess braze, it was found that the braze had not flowed sufficiently to fill the entire gap between the plug and the shell, leaving small areas of separations. The plugs were further relieved by grinding, and another braze application was performed at parameters identical to those of the first braze. The excess braze from the second braze cycle was ground away and, from a visual inspection, there appeared to be a sound seal.

At this point, a decision was made to polish the mating surfaces on the rotor and hub mechanically instead of using the ground and outgassed surfaces employed on rotor assemblies 1 and 2 and which was planned for rotor assembly 4. This decision was based on a desire to minimize heat cycles in an attempt to minimize costs and decrease cycle complexity. Figure 80 shows rotor 3 after the entire mating surface had been ground and polished in preparation for assembly with the hub.

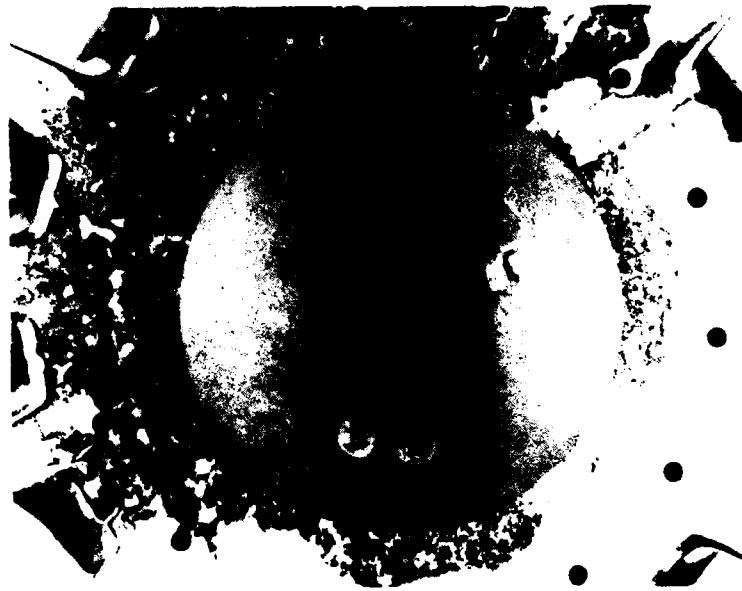


Figure 79. Plug braze of three printout holes in rotor No. 3.



Figure 80. Rotor No. 3 after grinding excess braze and polishing.

The casting (No. 7) for rotor 4 was cast with full conical surface ID core printouts which had been ground to identical rectangular dimensions prior to wax injection to facilitate uniformity in the plugging operation. Prior to plug brazing, the ID surface was rough machined to 0.020 mil over finish dimension. This allowed for a small amount of finishing stock in the casting to accommodate removal of the excess braze and to finish the rotor ID to its final dimension. The plugs used for rotor 4 were cut from a bar of Mar-M247 alloy which was ground to leave approximately a 0.003-inch gap per side for braze fill. As with rotor 3, a series of laser pips were then tacked on each plug to maintain a uniform fit in the printout, and a wire retainer was tack welded on the end of each plug. Figure 81 shows several plugs with laser "pips" and wire retainers. Following an acetone bath to remove surface contamination, the plugs were inserted into the rotor (Figure 82), Mar-M247 braze alloy was applied over the inserted plugs, and the 2225°F (30 min) + 2000°F (10 min) + 2100°F (60 min) vacuum braze cycle was performed. The appearance of the brazed rotor is shown in Figure 83 and again in Figure 84 following the final grind to finish dimension. Following the finish grind, the shell was placed in the vacuum outgas cycle (2100°F, 1 hr) along with the plug to prepare the mating surfaces for assembly. However, the surfaces of the pieces in the furnace load became coated with a smut-like film resulting from contamination from the residual core. The mating surfaces were hand polished and re-outgassed to a satisfactory condition.

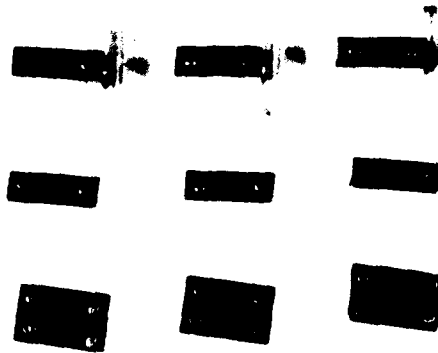


Figure 81. Mar-M247 core printout plugs showing laser "pips" and wire retainers to secure plugs in core printouts.



Figure 82. Rotor No. 4 rough machined showing three plugs prior to insertion into printouts.



Figure 83. Rotor No. 4 following plug braze cycle.

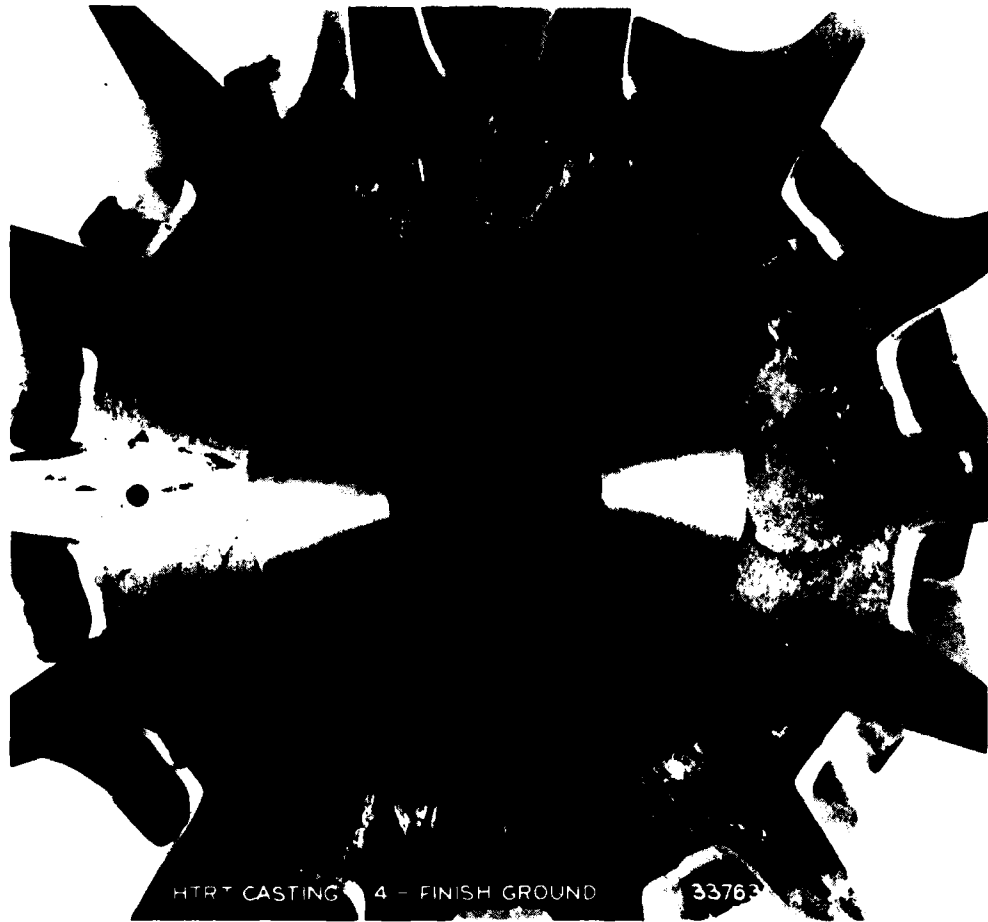


Figure 84. Rotor No. 4 following grinding operation in which excess braze was removed and the surface ground to final dimension.

The plug and shell details for rotors 3 and 4 were assembled in the same manner as for rotors 1 and 2. Following assembly, boron-silicon-modified Mar-M247 braze alloy was applied to the exposed joints and the assemblies were brazed at 2225°F (30 min) + 2000°F (10 min) + 2100°F (60 min) in vacuum. Upon cooling, the integrity of the braze seal was ensured by a leak check which exposed the braze seal to pressurized helium; a mass spectrometer was used to detect any bleedback of helium, which would be indicative of a lack of seal.

HIP bonding was again performed at Udimet Powder Division of Special Metals Corporation. The HIP run included rotor assemblies 3 and 4, a PA101 parent metal plug, and cast-to-size Mar-M247 test bars for baseline studies. The details of the HIP bonding cycle were maintained as closely as possible to those of the previous HIP run. Specifically, the pieces were loaded in a 6-in. diameter HIP can and suspended in spherical aluminum oxide packing material and HIP bonded at 2215°F/15 ksi for three hours.

Following HIP processing, rotors 3 and 4 were cut in half and polished to reveal the bond integrity. The rotors were deliberately sectioned through a printout plug to initially evaluate the effects of plugging as well as the shell/hub bond, as shown in Figure 85. As was expected, a closer view of the printout plugs (Figure 86) revealed a much more uniform plug seal in rotor 4 than in rotor 3, as evidenced by the pores in the rotor 3 braze. At high magnification (Figure 87), a certain amount of recrystallized grain was evident along the bond joint, as was a degree of grain growth from the PM alloy into the cast alloy. However, the overall bond quality appeared to be very good, as in the first set of rotors. Microscopic evaluation also proved that the bond was continuous across the printout plugs as shown in Figure 88. The overall results of the HIP bonding trial indicate that the plugging of the printout holes is sufficient to seal the rotors for complete bonding during the HIP bonding process.

Following metallographic examination, bonded assemblies 3 and 4, a PA101 plug, and cast-to-size Mar-M247 test bars were heat treated to the same 2050°F + 1550°F + 1400°F cycle employed for rotors 1 and 2. Subsequently, the two rotors and the PA101 plug were sectioned into specimen blanks and sent, along with the Mar-M247 test bars, to Metcut Research Associates for machining and specimen testing. The rotor and plug cut-up scheme was the same as that used for Trial 1.

The results of the testing of these specimens are presented in Table 9 for comparison with the results obtained for Trial 1. Excellent joint integrity was again realized both in tensile and stress rupture testing; all failures occurred away from the joint in the cast alloy portion of the specimens. Likewise, excellent strength and ductility results were obtained for the parent metal PA101 although the 1200°F stress rupture tests had to be conducted at significantly higher stress levels than the Trial 1 tests because of the long lives that were developed with the earlier 1200°F/125 ksi test condition.



Figure 85. Rotors No. 3 (top) and No. 4 (bottom) following HIP bonding. (Printout plugs are shown extending the conical surface to the right of center.)



Figure 86. Brazed plugs in rotors No. 3 (top) and No. 4 (bottom).

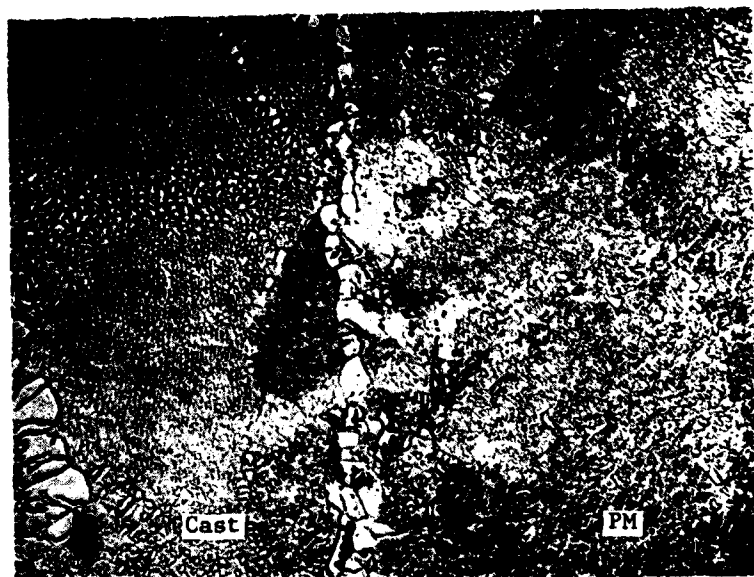


Figure 87. Bond line in rotors No. 3 (top) and No. 4 (bottom).

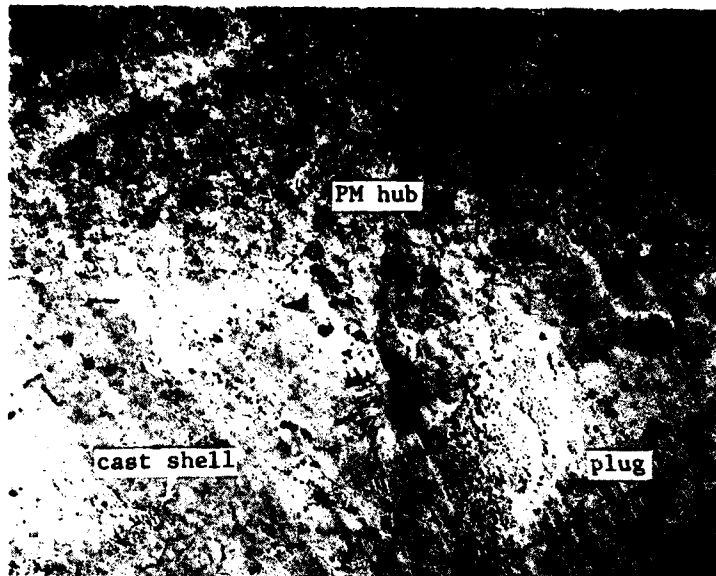


Figure 88. Interface of PM hub, cast shell, and printout plug in rotor No. 4. (Bonding between the three details is complete.)

With respect to the tensile and creep rupture results obtained for the cast-to-size Mar-M247 test bars, relatively good rupture lives were achieved, as was the case in the Trial 1 testing. The 1400°F rupture ductility, however, was again less than desired although adequate for the HTRT design. Relative to tensile testing, the results for the HIP-bond processed bars were very acceptable and typical of the alloy.

In all the 1200°F tensile and stress rupture testing of PA101/Mar-M247 butt-type specimens representative of the four stylized rotors produced, not a single failure occurred through a joint, indicating 100% joint efficiency. In all cases, failures were in the weaker Mar-M247 material at strength levels considerably higher than will ever be exerted on the joint during engine operation. With these levels of joint integrity and the results of tests of the parent metal PA101 and Mar-M247, the viability of the basic HIP-bond approach to dual-property rotors has been substantiated.

Conclusions and Recommendations

The following conclusions and recommendations have evolved from the completion of the Phase I process development effort:

- o Consistently high-quality HIP-bond butt joints with 100% efficiency were developed between PA101 plugs and Mar-M247 shells as verified by micro-macroexamination and mechanical property testing at 1200°F.

- o The mechanical properties of parent metal PA101, developed at room temperature and 1200°F in the plug portion of the rotor, are competitive with those of Astroloy, one of the strongest disk materials commercially available.
- o Stress rupture results at 1400°F and 1800°F were essentially as predicted. Lives were consistent with HTRT design requirements.
- o Successful plugging of core printout holes in ID conical locations was demonstrated; no significant detrimental effects of the processing complexity added by this step were observed.
- o Based on comparisons between rotors 3 and 4, vacuum outgas cycles appear unnecessary for high-quality bonds between details; polished surfaces appear adequate.
- o Residual microshrinkage was observed in cast Mar-M247 despite exposure to a 2215°F (3 hr)/15 ksi HIP cycle. Future work should address a modified HIP cycle to maximize casting soundness. HIP bond modifications of interest include higher pressure levels (25 ksi versus 15 ksi).

Weld Seal Development

The purpose of this limited effort was to assess the feasibility of using electron beam welding techniques in the vacuum sealing of dual-property turbine rotors prior to HIP bonding. Interest in this approach focused on its potential for low costs via automated technique capabilities for consistent quality and the elimination of the thermal cycling and associated potential for distortion peculiar to vacuum braze sealing techniques. Emphasis in this work centered on the use of 1/16-inch-diameter Hastelloy S filler wire because earlier DDA work had indicated a low crack sensitivity in this alloy when electron beam welded to simple PA101 and Mar-M246 test coupons.

The test coupon which formed the basis for these evaluations is shown in various stages of fabrication in Figures 89, 90, and 91. It comprised two outer PA101 details and an inner Mar-M247 detail. Following laser tacking of the Hastelloy S filler wire, electron beam welding, HIP bonding, and heat treatment, the test specimens machined through the cross section contained two bond joints in the specimen gage. Two groups of specimens were vacuum welded together in a near line-to-line contact during the effort.

Prior to weld sealing, the first group of coupons were vacuum outgassed at 2100°F for 1 hour to ensure a clean bond surface. The second group was weld sealed without prior vacuum outgassing to leave the surfaces in an "as-machined" condition. The purpose of these variations was to ascertain whether the high-temperature outgas cycle would be required for bond joint integrity. The potential payoff was to be the elimination of an additional processing step, resulting in further manufacturing cost savings.

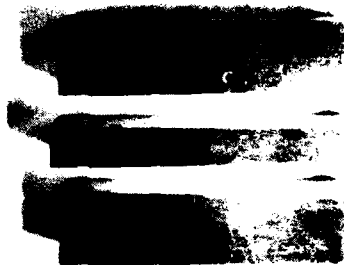


Figure 89. Weld seal test coupon prior to assembly. (Outer details are PA101 and inner detail is Mar-M247.)



Figure 90. Weld seal test coupon with Hastelloy S filler wire laser tacked over joint areas.



Figure 91. HIP-bond sample following vacuum sealing by electron beam welding.

During the initial welding trials, expulsion in the bead was encountered and was attributed to the presence of abrasive grit which was a carry-over from the grinding operation used to prepare the specimens. A more extensive cleanup of the ground surfaces prior to welding eliminated this problem.

In a repair attempt, the portion of the weld where the expulsion occurred was dry milled to remove the weld and rewelded with a new filler wire retacked in position. In general, the weld quality of the repaired area was excellent and demonstrated the feasibility of this method of repair.

Also encountered early in the program was a problem of alignment. On occasion, the fixturing of the specimen caused the beam to wander off the joint area, which led to a lack of fusion. To establish feasibility, a weld wire was tacked over the unfused area and was welded. The resulting quality was excellent, and this technique was subsequently used in the program to complete the welding of unfused joints.

During the welding of the first specimens, some fine hairline weld cracking in the Hastelloy S filler wire was also observed. (None, however, was detected in either parent metal PA101 or Mar-M247.) The incidence of this cracking was decreased by slightly defocusing the beam. However, despite these improvements, the occurrence of fine hairline cracking in the weld continued, as shown in Figure 92. In these cases, the cracks were readily repaired by laser welding with fresh filler prior to final electron beam closure. (The top weld in Figure 91 shows typical laser weld repairs in the Hastelloy S filler.)



Figure 92. Cracking observed in conventional electron beam welds.

After substantial efforts aimed at obtaining visually crack-free welds, a group of coupons was leak checked by exposing the assembly to pressurized helium and checking with a mass spectrometer for helium bleedback from a poor seal. In this case, extensive bleedback occurred from one coupon in which the weld quality was suspect; this finding was considered significant as it lent credibility to the use of this technique for efficiently detecting a lack of seal prior to HIP bonding.

In attempts to satisfy the requirements of the program for two groups of weld coupons (as-machined and vacuum outgassed bond surfaces), cracking in the Hastelloy S filler wire continued to be a problem which necessitated extensive repair to make the welds pressure tight. These cracking difficulties led to the application of a circle generator type of electron beam weld in which the beam is caused to oscillate in a circular fashion. This produces a wider but shallower weld and in tests on flat plates produced extremely promising crack-free welds. However, when this concept was applied to offset joints of the type being used for the bond specimens, gross center-line cracking through the length of the weld filler wire occurred as shown in Figure 93. Despite several attempts at modifying weld parameters, the promising welds developed on flat specimens could not be reproduced. Consequently, emphasis in the work reverted to the more conventional electron beam weld techniques in use at the beginning of the program.

After substantial efforts involving a variety of weld settings and repair procedures as shown in Table 10, the program weld requirements were met.



Figure 93. Cracking observed in circle generator electron beam welds.

TABLE 10. ELECTRON BEAM WELD PARAMETERS

Weld Type	Setting ranges					
	High Voltage (kv)	Focus Dial	Travel (in./min.)	Circle Generator*		
				X Axis Dial	Y Axis Dial	Speed Dial
Standard--new joint, reweld, and reweld with 2nd filler wire	23-25	5.90-6.10	40-45	---	---	---
Circle generator--new joint and reweld with 2nd filler wire	15.5-20	6.10	5	0.5-1.5	0.5-1.5	35
<p>Note: Machine: Sciaky Low Voltage Common settings for all runs: Gun spacer--0.200 Filament-cathode spacing--0.342 Filament current--58-60 amps Gun distance--4 in.</p>						
*All circle generator welds 60 cycle						

Four weld coupons were selected for the initial HIP trial--two in the as-ground condition and two in the as-ground plus outgas condition. The two outgassed coupons, however, required a braze on one end of each coupon for a complete seal of the mating surfaces following the occurrence of weld cracking of the Hastelloy S filler wire. All coupons were leak checked with pressurized helium before HIP processing.

The four weld coupons (AG-1, AG-2, OG-1, OG-3) were HIP processed in the initial trial with rotors 1 and 2. Following HIP, specimen AG-1 was cut in half and polished, only to reveal severe cases of no bonding on both joint surfaces. Further examination of the polished surface showed three electron beam weld cracks which did not appear to break out the surface; however, it suggested the possibility that other cracks could be present and break the seal.

In anticipation of additional bond separations, the three remaining coupons were leak checked. Coupon AG-2 indicated leaks, but OG-1 and OG-3 appeared to be good. The three coupons were then halved, similar to AG-1, and evaluated at the bond joint. Figure 94 shows the four weld coupons polished and etched. Coupon AG-2 revealed intermittent bonding in the bond joint and total separation of approximately 0.050 inch immediately below three of four welds. The outgassed weld coupons, OG-1 and

OG-3, displayed much better bonding characteristics. Coupon OG-1 had bond separation approximately 0.040 inch below three of the weld beads; however, the surfaces closed beyond the separations and bonded completely along the joint. Coupon OG-3 experienced no separations at the welds and had excellent bonding along the entire joint surface, as shown in Figure 95.

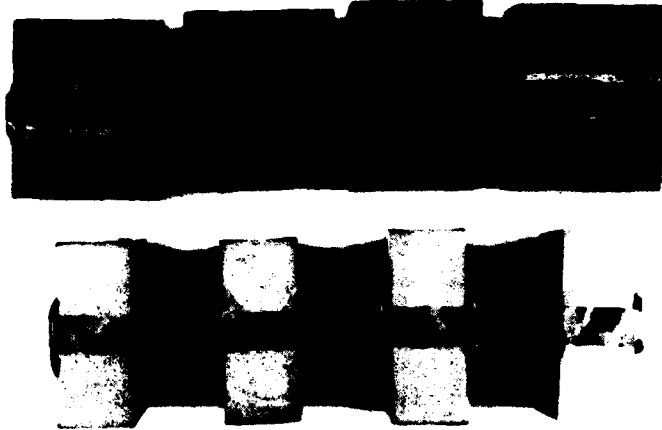


Figure 94. Weld coupons (left to right) OG-3, OG-1, AG-2, AG-1.

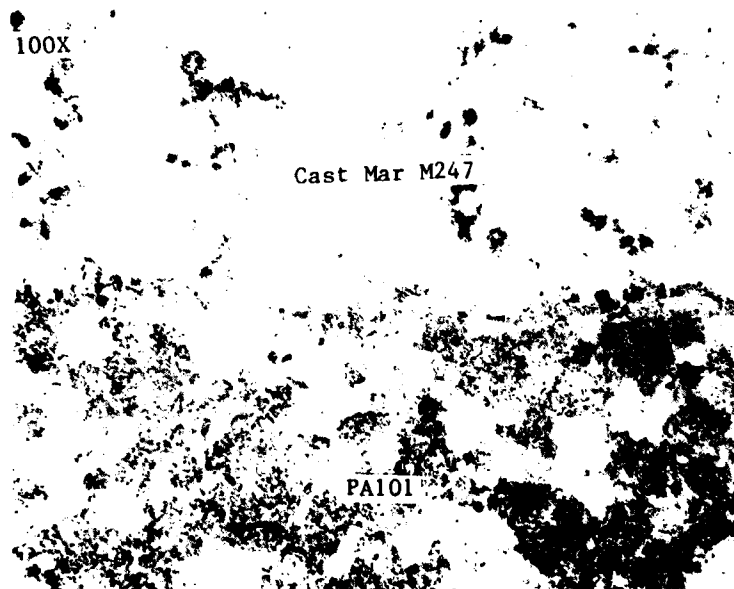


Figure 95. Weld coupon bond joint OG-3.

The existence of bond separation immediately below several of the weld beads is not quite understood. One explanation, though, may be that the mating surfaces were not flush at the edges prior to welding and that filler wire fused into the edge areas, creating an irregular surface that could not be healed by HIP.

Following HIP bonding and heat treatment with rotors 1 and 2, tensile and stress rupture specimens were machined from only the OG (vacuum outgas) specimens because of the poor bond quality in the AG (as-ground) series of test specimens.

The results of this testing, conducted at 1200°F, are presented in Table 11 and show excellent bond quality; all failures occurred in the cast portion of the specimen gage as shown in Figure 96. Because two butt-type joints were present in each specimen, the results are even more significant and attest to the high integrity of joints obtainable by HIP bonding techniques.

TABLE 11. TEST RESULTS FOR PA101/MAR-M247 JOINT SPECIMENS MACHINED FROM HIP-BONDED WELD SEAL COUPONS					
1200°F Tensile					
<u>Coupon</u>	<u>0.2% YS</u>	<u>UTS</u>	<u>% Elong</u>	<u>% RA</u>	<u>Failure Location</u>
OG-1	128.0	152.5	6.3	12.5	Cast
OG-1	124.8	149.8	6.9	12.8	Cast
OG-3	125.4	146.0	5.6	11.5	Cast
1200°F/125-ksi Stress Rupture					
<u>Coupon</u>	<u>Hours</u>	<u>% Elong</u>	<u>% RA</u>	<u>Failure Location</u>	
OG-1	271.8	9.3	18.3	Cast	
OG-3	75.2	1.4	6.2	Cast	
OG-3	19.7	2.6	8.7	Cast	
HIP bonded at 2215°F for 3 hours and 15 ksi					
Heat treated to 2050°F (2 hr) GFC + 1550°F (4 hr) AC + 1400°F (16 hr) AC					

Conclusions

- The weld seal development effort resulted in the following conclusions:
- o Earlier promise shown for Hastelloy S as a filler material could not be extrapolated to the specimen configuration employed in the program because of extensive cracking within the Hastelloy S filler wire.
 - o Cracked welds could be laser and EB repair welded.

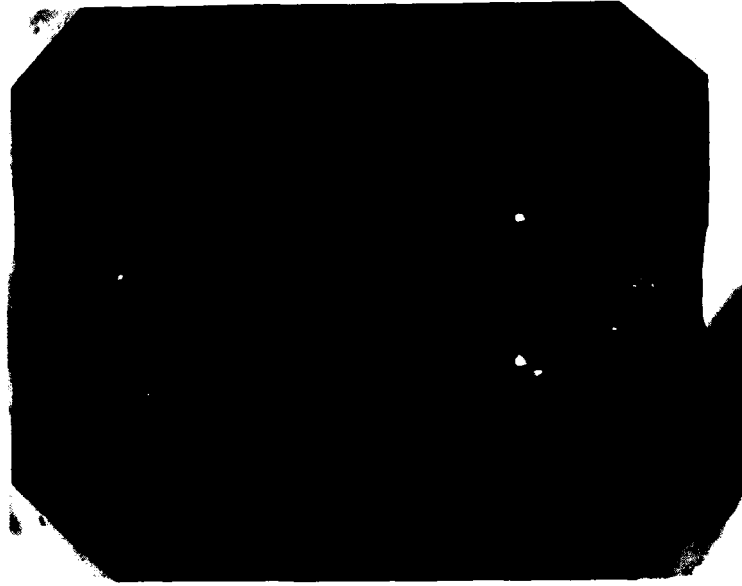


Figure 96. Cast alloy failure location in PA101/Mar-M247 weld sealed joint specimen tested at 1200°F.

- o As-machined and vacuum outgassed bond quality could not be compared because of sealing problems with as-ground samples.
- o Excellent bond quality and joint strength, despite subsurface cracking in weld seals, was achieved with specimens that passed the leak checks.
- o Because of the limited scope of the program, studies of the effect of joint configuration and in-depth investigation of weld parameters, which can be critical to weld quality, could not be undertaken.

Nondestructive Inspection Development

During the design of the HTRT rotor assembly, major consideration was given to the inspectability of the bond joint. Earlier work with HIP-bond axial wheel designs had demonstrated the feasibility of inspecting butt-type joints between cast alloy airfoil and near-net-shape PM hub details ultrasonically. Consequently, ultrasonic inspection was selected for this program.

Because the air-cooled radial turbine rotor has a hollow bore, it was decided to inspect the bond interfaces by using a transducer positioned in the bore. The bond line configuration shown in Figure 97 was selected as having a good potential for ultrasonic inspection from the bore as well as for cost effective manufacture.

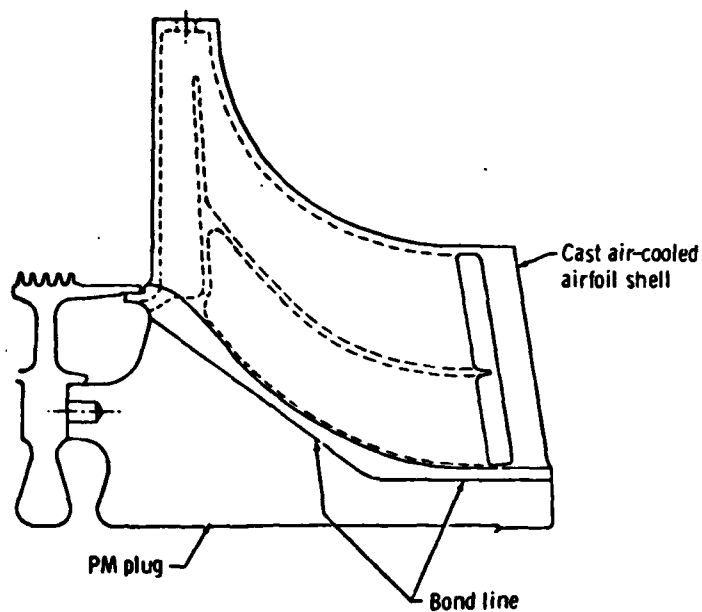


Figure 97. Schematic showing joint design for a HIP-bond processed air-cooled radial turbine wheel.

To demonstrate the feasibility of this concept, titanium test pieces (with a sonic velocity nearly identical to that of PA101) were made in the stylized Phase I HTRT configuration to simulate a bond line configuration.

Subsequently, based on the results obtained with the stylized standards, full-scale standards that were representative of the Phase II final design were produced in titanium. Specifically, bond inspection setup pieces representative of both the Phase I stylized and Phase II full-scale rotors were fabricated to represent both the cylindrical and conical sections of the joint.

Cylindrical Inspection Concept

Figure 98 shows a cross-sectional view of the portion of the test setup for cylindrical inspection. A pulse echo technique was used in which the ultrasonic transducer receives an electrical pulse which it converts to ultrasonic energy at its resonant frequency (10 MHz in this case). The ultrasonic energy is propagated through water into the wheel after a right-angle reflection from the beam reflector. (The ultrasonic beam is shown by the dotted lines.) The ultrasonic energy then propagates into the PM portion of the wheel until it reaches the interface with the cast alloy shell. In a case where the diffusion bond is incomplete so that an interface exists, the ultrasonic energy will be reflected as shown and return to the transducer by the same path. If the joint is well bonded,

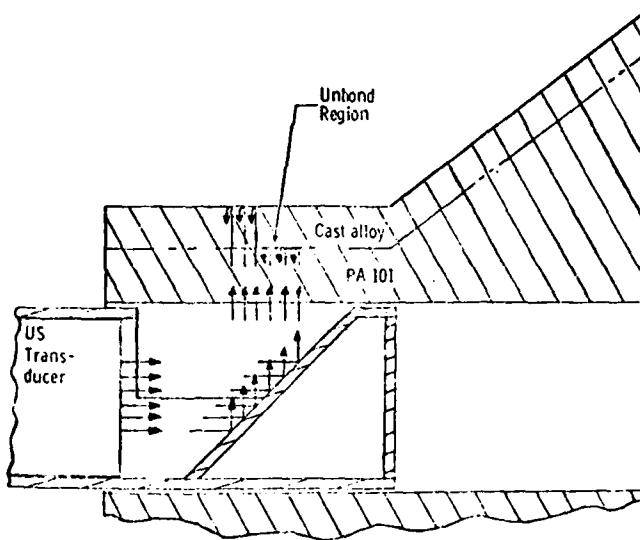


Figure 98. Test setup for the ultrasonic inspection of the cylindrical portion of a bond line.

the ultrasonic energy will continue into the cast alloy shell with very little reflection and travel to the free surface where it is scattered. A small portion will return along the previous path to the transducer. In this setup, the ultrasonic transducer converts the received signal into an electronic signal which is received by shaping and display electronics. Because of differences in metal path length, the return signals are time discriminated to determine if they were reflected from the bond interface or the wheel free surface. To fully inspect the cylindrical joint surfaces in this portion of a HIP-bond radial wheel, the wheel is rotated and the ultrasonic transducer is moved laterally to achieve a helical scan of the complete interface.

Conical Inspection Concept

Figure 99 shows a cross-sectional view of the inspection setup for the conical portion of the HIP-bond radial turbine wheel. The inspection technique is referred to as through transmission or a "pitch and catch" technique. The electrical "transmit" pulse is converted to an ultrasonic burst by the transducer. Ultrasonic energy then travels through water into the wheel. The signal from either the defective interface or the part-free surface is then reflected at an angle equal to the incident angle to the 36° surface. Therefore, a second transducer with a broad area is used to receive the reflected energy and provide an electronic signal output to the shaping and display electronics. Because of the difference in sound path length, the bond joint reflection and free sur-

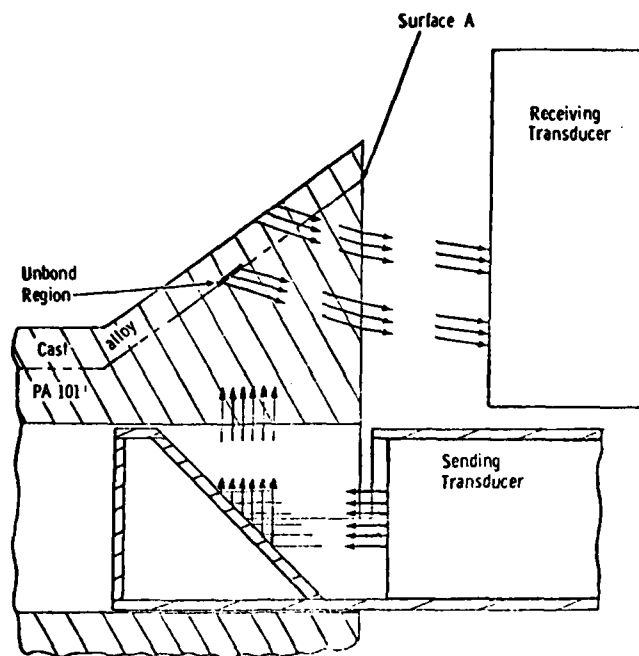


Figure 99. Test setup for the ultrasonic inspection of the conical portion of a bond line.

face reflection can be time discriminated. As in the inspection technique for the cylindrical bond portion of the wheel, a helical scan is used to cover the total conical surface interface.

Test Method

Titanium alloy test pieces were manufactured for transducer positioning and resolution determination. Both stylized and full-scale designs were manufactured because defect resolution is configuration sensitive. Similar test pieces, together with two ultrasonic transducers used in this inspection, are shown in Figure 100.

The transducer positioning pieces, which were machined to the same contours as the PM hubs for the stylized and full-scale radial wheels, were used to adjust the ultrasonic transducer for maximum signal return from the interface region and to adjust the electronic time discrimination.

Once the transducers and instrumentation were adjusted, the positioning piece was carefully replaced with the resolution piece which contained flat-bottom holes drilled to a depth equivalent to the interface as shown in Figure 101. Ultrasonic inspection of this piece defined the smallest-diameter flat-bottom hole, simulating an unbond area which could be detected. Figure 102 shows the resolution test pieces for the stylized and full-scale design to illustrate relative size.

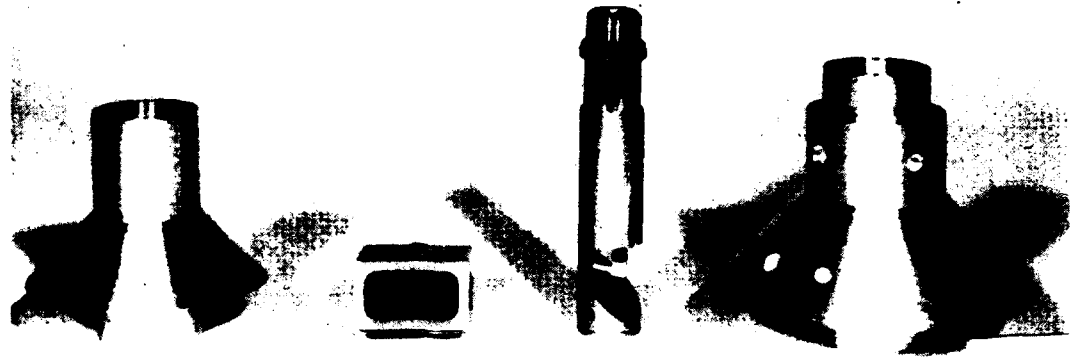
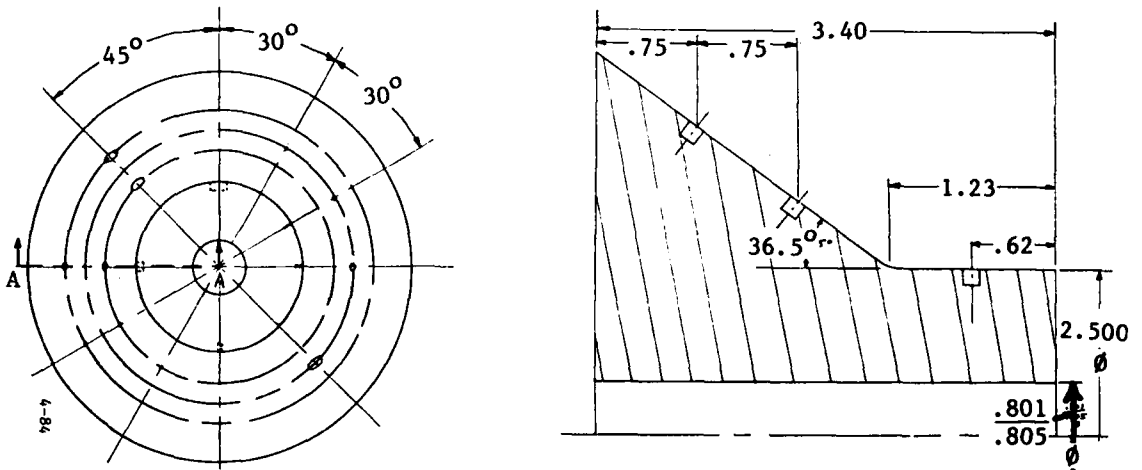


Figure 100. Test pieces and associated transducers employed to develop ultrasonic inspection techniques for HIP-bond air-cooled radial turbine wheels. (From left to right are the transducer positioning piece, broad area transducer, transducer with beam reflector, and resolution test piece.)



drill 4 each flat bottom holes in locations shown .125 in. deep; hole dia. are 1/4, 1/8, 1/16, 1/32, 1/64 in.

Figure 101. Resolution test piece sketch.



Figure 102. Stylized and full-scale resolution test pieces.

Test Results

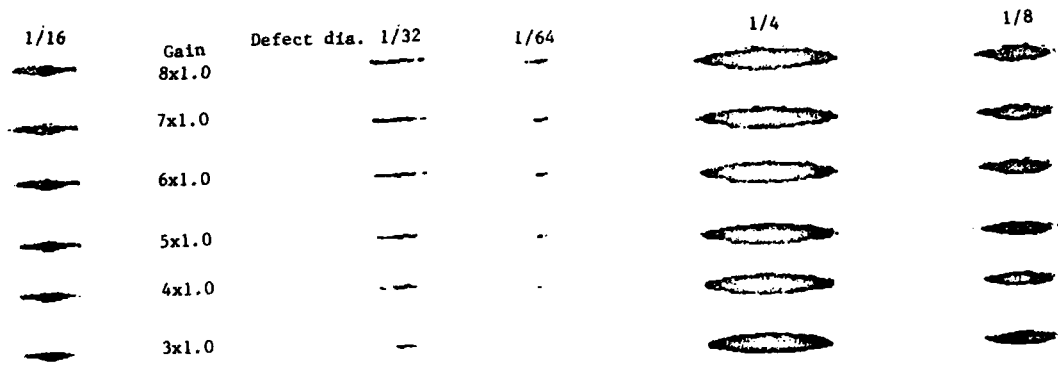
The stylized and full-scale resolution pieces were ultrasonically inspected with a variety of standard 10-MHz transducers. C-scan recording was used to determine the smallest flat-bottom hole that could be detected.

An inspection setup and operating technique was developed and used to inspect the resolution pieces. Transmitting transducers with various focal lengths were used to determine the effect of ultrasonic beam shape on defect resolution. Table 12 summarizes the smallest flat-bottom hole which could be repeatedly detected in each case.

TABLE 12. SMALLEST DETECTABLE FLAT-BOTTOM HOLE	
Stylized Design	Smallest Flat-Bottom Hole Detected (Diameter)
Cylindrical Portion	1/64 inch (0.40 mm)
Conical Portion	4/64 inch (1.59 mm)
Full-Scale Design	
Cylindrical Portion	4/64 inch (1.59 mm)
Conical Portion	8/64 inch (3.18 mm)

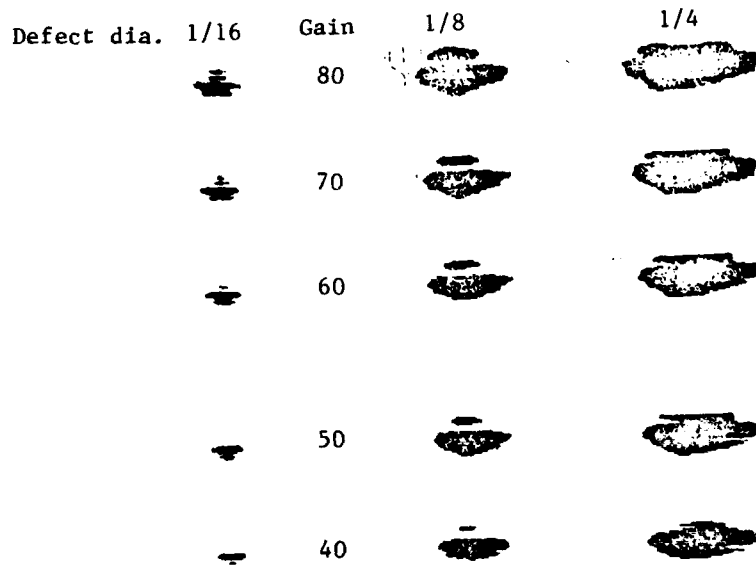
During inspection, flat-bottom holes were electrically recorded from the ultrasonic signal received by the instrumentation. Paper width was synchronized with the rotating mechanism to show 360° rotation, and paper length was directly related to the linear transducer movement to produce a circumference versus length record. Figures 103 through 106 show the C-scan recordings of flat-bottom holes detected in each of the stylized and full-scale resolution test pieces. The recorded flat-bottom holes are elliptical because the 360° rotation represented by the recording is not, in general, scaled to that of the flat-bottom hole.

These test results show the relatively good detection capability of standard ultrasonic transducers; however, defect sensitivity decreases as configuration size increases. The finer resolving capability in the stylized cylindrical portion (1/64-inch-diameter flat-bottom hole) resulted from the use of a standard transducer which had focal length nearly optimized for this surface.



Rotation 360°

Figure 103. Resolution piece multiple C-scans with increasing gain for stylized cylindrical section.



Rotation 360°

Figure 104. Resolution piece multiple C-scan record for stylized conical section.

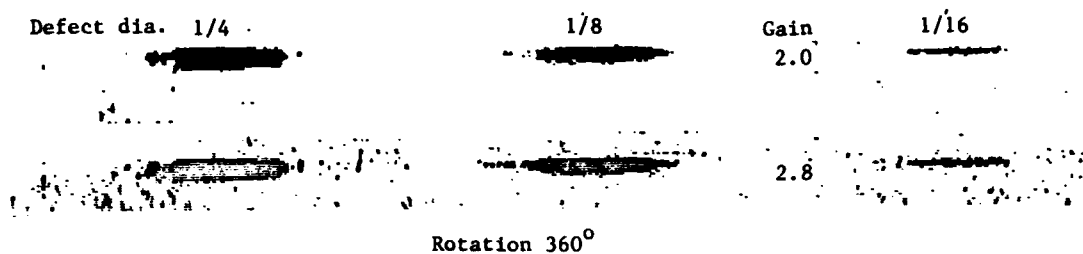


Figure 105. Resolution piece multiple C-scan record for full-scale cylindrical section.

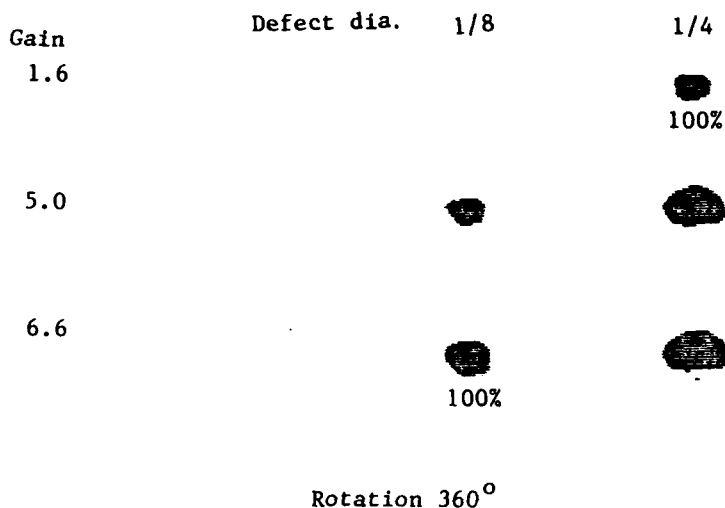


Figure 106. Resolution piece multiple C-scan record for full-scale conical section.

During the inspection of the conical section of the stylized configurations, mismatch between focal length and the surface increased and sensitivity decreased. The mismatch was further increased in going to the larger full-scale design and sensitivity was further decreased. Thus, special or tailored transducers made to focus the ultrasonic energy at the interface surface are necessary to concentrate the beam in an optimized fashion so that defect sensitivity can be improved in the stylized conical portion and in both portions of the full-scale design.

PRODUCTION COST ANALYSIS

A manufacturing cost study of the full-scale rotor design was conducted. The cost study was based on:

- o 2500 units over a ten-year period (21 units/month deliver, manufacturing rate by suppliers based on best utilization of labor and equipment within a year's run)
- o 1978 economics

Estimates were obtained from suppliers for the near-net-shape PA101 plug detail, the monolithic Mar-M247 cast airfoil shell, and the HIP bonding of the braze-sealed assembly. The factory costs of all other manufacturing operations, based on a process routing to which standard labor hours were applied, were prepared by DDA.

The Udimet Powder Division of Special Metals Corporation was supplied with a detail drawing and was requested to estimate the price of manufacturing the near-net-shape PA101 powdered metal plug at a rate of 21 per month for a ten-year period. For HIP bonding costs, the Industrial Materials Technology (IMT) Corporation of Woburn, Massachusetts, was asked to provide production quotes for a 2225^oF, 3 hour, 15 ksi HIP bond cycle. The resulting price estimates were:

- o PA101 Plug \$718.00 each
- o HIP bonding \$50-100 per assy
(variation dependent on HIP unit used and scheduling;
\$75 per unit was used in final estimate)

Austenal LaPorte Division of the Howmet Corporation, a leading manufacturer of cast turbine components, was requested to assess the production viability of producing the shell casting and to prepare a price estimate based on the previously listed ground rules. Prior to the initiation of the price estimate, Howmet personnel were briefed on the DDA casting experience with the seven stylized airfoil shells and HIP bonding. The resulting price estimates were:

- o EX-126264 casting detail \$920 each
(based on 250 units per year utilizing most efficient loading of their facility. This estimate also includes neutron radiation inspection to insure complete core removal.)
- o Casting tooling and gaging \$65,200

DDA Process Routing and Work Standards Departments prepared routing and labor estimates based on a detail drawing and the following process developed during Phase I:

1. Receiving Inspection: 100% ultrasonic inspection of plug, X-ray, FPI, and airfoil wall thickness check of cast shell. The airfoil wall thickness check is required at two locations on each of 12 airfoils. Material properties of both plug and shell to be checked on sampling basis.
2. Prepare Core Printout Plugs: 12 plugs, 0.006 in. undersized on diameter, to be laser pipped to ensure braze gap control.
3. Braze Airfoil Core Printouts: Core printouts at ID of cast shell to be plugged and brazed, tip printouts to be closed with bead of braze alloy only. Vacuum braze cycle 2240°F for 30 min, cool to 2000°F for 10 min, then 2100°F for 1 hour.
4. Machine Detail: Approximately 0.100 in. stock to be removed from ID of shell and OD of plug, 0.0005 in. interference fit required on cylindrical section; master template will be required to hold cone angle match to ± 10 min required concentricity and roundness, ± 0.0002 both surfaces, 31 RMS finish required.
5. Leak Check Shell: Seal off center cavity of shell and evacuate through mass spectrograph, introduce helium into blade cavities, braze plug leakage detected by mass spectrograph indication of helium.
6. Detail Cleanup: Diamond polish both plug and shell; thoroughly clean in ultrasonic tank using MEK solution.
7. Shrink Fit Assembly: Heat shell to 400°F; cool plug in liquid nitrogen; assemble.
8. Braze Seal: Seal plug to shell with circumferential braze at each end, vacuum braze cycle 2230°F for 30 min, cool to 2000°F for 10 min, then 2100°F for 1 hour.
9. Leak Check: Check braze seals by placing in pressurized helium tank (80 psi). Use probe on joints to locate any leakage.
10. Send to IMT for HIP: After controlled heat-up cycle, hold at 2215°F $\pm 25^\circ$ at 15,000 psi for 3 hours, furnace cool.
11. Interim Machining: Machine forward face normal to axis of bore.
12. NDI: Ultrasonic inspection; assume 2 hr for setup per lot plus 5 min per part.
13. Coating: Coat Mar-M247 airfoils with Si aluminide.

14. Heat Treat: Protective atmosphere 2050°F for 2 hr, rapid furnace cool, age at 1550°F for 4 hr, and 1400°F for 16 hr in protective atmosphere

15. Finish machine complement of surfaces.

The base labor required for DDA manufacturing operations for the EX-126264 rotor assembly was estimated to be 15.7 hours. It was also estimated that full efficiency (95%) in manufacturing would be achieved at 252 units or one year's production. This results in a ten-year program efficiency of 92%. When 1978 economics are applied, DDA factory costs are \$637 per unit for manufacture of the HTRT rotor.

The total costs of purchased parts and services and the DDA manufacture are estimated to be:

Casting price	\$ 920.00
PA101 plug price	718.00
HIP bond purchase price	75.00
DDA manufacturing	<u>637.00</u>
Total Factory Cost	\$2350.00

PHASE II--FABRICATION

TOOL CONSTRUCTION

Manufacturing process development work conducted in Phase I revealed that the casting tooling should include:

- o A core printout in the conical section of the casting shell for improved stability and yield
- o A circular rather than rectangular cross section conical core printout to facilitate plugging and brazing prior to machining and HIP bonding
- o Core printouts at the inducer inlet, the exducer, and the cooling air supply similar to those at the stylized rotor
- o Adjustment pins in the wax die for precise positioning of the core during injection of the wax

These features were included in the full-scale tooling, which consisted of a ceramic core die, core setter dies for core curing, a wax airfoil die, and an assembly fixture. These tools are shown in Figures 107 through 109.

MATERIAL PROPERTY SPECIMENS

In parallel with the fabrication of casting tooling for the full-scale HTRT design, two additional stylized rotors were fabricated. These rotors, which were produced to processing schedules established in Phase I, along with parent metal PA101 hubs and cast-to-size Mar-M247 test bars processed to equivalent thermal cycles, formed a basis for a limited mechanical property characterization effort which was conducted in Phase III.

Stylized Rotor Specimens

Two Mar-M247 airfoil shell castings and PA101 plugs were used in the fabrication of the two stylized rotors. Following braze plugging of the ID conical core, printout, and machining to form a 1.0-mil interference fit at the cylinder diameter, the shell and plug details were diamond polished, cleaned, and mated by heating the shell details to 400°F and cooling the plug in a liquid nitrogen bath. Subsequently, the assembled rotors (No. 5 and 6) were vacuum braze sealed at 2240°F with the boron-silicon modified Mar-M247 braze alloy. After braze sealing, the rotors

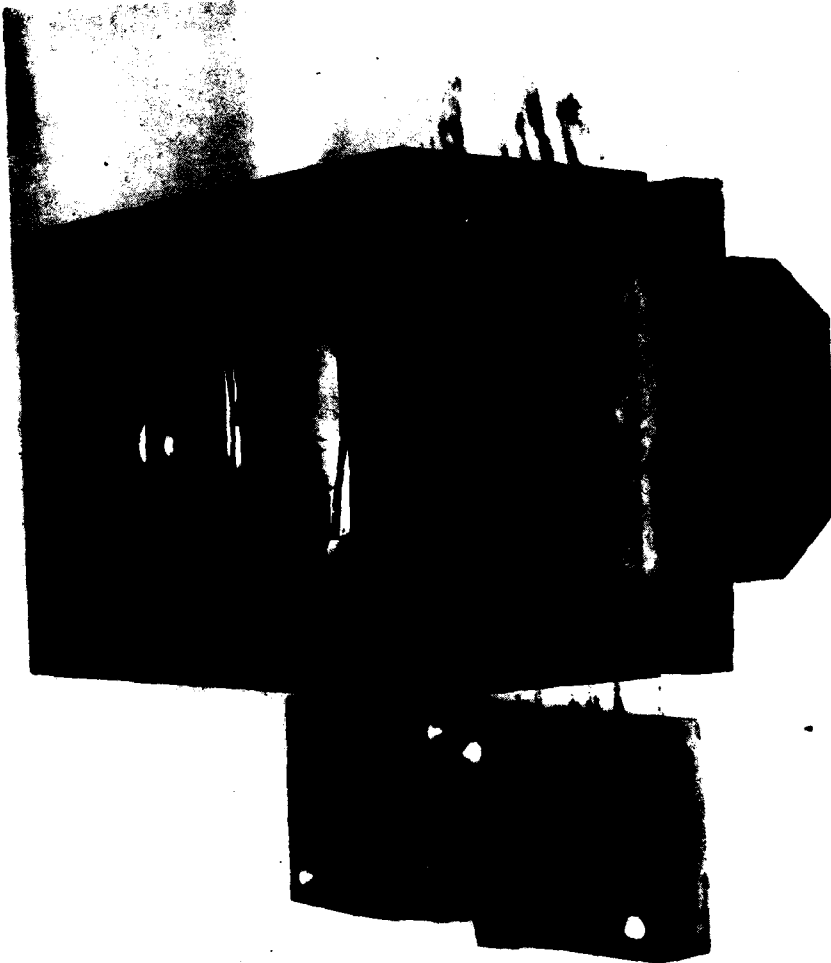


Figure 107. Wax injection die for full-scale HTRT airfoil shells.



Figure 108. Core die and resultant core for an air-cooled HTRT airfoil shell.



Figure 109. Fixture used to assemble full-scale HTRT airfoil patterns.

were leak checked to verify the seal integrity prior to HIP bonding. For the leak check, the rotors were placed in a vessel and exposed to pressurized helium at 80 psi. After approximately a 2-hr exposure, the rotors were removed and the braze seals were checked with a mass spectrometer for helium bleedback. During this inspection, the No. 5 rotor showed indications of a lack of braze seal at a single airfoil position in the general location of the aft section (cylindrical) circumferential seal.

The No. 6 rotor was free of bleedback and judged to be adequately sealed.

The seal area of the No. 5 rotor was rebrazed and leak checked, where it again revealed a bleedback. A further review indicated that the bleedback was associated with the core plug in the conical section of the bond interface rather than the circumferential seal. Because this printout was inaccessible for rebrazing, DDA decided to proceed with the HIP bonding of the rotor. After HIP bonding at 2215°F for 3 hours at 15 ksi, the two rotors were again leak checked. Evaluations failed to uncover any signs of bleedback, suggesting that the indication in the No. 5 rotor was pseudo or that it was closed during the bond cycle.

Ultrasonic C-Scan Inspection (Post-HIP Bonding)

The initial ultrasonic inspection of rotors No. 5 and 6 failed to reveal any indications of nonbond. However, as sensitivities were increased, indications of minor unbonding in the outer conical sections (approximately 1/8 in. from the rear face) of each rotor became evident. A significant amount of effort was spent in attempting to map their location and to ascertain whether the indications were associated with back reflections from other portions of the rotors.

At the conclusion of this inspection, the rotors were sectioned and suspected areas were examined for evidence of nonbond. The metallurgical quality of the bond between details (Figures 110 and 111) was good and generally consistent with that observed in the rotors previously evaluated.

However, rotor No. 5 exhibited some evidence of oxidation at a bond interface near an indication area, as shown in Figure 112. This suggests that the surface may not have been completely cleaned prior to assembly. The fact that a condition of this type is not believed to induce an ultrasonic indication of nonbond and that the metallographic examinations failed to reveal a delaminated bond line condition led to the conclusion that the observed ultrasonic indications in both rotors were the result of back-reflection detections.



Figure 110. Diffusion bond joint in rotor No. 5. (magn: 150X)

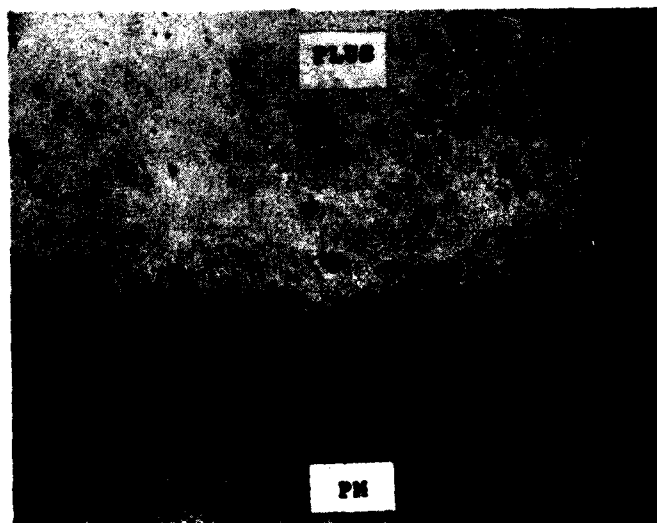


Figure 111. Diffusion bond between core printout plug and hub in rotor No. 5. (magn: 250X)



Figure 112. Contaminant layer in portion of joint in rotor No. 5. (magn: 500X)

Laboratory Specimens

Cast-to-size Mar-M247 test bars and specimens from PA101 plugs were processed to simulate the processing of the stylized rotors. A summary of the thermal history of these details is presented in Table 13.

TABLE 13. PROCESSING HISTORY FOR PARENT METAL PA101 AND MAR-M247	
Alloy Form	Heat Treatment History
Parent metal PA101 (plug material)	A (shell/hub seal) + B + C
Parent metal Mar-M247 (cast-to-size test bars)	A (shell plug seal) + A (shell/hub seal) + B + C
A = 2240°F (30 min) + 2000°F (10 min) + 2100°F (1 hr)--Vacuum braze seal cycle	
B = 2215°F (3 hr), 15 ksi--HIP bond cycle	
C = 2050°F (2 hr), vacuum gas fan cool + 1550°F (4 hr), air cool + 1400°F (16 hr), air cool--Post-HIP heat treatment cycle	

FINAL DESIGN ROTOR FABRICATION

With the availability of casting tooling, the fabrication of full-scale rotors was begun. These rotors were to provide the basis for component tests involving elevated-temperature low cycle fatigue and ambient-temperature spin testing to destruction to verify component integrity.

Castings

Upon receipt of the casting tooling, tool tryouts were conducted. Specifically, sample cores were produced and shown to have excellent detail. After firing, the cores were positioned and shot in the wax tooling; the injected waxes were then evaluated for wall thickness distribution and fit-up within the assembly fixture. As indicated in Table 14, wall thickness results for the injected cores showed good reproducibility from wax pattern to wax pattern. The rotor pattern assembly fixturing tool proved to be very effective and, as a result, little difficulty was encountered in producing full-scale rotor assemblies.

However, the larger hub OD of the full-scale rotor occasioned the use of a modified gating arrangement consisting of six individual gate attachments approximately 60° apart as opposed to the four gate attachments 90° apart used on the stylized rotor.

Full-Scale HTRT Casting No. 1

Following investing and burnout, the first HTRT casting was poured in the Mar-M247 alloy. The casting parameters (2000°F mold, 2950°F pour temperature, and 2-4 sec pour time) were identical to those applied to the stylized rotor castings.

As shown in Figure 113, misrun occurred on the convex portions of two airfoils because of the deflection of the core. Wall thickness measurements of the airfoils (Table 15) showed a trend in which thicknesses and thinning of the walls seemed to be a function of gating position. In general, every second airfoil exhibited a wall thinning in the critical convex core printout region that corresponded to the relative proximity of a gate. (Six gates were distributed among 12 airfoils; however, because of the contouring of the airfoils, the concave core surface was oriented in a "cupped" manner and received a more direct impingement of the incoming molten metal, causing the thin core to deflect and kiss out on the convex surface.)

Cut-up evaluations of the No. 1 casting were also conducted. Included in the cut-up evaluation was one completely filled airfoil which, on the basis of ultrasonic wall measurements, had a thin convex wall in the critical region, and one which had a normal wall thickness. For comparison, a section was also made through one of the airfoils with kissout. As indicated in Figure 114, the wall thickness measurements were essentially verified by metallographic examination.

TABLE 14. WAX PATTERN WALL THICKNESS MEASUREMENTS
(inches)

Pattern No.	Concave Location				Convex Location			
	1	2	3	4	5	6	7	8
1	0.031	0.026	0.030	0.068	0.027	0.029	0.026	0.055
2	0.030	0.028	0.028	0.065	0.027	0.028	0.028	0.054
5	0.029	0.027	0.027	0.068	0.028	0.031	0.028	0.050
6					0.029	0.029	0.027	0.054
7					0.029	0.031	0.025	0.053
9					0.030	0.032	0.028	0.052
10					0.028	0.030	0.025	0.053
11					0.029	0.031	0.026	0.052
12					0.025	0.031	0.027	0.052
13					0.030	0.031	0.027	0.053
14					0.027	0.030	0.027	0.053
15					0.026	0.031	0.028	0.053

Note: Locations 1-4 were not measured for patterns 6 through 15.

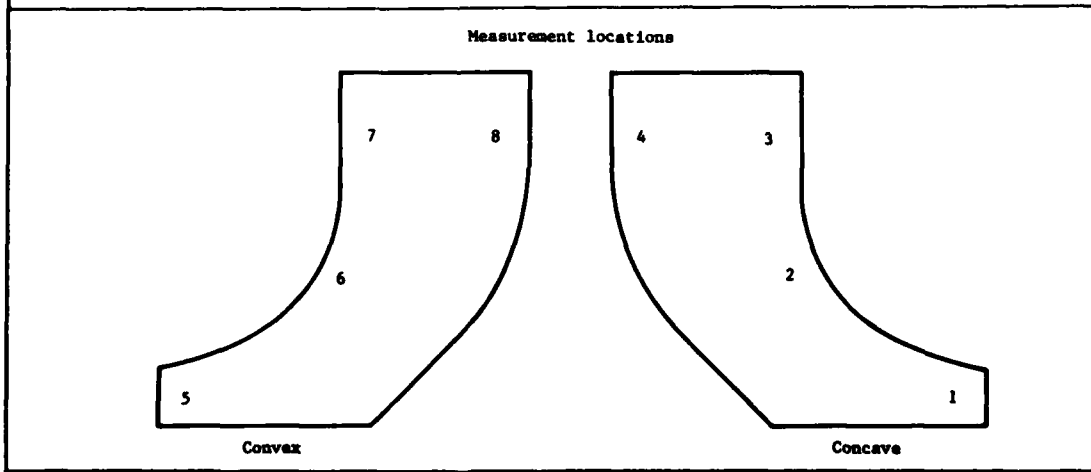




Figure 113. Full-scale HTRT casting No. 1. Note misrun and exducer tip cold-lap as well as fine grain.

TABLE 15. METAL WALL THICKNESSES OF FULL-SCALE HTRT CASTINGS					
Vane No.	Casting	Convex Location			
		5	6	7	8
1	1	0.025	*	*	0.049
	2	0.028	0.029	0.029	0.049
	3	0.025	0.021	0.025	0.049
	4	0.024	0.026	0.030	0.046
	5	0.032	0.024	0.028	0.044
	6	0.025	0.023	0.024	0.052
2	1	0.026	0.026	0.027	0.047
	2	0.026	0.023	0.024	0.042
	3	0.025	0.025	0.026	0.042
	4	0.025	0.024	0.026	0.045
	5	0.031	0.026	0.025	0.040
	6	0.026	0.027	0.029	0.054
3	1	0.023	0.023	0.025	0.047
	2	0.024	0.019	0.029	0.051
	3	0.025	0.026	0.030	0.044
	4	0.025	0.025	0.029	0.048
	5	0.029	0.027	0.025	0.042
	6	0.025	0.024	0.026	0.055

TABLE 15. METAL WALL THICKNESSES OF FULL-SCALE HTRT CASTINGS (cont)

Vane No.	Casting	Convex Location			
		5	6	7	8
4	1	0.024	0.024	0.024	0.050
	2	0.023	0.027	0.029	0.047
	3	0.025	0.018	0.031	0.049
	4	0.024	0.026	0.026	0.045
	5	0.030	0.021	0.030	0.050
	6	0.025	0.025	0.026	0.055
5	1	0.026	0.025	0.024	0.049
	2	0.026	0.027	0.025	0.049
	3	0.026	0.029	0.028	0.049
	4	0.027	0.030	0.032	0.047
	5	0.026	0.026	0.028	0.048
	6	0.025	0.022	0.030	0.056
6	1	0.030	0.027	0.025	0.048
	2	0.021	0.019	0.022	0.049
	3	0.026	0.029	0.030	0.043
	4	0.030	0.029	0.020	0.048
	5	0.027	0.023	0.026	0.048
	6	0.024	0.022	0.027	0.059
7	1	0.026	*	0.020	0.048
	2	0.026	0.022	0.023	0.048
	3	0.029	0.026	0.030	0.048
	4	0.026	0.026	0.029	0.050
	5	0.026	0.024	0.029	0.048
	6	0.024	0.027	0.026	0.059
8	1	0.025	0.017	0.020	0.045
	2	0.027	0.027	0.028	0.049
	3	0.025	0.026	0.028	0.048
	4	0.024	0.024	0.029	0.046
	5	0.025	0.025	0.028	0.050
	6	0.028	0.031	0.026	0.057
9	1	0.025	0.011	0.020	0.047
	2	0.022	*	0.028	0.048
	3	0.030	0.029	0.031	0.048
	4	0.026	0.031	0.029	0.052
	5	0.025	0.028	0.025	0.052
	6	0.024	0.027	0.029	0.053
10	1	0.023	0.022	0.021	0.045
	2	0.028	0.028	0.027	0.047
	3	0.030	0.028	0.025	0.046

TABLE 15. METAL WALL THICKNESSES OF FULL-SCALE HTRT CASTINGS (cont)

Vane No.	Casting	Convex Location			
		5	6	7	8
10	4	0.024	0.024	0.026	0.048
	5	0.026	0.026	0.028	0.052
	6	0.026	0.026	0.026	0.050
11	1	0.026	0.018	0.023	0.046
	2	0.024	0.023	0.026	0.045
	3	0.029	0.028	0.028	0.046
	4	0.029	0.028	0.030	0.046
	5	0.025	0.018	0.023	0.051
	6	0.024	0.024	0.026	0.052
12	1	0.024	0.023	0.021	0.045
	2	0.026	0.022	0.025	0.045
	3	0.027	0.027	0.027	0.047
	4	0.024	0.026	0.028	0.047
	5	0.030	0.025	0.028	0.048
	6	0.027	0.025	0.028	0.053

*Misrun at this location

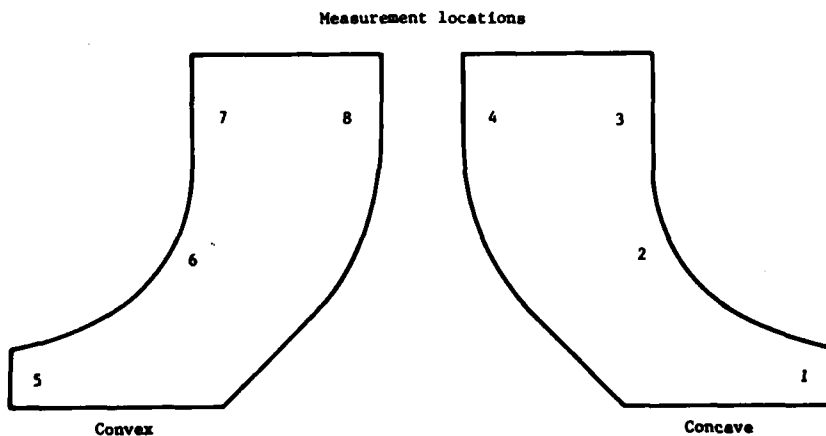




Figure 114. Wall thicknesses observed in comparable sections cut from eight airfoils (from full-scale rotor No. 1) in which ultrasonic inspection indicated uniform wall thickness (left) and shift (right). Airfoil at center experienced core kissout.

Also observed in the first full-scale HTRT casting were (1) a finer grain size than in earlier stylized castings and (2) cold laps which were unique to several different exducer airfoil locations. This indicated a faster cooling and associated solidification rate for this configuration than that obtained with the stylized rotor shells.

Full-Scale HTRT Casting No. 2

Based on the results of the evaluations of the No. 1 casting, the gating in the second wax assembly was changed in an attempt to reduce the turbulence and velocity of the molten metal entering the airfoil cavities

enough to prevent core shift or breakage. To accomplish this, the number of feeder gates was increased from six (first trial) to twelve to provide more uniform metal flow between adjacent airfoils. In addition, instead of channeling the flow directly into the ring gate, as was done on the first trial, a dogleg-shaped gate was used to make the metal take one additional turn and impinge against the inner surface of the ring gate before entering the airfoil cavities. The gating arrangement is shown in Figure 115. A pad on the exducer core print was also added to ensure that the core deflection was not caused by insufficient allowance for thermal expansion.

A modest bottom fill scheme also was employed to further reduce the shock of the molten metal impinging downward on the core. The addition of six 1/8-inch-diameter bottom "spoke-type" feeder gates coming off a center downpole was expected to allow some filling of the airfoil cavities from the bottom to provide some support on both sides of the core before the large mass of metal entered through the top gates. This approach was believed to reduce the tendency for airfoil misrun that was a problem on the first trial. The bottom feeding approach is shown in Figure 116.



Figure 115. Gating arrangement used for full-scale HTRT casting No. 2.

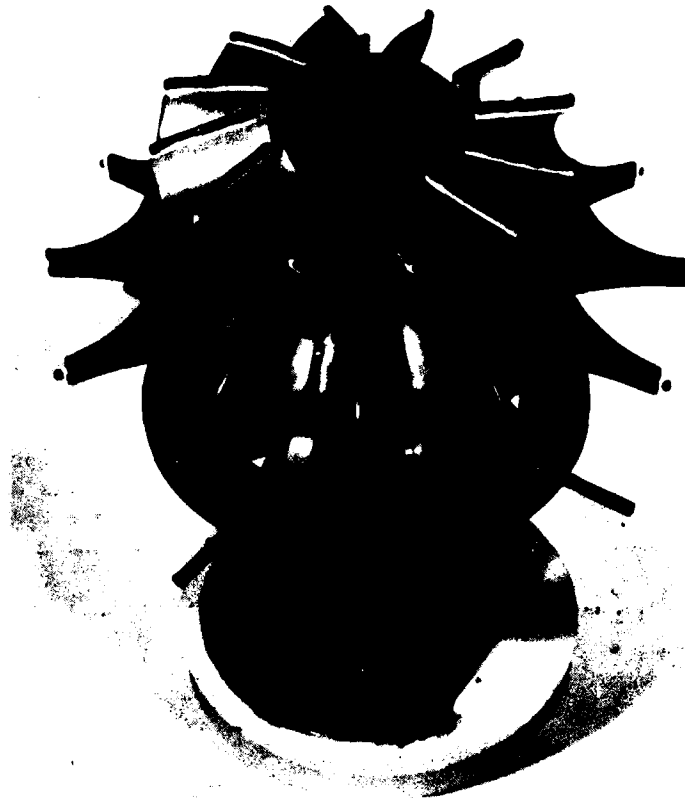


Figure 116. Bottom fill, to decrease core shock, and "spoke-type" gating used to improve fill in exducer airfoil tips of HTRT casting No. 2.

The pouring parameters were altered slightly from those of the first trial in an effort to eliminate the misrun problem. The mold temperature was increased from 2000°F to 2050°F, and the entire mold was wrapped with 1/2-in Fiberfrax before grog backup. The pour temperature was kept at 2950°F and the mold was hot topped.

The resultant casting had one core kissout on the convex side of the airfoil (Rotor 1 had two kissouts). Wall thickness measurements (Table 15) showed improved core stability in that the incidence of the number of airfoils which had walls below 0.020 in. in the critical No. 6 location was three as opposed to the five for casting No. 1. Two airfoils exhibited misrun (one of approximately 1/4-in. diameter, the other approximately 0.020 x 0.200 in.). Both were at the exducer core print near the leading edge of the airfoil. Neither of these airfoils showed indications of cold folds. Two of these airfoils had no bottom feeder gates.

The overall casting quality was generally good--specifically, the surface finish was good (no dirt, fins, or roughness); however, there was evidence of "heat wrinkling" as a result of the airfoils in the rib area. The grain structure is shown in Figures 117 and 118. Grain size was generally 1/8 to 1/4 in. equiaxed with some columnar grain originating at the exducer core print and areas of powder fine grain at the extreme airfoil tips and at the cold folds.

Full-Scale HTRT Casting No. 3

The gating of casting No. 3 was further modified to improve metal flow/fill dynamics (Figure 119). Included in these modifications was a feed cup to a disk which fed twelve axial gates favoring the convex side of each airfoil where kissout had been previously noted. In addition, the downpole was extended downward through the center of the casting to the



Figure 117. Microstructure of full-scale HTRT casting No. 2.

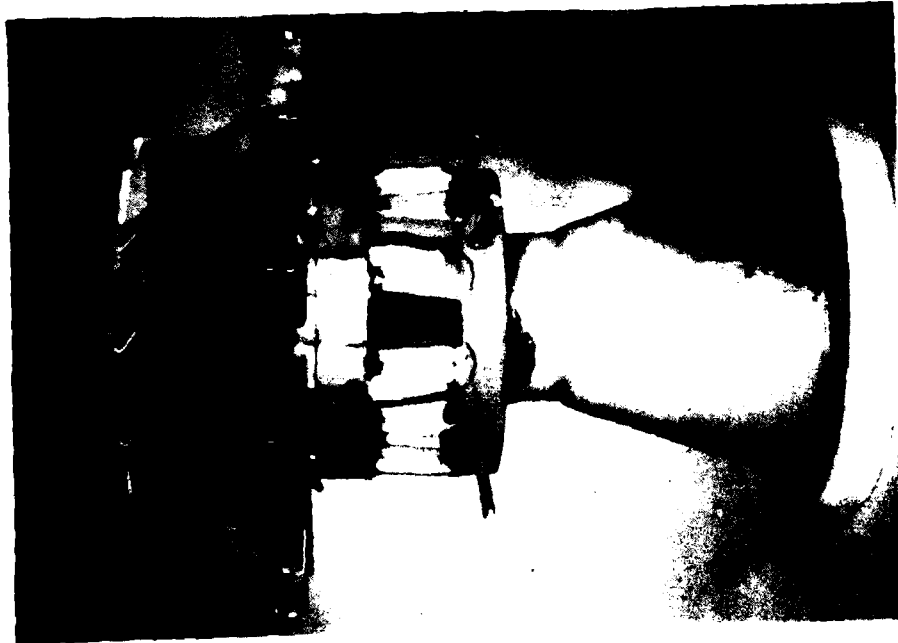


Figure 119. Wax pattern and gating assembly for full-scale HTRT casting No. 3 (inverted position).



Figure 118. Full-scale HTRT casting No. 2 (downstream view).

exducer section to feed twelve radial gates as shown in Figure 120. The philosophy behind this gating design was to fill more from the bottom and to reduce the flow pressure on the concave side of the core.

After pouring, the casting was found to be of excellent quality without casting defects, such as misruns or dirt. However, a minor cold fold on each of two airfoils was evident but both appeared to be surface conditions that would blend out with minor hand grinding.

The back side of the rotor casting is presented in Figure 121 which shows the gating modifications, i.e., gates shifted over the convex side of the airfoil, tapered center downpole, and exducer gates to each airfoil. This photograph also shows the equiaxed and uniform grain structure on the ID of the casting. Figure 122 shows the airfoil grain structure which is exceptionally uniform and fine considering the extremely high mold preheat (2050°F) and pouring temperatures (2950°F).

The results of the ultrasonic measurement of airfoil wall thickness (Table 15) indicate that, judging by the overall consistency of wall thickness data, the modified gating significantly improved the core stability.



Figure 120. Oblique view of wax pattern and gating assembly for HTRT casting No. 3, showing exducer feed gates (inverted position).



Figure 121. Ingates, tapered downpole, exducer gates, and ID grain size in HTRT casting No. 3.

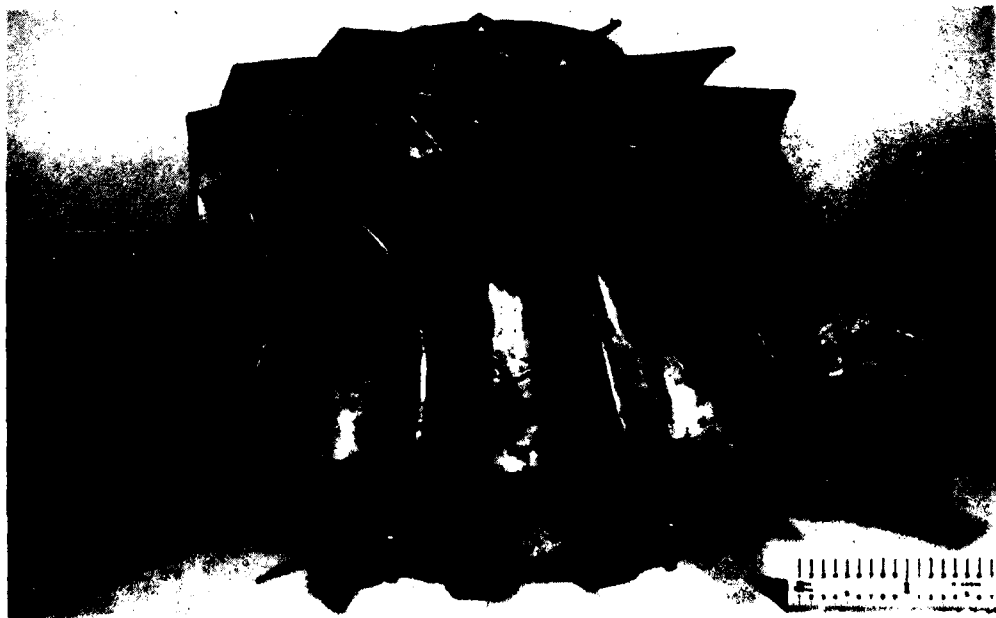


Figure 122. Macrostructure of HTRT casting No. 3.

Full-Scale HTRT Castings No. 4, 5, and 6

With core stability difficulties resolved by gating modifications, three additional castings were produced to the same parameters as used for rotor No. 3. In each case, the core stability and resultant airfoil wall quality was excellent, and no further difficulties with core printout were encountered. However, shrinkage was observed in the conical section of the bore of casting No. 4 as shown in Figure 123. This was caused by a small mold leak as indicated by a metal deposit in the cylindrical bore at the four o'clock position.

The overall casting quality achieved during the six casting trials was very encouraging. Emphasis had been placed on demonstrating that high-quality air-cooled integral shells could be produced with adequate control over wall thicknesses; that goal was achieved as evidenced by rotors No. 3 through 6. With this demonstration, a scale-up to a full-scale manufacturing development appeared to be feasible.

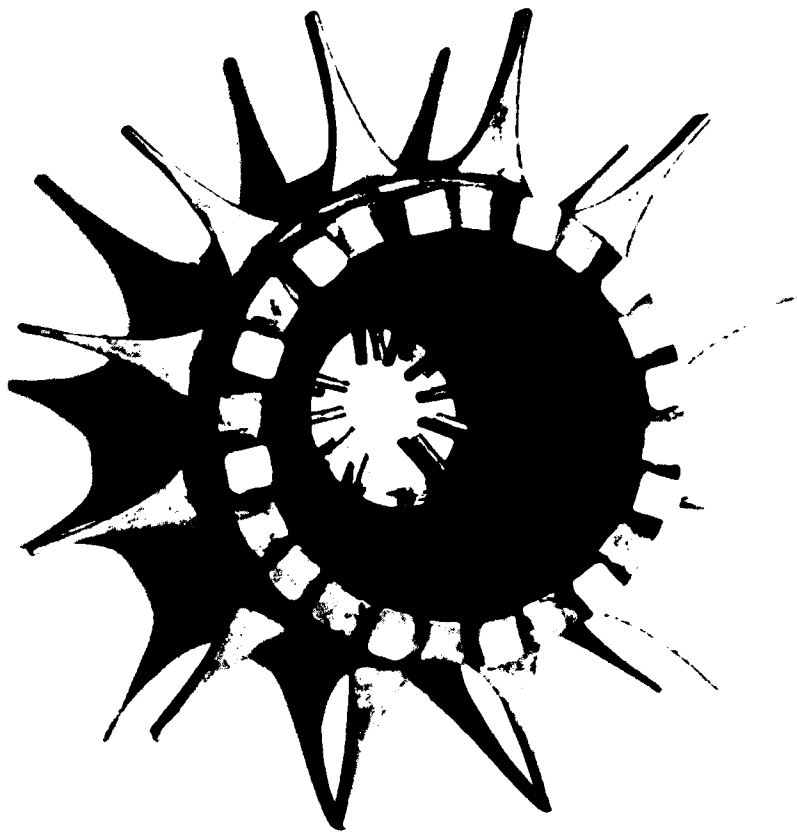


Figure 123. Casting No. 4 with area of shrinkage.

Disks

The near-shape PA101 plugs for the full-scale HTRT rotors were procured from the Udimet Powder Metals Division of the Special Metals Corporation, Ann Arbor, Michigan. The plugs, shown schematically in Figure 124, were produced from argon-atomized powder by direct HIP metal can consolidation techniques. The design emphasized near shape to minimize machining time. In general, the consolidation practice used for the full-scale plugs was equivalent to that used for the stylized plugs in the Phase I effort. However, in terms of mesh size, the full-scale plugs were produced from -150 mesh powder as opposed to the -60 mesh powder utilized for the stylized plugs. This was done in an attempt to minimize the incidence of ceramic inclusions in the final product and was based on industry experience and trends that were not available at the beginning of the Phase I effort.

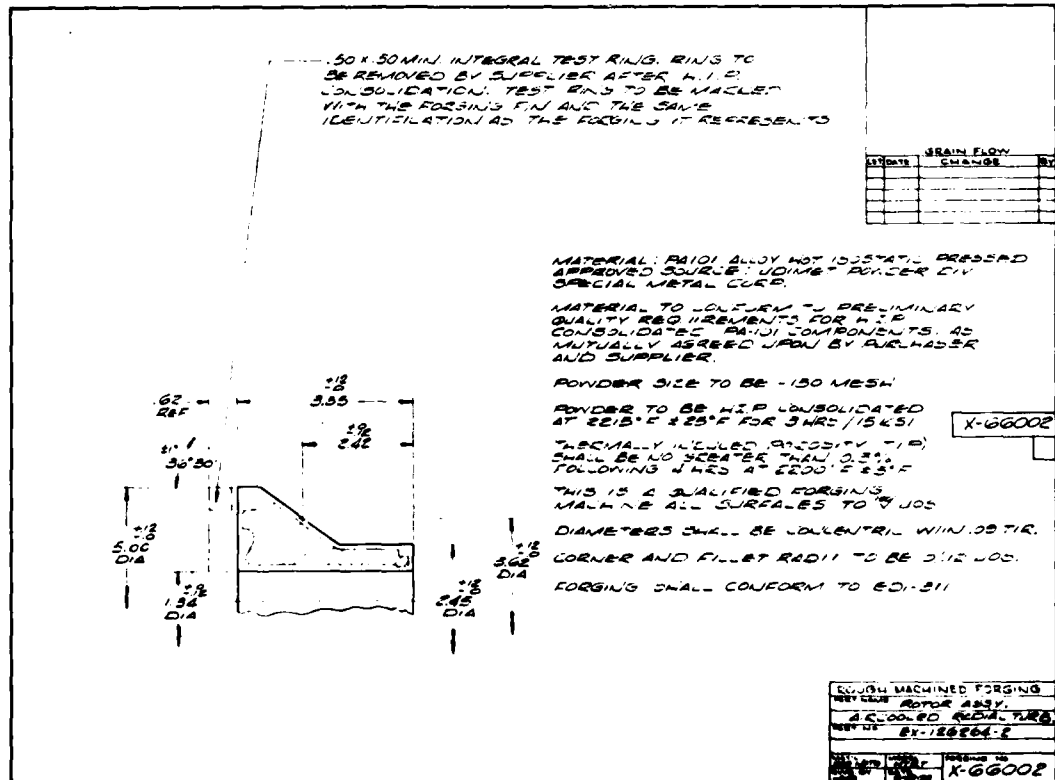


Figure 124. Schematic of a full-scale PA101 plug detail for HTRT rotors.

A typical PA101 plug as received from Special Metals is shown in Figure 125; pertinent processing details as well as qualification test results for the full-scale details are contained in Appendix C. (Similar information for the Mar-M247 alloy used in the program is contained in Appendix B.)

Assemblies

Four full-scale HTRT rotor assemblies were produced in the program; the assembly techniques and parameters employed were those which evolved from the Phase I effort. Of the four assemblies, one was cut up for metallurgical evaluations; the others were used for component evaluations.

Rotor No. 1

HTRT casting No. 2 with one core kissout was selected for use in the first bonded assembly. (Because this rotor was to be used as a laboratory cut-up sample to verify machining/bonding techniques, the core kissout condition in one of the airfoils did not preclude its usefulness.) The first step in preparing the cast shell for mating to the plug and subsequent HIP bonding was to seal the conical core printout hole. This was accomplished by braze sealing a 0.112-inch-diameter by 0.125-inch-long Mar-M247 plug into the core printout hole. The printout holes were first cleaned by grit blasting, after which the pins were inserted. To ensure a secure location in the core printout hole, small weld pips were tacked to each plug in three places. A crosswire was tacked to the end of each plug to prevent the plug from being inserted too far into the hole. The boron-silicon modified Mar-M247 braze alloy was then applied over the plugs and the braze cycle was conducted at 2240°F (30 min) + 2000° (10 min) + 2100°F (60 min). Figure 126 is a photograph of a typical braze-plugged shell. The Mar-M247 rotor casting and PA101 plug detail were then match machined prior to assembly. The appearance of these details is shown in Figure 127. Following diamond polishing, the details were fitted together and then braze sealed. Visual inspection of the seal at the rear conical location revealed that the braze alloy had spalled off in several areas; as a result, a second braze cycle was required before the unit was able to pass its leak check.

The sealed rotor was then HIP bonded at a 2200°F, 25-ksi, 3-hour exposure cycle. The 25 ksi was 10 ksi higher than previously used in this program and was intended to maximize bond quality and minimize the potential for residual microshrinkage. (Previous work indicated that a 15-ksi pressure level would not completely eliminate shrinkage in Mar-M247 test material.) The 25-ksi pressure level was selected on the basis of previous successes with this cycle for axial T63-A-720 dual-property wheels.

After completion of the HIP bond cycle, the rotor was heat treated and ultrasonically inspected. As shown in Figure 128, the C-scan inspection revealed a no-bond area over a 135° segment of the conical portion of the joint. In terms of length, the no-bond extended from the cylindrical to the conical transition rearward to the OD of the rear face.

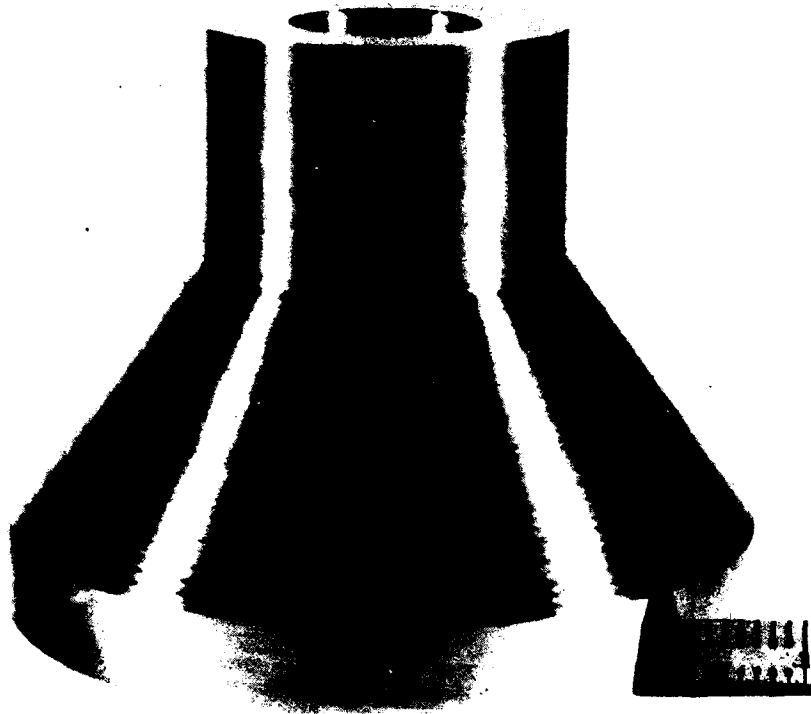


Figure 125. Full-scale PA101 plug detail as received from Special Metals.

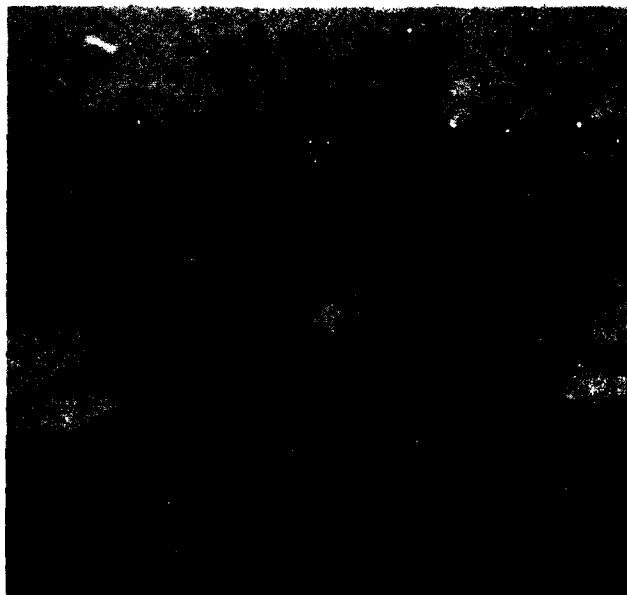


Figure 126. Typical braze-plugged shell for a full-scale HTRT assembly.

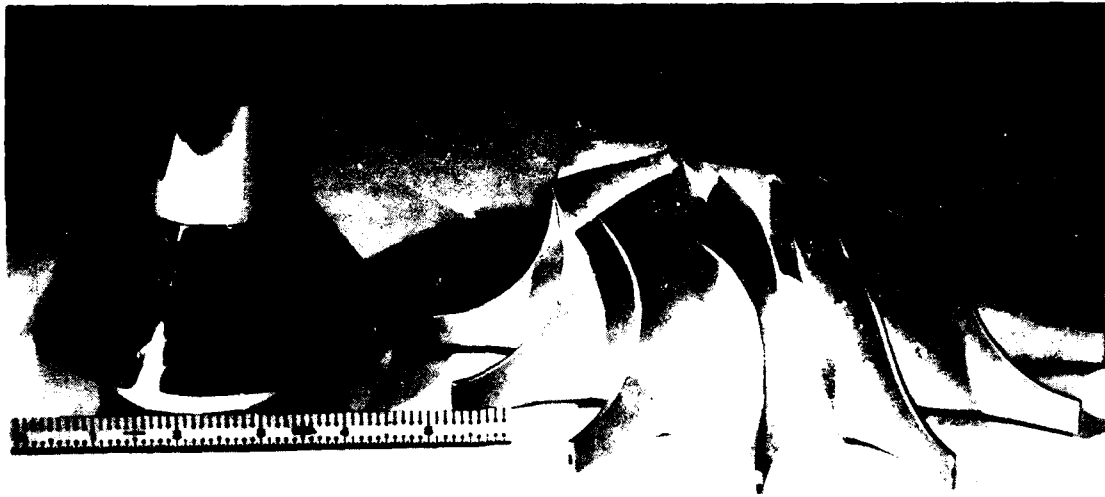


Figure 127. Machined details prior to assembly (Rotor 1).

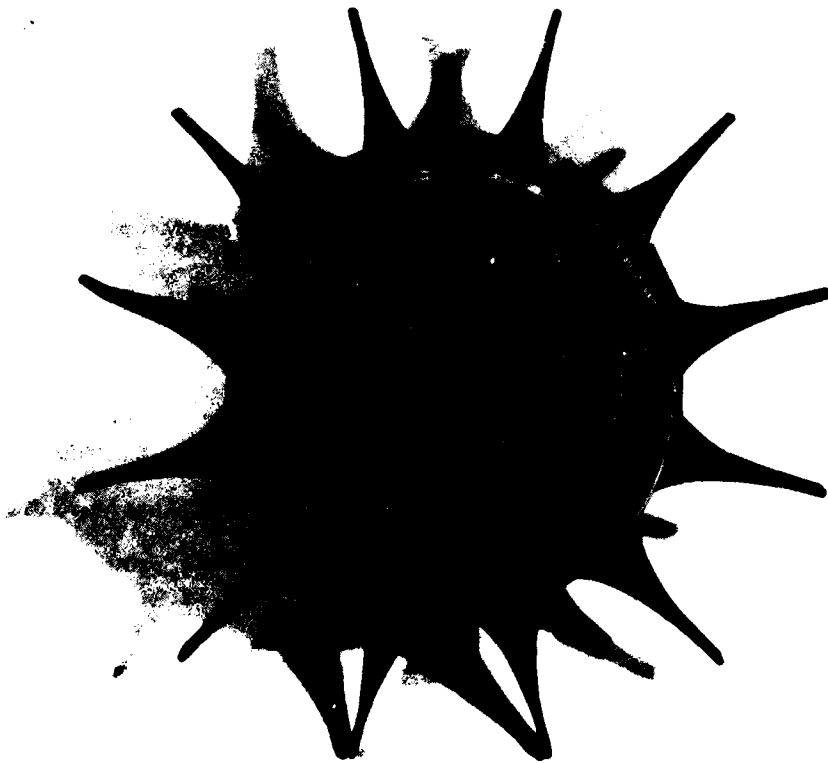


Figure 128. Ultrasonic C-scan trace showing predicted no-bond area on full-scale rotor assembly No. 1. Parallel arrows on rotor denote areas where post-HIP leak checks indicated seal distress.

To determine whether the rear braze seal was intact following the HIP cycle, the rotor was leak checked. Two braze seal leaks were indicated in a location approximately at the center of the defect area. This indication suggested that breakthrough of the seal occurred during the HIP operation.

Sectioning through a diameter which passed midway through the indicated defect area and into an area predicted to be free of defects verified the accuracy of the ultrasonic inspection. Specifically, as shown in Figure 129, predicted no-bond areas in the conical section were found. In the cylindrical and conical areas predicted to be bonded, a good-quality metallurgical bond was observed as shown in Figure 130.

Further metallurgical sectioning of the rotor disclosed that braze had penetrated into a portion of the conical joint during one of the braze cycles, as shown in Figure 131. This apparently was the result of the shell growing ahead of the hub during the heat-up cycle, and when the braze alloy became molten it penetrated into the joint. Upon solidification, the presence of the braze alloy is believed to have acted as a "shim" in the joint, creating a mismatch between mating surfaces.

During the bonding cycle, the pressure drop across the mating surfaces and the relatively large displacement required to collapse the shell into intimate contact with the hub caused further seal distress and, eventually, rupture. The effect appeared to be greatest in the vicinity of a plugged ID core printout hole in which the braze alloy apparently was sheared as the result of the large pressure drop between the external surfaces and the cavity created by the presence of the braze alloy in the joint. Figure 132 shows the appearance of the sheared core plug in the no-bond area.

Because of these difficulties, the HIP bond pressure was reduced to 15 ksi for the processing of full-scale rotors No. 2, 3, and 4. Although the role the higher pressure may have played in the processing of assembly No. 1 was not clear, a reduced pressure level was believed to be less taxing to the braze seal and to decrease its susceptibility to seal failure. In addition, the rear conical joint design was modified to minimize the braze alloy spalling problem. (This modification applied to assemblies No. 3 and 4; assembly No. 2 was beyond the point of modification.) In particular, a flange was machined into the hub detail in the joint region to form a ledge for the application of braze alloy. This provided support for the alloy powder and helped keep it from falling off the work piece before it became molten. Accompanying this fix was a modified braze seal cycle that incorporated slower heat-up rates to preclude wicking of the alloy into the joint.

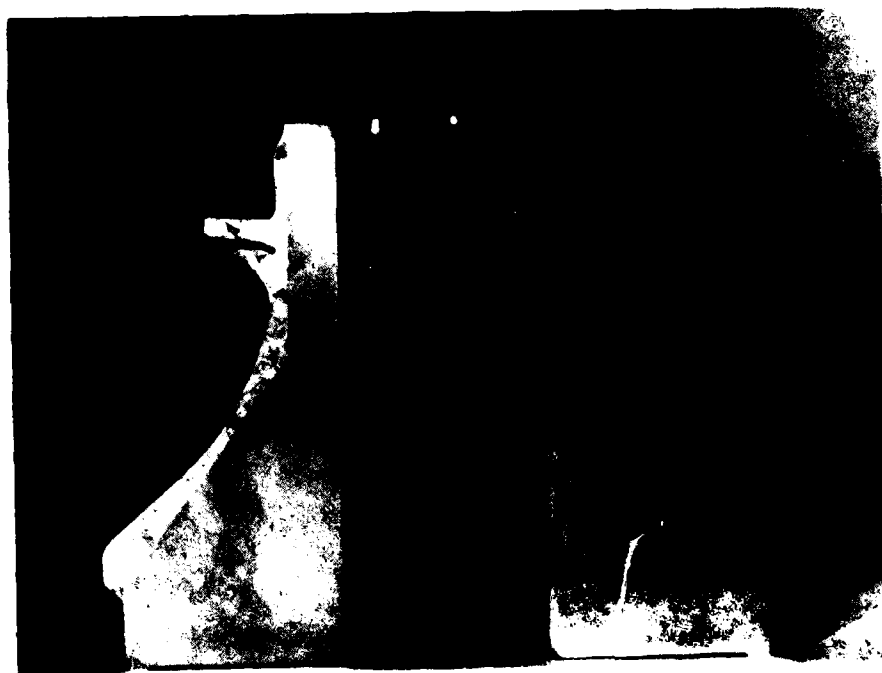


Figure 129. Macrostructure of section taken through HTRT assembly No. 1. Ultrasonic inspection indicated bond line in right section of conical portion to be defective.



Conical



Cylindrical

Figure 130. Microstructures showing good bond quality realized in selected sections of HTRT assembly No. 1. (magn: 500X)



Figure 131. Appearance of braze seals in rear conical joint locations: (top) region in which no-bond was encountered; (bottom) region in which good bond quality was seen.

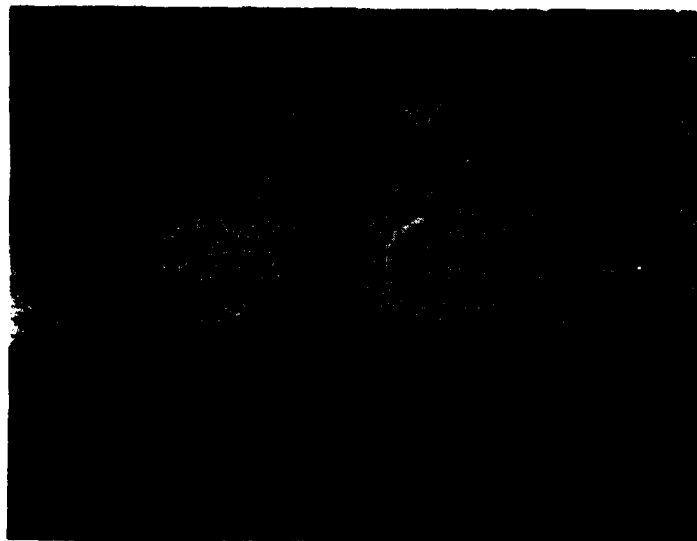


Figure 132. Core plug that has lost seal integrity. (Location is the conical section in HTRT assembly No. 1 which had shown no bond.)

Rotor No. 2

Upon completion of machining, a pinhole defect was found in the center of a core plug of the cast shell detail for assembly No. 2. Investigation disclosed that the defect was in fact a center hole that had been drilled into the end of the Mar-M247 plug material during the grinding operation for turning the plug to the desired diameter. As a result, the shell had to be rebrazed in the defect area. After the rebrazing operation, a second defect was uncovered in an unrelated core printout area. This defect was associated with apparent braze alloy porosity between the plug and shell details that opened during thermal cycling. An additional braze cycle finally yielded satisfactory results and the details were diamond polished, shrink fitted, and braze sealed.

As with rotor No. 1, the braze alloy spalled at the rear conical seal location, necessitating an additional sealing operation. The cause for the spalling problem at the rear seal location was not obvious at this point (the front seal on the cylindrical portion of the joint was of good quality); however, the problem was thought to have been brought about by differential heating effects between the massive hub section and the relatively thin airfoil shell which caused a displacement of braze alloy powder and a subsequent loss of powder adhesion. Consequently, to determine if a retarded heat-up rate could help to eliminate the spalling problem, the rotor assembly was braze sealed a third time. During this sequence a cylindrical susceptor was positioned around the

assembly to minimize radiation effects from the heating elements. However, this approach was not effective because the excessive shielding effect of the susceptor occasioned a poor braze alloy fluidity.

The next, or fourth, braze cycle applied to the rear conical seal was without a "shield" because the roughened condition that resulted in the braze fillet was felt to be highly conducive to entrapment and adherence of the braze alloy powder. The appearance of the braze seal was greatly improved but a leak check showed the seal to have a pinhole leak in one isolated location. Consequently, a fifth cycle was applied. Leak checking of the braze fillet again revealed a pinhole leak. After a sixth braze seal cycle, the rotor passed the leak check; it was then HIP bonded at 2215°F for 3 hours at 15 ksi. Ultrasonic inspection of the bonded rotor indicated that the bonding operation had been successful. After heat treatment, this rotor, because of its extensive braze sealing history, was placed in reserve for possible use in an aerodynamic rig test program.

Rotor No. 3

This rotor incorporated a modified rear conical joint design with a flange built into the PM hub to prevent braze spalling (Figure 133). After a braze seal cycle, in which the heating rate from 1900°F to the melting range of the braze alloy was approximately half that used for assemblies No. 1 and 2 (20°F versus 8°F per minute), the rotor was successfully leak checked. Significantly, the flange eliminated the alloy powder spalling problem experienced for assemblies No. 1 and 2. However, some questionable porosity after the first braze cycle in the conical location prompted the decision to braze a second time to maximize the probabilities for success.

Following braze sealing, the rotor was HIP bonded and, upon subsequent ultrasonic inspection, proclaimed to be sound. After heat treatment, rotor No. 3 was finish machined. Figures 134 through 136 show the rotor after machining.

Rotor No. 4

Assembly, braze sealing, HIP bonding, and heat treatment of this rotor proceeded uneventfully; only one braze cycle was required to vacuum seal the assembly. Following a successful ultrasonic inspection, the rotor was finish machined.

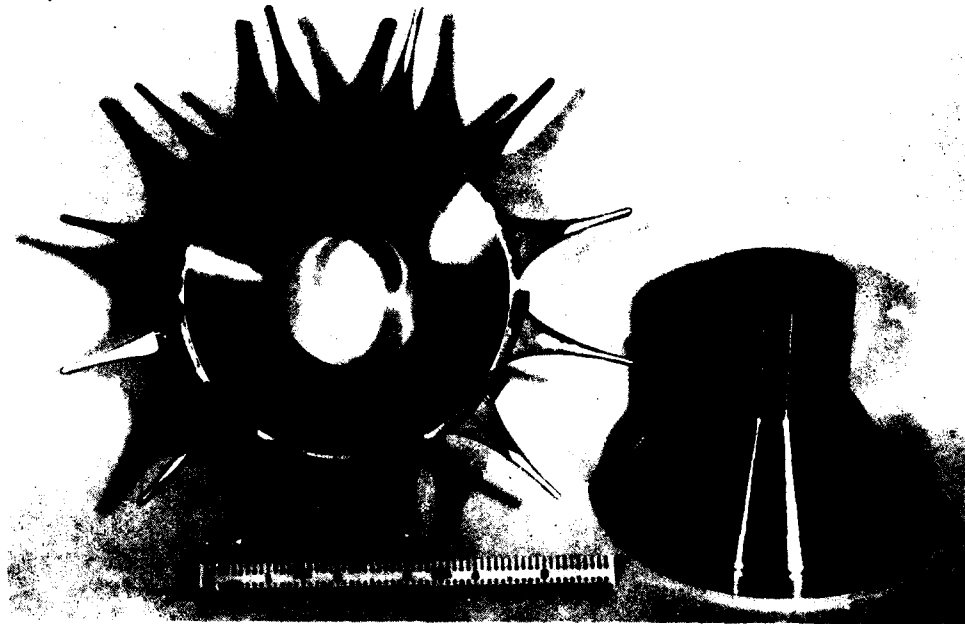


Figure 133. Machined shell and hub detail for rotor assembly No. 3.

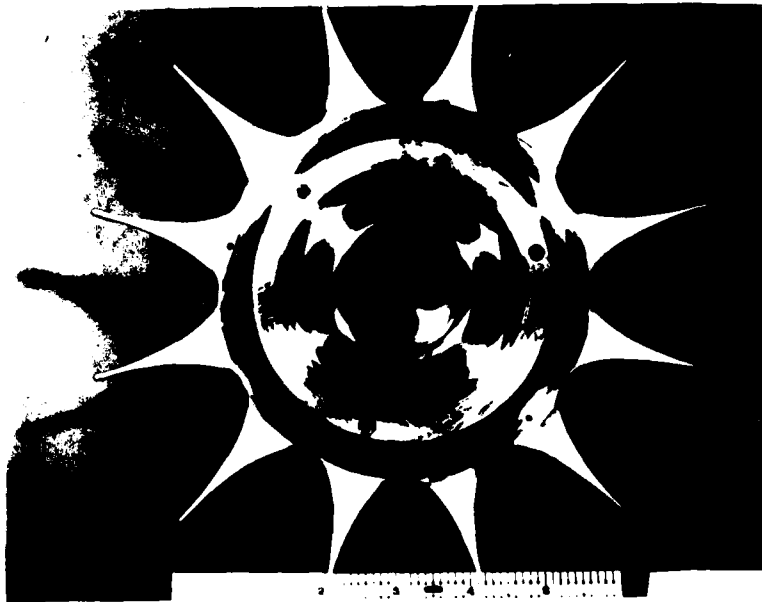


Figure 134. Forward face of finish-machined HTRT rotor assembly showing retention scheme.



Figure 135. Aft (exducer) face of HTRT rotor assembly.



Figure 136. Side view of finish-machined HTRT rotor assembly.

PHASE III--MECHANICAL INTEGRITY VERIFICATION

MATERIAL PROPERTY VERIFICATION

The mechanical property characterization program conducted during Phase I was designed to evaluate the response of the HIP-bonded joint, parent metal PA101, and Mar-M247 system constituents to the processing variations investigated. The Phase III effort was intended primarily to expand upon the Phase I data base in an attempt to better quantify the fatigue and rupture capabilities of the system. The evaluation specimens for this work were from stylized rotors, cast-to-size Mar-M247 test bars, and stylized PA101 hub sections. Typical locations from which test specimens were machined from PA101 plugs and stylized rotors are shown in Figures 137 and 138. This material was processed in accordance with schedules which were applied to full-scale rotors. The testing conducted during Phase III is summarized in Table 16.

PA101/Mar-M247 Butt Joint Test Results

As shown in the test schedule (Table 16), 1200°F tensile, low cycle fatigue, and stress rupture testing was performed on butt type specimens that were removed normal to the bond line in the conical portion of stylized rotors No. 5 and 6.

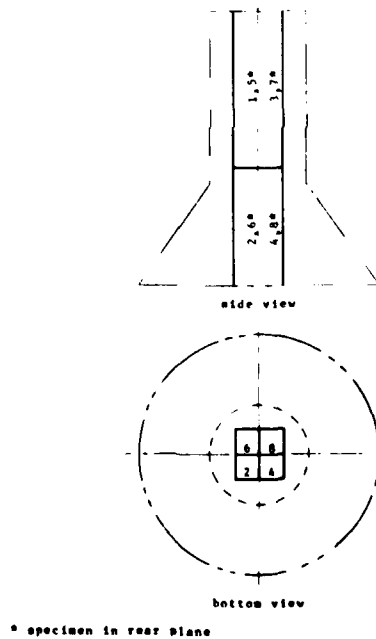


Figure 137. Specimen location for PA101 hubs.

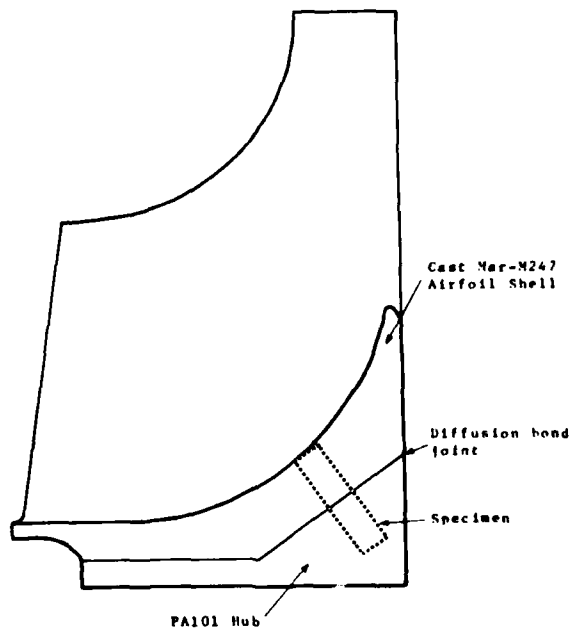


Figure 138. Specimen location for stylized rotors.

TABLE 16. PHASE III MATERIAL PROPERTY TESTS
PA101/Mar-M247 butt joint specimens 1200°F tensile 1200°F/125 ksi stress rupture LCF load control, $K_T = 1$, 1200°F
Parent metal PA100 specimens 1200°F/140 ksi stress rupture LCF load control, $K_T = 2.0$, 1200°F LCF strain control, $K_T = 1.0$, 1200°F
Mar-M247 cast-to-size bars Room temperature tensile 1400°F/100 ksi creep rupture 1600°F/65 ksi creep rupture 1800°F/30 ksi stress rupture
LCF A ratio = 1.0, 20 cpm, triangular wave

As shown in Table 17, all failures occurred away from the bond line in the cast Mar-M247. Significantly, in all the joint testing in Phases I and III of the program (over thirty 1200°F tensile stress rupture and LCF tests), not a single joint failure occurred, indicating 100% joint efficiency. However, in

TABLE 17. TEST RESULTS FOR PA101/Mar-M247 BUTT JOINTS

1200°F Tensile					
<u>Specimen No.</u>	<u>0.2% YS (ksi)</u>	<u>UTS (ksi)</u>	<u>% Elong</u>	<u>% RA</u>	<u>Failure Location</u>
5-1	129.2	156.0	3.8	7.8	Cast Mar-M247
5-2	116.7	132.3	4.6	9.6	Cast Mar-M247
1200°F/125 ksi Stress Rupture					
<u>Specimen No.</u>	<u>Life (hr)</u>	<u>% Elong</u>	<u>% RA</u>	<u>Failure Location</u>	
5-3	7.3	3.8	4.8	Cast Mar-M247 (shrinkage porosity observed)	
6-3	0	1.9	13.7	Cast Mar-M247 (apparent tensile overload, no shrinkage)	
1200°F LCF, 120 ksi (0 to max), $K_t = 1.0$, $A = 1.0$					
<u>Specimen No.</u>	<u>Cycles (N_f)</u>		<u>Failure Location</u>		
3A2	23,301		Cast Mar-M247		
5-4	101,000		Runout		
6-1	852		Cast Mar-M247		
6-2	2,908		Cast Mar-M247		
6-4	5,335		Cast Mar-M247		
6-5	123		Cast Mar-M247		

the case of one stress rupture specimen, microshrinkage was present in the Mar-M247 fracture surface (Figure 139). The occurrence of residual microshrinkage after HIP bonding was first observed in the Phase I effort; its resolution will require additional work that is outside the scope of the current program. The prognosis for success in eliminating residual microshrinkage is good, however. The approaches that could be pursued primarily involve modifications to HIP parameters and could include higher pressure, longer exposure times, or both.

Parent Metal PA101 Test Results

As indicated in Table 18, combined tensile, stress rupture, and notched LCF properties demonstrate good levels of ductility and strength as well as consistency. Smooth-bar LCF results, however, showed scatter which, according to Figure 140, appears to be influenced by the



Figure 139. Microshrinkage observed in cast alloy fracture surface of PA101/Mar-M247 butt joint specimen.

presence of inclusions. An EDAX analysis (Figure 141) of the pictured inclusion indicated that the inclusions were aluminum-hafnium rich and that they probably originated during the powder manufacturing process as a result of erosion of the ceramic nozzles which are used to atomize the PA101 alloy. In one long life case (Figure 142), the failure origin appeared to be a subsurface pore which was apparently caused by an argon-induced hollow powder particle. The use of a -150 mesh product in the full-scale rotors (the stylized PM product represented by these results was -60 mesh) should decrease the incidence of inclusions in future rotor configurations. Nevertheless, the threat of inclusion contamination in the PA101 alloy seems to be real, as others have experienced with AF95. The powder manufacturers, however, have recognized this threat and are moving aggressively to minimize it. Future PA101 procurement is expected to benefit significantly as a result.

TABLE 18. TEST RESULTS FOR HYBRID PROCESSED PARENT METAL PA101

<u>Specimen No.</u>	<u>Temp (°F)</u>	<u>0.2% YS (ksi)</u>	<u>UTS (ksi)</u>	<u>% Elong</u>	<u>% RA</u>
3-13	Room	135.3	197.7	10.7	8.6
11-14	Room	137.6	208.8	13.6	10.4
3-8	1200	125.0	189.7	17.1	18.1
11-8	1200	125.0	188.7	16.7	16.9

1200°F/140 ksi Stress Rupture				
<u>Specimen No.</u>	<u>Life (hr)</u>	<u>Elong %</u>	<u>% RA</u>	
3-7	64.6	12.0	16.6	
11-7	51.2	8.3	13.1	

1200°F LCF, $K_t = 1.0$, Strain Control, $A = 1.0$				
<u>Specimen No.</u>	<u>Total Strain Range (%)</u>	<u>Life Cycles (N_f)</u>	<u>Remarks</u>	
3-1	0.80	5,734	Fracture surface smeared	
3-3	0.75	4,047	Origin at surface inclusion	
3-5	0.70	46,815	Origin at internal pore	
11-1	0.70	3,940	Origin at surface inclusion	
11-3	0.70	7,563	Fracture surface smeared	
11-5	0.70	12,105	Origin at subsurface inclusion	

1200°F LCF, $K_t = 2.0$, Load Control, $A = 1.0$				
<u>Specimen No.</u>	<u>Max Stress (ksi)</u>	<u>Life (cycles)</u>	<u>Remarks</u>	
3-6	100	111,225	Understressed, stepped to 130 ksi	
	110	3,015		
	120	3,580		
	130	1,335		Failed
3-2	125	25,718		
3-4	125	65,758		
11-2	130	11,054		
11-4	130	21,997		
11-6	130	9,859		

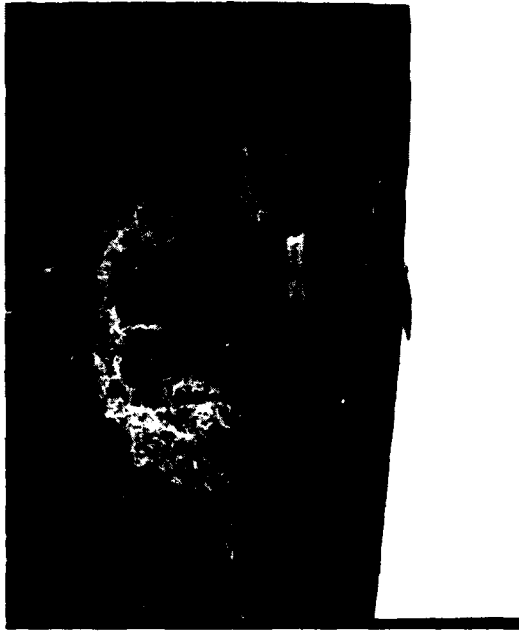


Figure 140. Photomicrograph of an aluminum-hafnium-rich inclusion, at surface of an LCF specimen, that contributed to data scatter.

Cast-to-Size Mar-M247 Test Results

Creep rupture, stress rupture, and room temperature results generated for cast-to-size test bars processed to hybrid schedules are presented in Table 19. Overall rupture properties, as shown in Figure 143, appear to be adequate for the HTRT design. However, 1400°F rupture lives and ductilities appear to be on the low side of those desirable. Residual microshrinkage of the type noted previously appeared to be a significant influencing factor.

FINAL DESIGN ROTOR SPIN TESTING

Spin tests were conducted on the final rotor configuration produced in Phase II. These tests consisted of stress correlation, low cycle fatigue at elevated temperature, and rotor burst tests. The DDA small spin pit facilities were used. Figure 144 shows the HTRT rotor mounted on the spin cover/drive assembly.

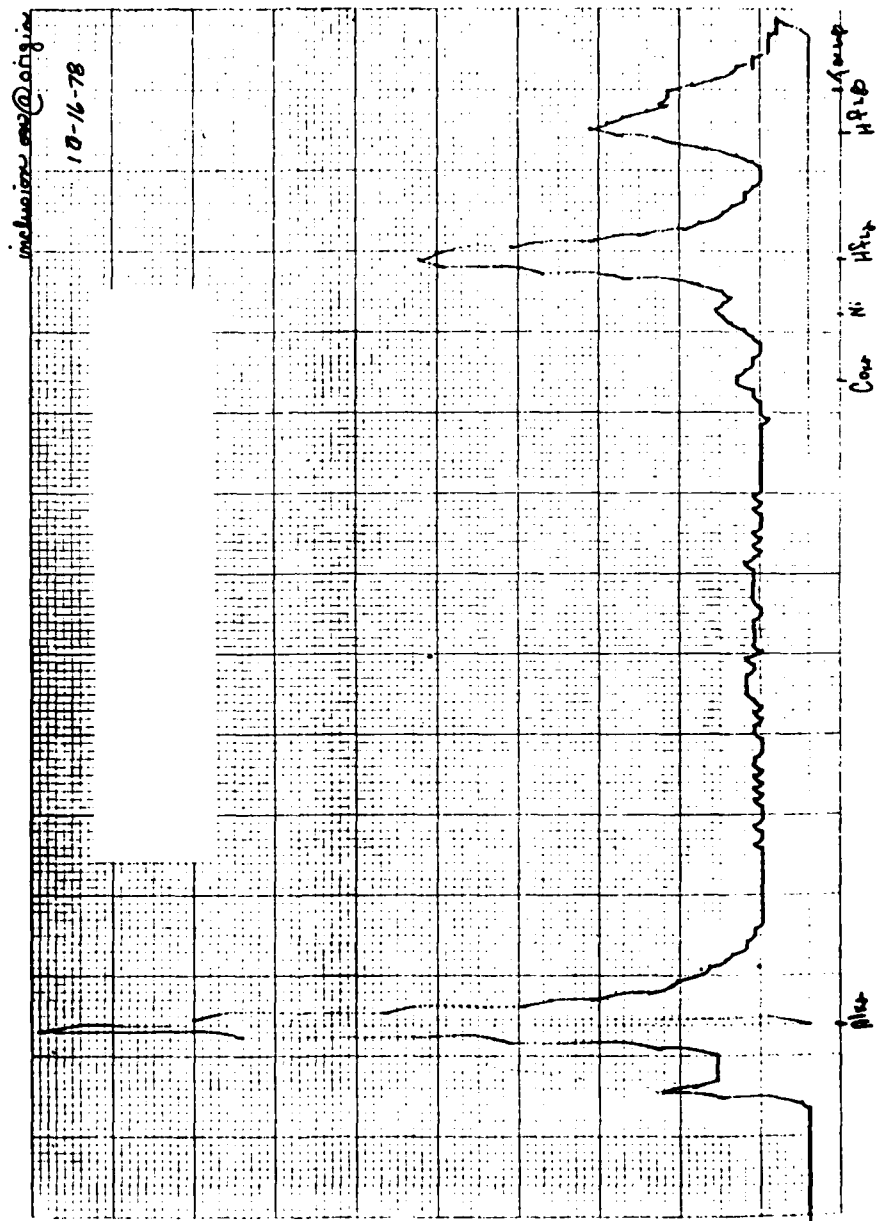


Figure 141. Analysis of inclusion in Figure 140 showing it to be aluminum-hafnium rich.

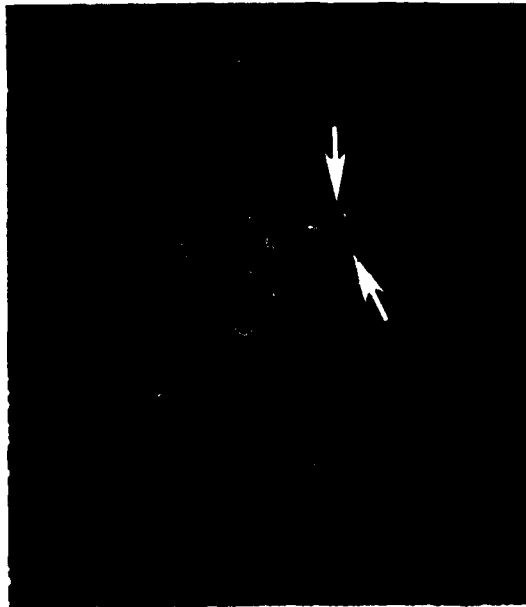


Figure 142. Pore-type origin (arrows) observed in fracture surface of smooth-bar LCF specimen 3-5. (magn: 100X)

TABLE 19. TEST RESULTS FOR HYBRID PROCESSED METAL Mar-M247 CAST-TO-SIZE TEST BARS						
Rupture						
Test	Specimen No.	Heat Code	Life (hr)	% Elong	Prior Creep	Remarks
1400°F/100 ksi Creep Rupture	29	2741	10.2	1.2	0.97	Shrinkage porosity
	30	5134	62.6	2.0	0.74	Shrinkage porosity
1600°F/65 ksi Stress Rupture	31	2741	62.4	6.1		Failed in radius
	32	2741	48.6	5.2		
	33	5134	60.2	5.4		
1800°F/30 ksi Stress Rupture	34	2741	44.5	7.5		
	35	5134	27.4	7.5		
Room Temperature Tensile						
Specimen No.	0.2% YS (ksi)	UTS (ksi)	% Elong	% RA	Remarks	
27	126.3	132.9	1.1	2.7	Shrinkage porosity	
28	125.2	153.6	5.7	6.0	Shrinkage porosity	

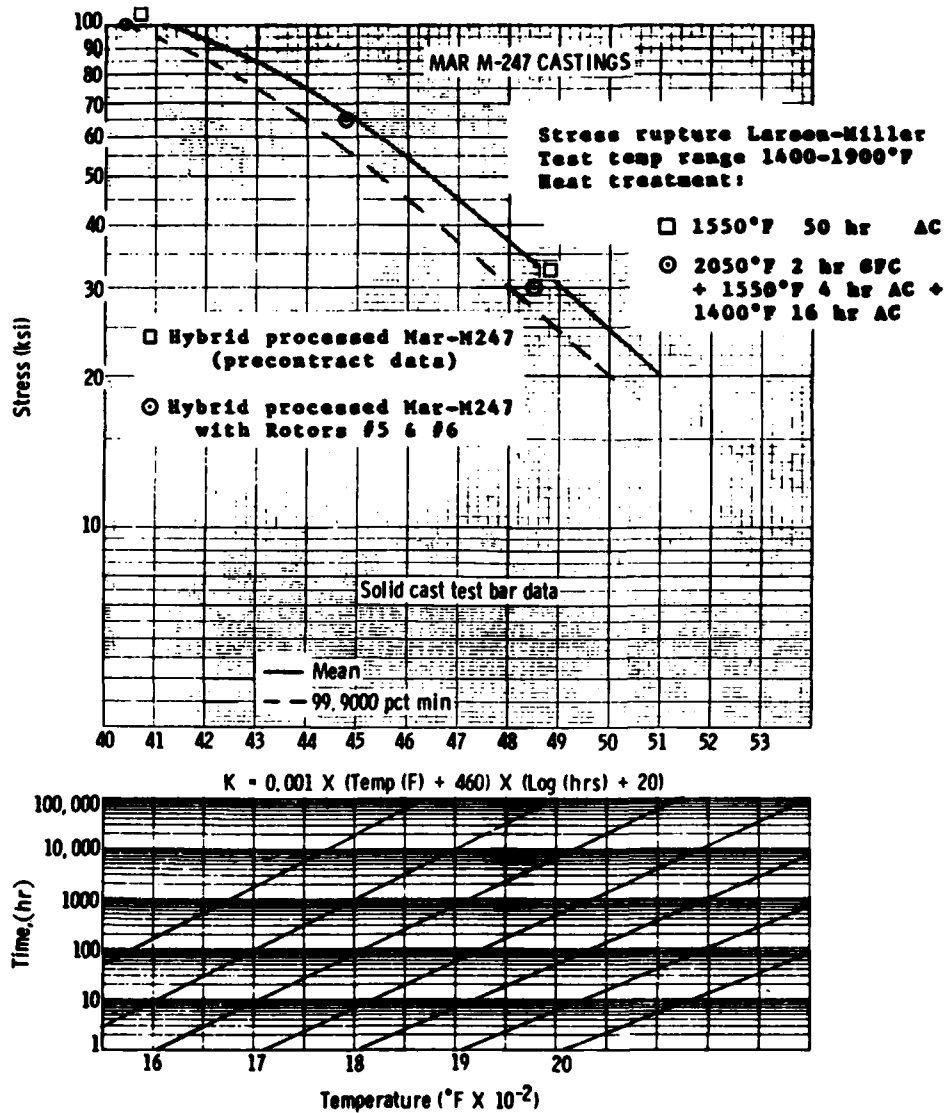


Figure 143. Comparison of hybrid processed Mar-M247 cast-to-size bars (processed with rotors No. 5 and No. 6) and non-HIP-bond-processed (baseline) cast-to-size Mar-M247.



Figure 144. HTRT rotor mounted on spin pit cover/drive assembly.

Stress Correlation Test

The purpose of this test was to obtain a correlation between the analytical stress predictions and measured strains (stresses). The results of this test were to be used to modify the analytical model if necessary.

Five strain gages were installed on rotor assembly number 3 at the locations shown in Figure 145. In addition, thermocouples were located adjacent to the strain gages to allow correction of the strain gage output. Prior to the spin test, an apparent strain calibration was run on each from room temperature up to 250°F.

The test method used was to accelerate slowly to design speed and record microstrain and temperature at the strain gages. Test results, which are compensated for temperature, are presented in terms of microstrain and stress versus rotor speed in Figures 146 and 147. Excellent agreement was obtained between predicted cold and actual cold stresses as indicated on Table 20. Also shown on Table 20 are the predicted hot gradient stresses.

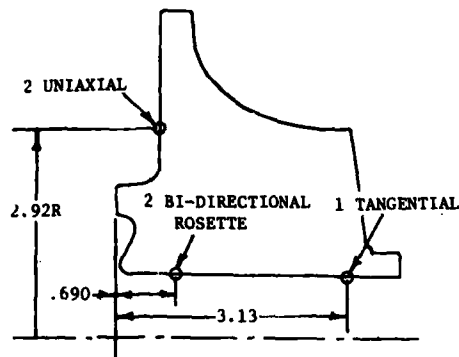


Figure 145. Strain gage locations.

TABLE 20. BORE STRESSES AT MAXIMUM STRESS LOCATION

Type of stress	Predicted cold stresses (psi)	Test cold stresses (psi)	Predicted hot gradient stresses (psi)
Axial	-13,751	-10,197	-11,382
Radial	-16	0	-334
Tangential	129,340	130,810	142,020
Equivalent	136,750	136,195	148,190

It was concluded from this stress correlation test that the analytical model is accurate and no modifications are required.

Low Cycle Fatigue Test

Prior to initiating the elevated temperature low cycle fatigue test a temperature correlation and spin pit shakedown run were conducted. Some difficulties were encountered with erosion of the heat enclosure. This problem was resolved by installing a heat enclosure liner or can of INCO 718 as shown in Figure 148.

Also shown on Figure 148 are the locations of the temperature correlation thermocouples. During the low cycle fatigue test the metal temperature was to be controlled to 1100°F at the bore or 1500°F on the blade tip on a not-to-exceed basis for each position.

The test method used was to evacuate the spin pit to a pressure level of 2 mm Hg absolute and to increase the power supplied to the heating elements with the rotor spinning. Once a temperature limit was encountered, the rotor was cycled from 5000 to 55,000 rpm.

HIGH TEMP. RADIAL TURBINE SPIN TEST

R/N 1358-1461

RUN 1

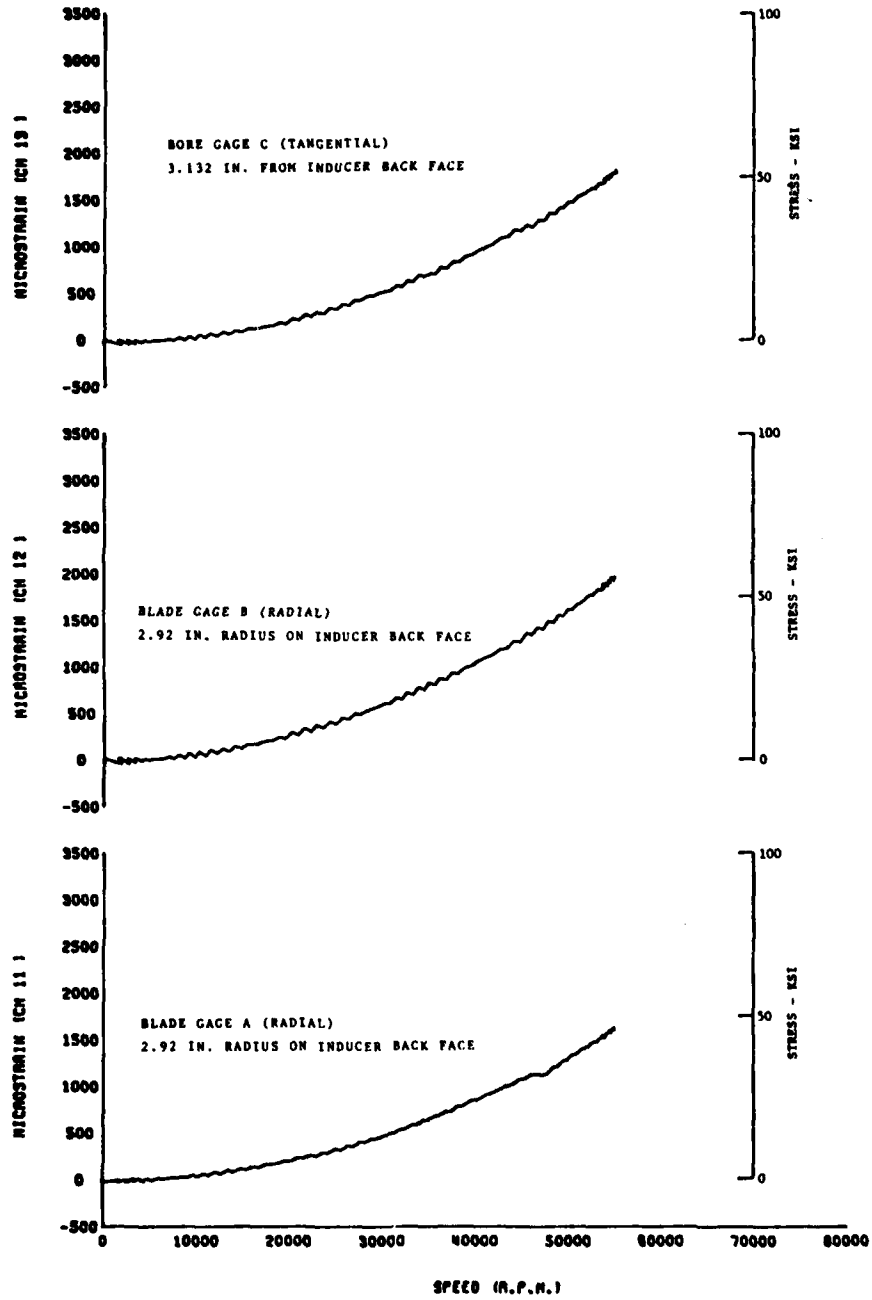


Figure 146. Microstrain and stress versus speed.

HIGH TEMP. RADIAL TURBINE SPIN TEST
RUN 2.

R/N 145-596

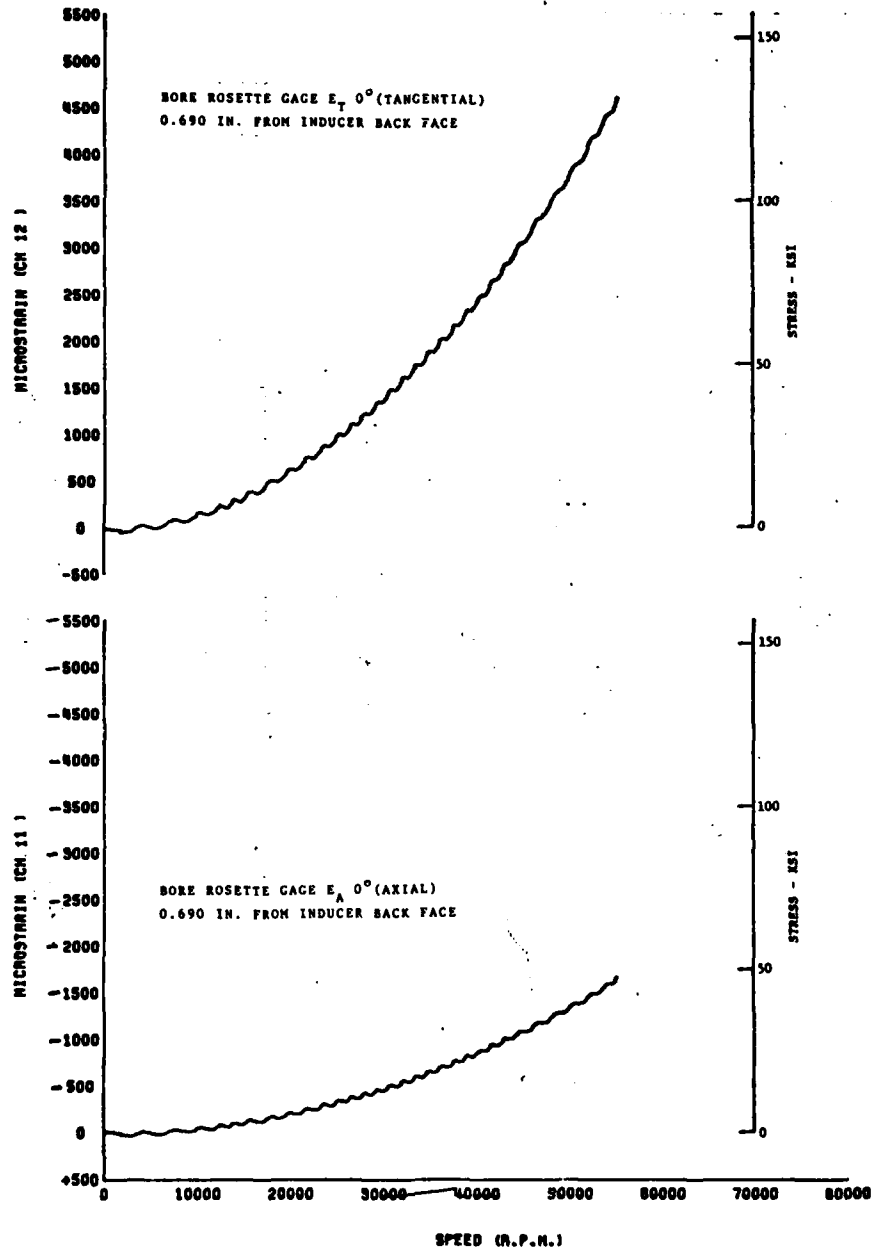


Figure 147. Microstrain and stress versus speed.

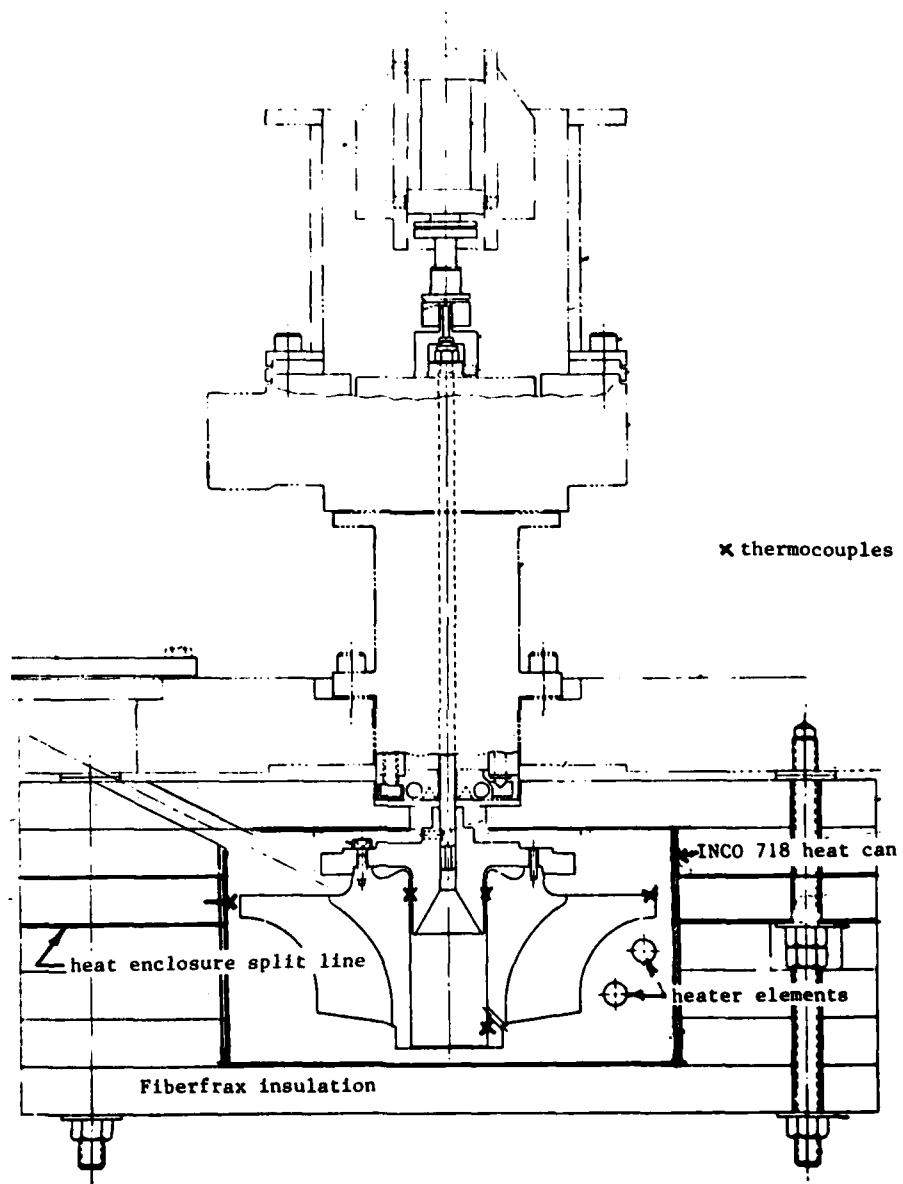


Figure 148. Heat enclosure configuration.

It was found that the evacuated heat enclosure produced an adiabatic situation with the bore, blade tip, and control thermocouples reading the same temperature. As would be expected in an adiabatic environment, the maximum bore temperature of 1100°F was the controlling metal temperature. Cycling the rotor speed between 5000 and 55,000 rpm produced temperature variations of $\pm 30^\circ\text{F}$.

In order to compensate for the lack of thermal gradient, the maximum cycle speed was increased from 55,000 to 57,000 rpm. Figure 149 shows that nonthermal gradient and thermal gradient maximum bore stresses match at this speed.

The spin pit was set up for unattended operation and cycling of the rotor assembly. Protective shutdown devices were provided for overspeed, overpressure, high vibration, whip, bearing noise, and overtemperature. During the low cycle fatigue test, periodic inspections of the test equipment and rotor assembly were performed.

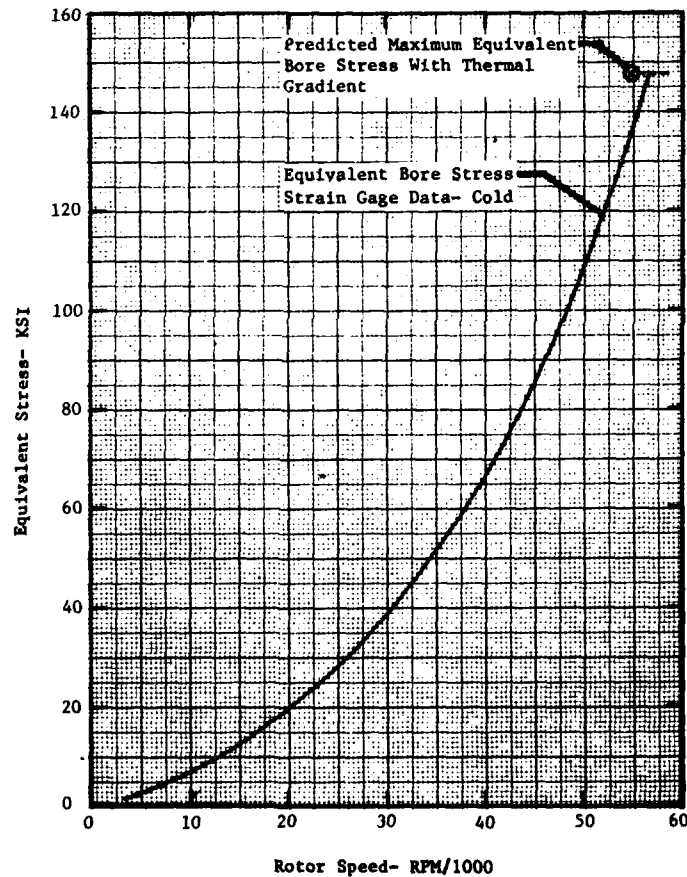


Figure 149. Equivalent bore stress versus speed.

Continuous recordings of speed and temperature were obtained. Figure 150 is such a record showing that the rotor was cycled between 5000 and 57,000 rpm in 55 sec. This figure also shows that the average temperature of 1100°F was maintained with a peak temperature of 1115°F at maximum speed and a minimum temperature of 1085°F at minimum speed. This fluctuation was a result of windage effects, even though the test chamber pressure was reduced to 2 mm Hg absolute.

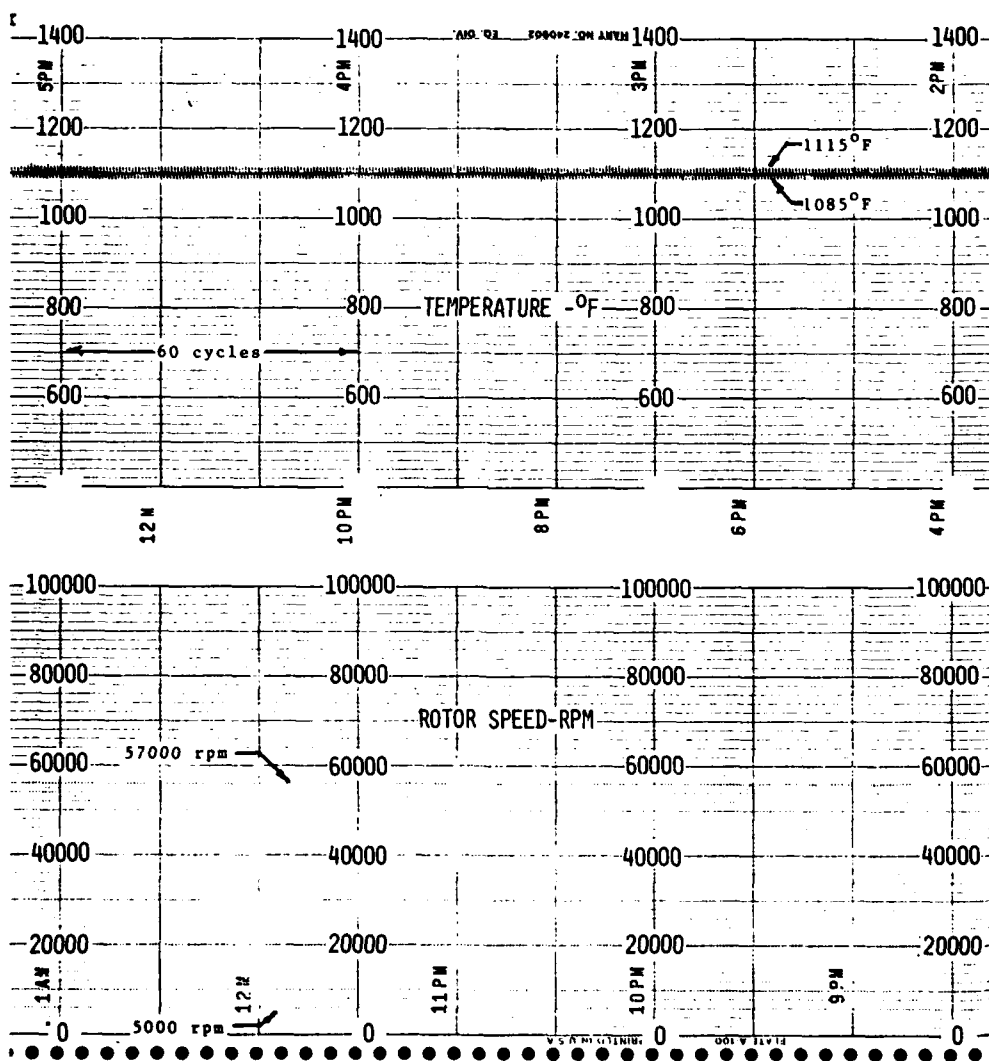


Figure 150. Elevated temperature low cycle fatigue test time-speed-temperature sample record.

The low cycle fatigue spin test was completed when 6001 cycles had been accrued. Zygo inspection revealed no indications. Measurements taken before and after the test, shown on Table 21, indicate that no measurable growth occurred during the LCF test.

TABLE 21. ROTOR DIMENSIONAL COMPARISON			
Diameter	A	B	C
Original	3.9722	1.6000	2.2303
Following LCF Test	3.9722	1.6001	2.2304

Rotor Burst Test

The purpose of this test was to spin the final configuration to burst speed and to determine failure mode and location. In order to accomplish this test, the 2-in.-diameter drive turbine, which has a 100,000 rpm capability, was installed. In addition, the spin pit was lined with approximately 6 in. of fibrous material sandwiched between thin sheet metal in an effort to soften the impact of the rotor burst and to preserve the failure evidence.

The test was conducted by increasing rotor speed slowly until burst occurred. Figure 151 presents the speed versus time trace taken during this test. At 72,000 rpm, a failure (which is indicated by a sharp increase in the acceleration rate of the drive turbine) occurred. Inspection of the pit after the failure revealed that the rotor was intact with the exception that considerable impact damage had occurred on the blade tips as shown on Figure 152. It was also found that the spin adapter (Figure 153) and the rotor assembly (Figure 154) had separated. Examination of Figure 154 shows that the three cap screws holding the two components together were failed. It is believed that the drive spindle failed, dropping the rotor, and that the two pieces were separated on impact with the spin pit liner.

Measurements were made of rotor pilot diameter and at various locations. These measurements are compared to the original measurements on Table 22. These comparisons indicate a significant yield in the bore in the high stress areas (Dia. A and Dia. B).

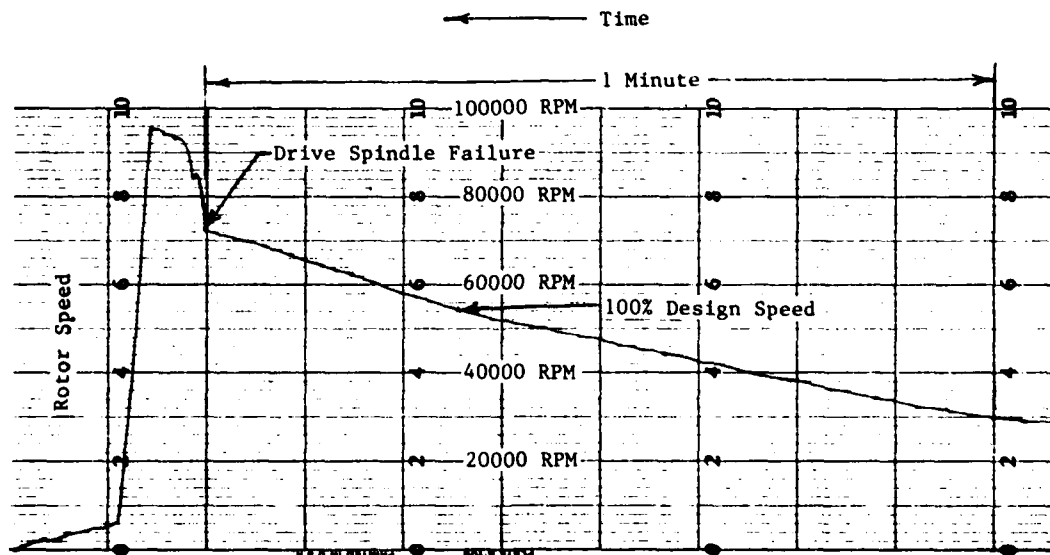


Figure 151. Attempted HTRT rotor burst.

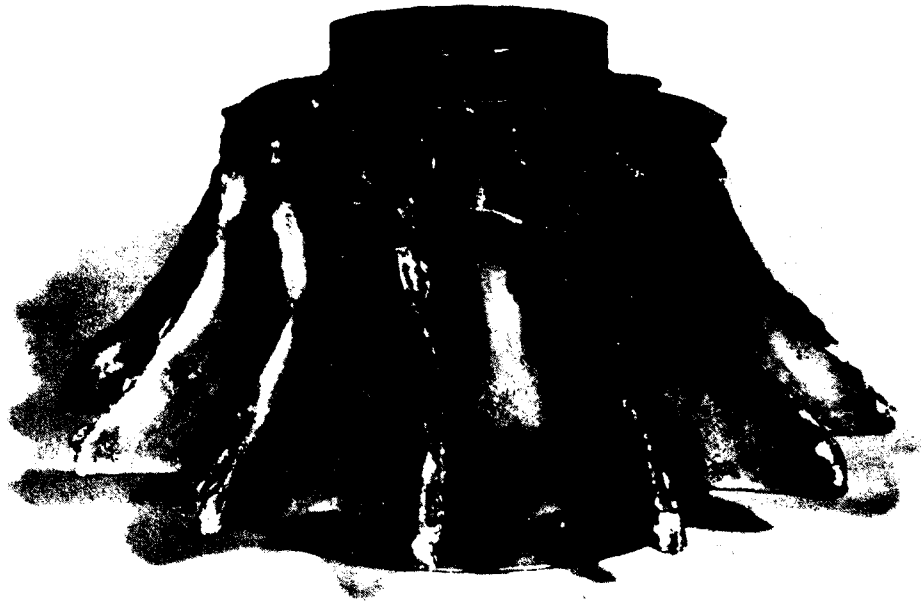


Figure 152. Rotor assembly following burst test.

The rotor bore was Zyglod and no crack indications were found.

A cut-up evaluation was then accomplished. Figure 155 is a photograph of a macroetched polished section of the rotor assembly after test. Photomicrographs of the bond line, Figure 156, at both the conical and cylindrical sections of the rotor indicate that the high stress encountered during this test did not affect bond line integrity.

The results of this test are significant in that the rotor remained intact at 131.2% of design speed. This represents 172% design speed stress which in this case (without thermal gradient) calculates to be 234.4 ksi.



Figure 153. Spin adapter.

120 GENERAL MOTORS CORP INDIANAPOLIS IN DETROIT DIESEL A--ETC F/G 21/5
HIGH-TEMPERATURE RADIAL TURBINE DEMONSTRATION.(U)
APR 80 B A EWING, D S MONSON DAAJ02-77-C-0031
DOA-EDR-9990 USAAVRADCOM-TR-80-D-6 NL

FIED

43

No.

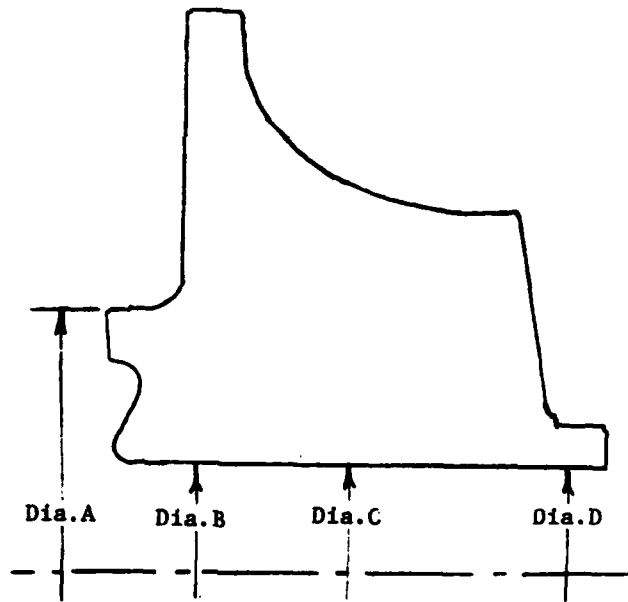




Figure 154. Rotor assembly front face.

TABLE 22 . ROTOR DIMENSIONAL COMPARISON

Diameter	A	B	C	D
	Inches			
Original	3.9756	1.599	1.599	1.599
Following Overspeed To 72,000 RPM	3.9822	1.6079	1.6072	1.5995
Difference	.0066	.0089	.0082	.0005
Percent Change	.16	.56	.51	-



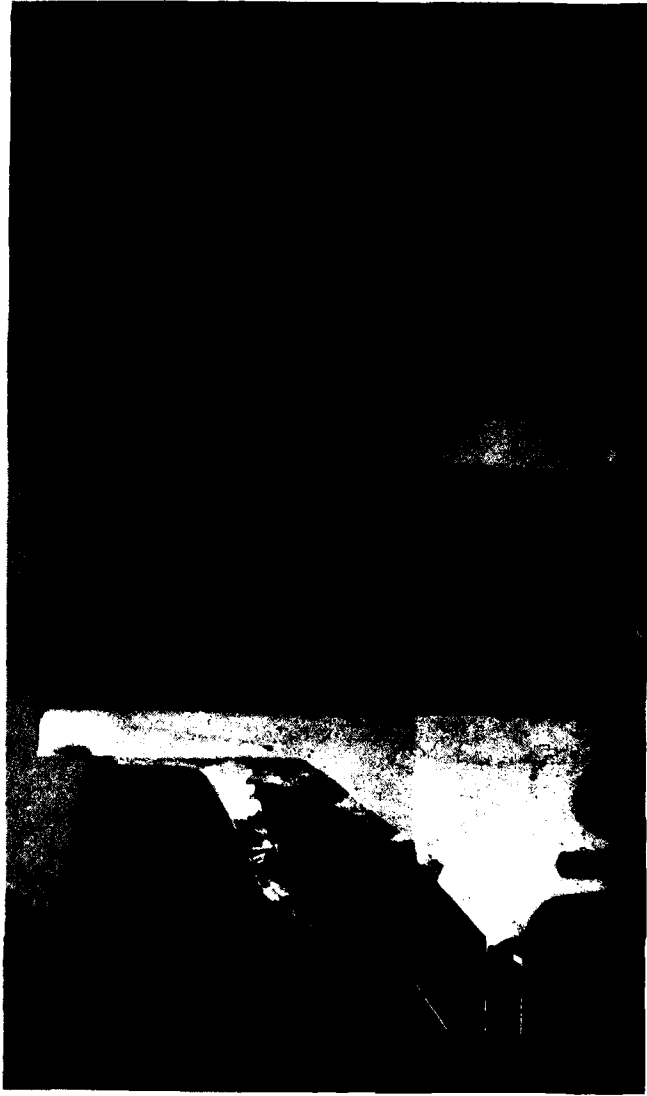
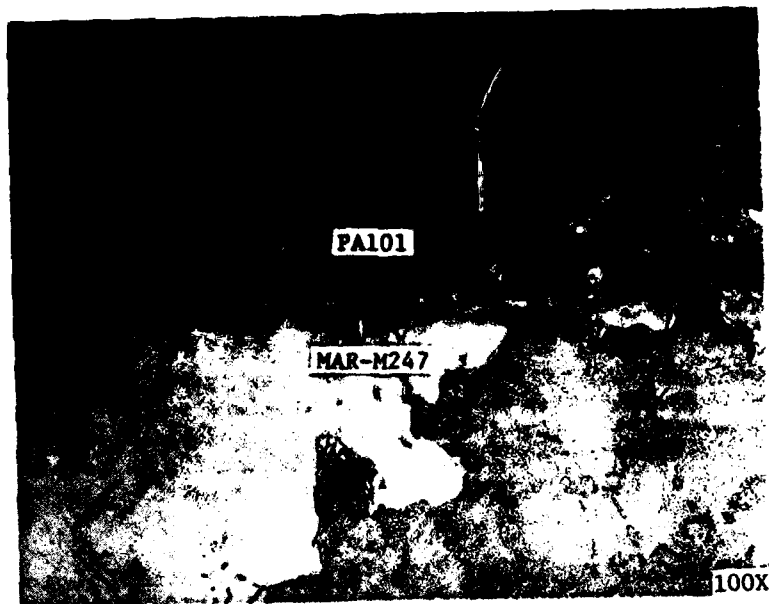


Figure 155. Macroetched polished section of rotor assembly.



cylindrical section



conical section

Figure 156. Photomicrographs of bond line.

CONCLUSIONS

As a result of the work accomplished on the High Temperature Radial Turbine Demonstration Program, the following conclusions are drawn:

1. The casting of air-cooled shells should be viable on a commercial scale. With the mold gating optimized to preclude core shift and misruns, excellent casting quality was realized; a high degree of consistency and wall thickness control was demonstrated.
2. The feasibility of the use of the hot isostatic pressure (HIP) bonding technique for joining a Mar-M247 casting to a near-net-shape PA101 powder metal hub was established. Microstructural examination of the bondline indicated excellent metallurgical quality. Tensile, stress rupture, and low cycle fatigue testing conducted on specimens machined from stylized rotors processed to schedules which were equivalent to those employed for full-scale rotors shows consistent 100% joint efficiencies. The load-carrying capability of the joints was judged to be more than adequate for the HTRT final design.
3. Good levels of parent metal PA101 tensile and stress rupture capability were realized for stylized hub sections processed to full-scale schedules. Low cycle fatigue properties, however, suffered from scatter attributed to the presence of ceramic inclusions in the -60 mesh product. The full scale hubs used -150 mesh powder in an effort to minimize the tendency for scatter.
4. Creep/stress rupture properties generated for cast-to-size Mar-M247 test bars processed with the rotors were considered as adequate for the HTRT design although rupture ductilities that appeared to be influenced by microshrinkage were less than desired at 1400^oF.
5. Good correlation between ultrasonic inspection techniques employed to evaluate the bond line between details and bond quality was demonstrated based on a cut-up evaluation of a rotor predicted to be defective.
6. The structural integrity of the rotor design was established by the successful completion of 1) a 6000-cycle elevated temperature low cycle fatigue test and 2) an overspeed test to 131% design without failure.
7. The mechanical design procedure was verified by the excellent agreement between predicted and measured stresses.
8. Manufacturing cost studies, which included casting and PA101 hub supplier quotes, indicate that the rotor design resulting from this program could be produced economically.

RECOMMENDATIONS

The results of the program were very encouraging and have indicated areas where additional work should be done:

1. Additional work is needed to eliminate the threat of residual microshrinkage in the HIP-bonded Mar-M247 and to more fully characterize the mechanical properties of HIP-bonded rotors.
2. Additional LCF testing should be accomplished using the rotor which accrued 6001 cycles. Such testing would more fully define the LCF capability of the dual property rotor and provide data which may allow designing to higher stress levels in the rotor bore.
3. An additional rotor burst test should be run to determine the failure mechanism and to verify the design procedure.
4. A heat transfer test should be conducted using the existing component test rig to verify existing design procedures and to provide data for future designs.

REFERENCES

1. G. S. Calvert and U. Okapuu, Design and Evaluation of a High-Temperature Radial Turbine, USAAVLABS Technical Report 68-69, U.S. Army Aviation Material Laboratories, Fort Eustis, Virginia, January 1969, AD688164.
2. G. S. Calvert, S. C. Beck, and U. Okapuu, Design and Experimental Evaluation of a High-Temperature Radial Turbine, USAAVLABS Technical Report 71-20, Eustis Directorate, U.S. Army Air Mobility R&D Laboratory, Fort Eustis, Virginia, May 1971, AD726466.
3. P. R. Smoot, Turbine Blade Joining by Casting, AMMRC TN78-9, Army Materials and Mechanics Research Center, Watertown, Maine, November 1978.
4. I. Watanabe, I. Arign, T. Maxhimo, Effect of Dimensional Parameters of Impellers on Performance Characteristics of a Radial Inflow Turbine, American Society of Mechanical Engineers Paper No. 70-GT-90, May 1970.
5. Mizumachi, Endo, and Kitano, A Study of Aerodynamic Characteristics of Rotating Blades in a Radial Inflow Turbine, JSME, October 1971.
6. Rizzo and Fiedler, Manufacturing Methods for Superalloy Powder Production and Consolidation, Lycoming IR271-3(IV) for interim period 1 May to 31 August 1974.
7. W. H. McAdams, Heat Transmission, McGraw Hill, 1954.

APPENDIX A
CERTIFICATE OF TEST

The results of the Special Metals chemical analysis and typical sieve analysis for the 12 stylized PA101 plugs are presented below:

CHEMICAL ANALYSIS:

Al	3.45 %	B	.017 %	C	.12 %
Co	8.8 %	Cr	12.4 %	Cu	%
Fe	%	Ni	%	O ₂	.0064 %
P	%	S	%	Si	%
Ti	4.18 %	W	4.15 %	Zr	.07 %
Al+Ti	7.63 %	Ta	4.12 %	Mo	1.95 %
Hf	1.10 %		%		%

COMMENTS:

These pieces, serial numbers 1, 3, 4, 5, 6, 7, 8, 9, 10, 11, and 12, were hot isostatically pressed at 2215°F/15 KSI/ 3 hrs. at temperature and pressure. Metallographic TIP test on all but #5 of the above items indicated no evidence of gas entrapment. Serial number 5 is unacceptable and should not be used. All items in this shipment except for S/N 5 meet acceptable purchase order requirements.

TYPICAL SIEVE ANALYSIS:

MESH	%
+60	Trace
+80	7.4
+100	6.4
+120	5.7
+140	8.1
+170	9.0
+230	14.9
+270	8.5
+325	12.0
+500	16.2
-500	11.3

**APPENDIX B
CHEMISTRIES AND CASTING PARAMETERS
FOR MAR-M247 CAST-TO-SIZE TEST BARS**

Chemistries

<u>W/O</u>	<u>Heat 2741</u>	<u>Heat 5134</u>
Ni	Bal	Bal
Cr	9.50	8.75
Co	9.90	9.70
W	9.10	9.80
Al	5.38	5.32
Ti	1.60	0.94
Ta	3.30	2.92
Hf	1.29	1.47
C	0.13	0.15
Mo	0.52	0.92
Mn	0.03	0.03
Fe	0.16	0.20
B	0.016	0.016
Si	0.07	0.05

Casting Parameters

Refine Temperature - 2650^o Optical
 Pour Temperature - 2400^o Optical
 Mold Temperature - 1900^oF
 Insulation Practice - MgO Backup - Inoculated Mold
 Pour Time - 0-1 Second

APPENDIX C
CHEMISTRY, TIP RESPONSE, AND MECHANICAL PROPERTIES
FOR TEST RINGS PARTED FROM FULL-SCALE HUB DETAILS

Chemistry (Heat Code X-2324)

<u>C</u>	<u>Mn</u>	<u>Cr</u>	<u>Mo</u>	<u>Si</u>	<u>Al</u>	<u>Ti</u>	<u>Co</u>	<u>Fe</u>	<u>Zr</u>	<u>W</u>	<u>Ta</u>	<u>Hf</u>	<u>B</u>
0.11	0.05	12.55	1.98	0.05	3.59	3.94	9.05	0.05	0.04	4.12	3.80	1.02	0.013

TIP Response*

<u>Serial No.</u>	<u>Percent change</u>
CX 43072	-0.15
CX 43073	-0.13
CX 43074	-0.18
CX 43075	-0.12

Tensile Properties**

<u>Serial No.</u>	<u>Test temp (°F)</u>	<u>0.2% YS (ksi)</u>	<u>UTS (ksi)</u>	<u>Percent El</u>	<u>Percent RA</u>
CX43072	70	157.1	218.1	11.3	11.4
73	70	151.1	216.6	12.3	12.2
74	70	153.1	233.1	15.2	16.3
75	70	153.6	219.6	13.0	13.4
CX43072	1200	135.2	205.1	16.5	16.2
73	1200	125.1	199.5	18.6	17.4
74	1200	134.7	203.5	17.1	18.6
75	1200	136.7	202.5	18.1	16.0

1200°F 140-ksi Stress Rupture Properties**

<u>Serial No.</u>	<u>Hours to failure</u>	<u>Percent El</u>	<u>Percent RA</u>
CX43072	264.0	8.0	9.1
73	284.4	8.7	11.1
74	211.6	8.6	12.6
75	225.7	6.0	7.6

*Following exposure to 2200°F for 4 hr.
 **2050°F (2) gas fan cool + 1550°F (4) AC + 1400°F (16) AC.

APPENDIX D
WALL METAL TEMPERATURES

The thermal analysis reported in the main text of this report used an axisymmetric model to calculate an average circumferential blade temperature. This effort was supplemented with an approximation of blade circumferential temperature gradients based on the Ref. 2 report.

Heat transfer to radial inflow turbine rotors is a highly complex phenomenon. Analytical and experimental research are required to accurately define the surface velocity and the convective film coefficients on both the gas and coolant side of the airfoil. The flowpath of the radial turbine adds complexities in the boundary layer and mainstream flow structures because of centrifugal and Coriolis forces. Current differential and integral boundary layer analytical methods assume velocity profiles which do not include these important body forces. Therefore, current analytical efforts are restricted to "best approximations."

Two aspects of the thermal analysis relating to circumferential blade temperatures are subject to question. First, the blade suction and pressure surface velocities near the inducer tip are not clearly defined. As noted in Ref. 2, analytical solutions do not agree with water flow visualization test results. Second, flat plate heat transfer coefficients have been applied universally without proper experimental verification. In view of the apparent lack of technology in radial turbine heat transfer, the circumferential gradient in blade metal temperature have been approximated based on the Ref. 2 work. (Because of the similarity in blade aerodynamic loading between the HTRT and the Ref. 2 design the velocity gradients experimentally determined provide a good approximation of the HTRT flow field. Therefore, the hot side heat transfer coefficients of Ref. 2 provide a good approximation for establishing circumferential gradients for the HTRT blade.)

The blade pressure and suction side inner and outer wall temperatures were calculated using a simplified circumferentially oriented finite element model shown in Figure D-1. As indicated on the figure this section is located at 20 percent along the mean streamline. At Intermediate Rated Power (IRP) the relative gas temperature is 1990°F and the coolant temperature is 990°F at this location. Representative coefficients were obtained from Figure 30 of Ref. 2 (50 and 375 B/hr ft² °F for the pressure and suction sides, respectively). Using these data and the finite element model, axial metal temperature gradients shown in Figure D-1 were calculated. The strong influence of the connecting walls on the pressure and suction side surface metal temperature gradients is noted.

The results of this analysis indicate that localized fins or pins may be required for an aircooled radial turbine entering Engineering Development.

Wall Metal Temperature @ 20% Mean Streamline
100% IRP Design Point

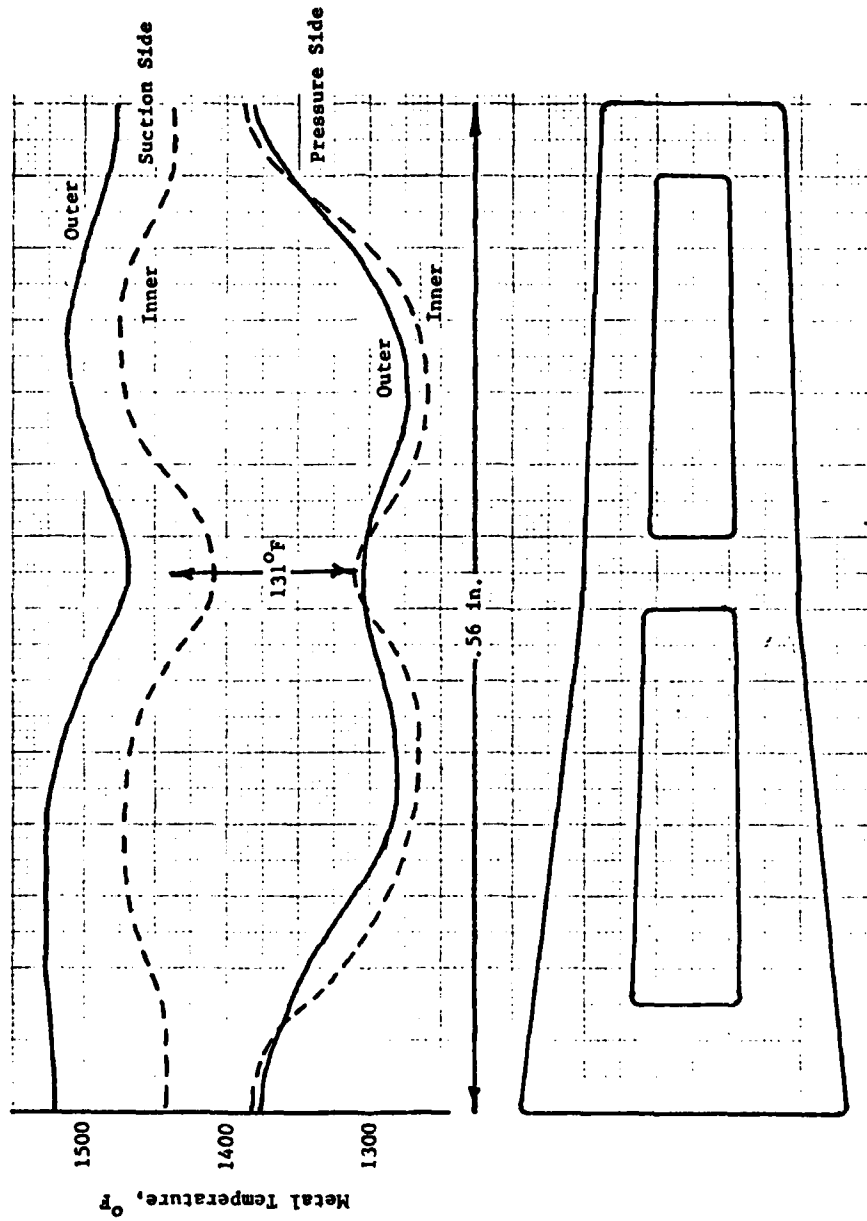


Figure D-1. Wall metal temperatures.